UNIVERSITÉ DE FRIBOURG
UNIVERSITÄT FREIBURG

Department of Physics
University of Fribourg (Switzerland)

Phononic and electronic excitations in complex oxides studied with advanced Infrared and Raman spectroscopy techniques

THESIS

presented to the Faculty of Science and Medicine of the University of Fribourg (Switzerland)
in consideration for the award of the academic degree of
Doctor of Philosophy in Physics

by

Fryderyk Lyzwa

from Göttingen, Germany

Thesis No. 2263
https://doi.org/10.51363/unifr.sth.2022.002
Fribourg, 2021

Accepted by the Faculty of Science and Medicine of the University of Fribourg (Switzerland) upon the recommendation of

Prof. Dr. Guillermo P. Acuña	University of Fribourg, Switzerland	President of the Jury
Prof. Dr. Christian Bernhard	University of Fribourg, Switzerland	Thesis Supervisor
Prof. Dr. Philipp Werner	University of Fribourg, Switzerland	Examiner
Prof. Dr. Matthieu Le Tacon	Karlsruhe Institute of Technology, Germany	Examiner

Fribourg, July 2nd, 2021

Thesis supervisor:

.....

Prof. Dr. Christian Bernhard

Dean:

.....

Prof. Dr. Gregor Rainer

Abstract

Complex oxides with perovskite structure exhibit a rich spectrum of exotic and emergent phases, including superconductivity, spin and charge ordering, ferroelectricity and flexoelectricity. Interestingly, several of these orders can coexist within the same material. A certain phase can be favored over the others by exposing the material to external stimuli. Decreasing the spatial dimensions in these materials to the atomic level, e.g. in the form of thin films, provides an additional control parameter.

In this thesis, several oxide-based materials, including the high-temperature superconductor $YBa_2Cu_3O_{6+x}$ (YBCO) in the form of bulk crystals and as thin films in heterostructures, and the dielectrics $SrTiO_3$ and $KTaO_3$, have been investigated. The measurements were performed as a function of various external stimuli, such as high magnetic or electric fields, temperature and UV-light illumination. Using advanced infrared and Raman spectroscopy techniques, novel experimental results have been obtained on the underlying physical mechanisms that lead to the interesting effects in these materials, which can be divided into three main topics:

I. Magnetic field effect on the optical response of an underdoped $YBa_2Cu_3O_{6.6}$ single crystal

The cuprate high-temperature superconductors are among the most intensively studied oxide-based materials. Even though they were discovered almost 35 years ago, there is still no consensus about the underlying pairing mechanism. Therefore, it is necessary to further investigate the cuprates' ground state orders and reveal their interplay. Special focus is drawn to the recently discovered three-dimensional (3D) copper charge density wave (Cu-CDW). Having its maximum in the underdoped region of the phase diagram, this 3D CDW was shown to develop at high magnetic fields above 15-20 Tesla, or when applying uniaxial pressure along the system's *a*-axis.

Here, the impact of a magnetic field of up to 30 Tesla on the infrared spectrum of an underdoped, twinned $YBa_2Cu_3O_{6.6}$ single crystal with T_c = 58(1) Kelvin was studied. The magnetic field was applied along the *c*-axis while the in-plane reflectivity was detected from 40 cm^{-1} to 6000 cm^{-1}. It was found that a magnetic field in excess of 20 Tesla suppresses the macroscopic response of the superconducting condensate. At the same time, surprisingly weak signatures of the 3D CDW have been observed in the form of a weak reduction of the Drude response which is compensated by an enhancement of the mid-infrared band and a narrow electronic mode around 240 cm^{-1} (and possibly a second one around 90 cm^{-1}). The latter modes were interpreted as the phasons of the CDW along the *b*- and *a*-axis, respectively. These findings suggest that short-ranged and slowly fluctuating CDW correlations are an intrinsic property of the YBCO crystal and are prominent already at zero magnetic field.

II. Observation of backfolded acoustic phonons in metal-oxide heterostructures

The quality control of thin film structures is a fundamental necessity for exploring the phenomena in such systems. Therefore, it is important to improve existing technologies as well as to find new approaches for studying thin films.

In this thesis, a promising ultrasonic probe was demonstrated in the form of backfolded acoustic phonons, which were observed for the first time in metal-oxide superlattices with Raman spectroscopy. These low-frequency modes originate from the reflection of sound waves at internal interfaces of the superlattice. They are independent of the substrate properties and their frequency is highly sensitive to atomic-scale thickness variations of the superstructure.

These modes can hence serve as a powerful characterization tool for thin film structures. In addition, a lineshape analysis of these superlattice modes can potentially yield further information about the coupling of sound waves to the low-energy spin, charge and orbital excitations.

III. ***Electric Field effect on $SrTiO_3$- and $KTaO_3$-based heterostructures***

Strontium titanate ($SrTiO_3$) has been one of the most studied perovskite oxides for decades, and yet new exotic phenomena and functionalities are still being discovered today. Currently, heterostructures of $AlO_x/SrTiO_3$ or $LaAlO_3/SrTiO_3$, which feature the formation of a two-dimensional electron gas at their interface, are heavily investigated. Especially interesting is the electric field effect, which can drive the system e.g. from an insulating to a metallic or even a superconducting state.

As part of this dissertation, back-gate voltages of up to 8 kV/cm were applied to heterostructures based on $SrTiO_3$ and $KTaO_3$ while investigating them using a combination of infrared ellipsometry and confocal Raman spectroscopy. We have observed anomalous polarization effects that are highly asymmetric and non-collinear with respect to the applied field. These polarization effects show a high remanence and hysteresis, and are strongly surface-sensitive. We have shown that these observations originate from the interplay of the oxygen vacancies and the tetragonal domain boundaries of $SrTiO_3$ below 110 Kelvin, which are absent in $KTaO_3$. In addition, we demonstrated that radiating UV light onto the sample surface suppresses these anomalous polarization effects. With this, we found an optical switch that allows to restore the original polarization state of the system.

The here presented results have implication for a broad field of ongoing research in solid state physics. They contribute in understanding the macroscopic effects in complex oxides, which might play a crucial role in future quantum technology. Moreover, the state of the art capabilities of optical spectroscopy were presented as a suitable characterization method in materials science.

Zusammenfassung

Komplexe Oxide sind erfolgversprechende Materialsysteme für zukünftige elektronische und phononische Bauelemente und aufgrund ihrer vielseitigen Eigenschaften potenziell sehr nützlich für Schalt- und Sensorelemente. In dieser Dissertation wurde eine Reihe komplexer Oxid-Systeme mittels Infrarot- und konfokaler Raman-Spektroskopie untersucht. Im Einzelnen wurden der Hochtemperatur Supraleiter $YBa_2Cu_3O_{6+x}$ (YBCO) in Form von Einkristallen als auch in Form von nanometergrossen dünnen Schichten in Heterostrukturen, sowie die Dielektrika $SrTiO_3$ und $KTaO_3$ untersucht. Die Messungen wurden als Funktion verschiedener externer Störungsparameter wie z.B. hoher magnetischer und elektrischer Felder, Beleuchtung mit UV-Licht sowie Variation der Temperatur durchgeführt. Die Ergebnisse können in drei Themenbereiche aufgeteilt werden:

I. Einfluss eines grossen Magnetfeldes auf die optische Antwort eines unterdotierten $YBa_2Cu_3O_{6.6}$ Einkristalls

Die kupferoxidbasierten Hochtemperatur-Supraleiter sind eine der am stärksten untersuchten Systeme unter den komplexen Oxiden. Obwohl sie bereits vor fast 35 Jahren entdeckt wurden, gibt es immer noch keine allgemein anerkannte Theorie für deren Paarungsmechanismus. Deshalb ist es wichtig deren Grundzustand und die darin vorkommenden Phasen weiter zu erforschen. Die kürzlich entdeckte dreidimensionale (3D) Kupfer-Ladungsdichtewelle (Cu-CDW), welche ihre maximale Stärke im unterdotierten Bereich des Phasendiagramms aufweist, erfährt momentan ein besonderes Interesse. Sie entsteht beim Anlegen hoher magnetischer Felder von über 15-20 Tesla, oder bei mechanischem Druck entlang der *a*-Achse des Systems.

In dieser Arbeit wurden die Auswirkungen eines magnetischen Feldes bis zu 30 Tesla auf das Infrarotspektrum eines unterdotierten, gezwillingten $YBa_2Cu_3O_{6.6}$ Einkristalls mit einer Sprungtemperatur von T_c = 58(1) Kelvin gemessen. Das magnetische Feld wurde entlang der *c*-Achse angelegt während die Reflektivität in der *ab*-Ebene von 40 cm^{-1} bis 6000 cm^{-1} gemessen wurde. Es wurde gezeigt, dass ein Magnetfeld oberhalb von 20 Tesla die makroskopische Antwort des supraleitenden Kondensats unterdrückt. Des Weiteren wurden überraschend kleine Auswirkungen auf die 3D CDW beobachtet: Es wurde lediglich eine schwache Unterdrückung des Drude-Beitrages beobachtet die kompensiert wird von einer Verstärkung des breiten mittleren Infrarotbandes (MIR) sowie einer schmalen elektronischen Mode bei 240 cm^{-1}, und möglicherweise einer weiteren bei ca. 90 cm^{-1}. Die beiden letztgenannten Moden wurden als Phasonen der CDW interpretiert, jeweils entlang der *b*- und *a*-Achse. Diese Ergebnisse deuten darauf hin, dass kurzreichweitige und langsam fluktuierende CDW Korrelationen bereits ohne ein angelegtes Magnetfeld existieren und damit einen wesentlichen Bestandteil der intrinsischen Eigenschaften des YBCO Kristalls darstellen.

II. Beobachtung von zurückgefalteten akustischen Phononen in Metalloxid-Heterostrukturen

Die Qualitätskontrolle von dünnen Schichten ist grundlegend für die Erforschung solcher Strukturen nach exotischen Effekten. Deshalb müssen bestehende Technologien weiter verbessert bzw. neue gefunden werden.

Mittels konfokaler Raman-Spektroskopie wurden in dieser Arbeit zurückgefaltete akustische Phononen erstmals in Metalloxid-Heterostrukturen beobachtet. Diese niederfrequenten Moden entstehen aufgrund der Reflektion von Schallwellen an internen Grenzflächen des Übergitters. Sie sind unabhängig vom Substrat und deren Frequenz ist höchst sensitiv auf eine Variation der einzelnen Schichtdicken. Daher ist deren Verwendung als präzise Untersuchungsmethode vielversprechend. Zusätzlich kann eine Analyse der Linienform dieser Übergitter-Moden potenziell weitere Informationen liefern, z.B. über die Kopplung von Schallwellen zu niederenergetischen Spin-, Ladungs- oder Orbitalanregungen.

III. Elektrischer Feldeffekt in $SrTiO_3$- und $KTaO_3$-basierten Heterostrukturen

Obwohl Strontiumtitanat ($SrTiO_3$) in den letzten Jahrzehnten intensiv erforscht wurde, werden aktuell immer noch exotische Phänomene und Funktionalitäten entdeckt. Heutzutage werden vor allem $AlO_x/SrTiO_3$ und $LaAlO_3/SrTiO_3$ Heterostrukturen untersucht, welche ein zweidimensionales Elektronengas an deren Grenzfläche bilden. Besonders interessant ist der elektrische Feldeffekt, durch welchen das System z.B. von einem elektrisch isolierenden in einen metallischen und sogar supraleitenden Zustand geschaltet werden kann.

In dieser Arbeit wurden elektrische Spannungen bis zu 8 kV/cm an $SrTiO_3$- und $KTaO_3$-basierten Heterostrukturen angelegt und mittels kombinierter Infrarot-Ellipsometrie und konfokaler Raman-Spektroskopiemessungen untersucht. Es wurden anomale elektrische Polarisationseffekte beobachtet, die asymmetrisch und nicht-kollinear zum angelegten elektrischen Feld sind. Diese Effekte weisen eine Hysterese und eine Remanenz auf und sind am stärksten nahe der Probenoberfläche. Diese Beobachtungen werden erklärt durch ein komplexes Zusammenspiel von Sauerstofffehlstellen mit den tetragonalen Domänengrenzen von $SrTiO_3$ unterhalb einer Temperatur von 110 Kelvin, welche in $KaTO_3$ nicht vorhanden sind. Zusätzlich wurde gezeigt, dass durch Beleuchten der Probenoberfläche mit UV-Licht diese anomalen elektrischen Polarisationseffekte unterdrückt werden können. Damit wurde ein optischer Schalter gefunden, mit dem der ursprüngliche Zustand des Systems wiederhergestellt werden kann.

Die aktuellen Möglichkeiten von optischer Spektroskopie als nützliche Untersuchungsmethode in den Materialwissenschaften wurden präsentiert. Die gefundenen Ergebnisse haben Bedeutung für mehrere aktuelle Forschungsbereiche in der Festkörperphysik. Sie tragen zum Verständnis der makroskopischen Effekte in komplexen Oxidsystemen bei, die potenziell wertvoll für zukünftige Quantentechnologien sind.

Abbreviations

AFM	atomic force microscopy
Å	angstrom
AFD	antiferrodistortive
ARPES	angle resolved photoemission spectroscopy
B	magnetic field
CCD	charge-coupled device
CDW	charge density wave
χ	electric susceptibility
cuprates, CuSC	cooper oxides superconductors with perovskite structure
Δ	energy gap; difference; phase shift between the reflected s-and p-polarized light
E	electric field; light polarization vector
EM	electromagnetic
e	electron charge
eV	electron volt
ε	dielectric function
ε_1, ε_2	real and imaginary part of the dielectric function
ε_0	dielectric constant or the permittivity
ε_∞	spectral weight from excitations at high energies
$\langle\varepsilon\rangle$	pseudo-dielectric function
$\hat{e}$	unit vector along the wave's polarization
FFT	fast Fourier transform
FIR	far-infrared
γ	broadening
high-T_c, HTSC	high-temperature superconductor
HWHM	half-widths at half-maximum
h	Planck constant
I	light intensity
IR	infrared
K	Kelvin
K	wave vector
k	extinction coefficient
KK	Kramers-Kronig
LO	longitudinal optical
LSAT	$La_{0.3}Sr_{0.7}Al_{0.65}Ta_{0.35}O_3$
LCMO	$La_{1-x}Ca_xMnO_3$
λ	wavelength
MIR	mid-infrared
m^*	effective mass
NA	numerical aperture
NCSMO	$Nd_{1-x}(Ca_{1-y}Sr_y)_xMnO_3$

NIR	near-infrared
NMR	nuclear magnetic resonance
n	real part of the complex refractive index
$\tilde{n}$	complex refractive index
ω	frequency
ω_0	eigenfrequency
ω_{pl}	plasma frequency
ω_c	cutoff frequency
$\Omega_{pl,SC}^2$	superfluid density of Cooper pair density
PDW	pair density wave
PLD	pulsed laser deposition
PPMS	Physical Property Measurement System
pnictide	iron-based high-temperature superconductor
P	polarization, polar moment
P	Cauchy principal value
p	hole doping
ϕ	phase of light
ϕ_o	quantized magnetic flux
φ	angle of incidence (AOI)
φ_B	Brewster angle
Ψ	amplitude-ratio of the Fresnel reflection coefficients
q	charge; momentum
RHEED	reflection high-energy electron diffraction
RIXS	resonant inelastic x-ray scattering
$\tilde{R}$	Raman tensor
R	reflectivity, electrical resistance
R_H	Hall coefficient
r_p, r_s	Fresnel reflection coefficients
σ	optical conductivity
σ_1, σ_2	real and imaginary part of the optical conductivity
SC	superconductivity, superconductor
SERS	surface-enhanced Raman spectroscopy
SOC	spin-orbit coupling
SNOM	scanning near-field optical microscopy
STM	scanning tunneling microscopy
SW	spectral weight
TEM	transmission electron microscopy
TERS	tip-enhanced Raman spectroscopy
TO	transverse optical
T	Tesla
*T**	transition temperature from the cubic into the tetragonal state in $SrTiO_3$
T_c	superconducting transition temperature
$T_{Curie,}$ T_C	transition temperature of ferro-, piezo- or pyroelectric state
UHV	ultra-high vacuum

UV	ultraviolet
V	voltage
VIS	visible
XRR	x-ray reflectivity
XRD	x-ray diffraction
ξ	correlation length
YBCO	$YBa_2Cu_3O_{6+x}$
Z_0	impedance
2DEG	two-dimensional electron gas

Preface

This thesis presents the main research that I conducted during my PhD from 2016 to 2021 in the group of Prof. Dr. Christian Bernhard in Fribourg, Switzerland. I studied several complex oxide materials in the form of bulk crystals and thin films via advanced infrared and Raman spectroscopy techniques and in combination with external perturbation parameters such as temperature change, application of high electric or magnetic fields and exposure to UV light. In particular, the high-temperature superconductor $YBa_2Cu_3O_x$, superlattices of complex perovskite oxides, and two-dimensional electron gases based on $SrTiO_3$ and $KTaO_3$ were investigated. These materials host a wide variety of emergent and tunable properties that could be used to improve existing and future quantum technological devices.

The temperature-dependent infrared spectroscopy measurements were done at the Fribourg University and the magnetic-field-dependent experiments at the High Magnetic Field Laboratory (*LNCMI*) in Grenoble, France in the group of Dr. Milan Orlita. The confocal Raman measurements were performed at the Max-Planck Institute for Solid State Research in Stuttgart, Germany in the department of Prof. Dr. Bernhard Keimer.

I designed and performed the measurements, the analysis and interpretation of the data in collaboration with Christian Bernhard, Benjamin Mallett, Premysl Marsik, Milan Orlita, Matteo Minola and Yurii Pashkevich. The studied samples were grown by the group of Dr. Manuel Bibes, CNRS Paris, or were 'home-made' at the University of Fribourg via pulsed laser deposition.

Chapter 1 provides a general introduction of the thesis topic. Chapter 2 presents the studied complex oxide systems and the state of the art of the research. The used experimental methods, infrared and Raman spectroscopy, are explained in chapter 3 in conjunction with the analysis methods. Special emphasis is given to the above mentioned applied external stimuli as well as to the probe's surface- and depth-sensitivity, interface-engineering and the resulting technical challenges. The main results are presented in chapters 4 to 6 in the form of published (or submitted) papers, each beginning with an additional introduction and an ensuing *Comments and Outlook* section:

The thesis ends with a general conclusion in chapter 7.

Contents

Physics appears to the layman mysterious and uncanny, not only because it produces technical miracles […], but also because it is such a dual world, containing on the one hand solid instruments and machines, and on the other hand invisible entities with incredible properties.

- Max Born, from [1]

Chapter 1

Introduction

Solid state physics has played a central role in designing our world as we know it today. A crucial task in this century for materials scientists is to improve computation and find new pathways to solve the energy problem. The rise in power consumption required by information and communication systems urgently needs to be curbed in order to sustain this growth [2]. The search for suitable materials in e.g. future computation devices is significant.

Promising candidates for next-generation devices are the *transition metal-oxide perovskites*, which host a plethora of novel physics, including emergent phases of spin, charge, orbital and structural origin. They are also often very susceptible to external stimuli, yielding complex phase diagrams of these materials.
Typical representatives of this family of materials are the *copper oxides* or *cuprates*, which can be tuned from e.g. a Mott-insulator into a superconducting phase that conducts electric current without an energy loss. A paramount goal is to understand their superconducting pairing mechanism, which is the reason why the investigation of their ground state orders has highest priority. One of these ground state phases is a charge density wave, which in recent years has gained much attention in the scientific community.
A relatively modern approach in tailoring a material's properties is to reduce the system's dimensions to the atomic level, such as thin films. By carefully controlling the interfaces between the layers of oxide heterostructures, it is possible to change the balance of competing orders and even to induce new exotic states, which are inaccessible in bulk materials.
A prominent example is the two-dimensional electron gas that is formed at the interface of two band-insulators such as $LaAlO_3$ (or AlO_x) and $SrTiO_3$. A gate voltage allows e.g. to tune the system from an insulator to a metal [3] and even to a superconductor [4], or to increase the magnitude of the Rashba spin-orbit interaction [5]. Other examples include cuprate/manganite multilayers, for which it has been found that the properties of the cuprate layers are drastically influenced by the manganite layers [6]. Among thin films, especially interesting are superlattices of complex oxide layers, in which the periodicity of the superstructures presents an additional control parameter and thus provides further application perspectives.
The macroscopic effects observed in these materials are governed, to a large extent, by the behavior of the phonons and electrons. Therefore, it is essential to study the low-energy dynamics of the material system.

A common approach to investigate a material's phononic and electronic properties is optical spectroscopy, in particular infrared (IR) and Raman spectroscopy. These techniques are sensitive to the low-energy excitations with no momentum transfer, $q \approx 0$, and can provide valuable information on the polarization state of the system.
Photons have several advantages over other probing methods: they are non-destructive and non-invasive for lower energy ranges, yet they can trigger light-induced transitions at higher energies. They can also be polarized, thus providing important information on the symmetry of the material structure.

However, despite IR and Raman spectroscopy being standard diagnostic tools in materials science, they have not been used extensively in combination with external stimuli such as high electric/magnetic fields, UV-light exposure, low temperatures, or high pressure.
This might be surprising, given that photons are not interacting with any of these perturbations (since they do not carry an electrical charge or magnetic moment), which makes optical spectroscopy an ideally suited probe – in principle. The incompatibility originates from technical issues, such as fitting the required optical elements into the experimental setup, a low signal-to-noise ratio, an insufficient signal stability over time or small features hidden within large background signals. Furthermore, it is not trivial to investigate and distinguish surface-effects from effects arising from the bulk, since the penetration depth of the probing light strongly depends on the material properties.
This highlights the importance of both improving the existing methodologies and finding new suitable approaches in order to explore in detail the underlying mechanisms which are present in strongly correlated materials.

In this work, advanced infrared and Raman spectroscopy techniques have been used in order to obtain information on the low-energy electronic and phononic dynamics of several complex oxide systems. The measured spectra were derived under various conditions of temperature, external electric or magnetic fields and/or UV-light exposure.
First, the optical signatures of the magnetic-field-induced charge density wave in the underdoped high-temperature superconductor $YBa_2Cu_3O_{6+x}$ have been studied by means of THz-infrared reflectivity (chapter 4). Secondly, confocal Raman spectroscopy was used to study the emergence of backfolded acoustic phonons in metal-oxide superlattices, and show their high potential as a state of the art characterization tool for superstructures (chapter 5). Finally, the electric field effect on $SrTiO_3$- and $KaTiO_3$-based heterostructures was explored using a unique combination of infrared ellipsometry and confocal Raman spectroscopy (chapter 6).

Chapter 2

Scientific background of complex oxides

The term *complex oxides* in this thesis stands for *complex transition metal oxides with perovskite structure*. Perovskites are a material group with general ABO_3 structure (see Fig. 2.1). They possess an inversion center (here it is the *B*-atom), so that Raman and infrared spectroscopy present complementary techniques to investigate members of this material class.

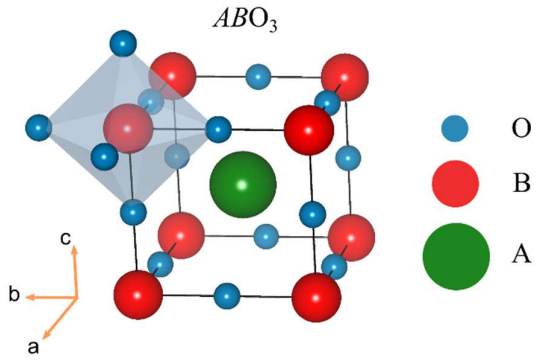

***Figure 2.1 Unit cell of an ideal cubic ABO_3 perovskite** [7].*

These materials have electrons which are strongly correlated and exhibit a high number of charge, spin and lattice degrees of freedom. Which order becomes dominant in the system can be influenced and tuned by external control parameters such as a magnetic and electric field, pressure, temperature, chemical doping etc., that can give rise to intriguing phenomena like metal-insulator transitions, colossal magnetoresistance, flexoelectricity and or superconductivity. Sometimes, their properties seem quite contradictory, e.g. the co-existence of magnetism and superconductivity in the cuprate family (see next chapter). Their macroscopic behavior is largely governed by the anisotropically shaped *d*-orbital. Whereas conventional metals and semiconductors can usually be described in a single electron band picture, in complex oxides the strong Coulomb interaction and the phenomena arising due to the partially filled *d*-shell make the understanding more intricate.

Embedding complex oxides as thin films in heterostructures multiplies the degrees of freedom and can lead to an enhancement or suppression of certain bulk properties or even create new phases [8]. Such heterostructures present a versatile tool to design and tune the properties of the complex oxides. Being able to deposit atomically sharp layers on top of each other, and even study separately certain layers and properties of this 'sandwich', is testimony for the scientific and technological progress in the last decades. An especially interesting aspect is the presence of metallic phases in normally dielectric and insulating oxides. Complex transition metal oxides are not only interesting because of their scientific importance, but are also promising candidates for future electronics and phononics.
In the following, the scientific (and partly historical) background on the here studied complex oxide systems will be displayed, which includes the high-temperature superconductor $YBa_2Cu_3O_{6+x}$ in bulk or placed as thin films in metal-oxide superlattices, and the dielectrics $SrTiO_3$ and $KTaO_3$ as sources of two-dimensional electron gases.

2.1 High-temperature superconductor $YBa_2Cu_3O_{6+x}$

In 1908, Heike Kamerlingh Onnes successfully fabricated liquid helium [9] with a temperature of 4.2 K, which set the foundation stone for the research field of *low-temperature physics*. Three years later, by performing temperature-dependent measurements of the electrical resistance of mercury, he could observe a sharp drop in the resistance *R,* which was later found to be really $R = 0$ [10], when cooling below a certain critical temperature T_c. This groundbreaking discovery of a 'super-conducting' state at low temperatures has been observed in several other materials and compounds (see Fig. 2.1.1). Since then, this topic has received much attention in the solid state community and still fascinates scientists today.

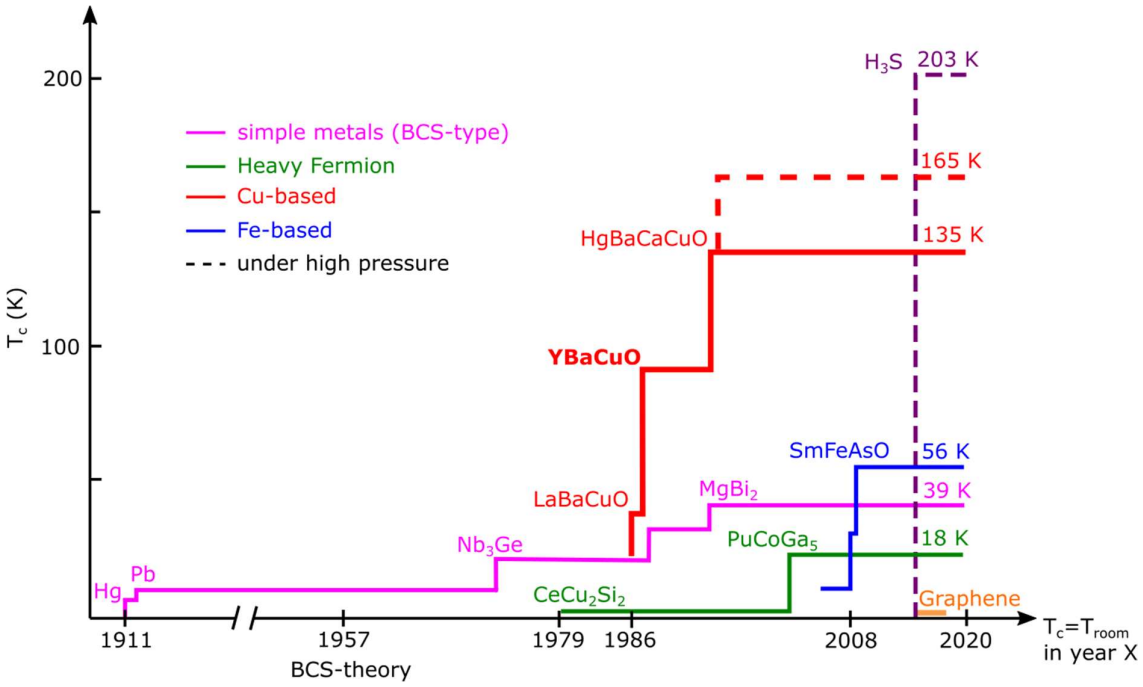

***Figure 2.1.1 Time line of T_c for a selection of superconducting materials (adapted and updated from** [11]**).** The graph shows the transition temperature T_c in the year when the material(-class) was discovered or found to be superconducting. Note that this sketch is not complete and does not contain all known superconducting materials.*

From a phenomenological point of view, a superconductor (SC) has: 1) zero electrical resistance and 2) expels magnetic field lines from its interior, which is known as the *Meissner effect* [10].
The microscopic picture of this quantum state is more intricate. In the late 1950s, such a theory was successfully delivered by J. Bardeen (the professor), L. N. Cooper (the postdoc) and J. R. Schrieffer (the PhD student), which is nowadays known as the famous BCS theory [12]. In principle it states: In any material, the electrons (fermions) experience generally a strong Coulomb repulsion. However, in superconductors, by coupling to phonons, this repulsion can be overcome such that two electrons bind to form a pair. All of those *Cooper pair*s simultaneously condense into the same state (as bosons) and have therefore a common macroscopic wave function [11]. The macroscopic nature of the common wave function prohibits the scattering of individual electrons on defects and thus enables dissipation-free electric currents. The BCS theory holds well for simple metals and compounds such as mercury, lead etc., where the formation of Cooper pairs originates from the electron-phonon interaction. Such materials are categorized as *conventional superconductors*.

Until 1986 it was agreed, following the BCS theory, that the T_c could not be much higher than ~30 K for any material[1]. In that year though, J. G. Bednorz and K. A. Mueller from the IBM laboratory in Rüschlikon, Switzerland, introduced the copper-based compound $La_{2-x}Ba_xCuO_4$ [13], which exceeded the record of T_c~23.3 K for Nb-Ge thin films. This breakthrough started the era of the *high-temperature superconductors* (*high-T_c*), which was honored with the Nobel Prize in the following year. Motivated by the isotope-effect, the application of external pressure causes an even further increase of the transition temperature to ~52 K. In analogy, substituting La by Y increases the chemical pressure in the lattice, and leads to a T_c~90 K for $YBa_2Cu_3O_{7-\delta}$ [14]. Until today, these *cuprates* still hold the record T_c value for materials at 'normal' conditions (i.e. ambient pressure) with ~135 K in the HgBaCaCuO system [15].

Another type of high-T_c superconductor was discovered in 2008 in the family of Fe-based materials [16]. These *pnictides* (compounds of N, P, As, Sb, Bi) and *chalcogenides* (with S, Se, Te) reach a maximum T_c of about 60 K. For such Fe- and Cu-based materials, the well-understood quantum theory for conventional metals and superconductors fails [11]. These highly correlated electron systems are often referred to as *unconventional superconductors*, where the pairing mechanism is not likely to be based on a simple electron-phonon interaction. They often exhibit both magnetic and SC ground state orders, which are antithetical in elemental superconductors.

Besides Fe-SC and Cu-SC, a superconducting order was found in other exotic material families, like in *Heavy fermion* systems (discovered in 1979 by Steglich et al. [17]), in which the application of high external pressure to a sulfur hybride system yields a T_c~203 K [18]. Even graphene can become superconducting [19], and several other materials which are not included in Fig. 2.1.1.

All of these examples and various classes of superconductors imply that the SC pairing mechanism is much more intricate than it was believed when discovered more than a century ago. Superconductivity has turned out to be not just a special case of a few materials but is recognized as an increasingly common property of matter.

Nowadays, superconductors already play a tremendous role in research, medicine, education and industry. They mostly come into action when a high magnetic field and therefore a large amount of electrical current is required. Prominent examples are particle accelerators (e.g. at the CERN in Geneva), magnetic resonance imaging (MRI) and nuclear fusion reactors. Superconductors can also be used to demonstrate the beauty of science to a broad audience. One example to introduce superconductivity and physics to students by presenting superconducting model trains, like it is done here at the University of Fribourg.

Primary goals for the future certainly include revealing the SC pairing mechanism, finding a theory which can accurately predict the T_c for a material and subsequently provide commercially available room temperature superconductors[2]. This dream of material scientists to create high magnetic fields without a loss in current and to transport electrical current over infinitely long distances would revolutionize our existing world once more.

[1] However, in 2001 a T_c~39 K was found in magnesium diboride (a simple metal), where the electron-phonon mechanism is optimized [281].

[2] Note, that in October 2020 room-temperature superconductivity was reported in pressurized carbonaceous sulfur hydride [282]. Still, there are conflicting arguments about these findings and the interpretation [283].

2.1.1 Ground state orders and properties of $YBa_2Cu_3O_{6+x}$

In copper-based systems, the underlying mechanism of superconductivity cannot be explained with the BCS theory, nor by any other conventional quantum theory (yet). One reason is their complexity and their various ground state orders, such as charge and spin ordered states that coexist or compete with superconductivity. Since the superconducting pairing mechanism is still unknown, intensive experimental and theoretical research is performed.

Figure 2.1.2(a) displays the unit cell of $YBa_2Cu_3O_{6+x}$ (with x = 1)[3]. The transition metal oxide has a perovskite-like structure, with Yttrium at its inversion symmetry center. The common structural feature of the cuprate HTSC family are the CuO_2 planes (*copper oxide planes*), marked in yellow color, which host the mobile charge carriers and the superconducting condensate. The 1D chains which are directed along the *b*-axis, play an important role as a charge reservoir for the CuO_2 planes.

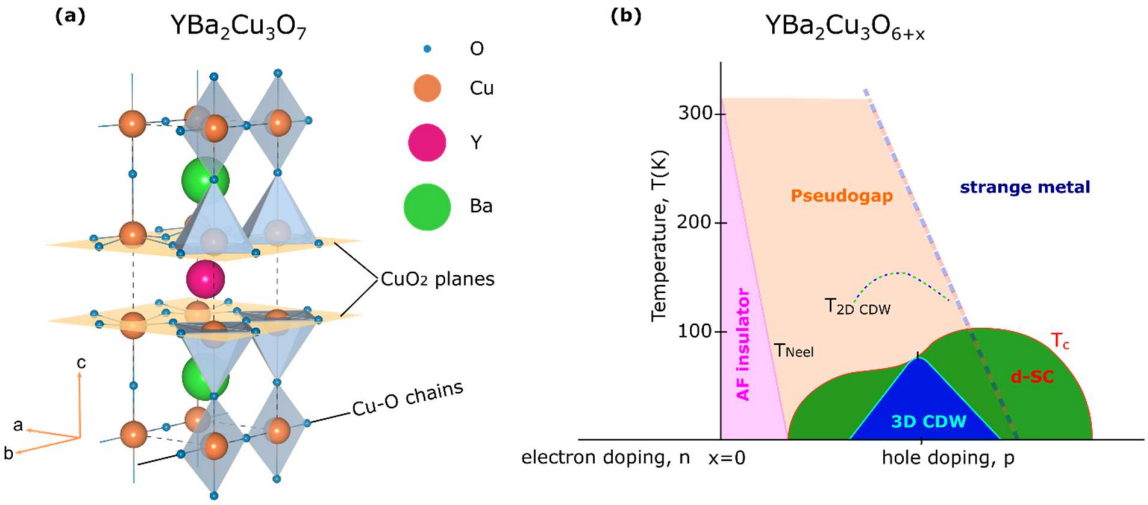

Figure 2.1.2 (a) Crystallographic structure and (b) phase diagram of the ground state orders of the high-temperature superconductor $YBa_2Cu_3O_{6+x}$ (adapted from [7] and [11], respectively). *In the temperature versus hole doping (=hole doping per planar Cu) phase diagram (b), the dark blue region represents the 3D CDW, which is induced by applying a high magnetic field.*

As can be seen in Fig. 2.1.2(b), the phase diagram of the cuprates resembles a 'zoo' of different ordered states. By changing e.g. the chemical substitution or tuning the stoichiometry (e.g. the oxygen content), temperature variation or by applying pressure or a magnetic field, the system can be driven into various states. Different phases are realized by changing the amount of oxygen in the CuO chains. That means, for more (less) oxygen in the CuO chains, there are electrons removed (added) from (to) the CuO_2 planes, which is referred to as hole doping (electron doping). Both doping sides exhibit a superconducting dome in the phase diagram (for a review see [16]). For electron-doped cuprates, the superconducting carriers are electrons, instead of holes, and have smaller maximum critical temperatures than the hole-doped ones [20].

[3] In other literature sources, another convention is used to define the oxygen content, namely $YBa_2Cu_3O_{7-\delta}$ with $\delta = 1-x$.

Here, we will focus on the hole-doped side. The undoped parent compound $YBa_2Cu_3O_6$ at x = 0, which has no oxygen in the CuO chains, is a Mott-insulator with a long-range antiferromagnetic (AF) order of the planar Cu spins (light magenta region). Upon increasing the oxygen content of the CuO chains to x=0.4 (corresponding to a hole concentration of p~0.05 in the CuO_2 planes) the long-range AF order and the Mott-gap are rapidly suppressed. At higher doping levels, a superconducting dome emerges in the range of 0.05 < p < 0.28. The *optimally doped* state with a transition temperature of about 93 K [14, 21] is reached at around x = 0.9 (i.e. p ~ 0.15). The regions in the phase diagram at lower or higher hole doping, at which T_c decreases, are called *under-* and *overdoped*, respectively. On the underdoped side, the normal state properties are highly anomalous and dominated by a so-called pseudogap phenomenon which gives rise to a partial, gaplike suppression of the low-energy electronic states. The origin of this pseudogap is still heavily debated and the explanations range from various kinds of competing orders to precursor superconducting pairing correlations [11]. In the overdoped regime, the normal state properties become more conventional and resemble the ones of a bad metal with a rather high electron scattering rate.

This large variety of different ground state orders makes the cuprate family so fascinating. Especially the co-existence of magnetic order (arising from strong repulsive interactions between the electrons) and superconductivity are seemingly antithetical forms of orders compared to BCS-type SCs [11]. Completing this phase diagram, as well as revealing the orders' relationship, presents the key for finding the superconducting pairing mechanism.

Suppressing the superconducting condensate

A common approach to further study the superconducting order, i.e. to obtain more information on the possible pairing mechanism and its relationship to other ground state orders, is to suppress the condensate. In order to break superconductivity, an energy barrier of 2Δ must be overcome. This is for instance achieved by chemical doping, raising the temperature above T_c or by applying a sufficiently high electrical current or magnetic field. The latter approach plays a main role in this thesis.

The material's behavior when exposed to a magnetic field depends on its type of superconductor class [10]. For *type I* superconductors (e.g. mercury, lead) the application of relatively small magnetic fields fully suppresses the condensate at an upper critical field, B_{c1}. For *type II* superconductors, encompassing most of the high-T_c materials, there exist two critical magnetic fields with $B_{c1} < B_{c2}$. From zero Tesla to B_{c1}, which is typically quite low, no magnetic field lines enter and therefore the material behaves similar to a *type I* SC for which the magnetic field is completely screened from the interior. Between B_{c1} and B_{c2}, the magnetic field can partially enter into the material in the form of vortex lines which have a normal state core that is surrounded by superconducting ring currents that create a quantized magnetic flux of $\phi_o = \frac{h}{2e}$. Above B_{c2}, superconductivity is completely suppressed. Especially for the cuprates, this upper critical field tends to be large, i.e. on the order of about 100 Tesla for optimally doped YBCO, and thus difficult to access with laboratory-based magnets [10]. Note, that destroying the superconducting state is not necessarily the same as suppressing the macroscopic response of the condensate, since short-ranged and/or fluctuating superconducting correlations may persist in even higher fields. Interestingly, the application of a magnetic field can also restore the coherent superconducting response of some materials, which is for instance the case in certain YBCO/Manganite-based multilayers [22, 23].

Charge density waves and intertwined orders

Ordered modulations of the spin (i.e. spin density wave, SDW), of the charge (charge density wave, CDW) or even of the superconducting order parameter (pair density wave, PDW) are further ground state orders, and are believed to play an important role in the properties of high-T_c SCs and to potentially help to reveal the superconducting pairing mechanism. Their exact patterns, characteristics, and their interplay are debated and under current research. For instance, for a long time it was assumed that for the underdoped cuprates a *stripe order* exists, i.e. a phase of intertwined charge and spin modulations. Recent *nuclear magnetic resonance* (NMR) measurements at high magnetic fields however found a long-range CDW order [24].

In this work, we focus on charge density waves. Two different types of charge orders are found in the cuprates, as displayed below. In both types, their period is incommensurate with the underlying lattice, i.e. q/a is irrational, with q being the wave vector and a the lattice constant [25]. They are spread along the CuO_2 planes (just as the superconducting carriers) and are referred to as *Cu-CDWs*.

2D CDW. The two-dimensional charge density wave (2D CDW) in cuprates has its maximum strength for hole dopings of p ~ 0.11 - 0.12, with an in-plane wave vector of about $q \sim 0.25 - 0.33$ r.l.u. and a rather small correlation length of less than 10 nm [26]. These short-ranged quasi-2D charge density correlations appear in the underdoped region below a temperature of ~150 K and become gradually stronger with further cooling until a sharp decrease occurs when reaching the T_c - line [26-28]. There is even compelling evidence that charge density wave correlations are present in large parts of the temperature and doping phase diagram of $YBa_2Cu_3O_{6+x}$ [11]. Several reports show that this 2D CDW can be further enhanced by applying a magnetic field along the *c*-axis [24, 29-32] or pressure along the *a*-axis [33].

3D CDW. The long-ranged and three-dimensional charge density wave (3D CDW) [11] is observed when applying uniaxial pressure [33] or a magnetic field above a threshold value of ca. 15-20 Tesla [29, 30]. This 3D Cu-CDW appears in strongly underdoped samples and is presumably fully located inside the SC dome (dark blue area in Fig. 2.1.2(b)) and shows maximum strength at p ~ 0.11-12 (just like the 2D CDW). This doping range is also known as the *1/8-anomaly* (e.g. [34]), where the superconducting T_c - line (marked in red color in Fig. 2.1.2(b)) exhibits a local plateau.

Whether these two types of incommensurate CDWs constitute the same order is unclear. They have identical wave vectors along the crystallographic *b*-axis [35], but show different temperature and magnetic field dependences [30]. The origin of these CDWs in the cuprates, and in several other materials, remains to be understood. Their connection with superconductivity is also unknown. Applying a magnetic field certainly suppresses superconductivity, so that periodic modulations in the electronic density become the governing order in the phase diagram for underdoped cuprates.

As was shown by Gerber et al. [30], by using a pulsed magnet and an x-ray free electron laser, the in-plane wave vector of the 3D CDW is field independent whereas its strength increases with higher magnetic field. This suggests that superconductivity and the magnetic-field-induced charge ordering are closely connected.

Gap features in the optical spectra of cuprates and other high-T_c superconductors

Investigating the superconducting ground state means studying the low-energy excitations of the system, as well as the electronic behavior of these materials, namely the Fermi surfaces.

Figures 2.1.3(a) and (b) sketch the Fermi surfaces of members of the pnictide and cuprate family, respectively. The images show that the pnictides are *s-wave* superconductors (just as BCS-type superconductors, but with additional electron pockets located at the Brillouin zone edges), whereas the cuprates have *d-wave* symmetry [16]. The Fermi surface of a material is typically derived via *angle resolved photoemission spectroscopy* (ARPES). The observation of quantum oscillations and of a negative Hall coefficient R_H provided strong indications of small electron pockets[4] in the Fermi surface of cuprates [36]. This reconstruction of the Fermi surface can be explained by a charge density wave that breaks the translational symmetry [36, 24].

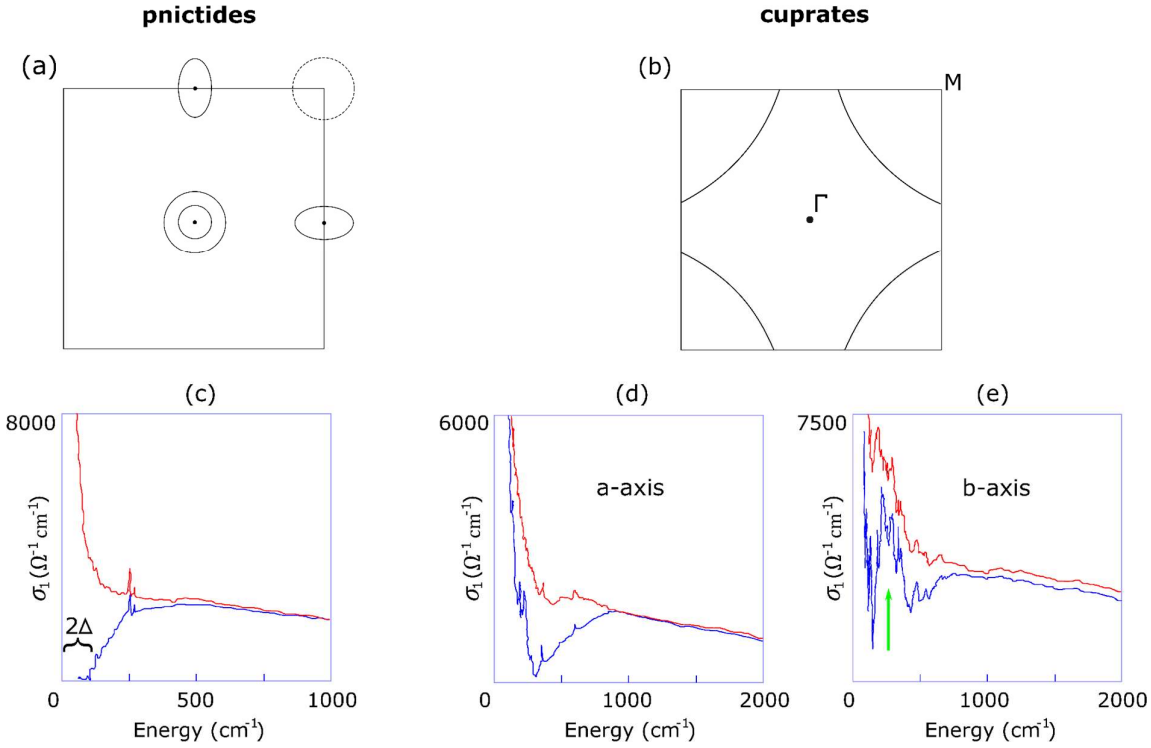

***Figure 2.1.3 Fermi surfaces and optical response of superconductors. (a), (b)**: Sketch of two-dimensional cross sections of the Fermi surfaces of pnictides and of weakly doped cuprates, respectively [14]. Real part of the optical conductivity for **(c)** a pnictide ($Cs_1Ca_2Fe_4As_4F_2$ single crystal [35]) and **(d)**, **(e)** the a-axis and b-axis response of a cuprate (single crystal of optimally doped, detwinned $YBa_2Cu_3O_{6.95}$) [36]. The red curves represent the optical spectra of the normal state (just above T_c), the blue curves the ones of the superconducting state. The green arrow indicates a strong and broad mode at around 240 cm^{-1}.*

Infrared spectroscopy (IR) is also a well-suited technique to study superconducting materials, i.e. the gap formation, collective modes, and in general pair-breaking excitations [39]. For instance, the superconducting energy gap Δ can be determined, as shown in Fig. 2.1.3(c) for the case of an iron arsenide SC [37] with an isotropic gap with s-wave symmetry.

Here, the real part of the optical conductivity σ_1 in the SC state well below T_c (blue curve) drops down to zero below a threshold frequency that corresponds to roughly twice the SC energy gap.

[4] The exact location of the electron pocket in k-space is still unknown [36].

For the cuprates, on the other hand, the low-energy optical spectra are very different: For $T < T_c$, the low-energy part of σ_1 is only partially suppressed, but does not reach zero (the spectra for the *a*- and *b*-axis response are displayed in Fig. 2.1.3(d) and (e)). Instead, there is a large part of spectral weight (SW) which is undefined (marked by a green arrow in Fig. 2.1.3(e)). The origin of this additional SW has been debated for decades: Opinions range from impure crystals [40], whereas others suggested a relationship of this SW to the charge ordering [38,41]. In the spectra shown below, the most pronounced feature is a very broad and strong mode around 240 cm^{-1} (marked with a light green arrow), which mostly appears in the optical response of the *b*-axis component.

Infrared spectroscopy is a promising tool to reveal valuable information on CDWs, since these typically form a dipole moment, which can be probed by electromagnetic waves (i.e. infrared light). However, there have been only few infrared studies carried out at high magnetic fields for cuprates [42-44]. This is mostly due to the low signal-to-noise ratio and other aforementioned technical challenges when measuring the optical response of superconductors.

2.2 Transition metal-oxide thin films and multilayers

So far, we have discussed phenomena found in bulk samples of functional oxides. A whole new set of exotic effects occurs when going to the nanoscale, with samples in the form of epitaxially grown thin films (see Figure 2.2.1). Their typical thicknesses range from a few unit cells up to hundreds of nanometers. Thin films are referred to as single layers of a material system deposited onto a substrate, or as bilayers, trilayers up to superlattices. Often, such systems show unusual electronic and phononic behavior which does not occur in the constituent layers [8]. Superlattices are particularly interesting since they exhibit additional periodicity that can lead to modifications of the electronic bands and the phonon modes.

A prominent example are multilayers made from perovskite manganites and the cuprate high-T_c superconductor $YBa_2Cu_3O_{6+x}$ (YBCO). They allow one to study the ground state phases of YBCO and their interaction with the various electronic, orbital, and magnetic orders of the adjacent manganite layers [6, 22, 23]. Generally, the search for *emergent phases* (*EP*) due to the break in symmetry at interfaces of perovskite heterostructures has become a popular topic of research. These *EP* are typically confined to the interfacial regions, with characteristic length scales on the order of atomic distances, and thus are considered as quasi two-dimensional. Notably, their properties can often be strongly modified by changing the layers' thickness [7]. A prominent example is the metallic (or even superconducting) phase at the interface between the two band-insulators $LaAlO_3$ and $SrTiO_3$ that is discussed in more detail in the next chapter.

The thin film growth can also be motivated by the lack of single crystals that are of sufficient size or quality. This makes it hard to study the bulk crystals with infrared spectroscopy where the large wavelength as compared to the sample size leads to diffraction effects. Thin films, on the other hand, can be typically grown on 5 × 5 mm^2 or even 10 × 10 mm^2 large substrates, which helps to overcome diffraction issues.

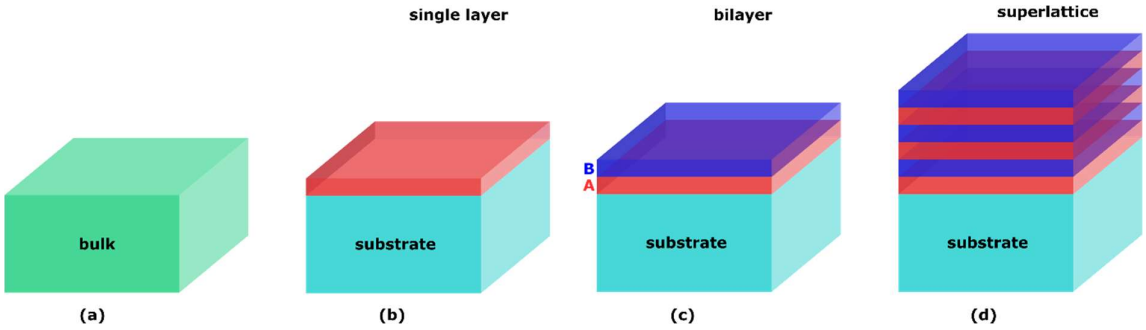

Figure 2.2.1 Different forms of solid state samples. (a) *Bulk single crystalline or polycrystalline materials.* ***(b)-(d)*** *Thin films grown on a substrate in the form of a single layer, a bilayer, and a superlattice (with N=3 repetitions), respectively.*

Besides the scientific interest, there is also a persistent need to grow high-quality films for technical applications. Great progress has been made in the fabrication of thin films, mainly thanks to the progress in molecular beam epitaxy, pulsed laser deposition and chemical vapor deposition techniques. Ensuring a high growth precision is crucial for the study and control of electronic correlations down to the atomic scale [45].

Likewise, it is important to develop and improve characterization techniques that allow monitoring and control of the quality and thickness of metal-oxide thin films. This is typically done *ex situ* but also *in situ* monitoring techniques exist.

In particular the *in situ* methods (RHEED [46], optical ellipsometry [47, 48]) will be promising in the future to further understand emergent phases in oxide thin films (e.g. [49]).
The established *ex situ* techniques, such as x-ray diffraction, x-ray reflection, transmission electron microscopy (TEM), and VIS-UV ellipsometry, are widely applied but still have certain disadvantages. Especially for heterostructures with atomic scale layer thickness, the quality control becomes a very challenging task. For instance, these techniques typically probe a large area of the film and thus provide only a poor lateral (*in-plane)* resolution (unless the measurements are taken at a synchrotron facility). Therefore, for thin films with an inhomogeneous thickness profile one obtains only averaged thickness values. TEM involves a destructive and technically challenging procedure. In the case of optical ellipsometry, a theoretical model is needed to derive the film thickness, which can be complex for superlattices with a large number of layer repetitions. Ultrasonic probes of internal interfaces also become rather ineffective for thin film structures since the substrate signal is typically dominating [50]. More suitable for superlattices would be a probe which can detect even local thickness variations and is not governed by the substrate response. Chapter 5 presents a new approach to determine the laterally resolved layer thickness of oxide multilayers based on studying backfolded acoustic phonons via confocal Raman spectromicroscopy.

2.3 Strontium titanate ($SrTiO_3$)

Strontium titanate, just like $YBa_2Cu_3O_{6+x}$, is one of the most famous perovskites. It has been studied for many decades and its exotic properties are still fascinating. In introductory courses on solid state research, $SrTiO_3$ is often presented as a standard and 'simple' member of the perovskite family. In science and industry, it is widely used as a robust and relatively cheap substrate for epitaxial thin film growth. On the other hand, it exhibits a very complex phase diagram, as its physical properties can be drastically changed in many different ways, for bulk as well as for thin film systems. Recently, additional attention has been drawn to $SrTiO_3$ since the discovery that it can serve as a source of a two-dimensional electron gas. Here, especially interesting is the electric field effect which provides a wide platform to study novel physics.

2.3.1 Physical properties of bulk and thin films of $SrTiO_3$

At **room temperature**, $SrTiO_3$ has an ideal cubic perovskite structure (see Fig. 2.1 and Fig. 2.3.1) with the symmetry group $Pm\bar{3}m$ and a lattice constant of $a = 3.905$ Å. It is non-magnetic and an electrical insulator with a direct bandgap of 3.75 eV and an indirect one of 3.25 eV [51]. The relative movements of the ions within the unit cell give rise to several phonon modes. The infrared-active modes at 300 K are displayed in Fig. 2.3.1(a)-(c). Not shown are the so-called *silent* modes, which involve the movement of only the oxygen atoms and do not induce a finite dipole moment or polarizability.

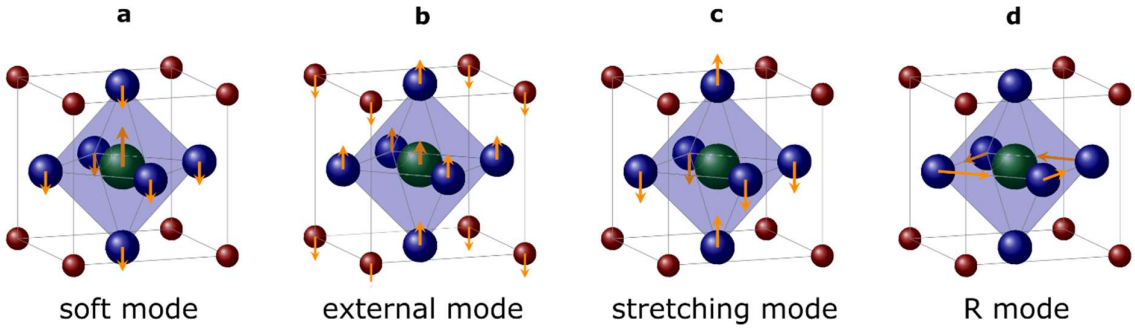

Figure 2.3.1 Ionic vibrations in $SrTiO_3$ (indicated with arrows) which give rise to infrared-active phonon modes [52]. *Strontium is sketched in red, oxygen in blue and the titanium center ion in green color.* ***(a)-(c)*** *are infrared-active already at room temperature, whereas* ***(d)*** *occurs only in the tetragonal state below T*= 105 K.*

The *soft mode* (or *Slater mode*) takes an important role for the electronic and structural properties of $SrTiO_3$. It arises from the movement of the titanium central ion (the inversion center of the system) with respect to the oxygen O^6 octahedron. Its eigenfrequency amounts to about 90 cm^{-1} at room temperature and decreases strongly upon cooling. Below ca. 30 K the eigenfrequency saturates at a minimal value of about 15 cm^{-1}. This anomalous softening of the strongly IR-active phonon mode gives rise to a very high value of the dielectric constant of up to $\varepsilon_0 \approx 20.000$ [53, 54] at low temperatures. Therefore, the soft mode governs the dielectric constant (permittivity) at low temperatures and makes it prone to ferroelectricity (see more details in the following chapter).
The oscillation of the strontium sub-lattice against the TiO^6 octahedra leads to the *external mode* (or *last mode*) centered at 170 cm^{-1}. The *stretching mode* at 540 cm^{-1} involves the stretching of the oxygen octahedron, as shown in Fig. 2.3.1(c). In the IR spectra, these phonon modes are split into their transverse-optical (TO) and longitudinal-optical (LO) branches because of the high ionicity of $SrTiO_3$.

The ideal cubic structure of $SrTiO_3$ has no *Raman active phonon* modes. The measured Raman response thus arises from multi-phonon excitations and from first-order modes that are activated by defects and distortions which break the inversion symmetry of the ideal lattice. The macroscopic inversion symmetry can be broken by disturbing the system, via e.g. the application of electrical fields or mechanical strain (see further below) which make normally infrared-active modes weakly Raman-active.

At ***T*~ 105 K***, $SrTiO_3$ undergoes a structural phase transition from the cubic to a tetragonal state, with lattice parameters of $a = b = 5.5515$ Å and $c = 7.8801$ Å (at 40 K). In this ***antiferrodistortive*** (AFD) state (in analogy to a ferroelectric phase transition), two adjacent oxygen octahedra rotate in opposite directions around the C_4-axis (the crystallographic axis with the highest symmetry within a unit cell). This antiphase rotation at $T < T^*$ leads to a doubling of the crystallographic unit cell around the *R*-point in the Brillouin zone and a sizeable macroscopic polarization. Subsequently, the phonon modes at the *R*-point are backfolded to the Brillouin-zone center (Γ-point). One of them is the infrared-activated *R*-mode at around 438 cm^{-1}, which presents a sensitive tool for studying the structural properties of STO in its low-temperature regime, and plays an important role in this thesis. In the Raman spectra, additional R-modes are activated at 15, 45, 144, 229 and 447 cm^{-1}.

The oscillator strength of these R-modes is proportional to the magnitude of the antiphase rotation of the TiO^6 octahedra. This gives rise to a characteristic dependence of the R-mode intensity on the polarization of the incoming IR light, i.e. the ***E*** field vector of the electromagnetic wave, which is maximal (zero) in the direction perpendicular (parallel) to the C_4-axis, the tetragonal axis (see also appendix B). Therefore, the *R*-mode presents a valuable indicator of the orientation of the tetragonal domains [55].

As shown by Rössle et al. [56], this IR-active R-mode can also serve as a sensitive probe of a polar distortion of the TiO^6 octahedra as it occurs below the ferroelectric phase transition in oxygen-isotope exchanged ferroelectric $SrTi^{18}O_3$ single crystals or can be induced with a gate-voltage in $LaAlO_3/SrTiO_3$ heterostructures. Here, the polar displacement of the Ti ion from its center position leads to a characteristic splitting of the R-mode into a red-shifted (unshifted) peak that arises from the component for which the light polarization is perpendicular (parallel) to the polar displacement vector.

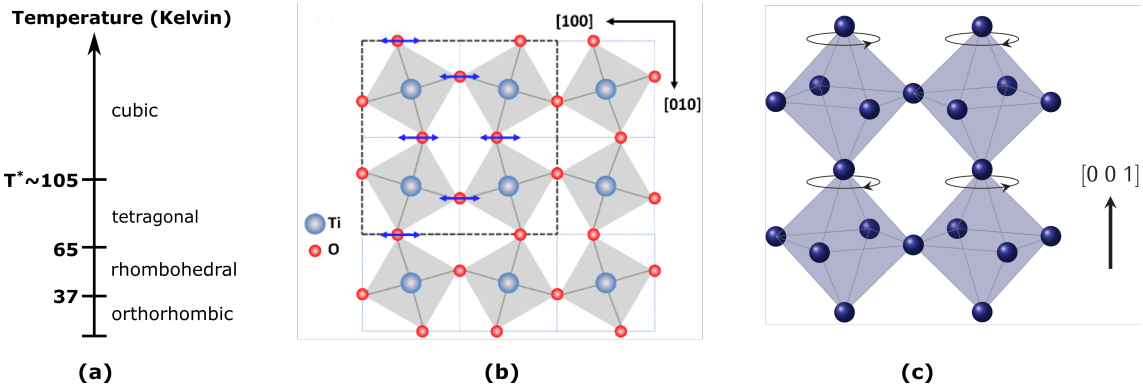

Figure 2.3.2 Structural properties of $SrTiO_3$. (a) *Temperature-dependent phase transitions of $SrTiO_3$.* ***(b,c)*** *Top and side view of the antiphase-rotation of the oxygen octahedra below T*, which leads to a doubling of the unit cell and thus gives rise to an IR-active R-mode [52, 55].*

The AFD transition is accompanied by the formation of structural domains with different orientations of the C_4-axis (tetragonal axis) that is pointing either along the [001], [010] or [100] direction (of the high-temperature cubic unit cell).
The domains are separated by domain boundaries/-walls. These boundaries are strained and can typically serve as pinning centers for e.g. oxygen vacancies [57]. There are indications that these boundaries can be polar and even conducting, likely because of the trapped oxygen vacancies [58]. Also, a polar order in the vicinity of the domain boundaries has been observed which is likely induced by flexoelectric effects. Honig et al. [59] demonstrated, that the domain walls (at least some of them, and most likely the charged ones) can be moved by applying an external electric field. As in other oxide materials, the oxygen stoichiometry in $SrTiO_3$ can strongly influence the material's properties.

Upon further cooling, the structure of $SrTiO_3$ becomes orthorhombic below about 60K and there are reports that at even lower temperature it becomes rhombohedral (e.g. [64]).

Oxygen vacancies, which can be neutral or positively charged, are naturally appearing in the material. They can also be inserted artificially, i.e. oxygen is extracted from the material, by e.g. annealing the sample at UHV conditions or by Ar^+-irradiation [60].
The insertion of oxygen vacancies can lead to drastic changes of the material's properties: reduced (i.e. oxygen-deficient) $SrTiO_3$ shows a characteristic blue luminescence signal whose intensity increases with the density of oxygen vacancies [60]. Such crystals exhibit a metallic conductivity, due to the accompanied insertion of free electrons. Also, a relatively high electron density of $n \approx 15 \times 10^{19}$ cm^{-3} can decrease T^* by about 15 K [61]. Interestingly, reduced $SrTiO_3$ can even become superconducting at very low temperatures [62]; with this discovery in 1964, $SrTiO_3$ was the first oxide material found to be superconducting. In addition, the accumulation of oxygen vacancies within the crystal creates an expansion in the lattice parameter [63], which is counterintuitive at first glance.

Surface and thin films of $SrTiO_3$
Epitaxially grown thin films provide additional possibilities to modify and tune the dielectric and electronic properties of $SrTiO_3$. For instance, the usage of thin films facilitates efficient electric field gating experiments [65], and the engineering of the lattice mismatch with respect to the substrate allows one to tune the internal tensile or compressive strain [66]. The dielectric properties can drastically differ from the ones of the bulk systems (e.g. [67-69]), as is the case for most material systems with reduced dimensions (see previous chapter).
The surface properties of $SrTiO_3$ can also be quite different from the ones in the bulk. For instance, it was shown that the antiferrodistortive state at the surface can persist to much higher temperatures than in the bulk with T^*= 105 K [70]. Moreover, the formation and population of the structural domains may be different near the surface [71-74].

2.3.2 Electronic states of $SrTiO_3$

In the ideal cubic perovskite structure of $SrTiO_3$, the titanium (Ti) ion is located at the *B*-site (ABO_3) and represents an inversion center. When this inversion symmetry is broken, e.g. by displacing the Ti ion, a net polar moment is created [10]. Materials which can exhibit such a dipole moment are termed *polar*. The electric polarization vector ***P***, pointing from negative to positive charges, creates an electric field ***E***, which is by definition antiparallel to ***P***, i.e. pointing from positive to negative charges. These electronic states have several exotic properties and useful application prospects.

The terminology differentiates between pyro-, ferro-, piezo- or flexoelectricity, depending on how the macroscopic dielectric polarization is induced.

Pyroelectricity

Materials, which exhibit a spontaneous magnetization, i.e. even without an external magnetic field, are referred to as *ferromagnetic*. In analogy, materials which exhibit *spontaneous polarization* without an external *electric* field are called *pyroelectric* (greek: *fire*). The macroscopic dielectric polarization develops upon cooling the system below a critical temperature T_{Curie} at which the dielectric function ε diverges (see Fig. 2.3.3) according to the Curie-Weiss law [10]:

$$\varepsilon = \frac{C}{T - T_{Curie}} \tag{1}$$

Here, T_{Curie} is the paraelectric Curie temperature and C is a material specific constant that is proportional to the magnitude of the polar moments. The order parameter is the 'spontaneous polarization' $\boldsymbol{P}$ which develops spontaneously below T_{Curie} and increases towards its maximal saturation value at $T << T_{Curie}$.

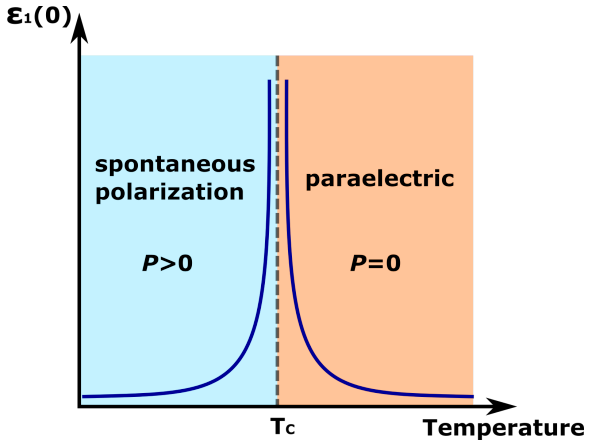

Figure 2.3.3 Schematic of the Curie-Weiss law. *The dielectric permittivity diverges as the sample temperature approaches T_{Curie}. For $T < T_{Curie}$, the system exhibits a total net polarization* ***P****, whereas above T_{Curie} the system either has no dipole moment, or they cancel each other out so that no macroscopic polarization can form.*

A spontaneous polarization is only possible if the crystal has a *polar* axis. If there is more than one polar axis, the material is piezoelectric (see more details below). One condition is the absence of inversion symmetry. Consequently, amorphous materials cannot be piezoelectric [10].

The strength of the pyroelectric effect can be quantified by the pyroelectric coefficient vector, which is defined as:

$$p_{pyro} = \frac{\partial \boldsymbol{P}}{\partial T} \tag{2}$$

Pyroelectricity is not to be confused with *thermoelectricity*. Both convert a change in temperature into an electrical potential: for pyroelectric materials, the temperature of the entire material is varied, resulting in a temporary voltage across the crystal. In thermoelectric materials on the other hand, a temperature gradient across the sample causes a permanent voltage across the material. These materials are used e.g. for heat sensors, to detect and control small changes in temperature.

Piezoelectricity

In piezoelectric materials, derived from *piezein* (greek: *to squeeze* or *press*), a dielectric polarization is induced by a homogeneous mechanical deformation. Applying homogeneous mechanical stress results in lowering the symmetry and creating a dipole moment. This effect can only occur in non-centrosymmetric systems, which limits the number of suitable material classes to profit from this phenomenon for technological applications [75]. An important aspect is that the polarization can be changed by mechanical deformation, but it cannot be switched.

Piezoelectric materials are very interesting for industry and research. They are used as e.g. high precision motors and sensors, microbalances, as well as for atomic resolution scientific instrumental techniques like STM, AFM, SNOM or quartz switches.

Ferroelectricity

A material is called ferroelectric if two conditions are fulfilled: Firstly, the system exhibits a spontaneous and macroscopic electric polarization ***P*** (i.e. it is pyroelectric). This is given by the direction of the net dipole moment of the crystal. Secondly, ***P*** can be flipped (i.e. its sign reversed) by the application of an external electric field, and thus shows a reciprocal hysteresis loop (see Fig. 2.3.4(a)).

The term *ferro*electricity comes from its in many ways similar, phenomenological characteristics to *ferromagnetism*: Within a domain, the polarization vector in the case of ferroelectricity, and the magnetization vector in the case of ferromagnetism, points in the same direction. The size of the ferroelectric domains are typically on the order of a few nanometers, and thus only a 10^{th} of the ferromagnetic ones, which make them promising candidates for future electronic data storage devices. Both ferromagnetic and ferroelectric materials exhibit characteristic hysteresis curves as a function of an applied electric/magnetic field. Systems in which ***P*** is not the main order parameter are referred to as *improper ferroelectrics*.

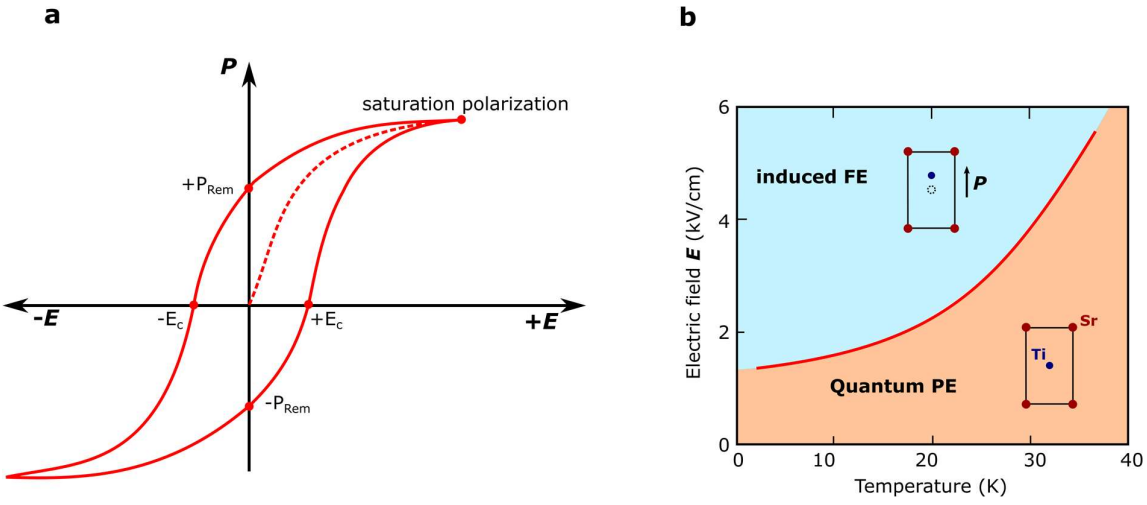

Figure 2.3.4 Characteristics of Ferroelectricity. (a) *Typical hysteresis curve of a ferroelectric material.* P_{Rem} *is the remnant polarization after switching off the electric field, and* E_c *the coercive field at which the net polarization is zero.* ***(b)*** *Electric field versus temperature phase diagram of the quantum paraelectric (PE) material* $SrTiO_3$*, where a ferroelectric (FE) order can be induced at high fields and low temperatures (adapted from [76]).*

Above the transition temperature T_{Curie}, i.e. in the *paraelectric*/*paramagnetic* state, the net magnetization/polarization becomes zero. However, the two phases originate from very different microscopic behavior, whereas the origin for ferroelectricity is much more complex [10].
Different types of ferroelectrics are possible [52], with two major divisions: There are ferroelectric materials, for which the pre-existing dipole moments become ordered upon crossing T_{Curie} and thus give rise to a macroscopic polarization ***P*** (*order-disorder transition*). In the second type, the ferroelectric transition is accompanied by a lattice phase transition, in which the charged ions within a unit cell are displaced in a such way that a dipole and thus a spontaneous polarization develops below T_{Curie} (*displacive transition*). Typical representatives for the latter type are ionic crystals with a perovskite structure, e.g. $BaTiO_3$ [10].

$SrTiO_3$ is a *quantum paraelectric*, for which the ferroelectric order is inhibited by quantum fluctuations of the lattice. Consequently, $SrTiO_3$ remains paraelectric at any temperature due to the lack of a macroscopic polarization. However, the incipient ferroelectric order can be induced by suppressing the lattice fluctuations. This is achieved by e.g. isotopic substitution (replacing ^{18}O for ^{16}O [77]), chemical doping (substituting some of the Sr with Ca [78]), applying mechanical stress [79] or an electric field [80] for bulk $SrTiO_3$, or e.g. by inducing compressive or tensile strain in thin films of $SrTiO_3$ grown on a substrate with a lattice mismatch [66]. Note, that even though the ferroelectric transition temperature can be tuned via doping, the induced heterogeneity of the sample in form of micro-regions also leads to a broadening of the T_{Curie} value [81], which is detrimental for industrial applications.
The reason why $SrTiO_3$ is called an incipient ferroelectric, in which long-range ferroelectricity is suppressed via quantum fluctuations, is the appearance of a soft mode in the optical spectra, which is a typical indicator of a displacive type ferroelectric. For an ideal displacive type ferroelectric material, the soft mode approaches 0 cm^{-1} at T_{Curie}, which corresponds to the formation of the static lattice distortion that gives rise to the polar moment below T_{Curie}. This transition is accompanied by a divergence of the static dielectric constant with a sharp peak at T_{Curie}. In the case of $SrTiO_3$, the complete softening of the IR-active mode is avoided by competing effects due to other kinds of interactions and/or disorder. This leads to a broadening of the mode until a related mode emerges at $T << T_{Curie}$ that hardens as the polar moment increases towards its saturation value. Such a characteristic behavior has been reported for $SrTi^{18}O_3$ via Raman [82] and infrared spectroscopy [56].

Flexoelectricity

A special type of polarization phenomenon, which is quite distinct from the other polarization states discussed above, is flexoelectricity. Here, a strain *gradient* is applied to break the inversion symmetry of a material [75] in order to induce a dielectric polarization ***P*** and a subsequent electric field ***E*** (see Fig. 2.3.5). The flexoelectric effect is a universal property of matter and occurs in all solid state materials, i.e. not just in non-centrosymmetric systems that show a piezoelectric effect. Its occurrence was reported e.g. in oxide semiconductors [83] and even in bones [84]. However, this flexoelectric effect tends to be extremely weak and hardly useful for technical application. As discussed below, $SrTiO_3$ is one of the rare exceptions for which sizeable flexoelectricity can be realized.
In a simple bulk picture, flexoelectricity can be differentiated between the *direct* (a strain gradient induces ***P***), the *inverse* (***P*** induces a strain gradient) and the *converse* response (a ***P*** gradient induces strain). Further differentiations of the phenomena, such as the *static* and *dynamical* response (in form of strain gradient waves), are described in detail for instance in [75].

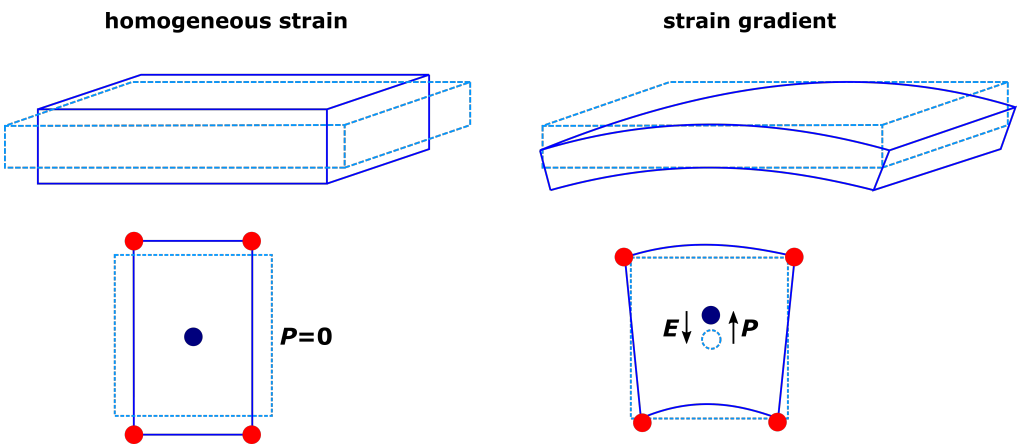

***Figure 2.3.5 Strain effects on the polarization of a material with inversion symmetry**. Left: Homogeneous mechanical strain maintains the inversion symmetry and thus does not induce a macroscopic polarization, **P**. Right: A strain gradient breaks the inversion symmetry and creates a finite polarization (adapted from [75]).*

The induced total macroscopic polarization can be described as a composition of the piezoelectric and flexoelectric response

$$\boldsymbol{P} = \boldsymbol{P}_{piezo} + \boldsymbol{P}_{flexo} = \chi\, \boldsymbol{E} + \mu \frac{\partial s}{\partial x} \tag{3}$$

with the dielectric permittivity χ and a strain gradient $\partial s/\partial x$. The external electric field ***E*** is also termed the flexoelectric field. The flexoelectric coefficient μ is directly proportional to the dielectric permittivity of a material. Consequently, the flexoelectric response is expected to be strongest in materials with a high dielectric constant.

Even though flexoelectric effects have been known for decades [75], due to the small magnitude of the effect in bulk materials they have only drawn little attention from the science community. Thanks to recent technological development, however, low-dimensional systems such as thin films have become available. Thin films present an important step towards creating much higher flexoelectric fields, since reduced dimensions imply larger strain gradients. A cardinal prototype is $SrTiO_3$, as it exhibits an enormous dielectric permittivity at low temperature, which is not the case for most other materials. It was shown that strong flexoelectric fields can be created in $SrTiO_3$ thin films when exposing them to an inhomogeneously applied mechanical force, which can be done for instance via pressing with a small AFM tip onto the sample surface [75, 85, 86].
Since flexoelectricity has been a subject of intensive research only in the last couple of years, there is still a wide playground, with several contradictory results among experiment and theory. Controlling flexoelectric fields enables developing new and potentially useful applications. For instance, it allows the switching of polarity and could therefore be useful for sensors and mechanical actuators.
A further step in using strain gradients in order to engineer future electronics is the concept of flexomagnetism. Here, an inhomogeneous mechanical deformation leads to an atomic displacement, which is accompanied by a rearrangement of spins. Flexomagnetism has only been theoretically predicted, with no convincing experimental proof (yet) [75].

2.3.3 Comparison with $BaTiO_3$ and $KTaO_3$

In the following, two other well-studied perovskites, $BaTiO_3$ and $KTaO_3$, will be briefly presented and compared to $SrTiO_3$.

$BaTiO_3$ is already ferroelectric at room temperature with T_{Curie}∼395 K. It has a rather high permittivity, which is typical for ferroelectric materials, and shows a strong hysteresis loop and is therefore highly tunable by an external electric field [87]. $BaTiO_3$ exhibits several structural phase transitions, for which the macroscopic polarization is rotated [88]: Below about 183 K the structure is rhombohedral. At higher temperatures, the structure is first orthorhombic between 183 K and 278 K, then tetragonal between 278 K and 395 K. Above T_{Curie}∼395 K, $BaTiO_3$ is cubic, loses its macroscopic polarization and becomes paraelectric. $BaTiO_3$ is being used for technological applications e.g. as a dielectric for ceramic capacitors. A drawback is that its efficiency depends on the temperature as well as on the applied voltage, which is accompanied by partially immense electrical losses.

$KTaO_3$ is a non-magnetic, strongly polar, and a wide-bandgap insulator (≈2.15 eV) with strong spin-orbit coupling (SOC). It has a cubic crystal structure (a = 3.989 Å) for all reported temperatures (at least from 4.2 K to 300 K), and is therefore void of the tetragonal boundaries that develop in $SrTiO_3$ below T^*∼105 K [89]. $KTaO_3$ is a quantum paraelectric, similar to $SrTiO_3$, in which long-range ferroelectric order can be stabilized by applying an electric field [90, 80] or mechanical strain [91, 92]. A crucial difference is that $KTaO_3$ is further away from the ferroelectric critical point and it has a smaller dielectric constant at low temperatures than $SrTiO_3$ [93].

2.3.4 Confined electron gas at the interface of $SrTiO_3$

Besides investigating its bulk and thin film properties, in the last two decades $SrTiO_3$ became known as a source of a two-dimensional electron gas (2DEG) with highly mobile charge carriers. In 2004, Ohtomo and Hwang showed that by growing two insulator materials on top of each other, namely a thin $LaAlO_3$ film on top of a $SrTiO_3$ substrate, a high-mobility 2DEG can be formed in-between [94]. Since in two-dimensional systems the effects of electron correlation are enhanced due to a reduced kinetic energy [8], this pioneering work opened a further wide playground to create novel and highly tunable states at interfaces. Such a 2DEG can have a sheet carrier concentration of ca. 5×10^{14} cm^{-2} [95], with a relatively high mobility of ca. 10^4 cm^2/Vs [94], and it is generated only when the LAO film thickness is larger than 4 unit cells, and if the $SrTiO_3$ surface is TiO_2-terminated; otherwise it remains insulating. Further reports have demonstrated that an interfacial electron gas can likewise be formed by depositing, instead of $LaAlO_3$, other polar materials onto $SrTiO_3$, including $LaVO_3$ [96] and $GdTiO_3$ [97]. The origin of this interface conductivity is not elucidated and still debated. The most prominent explanations are the originally proposed concept of a polar catastrophe, and/or the emergence of oxygen vacancies.

Polar catastrophe

Along the (001) direction, the unit cell of $SrTiO_3$ consists of a stacking of the neutral sublayers $(SrO)^0$ and $(TiO_2)^0$, whereas $LaAlO_3$ is composed of electrically charged $(LaO)^+$ and $(AlO_2)^-$ layers. The resulting polar discontinuity at the interface between $SrTiO_3$ (STO) and $LaAlO_3$ (LAO) thus leads to an electrostatic potential, which is growing proportionally as the film becomes thicker.

In order to avoid a divergence of this potential, the system relaxes by an interfacial reconstruction: At a certain threshold potential, which apparently is reached at approximately 4 unit cells of LAO, on average half an electron per LAO unit cell is transferred from the LAO/ambient to the LAO/STO interface [95]. This causes the interface to become an electron-type conductor. This *electronic* reconstruction scenario is rather unusual compared to classic semiconductors, in which a*n atomic* reconstruction, such as lattice distortions, can cause an enhanced roughness at the interfaces.

Oxygen vacancies

An alternative scenario to explain the interfacial conduction layer is by considering the behavior of *oxygen vacancies* [98]. Recent studies have shown that equivalent 2DEGs can be generated by depositing a thin film of a few nanometers of aluminum (Al) under UHV conditions [99] or even strontium (Sr) under ambient pressure [100] on the $SrTiO_3$ surface. The highly oxidizing character of Al and Sr leads to such thin conductive layers, which consist mostly of oxygen vacancies with no polar discontinuity, as is the case for $LaAlO_3$ top layers or other polar materials. In addition, the fabrication of AlO_x/STO heterostructures requires much less effort than that of complex $LaAlO_3$, $LaTiO_3$ or $GdTiO_3$ films, which require the correct surface termination of $SrTiO_3$.

Another possibility is to shine UV light, which includes energies above the band gap of the substrate material, onto the sample surface and thus generates electron-hole pairs. This *photodoping* enables the creation of a comparable sheet carrier concentration as by the deposition of $LaAlO_3$ [101].

In addition, the surface of $SrTiO_3$ can be made conducting in further ways, which however is not necessarily the same as creating a two-dimensional metallic layer. This can be achieved by hole doping, e.g. Ar^+-irradiation [60], which introduces oxygen vacancies into the system, or electron-doping, via substituting La^{3+} for Sr^{2+} or Nb^{5+} for Ti^{4+} [102], which produces additional electron carriers. Whether one and/or the other scenario is valid is still being debated and might vary from system to system.

An alternate host for interfacial 2DEG is $KTaO_3$ [103], which is, unlike $SrTiO_3$, a polar material. Its interface also exhibits a high electron mobility at low temperatures and is comparable to the one of STO-based devices [103-106].

2.3.4.1 Electric field effect

The highly mobile electrons at the $SrTiO_3$ interface with other oxide insulators offer fascinating physics and provide prospective applications. Their properties can be drastically tuned between different phases when exposed to external perturbations such as temperature, magnetic and electric fields. For instance, the LAO/STO system can exhibit a large magnetoresistance [107] or the coexistence of magnetism and superconductivity at the LAO/STO interface [108].

Especially interesting is the electric field effect on such back-gated heterostructures. It allows one to modulate the charge carrier density, it can induce a superconductor-insulator [4] or metal-insulator transition [109, 3], and it even offers a novel platform to study Rashba physics. Rashba interaction is an electronic property, and presents a special type of spin-orbit coupling (SOC). A large Rashba spin-orbit interaction is arising from interfacial breaking of inversion symmetry, whose magnitude can be modulated via applying an electric field [5, 8]. Controlling the strength of the asymmetric potential by a back-gate voltage will be advantageous for tuning the spin polarization at such interfaces.

In analogy, electric field studies have been done on $KTaO_3$-based 2DEGs. The 2DEG can also be modified with a back-gate voltage, albeit, the carrier localization effects at negative voltages seem to be less pronounced [110].

From a technological point of view, these structures are very promising, and can be important elements for future electronic and phononic devices. Conventional metal-oxide-semiconductor field-effect transistors (MOSFET) and field-effect transistors (FET) could be replaced by these structures. Here, one example is given: Manipulating the Rashba-type SOC enables spintronic devices for which the conversion of the charge- and spin currents can be controlled and switched with an electric field (via the sign of the Rashba-field) rather than with a magnetic field (via the magnetization direction of a ferromagnetic layer) [111, 2]. This allows to engineer non-volatile technological devices. Despite these interesting prospects, the relationship between the applied gate voltage and the induced polarization at the interface is intricate and remains to be understood.

Chapter 3

Experimental techniques

Optical spectroscopy has a long history of being used to study diverse systems, ranging from liquids, to solid state materials, even to stars. In materials science, it is used to study, for instance, the free charge carrier response, the superconducting condensate, phonons, magnons and bandgaps. Revealing the electronic and phononic excitations can yield clues for understanding the macroscopic properties and the role of competing degrees of freedom in several materials.
Since optical spectroscopy is applied in a wide range of the electromagnetic spectrum, different units are typically used (such as THz, cm^{-1}, µm, nm, eV). The choice depends on the technique and the spectral range under investigation.

In this thesis, Raman and infrared spectroscopy will be used to investigate several types of material systems. Both techniques are sensitive to low-energy excitations, and especially suitable to investigate polarization effects.
Photons in the visible part of the electromagnetic spectrum with energies of only a few eV carry negligible momentum, $K = 2\pi/\lambda$, in comparison to the quasi-momentum of elementary excitations [112]. Therefore, Raman and infrared spectroscopy both probe at the Brillouin zone center (except e.g. 2-phonon processes), as sketched in Figure 3.1. In order to study excitations with momenta $q > 0$, other experimental techniques are required, as discussed in section 3.3.

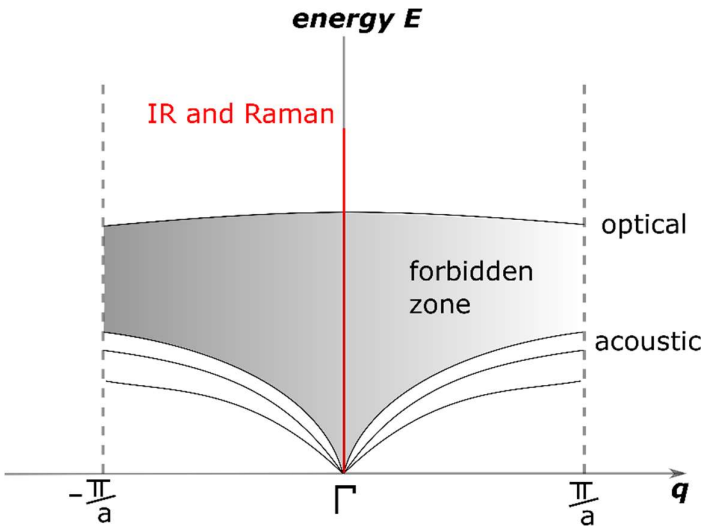

Figure 3.1 Schematic of the 1st Brillouin zone of a primitive cell with a basis of 2 atoms, with 3 acoustical and 1 optical branch. *Both infrared and Raman techniques probe at the Brillouin-zone center Γ, due to their small momentum transfer (q ≈ 0).*

Raman and infrared (IR) spectroscopy present complementary measurement techniques. Following the optical selection rules, a material with an inversion center can exhibit Raman-active modes, which are not observable in the infrared spectrum, and vice versa [113]. The here studied oxide systems with perovskite structure have an inversion center (e.g. in $SrTiO_3$ it is the titanium ion) and are therefore prominent examples.

On the other hand, a break of this inversion symmetry can induce Raman-active modes, which are usually only infrared active.

An important aspect of Raman and IR spectroscopy, as well as all other techniques which use photons as the probing tool, is that they usually probe excitations which are parallel to the electric field vector ***E*** of the incoming light, which is by default perpendicular to the wave vector *K*. Thus, for normal incidence reflectivity one solely obtains information on the in-plane response (i.e. the component which is perpendicular to the surface normal).
In this thesis, new ways will be explored on how to separately derive information on the in-plane and the out-of-plane component. This is achieved with the study of low-frequency backfolded acoustic phonons via Raman spectroscopy, or the features occurring close to certain longitudinal optical phonons (LO edge) via the ellipsometry technique.
In addition to characterizing material systems *ex-situ*, especially optical ellipsometry represents a convenient *in-situ* tool during thin film growth. For instance, it has been used to monitor and control the deposition of atomic layers of the complex Ruddlesden-Popper series $SrO(SrTiO_3)_n$ [47, 48] and to confirm a charge transfer across $LaMnO_3/SrMnO_3$ interfaces [49]. This approach is advantageous compared to the commonly used RHEED technique, since it does require high-vacuum conditions and therefore expands its applicability to various deposition techniques.

The first section will give an insight into infrared spectroscopy, starting from a theoretical point of view and then going to the instrumental details. This includes *normal incidence reflectivity*, *magneto-optics* and *ellipsometry*. The infrared spectra were taken over a wide energy scale, ranging from THz ($\sim$33 cm^{-1}) up to several electron volts (eV). This chapter also includes the basic modelling approaches. Many aspects presented here are equally valid for Raman spectroscopy, which will be discussed in the second section. A short outlook for further advanced Raman techniques will be given. The last chapter provides perspectives on the limitations of Raman and infrared spectroscopy by briefly comparing them to other spectroscopy techniques such as RIXS and ARPES.

3.1 Infrared spectroscopy

In the following, the basics of light-matter interaction at interfaces will be discussed, including the analysis procedure of optical spectra and the corresponding instrumental setups. In this study, two infrared spectroscopy techniques were used: Normal incidence reflectivity and ellipsometry. The following formalism is valid for low-energy excitations, such as lattice vibrations (phonons), spin excitations (magnons) and even interband transitions.

3.1.1 Light-matter interaction

The time-varying electric and magnetic fields, $\boldsymbol{E}(\omega,K)$ and $\boldsymbol{B}(\omega,K)$ are fully described by the Maxwell equations, with the energy $\hbar\omega$ and the wave vector K (see e.g. [10]). For infrared (and also Raman) spectroscopy, the wavelength of the radiation is large compared to the lattice parameter, and therefore the dependence of K can be neglected. Furthermore, only non-magnetic and laterally homogeneous structures are considered in the following. Depending on the medium, $\boldsymbol{E}(\omega,K)$ creates electric dipoles and therefore induces a displacement field

$$\boldsymbol{D}(\omega) = \varepsilon\boldsymbol{E}(\omega) = \varepsilon_0\boldsymbol{E}(\omega) + \boldsymbol{P}(\omega) \tag{4}$$

with the permittivity in vacuum ε_0, the complex dielectric function $\varepsilon(\omega) = \varepsilon_1(\omega) + i\varepsilon_2(\omega)$ and the induced macroscopic polarization

$$\boldsymbol{P}(\omega) = \chi(\omega)\varepsilon_0\boldsymbol{E}(\omega) \tag{5}$$

Important quantities are the susceptibility $\chi(\omega)$ and the dielectric function $\varepsilon(\omega)$, which relate as $\varepsilon(\omega) = 1 + \chi(\omega)$. They are essential for analyzing the Raman and infrared spectra. The dielectric function is typically used to describe the optical response of a system, especially of dielectric materials. In addition, the Maxwell relations relate $\varepsilon(\omega)$ to other optical response functions. The optical conductivity $\sigma(\omega) = \sigma_1(\omega) + i\sigma_2(\omega)$ is commonly used to describe the behavior of conducting materials such as metals and superconductors:

$$\sigma(\omega) = -i\omega(\varepsilon(\omega) - 1)\varepsilon_0, \quad \varepsilon(\omega) = 1 + \frac{4\pi i}{\omega}\sigma(\omega) \tag{6}$$

The complex refractive index $\tilde{n} = n(\omega) + ik(\omega)$ is related to the dielectric function as

$$\tilde{n} = \sqrt{\varepsilon} \tag{7}$$

which leads to

$$\begin{aligned} \varepsilon_1 &= n^2 - k^2 \\ \varepsilon_2 &= 2nk \end{aligned} \tag{8}$$

The real part n is typically called the index of refraction and k the extinction coefficient, which is a measure for the attenuation of the wave in a material.

Penetration depth of the infrared light

The penetration depth *d* for (normal-incident) light inside a material is given by

$$d = \frac{\lambda}{4\pi\, k(\omega)} \tag{9}$$

with λ the wavelength of the light, and $k(\omega)$ the imaginary part of the complex refractive index, i.e. the extinction coefficent. The penetration depth defines the distance from the surface towards the interior of the sample at which the light's intensity is reduced to 1/e of its incident value. Note that the frequently used *skin depth* is the analogous case for which the *amplitude* of the electric field vector is reduced to 1/e.

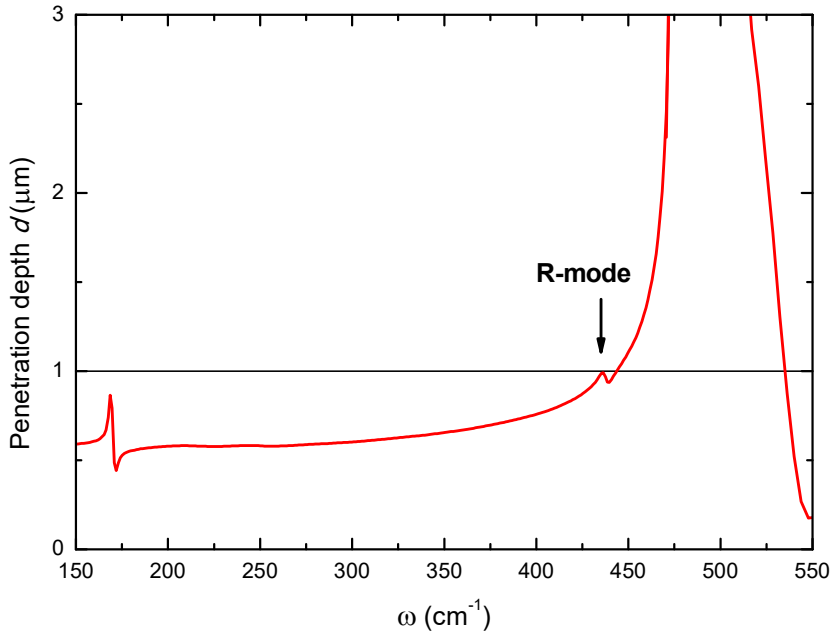

Figure 3.1.1 Penetration depth d of the far-infrared radiation in pristine $SrTiO_3$ at low temperatures.

Figure 3.1.1 shows the penetration depth evolution in $SrTiO_3$ at 10 K for the low-frequency spectral region. Around the R-mode at 438 cm^{-1} (black arrow) the light penetrates less than ~1 µm inside the sample. Near the LO_4 edge at ~800 cm^{-1} (not shown), the refractive index of the sample falls below unity ($n < 0$). In this so-called *Reststrahlenband*, as discussed further below, the light becomes an evanescent wave due to total reflection, if the incident light is at a grazing angle to the sample surface.

3.1.2 Electromagnetic waves at interfaces

Electromagnetic waves do not interact with an applied magnetic or electric field. Their properties, such as amplitude, phase and direction of *K* are only changed when the light beam arrives in a medium with a different complex refractive index $\tilde{n}$. The light is then partially reflected, transmitted or absorbed. In a reflection experiment, information on the optical properties are thus derived from the reflected component. For simplicity, we will neglect the effect of absorbance in the following formalism.

In a simple picture, the change of the direction of the incident light beam at an interface is described by *Snell's Law*:

$$n_1 \sin\varphi = n_1 \sin\nu \tag{10}$$

When the light, travelling through a medium with the refractive index n_1, enters a second medium with n_2 under an angle φ, the light is diffracted inside the second medium under the angle ν.
The general case is described by the *Fresnel coefficients*, which define the change of the amplitude and the phase of the electromagnetic wave at the interface. Hereby, the electromagnetic field vector is separated into the component parallel and perpendicular (german: '*senkrecht*') to the plane of incidence, which are termed as *p-polarized* and *s-polarized*, respectively (see Figure 3.1.2(a)).

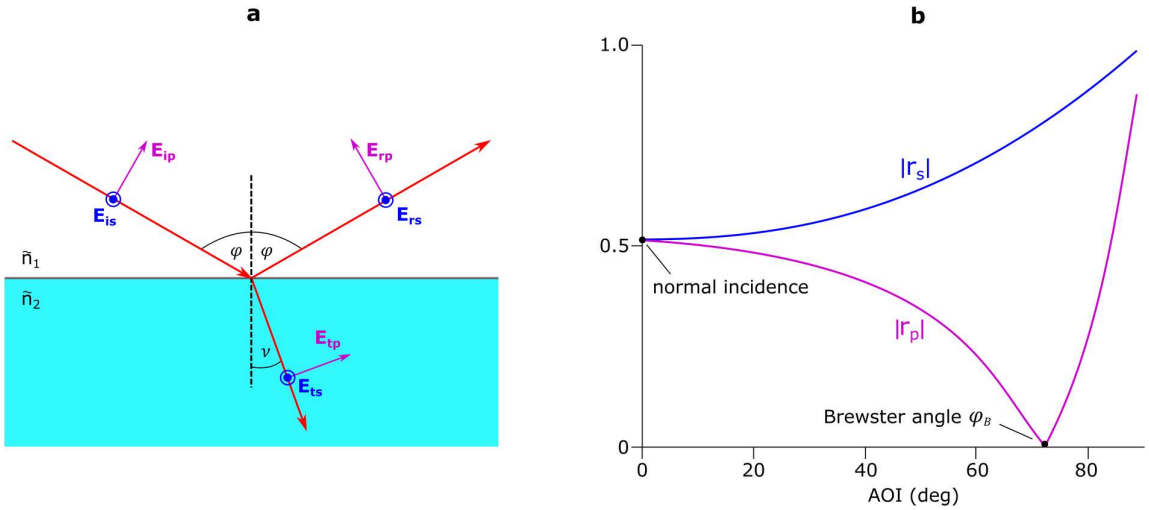

Figure 3.1.2 Light-matter interaction at an interface between media with different refractive indices. ***(a)*** *The plane wave vector can be divided into its component parallel (p) and perpendicular (s) to the plane of incidence. At interfaces, the incident beam (i) is in part reflected (r) or transmitted (t).* ***(b)*** *Amplitude of the Fresnel reflection coefficients* $r_{p,s} = |r_{p,s}|e^{i\delta_{p,s}}$ *as a function of the angle of incidence.*

In this thesis, the main interest is on the reflected part of the light, which is expressed in terms of the ratio of the reflected and incident electric fields. The Fresnel reflection coefficient for p-polarization is

$$r_p \equiv \frac{\boldsymbol{E_{rp}}}{\boldsymbol{E_{ip}}} = \frac{\tilde{n}_2 \cos\varphi - \tilde{n}_1 \cos\nu}{\tilde{n}_2 \cos\varphi + \tilde{n}_1 \cos\nu} \tag{11}$$

Analogously, the Fresnel coefficient for s-polarization reads:

$$r_s \equiv \frac{\boldsymbol{E_{rs}}}{\boldsymbol{E_{is}}} = \frac{\tilde{n}_1 \cos\varphi - \tilde{n}_2 \cos\nu}{\tilde{n}_1 \cos\varphi + \tilde{n}_2 \cos\nu} \tag{12}$$

The formalism for the transmission coefficients $t_{p,s}$ can be found e.g. in [114, 115]. Figure 3.1.2(b) displays the amplitude of the Fresnel reflection coefficients as a function of the angle of incidence φ. For φ = 0 degree, i.e. for a normal incidence geometry, the p- and s- reflection coefficients are indistinguishable.

At the Brewster angle $\varphi_B = \tan^{-1}\left(\frac{n_2}{n_1}\right)$, the Fresnel coefficient r_p is zero, which means that p-polarized light is completely transmitted and only s-polarized light is reflected. Here, the difference between the reflection coefficients is maximal. This condition can serve as a powerful tool to investigate the polarization effects in matter. Ellipsometry measurements are typically performed at an angle close to φ_B due to the high sensitivity, in which r_p is used in reference to r_s. Further details are found in the subsection 3.1.6.

3.1.3 Analysis of optical spectra

In the following, the basic tools for describing and analyzing optical spectra will be discussed. They are presented for treating infrared spectra, but are mostly also valid for Raman spectra. The total optical response function of a material is a superposition of all of its excitations

$$\varepsilon(\omega)_{sample} = \sum_{i}^{N} \varepsilon(\omega)_i \tag{13}$$

These excitations can arise from for example free electrons, phonons, magnons or interband transitions. Here, we will mainly focus on excitations of *phononic* or *electronic* origin, for which the major part of optical spectra can be well described and modelled.

3.1.3.1 Phonon excitations

In a dielectric material, the relatively light negative electronic charges (*-q*) are bound to the rather heavy positive charges (*+q*) of the nuclear cores via the Coulomb force. These harmonic oscillations, so-called *lattice vibrations* in the classical picture or *phonons* in the quantum mechanical one, can be well described by Hooke's law in terms of a spring-like force (Figure 3.1.3(a)). Together with Newton's second law, we derive for the mass displacement from its equilibrium position, x, as a function of time the differential equation

$$m\frac{d^2x}{dt^2} + m\gamma\frac{dx}{dt} + m\omega_0^2 x = q\boldsymbol{E}(\omega) \tag{14}$$

which describes a classical damped harmonic oscillator, with the resonance frequency ω_0, the damping constant γ and the driving electric field $\boldsymbol{E}(\omega)$. This 2nd order differential equation can be solved with the periodic Ansatz $x(t) = Ae^{-i\omega t}$, which yields for the amplitude of the displacement

$$A = \frac{\frac{q}{m}}{\omega_0^2 - \omega^2 - i\gamma\omega} \tag{15}$$

The displacement *A* of a negative charge leads to a local dipolar moment qA. For a carrier concentration *n* per unit volume, the induced net polarization density is $\boldsymbol{P} = nqA$. According to Eq. (5), this relation can be expressed in terms of the dielectric constant of a material as:

$$\varepsilon(\omega)_{Lorentz} = \varepsilon_\infty + \sum_{i}^{N} \frac{\omega_{pl,i}^2}{\omega_{0,i}^2 - \omega^2 - i\gamma_i\omega} \tag{16}$$

This is the *Lorentz model*, which is typically used to describe the response of phonons. ε_∞ accounts for the contribution of oscillators for which the eigenfrequency is at significantly higher energies such that the impact in the relevant regime at lower frequency can be represented with a constant.
Figures 3.1.3(b)-(e) show an exemplary model with a resonance frequency of $\omega_0 = 300$ cm^{-1}, described by the Lorentz model in terms of the dielectric function and the optical conductivity. As can be seen, ε_2 (the inductive part) has a similar shape to the σ_1 spectrum, and in analogy, ε_1 (the oscillatory part) looks similar to the inverted σ_2.

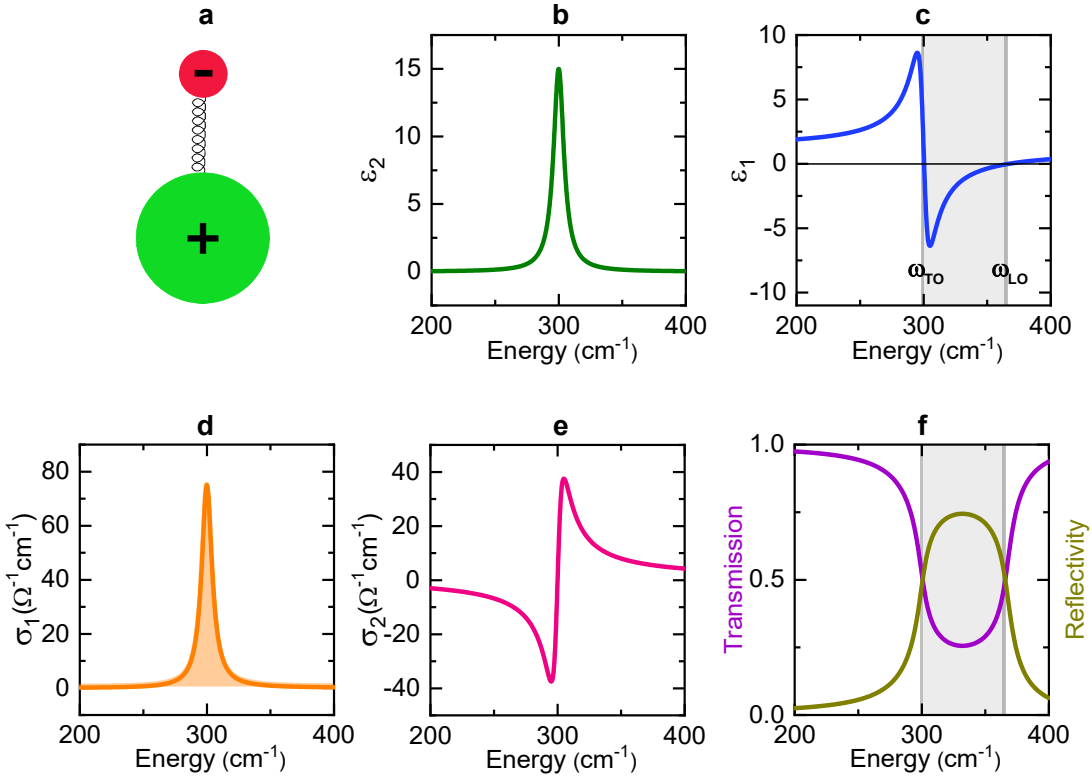

Figure 3.1.3 Lorentz model. (a) *Sketch of a spring model to describe an infrared-active phonon.* ***(b), (c)*** *show the real and imaginary part of the dielectric function* $\varepsilon = \varepsilon_1(\omega) + i\varepsilon_2(\omega)$ *and* ***(d), (e)*** *the real and imaginary part of the corresponding optical conductivity* $\sigma(\omega) = \sigma_1(\omega) + i\sigma_2(\omega)$*, for a mode at 300 cm*$^{-1}$*.* ***(f)*** *Transmission and reflectivity spectrum, with* $T = |1 - R|$*. In the frequency range where* $\varepsilon_1 < 0$*, indicated by the grey area, the light cannot be transmitted and instead becomes an evanescent wave. In this Reststrahlenband, a large amount of the light is reflected.*

The squared plasma frequency

$$\omega_{pl}^2 = \frac{nq^2}{\varepsilon_0 \varepsilon_\infty m^*} \tag{17}$$

with the effective mass m^*, is a measure of the strength of a mode[5]. It is directly related to the spectral weight *SW* of an optical excitation, with the vacuum impedance $Z_0 = \sqrt{\mu_0/\varepsilon_0} = 377$ Ohm, and is typically given in units of Ω^{-1}cm^{-2}

$$SW = \frac{\pi^2}{Z_0}\,\omega_{pl}^2 \tag{18}$$

[5] Note that ω_{pl} is in units of s^{-1} in Eq. (17), and of cm^{-1} in Eq. (18).

The *screened* plasma frequency $\left(\omega_{pl,screened}^2 = \frac{\omega_{pl}^2}{\varepsilon_\infty}\right)$ can be directly obtained from the optical spectra, as it coincides with the frequency at the zero crossing of ε_1. Alternatively, the spectral weight can be obtained via the peak area underneath the σ_1-curve (see Figure 3.1.3(d)):

$$SW = \int_0^\infty \sigma_1(\omega)\, d\omega \tag{19}$$

One important aspect is, that the infrared light is solely probing excitations which induce a change of the electric dipole moment. This is the case for transverse optical (TO) modes, since the electric field vectors (the one from the dipole moment and the one from the incident electric field ***E***) are parallel and can resonate. Longitudinal optical (LO) modes on the other hand are not accompanied by an electric charge displacement in the direction of the electric field vector of the light wave and therefore do not couple to ***E***. In addition, neither infrared nor Raman spectroscopy is sensitive to acoustic phonons, because these are located at the Brillouin-zone center and at zero energy (see Fig. 3.1).
The LO-mode frequency can be indirectly determined from the zero crossing of the real part of the dielectric function, $\varepsilon_1(\omega_{LO}) = 0$ (see Fig. 3.1.3(c)). Alternatively, it can be derived from the Lyddane-Sachs-Teller relation [116], in which the splitting of ω_{TO} and ω_{LO} depends on the ionicity of the system:

$$\frac{\varepsilon_0}{\varepsilon_\infty} = \frac{\omega_{LO}^2}{\omega_{TO}^2} \tag{20}$$

The Lorentz model is well-suited to describe the response of bound charges, and is used for example for covalently and ionically bound crystals. One extension of this model is the *Cauchy model*, which is useful to describe spectral ranges in which the material is transparent, i.e. $\varepsilon_2 = k = 0$, with *k* as the extinction coefficient. This is typically the case for energies $\omega \geq \omega_{pl}$. Details can be found e.g. in [115].

Gaussian and Voigt oscillators
The line shape of a phonon in optical spectra is in many cases well described by a Lorentzian oscillator. An alternative to describe an optical excitation is to use a *Gaussian* oscillator

$$G(\omega) = \frac{1}{\sqrt{\pi}\ln 2}\, e^{-\ln 2\left(\frac{\omega-\omega_0}{\gamma_G}\right)^2} \tag{21}$$

with the broadening γ_G. As can be seen in Figure 3.1.4, a Gaussian oscillator does not have a long tail toward higher and lower frequency such as the Lorentzian (see inset). This makes using a Gaussian oscillator convenient for instance in order to describe the evolution of a peak in a Raman spectrum as a function of temperature, whereas a Lorentzian fit (if not fitted over a sufficiently long spectral range) could give rise to a misleading interpretation. Importantly, a Gaussian function is not Kramers-Kronig consistent, i.e. its parameters do not have a clear physical interpretation.

Phonon modes in Raman spectra are best described by a convolution of a Gaussian (G) and a Lorentzian (L) profile, which yields an intensity profile of

$$I(\omega) = S\,[\eta L(\omega, \omega_0, \gamma_L) + (1-\eta)G(\omega, \omega_0, \gamma_G)] \tag{22}$$

Here, *S* is the peak area of a mode in the Raman spectrum and η is the mixing factor used to approximate the exact convolution function.

This *Voigt* profile takes into account the line shape of a phonon (Lorentz) which is superimposed by a Gaussian line shape that typically results from the instrumental resolution of the spectrometer [117].

Fano resonance

Some excitations exhibit a non-symmetric line shape around the center frequency in the optical spectra. In this case, an additional value in Eq. (13) needs to be included which accounts for the asymmetry of the phonon line shape. Asymmetric line shapes in the spectra can have different origins. One of them is the Fano resonance, which can occur in materials with strong electron-phonon or spin-phonon coupling [118, 119].

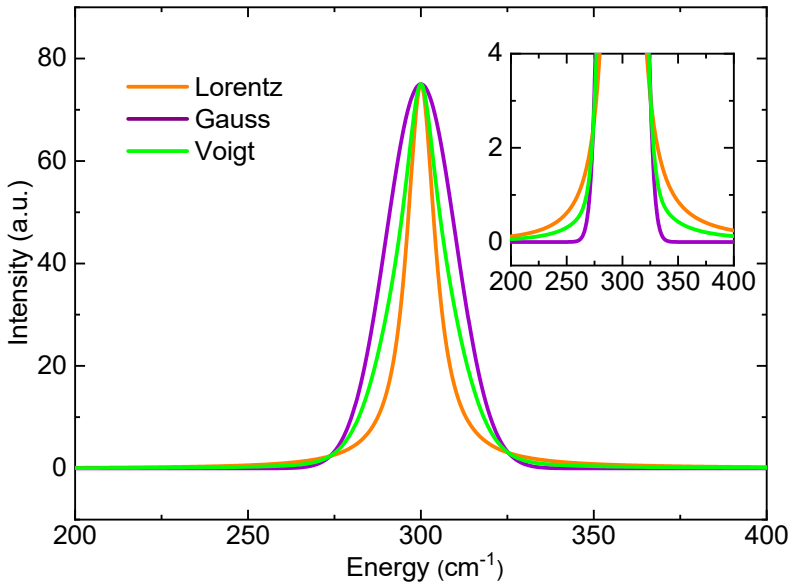

***Figure 3.1.4 Comparison of Lorentzian, Gaussian and Voigt line shapes**. For the Voigt profile, a mixing parameter of $\eta = 1/2$ was used.*

3.1.3.2 Electronic excitations

In contrast to phonons, electrons in a metal are not bound to the nuclei, but instead are moving freely throughout the entire material, according to the Drude-Sommerfeld model [10]. We assume that, apart from the electron-electron and the electron-nuclei collisions, there is no further interaction of the electrons. The electrons do not experience any restoring force (which is the case in the Lorentz model), and thus the resonance frequency is set to $\omega_0 = 0$. For the optical response of free carriers this yields

$$\varepsilon(\omega)_{Drude} = \varepsilon_\infty - \frac{\omega_{pl}^2}{\omega^2 + i\gamma\omega} \tag{23}$$

In the zero frequency limit the real part of the optical conductivity corresponds to the *dc* conductivity, which can be directly obtained via transport measurements as well, e.g. by means of a PPMS (*Physical Property Measurement System*). If there are no additional excitations at higher energies, then $\varepsilon_\infty = 1$.

Metals or semiconductors with multi-bands crossing the Fermi-level can have several different types of carriers, e.g. holes or electrons, so that more than one Drude term is required for an accurate description. Figure 3.1.5 displays an exemplary spectrum of a Drude term, with a plasma frequency $\omega_{pl} = 50$ cm^{-1}.

The spectral weight SW of the free carriers can be calculated by integrating the area below the σ_1-curve, according to Eq. (19). Alternatively, the plasma frequency ω_{pl} can be derived from the zero-crossing of ε_1 (with the knowledge of ε_∞) or by fitting the ε_1 curve using Eq. (23).

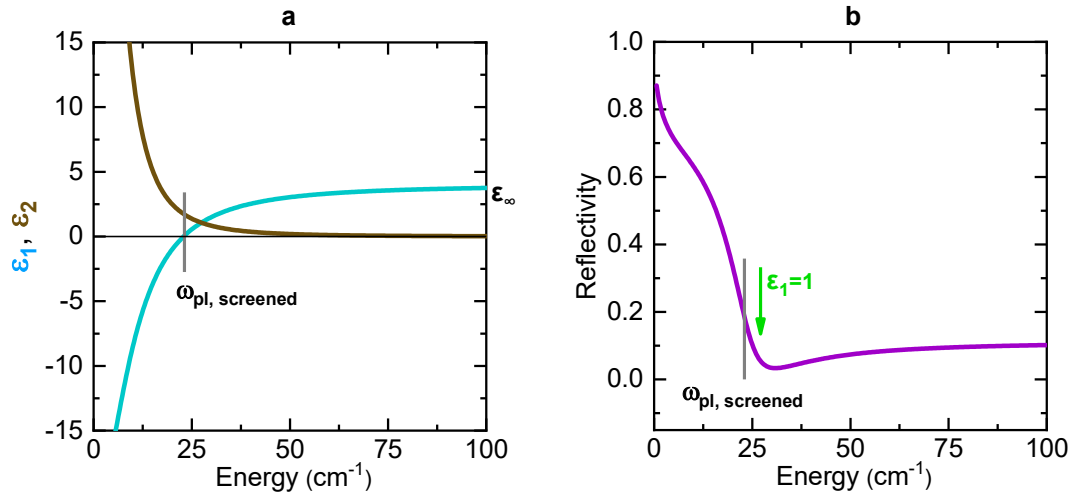

Figure 3.1.5 Drude model. (a) *Complex dielectric function of a Drude oscillator with $\omega_{pl} = 50$ cm^{-1} and $\varepsilon_\infty \sim 4$. The gray line indicates the screened plasma frequency, which is located at $\varepsilon_1 = 0$.* ***(b)*** *shows the corresponding reflectivity spectrum. The green arrow indicates $\varepsilon_1 = n = 1$, at which the reflectivity exhibits a minimum.*

For the case of Cooper pairs, i.e. the superconducting condensate, the situation is less trivial. After obtaining the superconducting part of the real part of the dielectric function $\varepsilon_{1,SC}$, this can equally be fitted via Eq. (23) to derive the squared plasma frequency (here called *superfluid density* or *Cooper pair density* $\Omega_{pl,SC}^2$). Another approach to obtain the superfluid density is to calculate the missing spectral weight in σ_1 according to the *Ferrel-Glover-Tinkham* (FGT) rule [120, 121]:

$$\begin{aligned}\Omega_{pl,SC}^2 &= \frac{Z_0}{\pi^2}\int_{0^+}^{\omega_c}\left[\sigma_1^{normal} - \sigma_1^{supercon.}\right]d\omega \\ &= \frac{Z_0}{\pi^2}\int_{0^+}^{\omega_c}\left[\sigma_1(\omega, T \simeq T_c) - \sigma_1(\omega, T \ll T_c)\right]d\omega\end{aligned} \tag{24}$$

This sum rule states that all spectral weight of a system must be conserved. In the superconducting state ($T < T_c$), some of the low-frequency optical conductivity is suppressed due to the formation of Cooper pairs, and transferred to a δ function at zero energy which accounts for the loss-free response of the superconducting condensate. The opening of this superconducting energy gap $\Delta_{Gap,SC}$ depends on the type of superconducting material (see chapter 2). The FGT rule is fulfilled in the high frequency limit at which the spectra of σ_1 for the normal and superconducting state are the same (here indicated with a cutoff frequency ω_c).

Spin density wave (SDW) or charge density wave (CDW) orders occur when the spin or charge density is periodically modulated within a crystal. They also give rise to an optical gap in the infrared spectra. Most of the missing spectral weight from the gap region is transferred to higher frequency (above the gap edge) where it gives rise to a broad peak in the spectra [25].
This pair breaking peak can be well described by a Gaussian or a broad Lorentzian oscillator. In contrast to the SC condensate, these states are typically pinned to the lattice so that the phase mode of the corresponding order parameter has a rather low spectral weight and occurs at finite frequency.

3.1.4 Normal incidence reflectivity measurements

Generally, the electric field vector of a propagating planar electromagnetic wave is described as

$$\mathbf{E}(\boldsymbol{\omega}) = \hat{e} \cdot \underbrace{E(\omega)}_{amplitude} \cdot \underbrace{e^{i(\tilde{n}K\boldsymbol{r}-\omega t)}}_{phase} \tag{25}$$

with the complex refractive index $\tilde{n} = n + ik$, the wave vector *K* and the unit vector along the scattered (or incident) wave's polarization, $\hat{e}$. The intensity is given by the complex conjugate of the electric field vector:

$$I(\omega) = |\mathbf{E}(\boldsymbol{\omega})|^2 = \mathbf{E}(\boldsymbol{\omega})\mathbf{E}^*(\boldsymbol{\omega}) = E^2(\omega) \tag{26}$$

In reflectivity measurements, the value of interest is the reflectivity R(ω), which is defined as the change of the light's intensity upon reflection, i.e. the ratio of the reflected to the incident light's intensity:

$$R(\omega) = \frac{I_r(\omega)}{I_i(\omega)} \tag{27}$$

In terms of the dielectric function ε(ω) and the complex refractive index $\tilde{n}$, the reflectivity can be expressed as:

$$R = \left|\frac{\sqrt{\varepsilon}-1}{\sqrt{\varepsilon}+1}\right|^2 = \frac{(n-1)^2+k}{(n+1)^2+k} \tag{28}$$

In normal incidence reflectivity however, no information is obtained on the change in the light's phase upon reflection, and the optical functions cannot be directly derived. In order to derive the optical conductivity σ, the dielectric function ε or the refractive index $\tilde{n}$, information on the intensity and the phase change are necessary. This is done by considering the complex reflection coefficient

$$r(\omega) = \frac{\mathbf{E_r}(\boldsymbol{\omega})}{\mathbf{E_i}(\boldsymbol{\omega})} = \sqrt{R(\omega)}e^{-i\Delta\phi(\omega)} \tag{29}$$

which is given by the ratio of the electric field vectors. It is an optical response function, in which the amplitude ratio R(ω) and the phase change of the electric field upon reflection, Δϕ, are related through the *Kramers Kronig transformation (KKT)*

$$\Delta\phi = -\frac{2\omega}{\pi}P\int_0^\infty \frac{ln\sqrt{R(\omega')}}{\omega'^2-\omega^2}d\omega' \tag{30}$$

The *Cauchy principal value P* accounts for the special case when $\omega = \omega'$ for which the relation exhibits a singularity [122]. As seen from Eq. (30), the KKT can only be performed if $\sqrt{R}$ is known for the entire energy spectrum, i.e. from zero to infinite frequency. Consequently, prior to a KKT, there is the need of a suitable extrapolation for the spectral areas outside of the measured energy window (here ca. 40 to 8000 cm^{-1}). The choice of the extrapolation depends on the material system.
In case of a superconductor such as $YBa_2Cu_3O_{6+x}$, for the low-energy part we used a superconducting extrapolation $(R(\omega) = 1 - A\omega^4)$ for $T > T_C$, and a Hagen-Rubens extrapolation $\left(R(\omega) = 1 - A\sqrt{\omega}\right)$ for the normal state ($T > T_c$), where A is a scaling factor. On the high-frequency side (> 5000 cm^{-1}), the reflectivity spectra are merged with the spectra taken by a *Woollam ellipsometer*, which measured the dielectric function up to ~50 000 cm^{-1} (for details see further below). For even higher frequencies (up to infinity) we assumed a constant reflectivity up to 28.5 eV that is followed by a free-electron (ω^{-4}) response.

Experimental setup
The temperature-dependent reflectivity measurements at the University of Fribourg were performed using an ARS-Helitran flow-croystat attached to a Bruker VERTEX 70v Fourier transform infrared spectrometer [123]. Reflectivity spectra from ca. 40 cm^{-1} to 8000 cm^{-1} were collected for several temperatures, from room temperature down to 12 Kelvin. For each frequency region, the choice of experimental devices differ, as indicated in Table 3.1.
Prior to measuring, a proper choice of the components including the light source, type and thickness of beamsplitter, polarizers (in the case of ellipsometry) as well as the detector, is thus paramount. When the sample size approaches the wavelength of the light, diffraction artefacts are arising, which limits the low-energy spectral region for reliable measurements.

Regime	Range	Source	Beamsplitter	Detector
FFIR	10 - 130 cm^{-1}	Hg-Arc lamp	Mylar (40 µm)	Bolometer (< 1.8K)
FIR	30 - 700 cm^{-1}	Hg-Arc lamp/ Globar	Silicon (2 mm)	Bolometer (< 1.8K or 4.2.K)
MIR	500 - 5000 cm^{-1} 500 - 8000 cm^{-1} 500 - 8000 cm^{-1}	Globar	KBr	Bolometer (4.2K) MCT DGTS
NIR	3000 - 12000 cm^{-1}	Tungsten lamp	CaFl/Quartz	Bolometer (4.2K) MCT DGTS
VIS-UV Woollam)	0.5 - 6 eV (4032 - 48393 cm^{-1})	Xenon-lamp	-	CCD/photomultiplier

***Table 3.1 Optical components for infrared and optical spectrometers**. Depending on the energy range, different optical elements are employed. The different spectral regions are in general termed far-far-infrared (FFIR) or terahertz (THz), far-infrared (FIR), mid-infrared (MIR), near-infrared (NIR), visible (VIS) and ultraviolet (UV). Note that for FFIR- to NIR-ellipsometry, only bolometers are used as detectors because of their high sensitivity as compared to the MCT or DGTS.*

For the low-energy range, bolometers have for many decades been well established in infrared spectroscopy as the detector of choice. Here, a resistor element changes its resistance when being irradiated by light, which is detected as a variation in an electric current through the circuit as a function of light intensity. Bolometers perform best when operated at low temperatures and are therefore cooled to the temperature of liquid helium (4.2 K). Their sensitivity can be further enhanced by pumping on the He reservoir of the bolometer, which lowers the temperature further to ~1.8 K. For the MIR-NIR region, alternatives are MCT (*Mercury Cadmium Telluride*) or DTGS (*deuterated triglycine sulfate*) IR detectors.
For the DTGS detector, the absorption of the incoming light leads to a change in the temperature and thus a change in the capacitance of the DGTS element. These detectors are rather inexpensive but relatively slow and have a comparably low sensitivity.
The MCT is only cooled with liquid nitrogen which results in less noise in the spectra than for the DTGS (yet more noise compared to the liquid helium cooled bolometers). Here, the incoming light causes electrons to move from the valence band into the conduction band, for which the induced current is proportional to the light intensity. On the other hand, MCT detectors saturate easily and show a noisy and hysteretic signal when its cooling is performed in an inappropriate manner, which might lead to artefacts in the spectra and to a false interpretation of the results [124].

For the higher energy part (5000 - 50000 cm^{-1}) and in order to perform a Kramers-Kronig transformation (as explained earlier), the dielectric function was obtained via a *Woollam Vase* (*Variable Angle Spectroscopic Ellipsometry*) spectrometer. This commercial setup was modified to be compatible with a UHV liquid helium flow cryostat, which enables measurements from 7 to 750 K.
Two different detectors are exchanged automatically during the measurements, i.e. for energies below 3.4 eV the signal is detected via a silicon-based CCD camera, and for energies above 3.4 eV via a photomultiplier device. In contrast to FT-interferometers, where the entire spectrum is taken in a single scan, here, for every single wavelength a data point is acquired. More details about the *Woollam* setup can be found in [125, 52].

Experimental precautions
Low-temperature normal incidence reflectivity measurements are prone to several sources of error. Three major ones can be categorized into error sources based on (i) the instrumental setup itself, (ii) the morphology and size of the sample and (iii) the ice condensation on the sample surface at cryogenic temperature.

(i) The obtained signal can be distorted via the **setup itself**, e.g. due to a low brilliance of the light sources, the shape of the beam profile, the alignment of the interferometer. This can cause a temporally unstable signal during measurements and thus a low signal-to-noise ratio. Therefore, it is important to continuously calibrate the system and to make a reference measurement, as explained in the following: First, the reflected light intensity of the sample and then of an inserted mirror of polished steel, which has a known reflectance close to 100 % in the infrared range, is measured. This switching between sample and reference-mirror is done automatically with a motorized rotation of the sample/reference stage, in order to enhance reproducibility.

(ii) The **morphology and size of the sample** also has an impact on the intensity of the reflected light. A small sample or a sample with a rough surface back-reflects less light into the detector than a large sample with a flat surface. In order to minimize this experimental error, in a second measurement run an overcoating procedure was preformed, which was introduced by Homes et al. [126] and works as follows: The sample surface is coated with a highly reflecting material (in general aluminium or gold) at room temperature and in an ultra-high vacuum ($\sim 10^{-7}$ mbar), in order to avoid contamination with impurities. Three rings made from a gold wire (with a purity of 99.95 %) are hooked to a tungsten wire. Applying a current of $\sim$2.4 Ampere through the wire causes the gold to evaporate, so that after about 18 seconds a gold layer with a thickness of $\sim$200 nm is obtained. This value is a good compromise in that it is thin enough to reproduce the morphology of the sample surface but thicker than the penetration depth of the infrared light. Following procedure (i) and (ii), the influence of an irregular surface structure and of instrument-related features can be removed from the spectra in order to obtain the absolute reflectivity value *R* of the sample:

$$R(\omega) = \underbrace{\frac{I_{sample}}{I_{mirror}}}_{1^{st}\ meas.} \cdot \underbrace{\left(\frac{I_{gold}}{I_{mirror'}}\right)^{-1}}_{2^{nd}\ meas.} \cdot R_{gold}(\omega) \tag{31}$$

(iii) **Condensation of ice** on the sample surface can occur due to a non-perfect vacuum inside the sample chamber, with the remaining water molecules subliming into ice inside the sample chamber. This leads to a total drop of the reflected light's intensity as well as the formation of a broad mode slighly above 3000 cm^{-1}. This ice condensation can only be completely avoided if the sample is kept under true UHV conditions ($\lesssim 10^{-10}$ mbar). For the standard high vacuum cryostats ($< 10^{-6}$ mbar) there is always some condensation but the layer of ice typically remains thin enough such that it hardly affects the optical meaurements. Special care is taken here to ensure that the shields and the coldhead of the cryostat are at a lower temperature than the sample surface. Typically, the sample is first cooled to low temperatures (below 150 K) and heated up again above 150 K, so that the formed ice evaporates. After cooling back down to base temperature, the measurement itself can begin. Then, one takes spectra at a temperature below and one right above the sublimation point of 150 K. The spectra can thus be normalized, since due to the small temperature difference, these spectra should not differ from each other (unless in the unlikely event, that at exactly this temperature the sample is experiencing a phase transition). Exemplary plots of the impact of the correction procedures, as well as pictures of the setup can be found in [127].

Note that this ice-condensation may not be only a burden, indeed, the ice-band at around 3000 cm^{-1} can serve as a temperature indicator for certain phase transitions, for which e.g. the real sample temperature is otherwise unkown.

3.1.5 Optical spectroscopy in magnetic fields

3.1.5.1 Basics of magneto-optics

An external magnetic field *B* is a common perturbation parameter in solid-state research. For instance, via Hall effect measurements it is possible to derive the material's charge-carrier-concentration [10]. Magnetic fields are also used to reconstruct Fermi surfaces, which play a major role in understanding the electronic behavior of matter. Such experiments include De-Haas-van-Alphén-oscillations, ultrasonic absorption or the study of the cyclotron frequency

$$\omega_{cyl} = \frac{eB}{m^*} \tag{32}$$

with the electron charge *e*, the magnetic field *B* and the effective mass m^*. The application of a *B* field on superconductors normally[6] suppresses (fully or partially) the superconducting condensate, and thus enables the study of other competing ground state orders (like CDW, SDW etc.). This approach is used in this thesis in order to better understand the rich phase diagram of the cuprates, and especially to determine the relationship between superconductivity and the CDW order.
Optical spectroscopy in combination with an applied magnetic field, such as spectroscopic magneto-ellipsometry, involves a more complex analysis of the spectra. Here, instead of a linear function for the optical conductivity, the magneto-optical counterpart is a 3 × 3 tensor [128].
Normal-incidence reflectometry requires a Kramers-Kronig transformation in order to obtain the optical response functions. However, when measuring the reflectance of the sample, some elements of the 3 × 3 tensor are missing. The Kuzmenko group at Geneva University demonstrated that by additional measurements of the Kerr-rotation for reflection (or the Faraday-rotation for transmission), a full description of the magneto-optical properties and therefore a reasonable Kramers-Kronig relation can be performed [128].

Here, we study the intensity changes of the reflectivity of an underdoped YBCO-crystal when exposed to high magnetic fields up to 30 Tesla. In this special case, we can neglect performing additional Kerr (or Faraday) rotation measurements, and instead choose an extrapolation for the spectra outside of our measurement window to perform a reasonable Kramers-Kronig transformation. This approach is justified, since we do not see any sign of Landau-level transitions or cyclotron oscillations. This is most probably due the high effective mass $m^* \approx 4m_e$ and the large scattering rate in cuprates [129] and the relatively small magnetic field of maximum 30 Tesla. Following Eq. (32), one would indeed expect a fairly small cyclotron frequency of around 40 cm^{-1}, which is outside of our measurement window.

3.1.5.2 Magneto-optical experiments

The magnetic-field-dependent reflectivity measurements for this thesis were performed at the High Magnetic Field Laboratory (*Laboratoire National des Champs Magnétiques Intenses*, LNCMI) in Grenoble France, in collaboration with Dr. Milan Orlita. The setup is displayed in Figure 3.1.6.

[6] There are certain types of superconducting systems, where the application of an external magnetic field can recover the macroscopic coherence [22, 23].

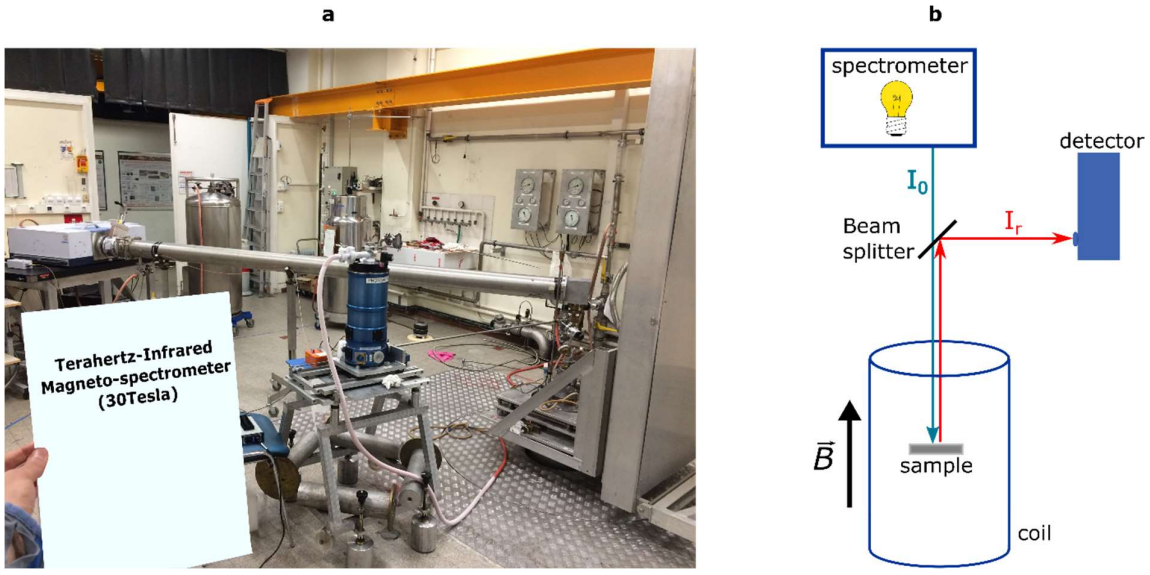

Figure 3.1.6 Magneto-optical reflectivity setup at the High Magnetic Field Laboratory (LNCMI) in Grenoble, France. (a) *Image of the setup, showing the spectrometer, the long optical pipe and the bolometer (in blue color).* ***(b)*** *Sketch of measurements, with the incoming light intensity I_0 and the reflected and detected light intensity I_R.*

A VERTEX 80v Fourier transform infrared spectrometer[7] is connected to a beam splitter (BS) which leads to the sample via a long metallic pipe, in order to ensure that the optical components inside the spectrometer chamber are not affected by the magnetic field. The sample is placed in a sealed chamber with low-pressure helium exchange gas and surrounded by a resistive coil, which creates magnetic fields of up to 34 Tesla by running a high current through the coil. It is possible to apply the magnetic field parallel or anti-parallel to the incoming/outgoing light and perpendicular to the sample surface. In this so-called *Faraday configuration*, the light beam I_0 travels from the spectrometer through the pipe to the BS and arrives at the sample surface, gets reflected back to the BS and finally reaches the bolometer, where the total reflectivity I_r is detected. The sample was first cooled down to low temperatures, and then the magnetic field was applied. Prior to measuring the spectra, the magnetic field was ramped up and down at least a couple of times, to settle any field-induced movements of the optical components.
The sample temperature is set to 4.2 K (77 K) by placing the sample rod into a liquid helium (nitrogen) bath. Inside this rod (see Figure 3.1.7(c)), the sample is mounted on a brass holder together with a reference mirror (made of gold or polished steel), which can be rotated manually. Due to the high magnetic field, electrical motors as in Fribourg cannot be used.

Applying a magnetic field to a superconducting sample induces a strong repulsion force $\boldsymbol{F_R}$ which can lead to a movement of the sample and thus unwanted artefacts in the spectra. Cuprates are *type II* superconductors and therefore have a rather small H_{c1} of around 10^{-2} Tesla [130, 131] and a high upper critical field of up to $H_{c2} \approx 25$ to 150 Tesla [132], depending on the doping level. For the relevant range of magnetic fields (up to 30 Tesla) the sample is therefore in the vortex phase. The magnetic force on the sample occurs due to the vortex pinning P_V (with $\boldsymbol{F_R} \propto P_V$) which is the pinning of magnetic vortices (magnetic flux quanta) by different types of defects in the sample.

[7] The spectrometer in Grenoble is the new version (VERTEX 80v) of the one at Fribourg University (VERTEX 70v) and quite similar so that the principles mentioned above still hold.

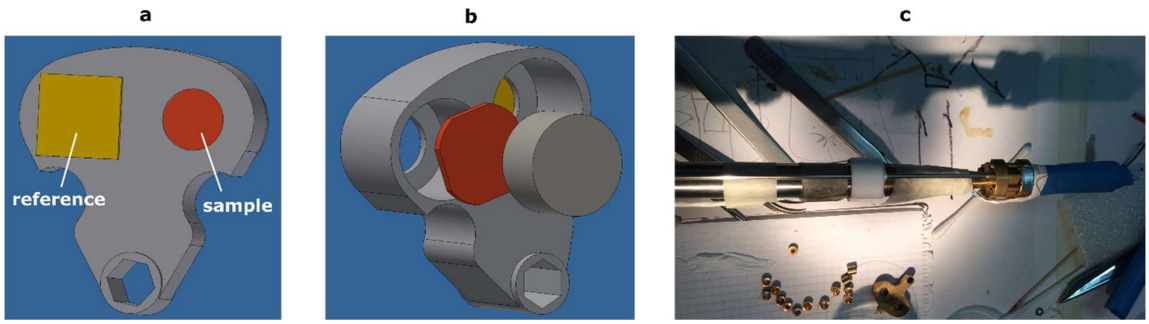

Figure 3.1.7 Sample holder configuration for optical measurements of superconductors in high magnetic fields. *The reference gold mirror (yellow) is mounted on the frontside of the holder* ***(a)****, whereas the sample (red) is fixed with an additional holder piece (grey cylinder) from the backside* ***(b)****. An image of the sample rod is shown in* ***(c)****.*

One way to avoid this movement is to cool the sample below T_C, while the magnetic field is already applied. In this case no forces should occur. This is unfortunately not possible due to technical reasons of the used setup. Here, the problem was solved in a different manner. Normally, the sample fixed on top of the holder. Instead, the sample was placed inside the holder and fixed with an additional piece of brass from the backside (see Figure 3.1.7(a) and (b)) so that no field-induced movement is possible. One condition for using this approach is of course, that the sample size is adequate for the rather tiny holder-opening, and thick enough so that is does not run risk of breaking or cleaving due to the induced forces.

For each applied magnetic field (zero up to 30 Tesla), the intensity ratio between the sample and the gold reference mirror, $I(B)$, is measured. An additional in-situ gold-coating of the sample is not possible. Still, the total reflectance of the sample in a magnetic field can be derived by comparing the measured intensities with the absolute reflectivity value, which yields

$$R(B) = \frac{I(B)}{I(0T)} R(0T) \tag{33}$$

By measuring the *R(0T)* spectra with the setup in Fribourg, the absolute reflectivity spectrum $R(B)$ in the range from ca. 50 to 6000 cm^{-1} at different magnetic fields up to 30 Tesla was obtained.
The derivation of the full complex optical functions from the reflectivity data can be done by KK-consistent fitting of the reflectivity directly, e.g. with the program *RefFIT* [133]. This is inconvenient when studying very small magnetic-field induced features, since such a fitting procedure necessarily induces an error which might be of the same order as the small effect.
Another option, which was used here, is to consider an extrapolation for the low-frequency and the high-frequency part of the reflectivity, in analogy to the procedure described above, followed by a direct KK transformation of the data.

3.1.6 Ellipsometry

In ellipsometry, the change in the state of polarization is measured, rather than the total *reflectivity* value in normal-incidence measurements. Being a self-referencing technique, no reference measurements are required. Here, information on both the amplitude and phase of the reflected electric field vector are obtained, which allows to derive the optical functions ε and σ directly, without the need to perform a Kramers-Kronig analysis.

The state of polarization is defined by the orientation of the electric field vector ***E***. Light sources such as commercial light bulbs typically yield unpolarized radiation, i.e. ***E*** does not have a preferred orientation. Naturally polarized light sources are for instance lasers. An electromagnetic wave can be polarized by using certain optical elements known as *polarizers*. The orientation of the polarization can also be rotated by optical elements known as $\frac{\lambda}{4}$ and $\frac{\lambda}{2}$ plates. In transmission geometry, these are optically anisotropic materials, i.e. in which the refractive index is different along the *x*-axis than the *y*-axis. Electromagnetic waves can be *linearly* polarized (orientation of ***E*** is constant in time), *circularly* polarized (***E*** rotates with a constant angular frequency in the plane perpendicular to the wave propagation direction *K*). In the general, the light is elliptically polarized, i.e. the amplitude changes with time while the tip of ***E*** describes an ellipse on the plane perpendicular to *K*.
A full mathematical description of the ellipsometry response is done by means of the Mueller matrix formalism. The electromagnetic wave is described by the Stokes vectors and the 4 × 4 Mueller matrices. In the special case with no depolarization effect upon reflection on the sample (depolarization can be caused e.g. by non-uniform film thickness, surface roughness), the simpler Jones formalism with 2 × 2 matrices, in which the Jones vectors have only two components, E_x and E_y, is sufficient. Detailed literature can be found for instance in [134, 135].

In ellipsometry experiments, the two measured quantities are the relative phase shift between the reflected s-and p-polarized light, $\Delta = \Delta_p - \Delta_s$, and the amplitude-ratio of the Fresnel coefficients Ψ (see Figure 3.1.8). They are related to the Fresnel coefficients as

$$r_p = \frac{\mathbf{E_{rp}}}{\mathbf{E_{ip}}} = |r_p| e^{i\Delta_p}$$
$$r_s = \frac{\mathbf{E_{rs}}}{\mathbf{E_{is}}} = |r_s| e^{i\Delta_s} \tag{34}$$

and to the *pseudo-dielectric function* $\langle\varepsilon\rangle$ as

$$\rho = \frac{r_p}{r_s} = \tan\Psi \cdot e^{i\Delta} \tag{35}$$

$$\langle\varepsilon\rangle = \sin^2(\varphi)\left[1 + \tan^2(\varphi)\cdot\left(\frac{1+\rho}{1-\rho}\right)\right] \tag{36}$$

with φ being the angle of incidence on the sample and ρ the complex reflectivity ratio of the p- and s-polarized light [134]. Ellipsometry measurements are typically performed in the vicinity of the Brewster angle φ_B, where the difference between r_s and r_p is maximal (see Fig. 3.1.2(b)).
Consequently, ellipsometry is especially useful for the investigation of thin films: For measuring close to φ_B of the substrate, most of the reflected (p-polarized) light is coming from the thin films. This high sensitivity can also be a curse, because anything is seen in the signal, such as contributions from electrical wires and of dirt particles. Furthermore, the diffraction problem is more severe [136] than for normal incidence reflectivity.
The obtained pseudo-dielectric function $\langle\varepsilon\rangle$ is in general dominated by the response of the x-component of the dielectric function [135], with the *x*-axis defined by the cross section of the plane of incidence of the photons with the sample surface. In the case of anisotropic systems, the optical response depends on the surface orientation direction with respect to the plane of incidence of the light.

Therefore, ellipsometry is normally insensitive to the z-component. Exceptions occur close to the energy of a LO-mode in the out-of-plane component (z-component) of the dielectric function at which $\varepsilon_1 = 0$ [137, 135]. The strength of the *z*-axis response is proportional to the loss-function, $Im\left\{-\frac{1}{\varepsilon_z}\right\} = \frac{\varepsilon_{2,z}}{\varepsilon_{1,z}^2+\varepsilon_{2,z}^2}$, which becomes sizeable if ε_2 is small.

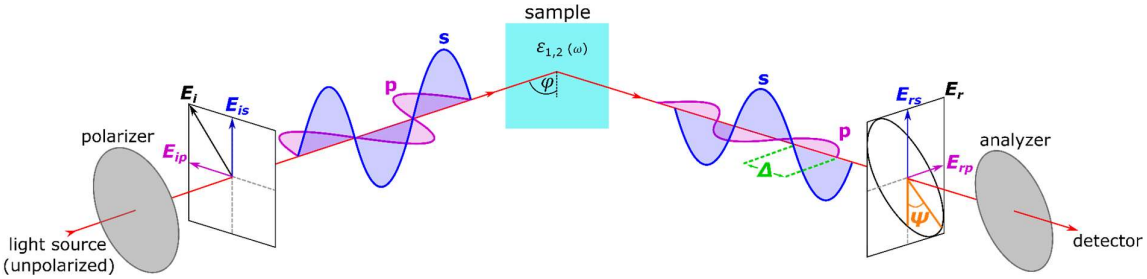

Figure 3.1.8 Schematic of an ellipsometry experiment. *The incident light polarization is defined by the electric field vector $\boldsymbol{E}_i$, which can be divided into its s-polarized and p-polarized component. Upon reflection on the sample surface under a grazing incidence, $\boldsymbol{E_{rp}} = r_p\boldsymbol{E_{ip}}$ and $\boldsymbol{E_{rs}} = r_s\boldsymbol{E_{is}}$ are obtained in terms of Δ (green) and Ψ (orange).*

An ellipsometry experiment can be performed in several ways. The simplest arrangement is the rotating analyzer-configuration (RAE), which is used for most ellipsometry measurements in this thesis: A light source radiaties unpolarized light. A polarizer is placed in front of the sample and its polarization direction is fixed to a certain angle. After the sample, a second polarizer (called the *analyzer*) is rotated in discrete steps from 0 to 180° degrees. The detector is (should be) polarization-independent, and measures the intensity variation as a function of the analyzer angle. This signal can be fitted via an intensity function from which the ellipsometric angles Δ, Ψ and thus the optical functions are reconstructed. Details are found in [52, 138]. The measurements in the UV-VIS and the FIR-MIR range were done in different setups, as detailed in the following.

Visible-Ultraviolet ellipsometer

In this study, the optical response in the visible to ultraviolet region (5000 - 50 000 cm^{-1}) was obtained with a *Woollam Vase* (*Variable Angle Spectroscopic Ellipsometry*) setup. It was subsequently used to perform a Kramers-Kronig transformation with the normal-incidence reflectivity spectra in the THz-near-infrared region (see the previous chapter). Note that this technique is likewise well suited to directly measure the band gaps of certain materials, or to determine the layer thickness of thin films. More technical details can be found in [52, 125].

It is important to mention that these spectra contain not only contributions from the in-plane but also from the out-of-plane component of the sample's dielectric function, since the measurements are taken at grazing incidence. Therefore, a correction of the raw spectra is required in the case of anisotropic systems.

$YBa_2Cu_3O_{6.6}$, as studied here, is indeed such an example. The spectra are shown in Figure 3.1.9(a), in which a *c*-axis correction leads to a shift of the plasma edge of the real in-plane response compared to the as-measured raw data. Figure 3.1.9(b) shows for comparison the temperature-dependent shift of the plasma edge.

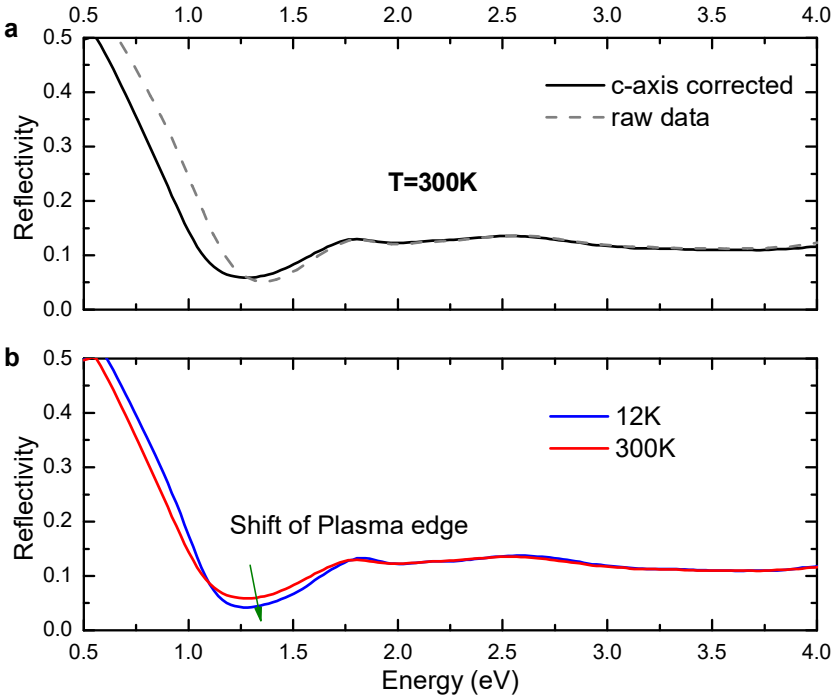

Figure 3.1.9 Visible-Ultraviolet response of an underdoped $YBa_2Cu_3O_{6.6}$ crystal. (a) *In-plane reflectivity spectra as calculated from the pseudo-dielectric (gray dashed line) and the dielectric (black solid line) function, respectively. The latter has been obtained by performing additional ellipsometry measurements on a side face of the sample with the c-axis in the plane of incidence and a subsequent numerical procedure to determine the in-plane and the c-axis components of the dielectric function.* ***(b)*** *Comparison of the c-axis corrected spectra at 12 K (blue line) and at room temperature (red line).*

Far- and mid-infrared ellipsometer

The FIR-MIR (ca. 100 - 3000 cm^{-1}) ellipsometry setup is shown in Figure 3.1.10. As sketched in (a) and pictured in (b), the setup consists of a Bruker VERTEX 70v spectrometer that is attached to a separate sample chamber, which contains the rotating analyzer ellipsometer (RAE configuration) and is equipped with a He-flow cryostat. The He-flow cryostat enables sample temperatures from ca. 5 K - 350 K. A bolometer is used here to detect the signal. All chambers are pumped to have a rough vacuum of about 7 mbar, in order to decrease the absorption of the light by the air, especially by water molecules, and thus to increase the intensity and stability of the signal. The sample can be *in-situ* radiated with UV light from a 100 Watt Xenon lamp. This feature can be for instance used to study photodoping effects on systems like $SrTiO_3$ with an indirect bandgap of 3.25 eV and a direct one of 3.75 eV (which justifies the need for a Xenon lamp, which outputs a broad range of energies from 1.2 eV to 6.2 eV). In addition, the sample stage is equipped with electrical wires (see Figure 3.1.10(c)).

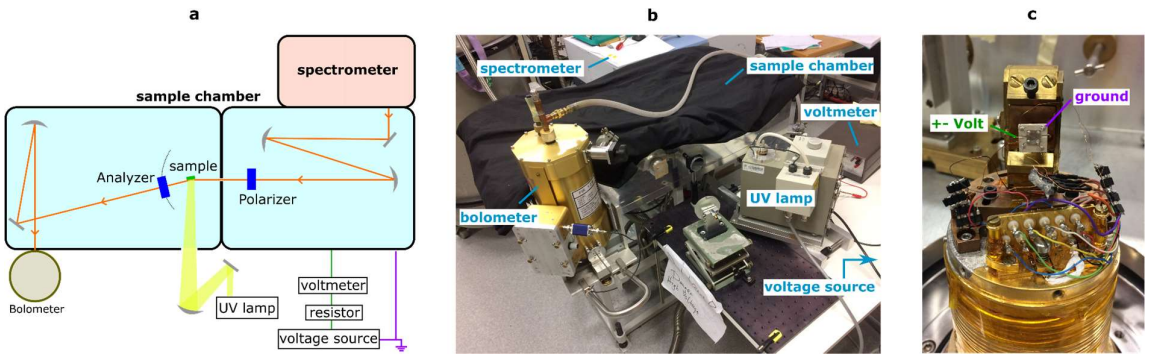

Figure 3.1.10 Far- and mid-infrared ellipsometry setup. (a) *Sketch and* ***(b)*** *image of the experimental setup in the rotating analyzer configuration (RAE). The black cloth on top of the sample chamber is to avoid undesired photodoping effects during the measurement.* ***(c)*** *Image of a sample being mounted on a ceramic plate and connected with electrical wires in order to perform voltage dependent studies.*

A combination of a voltage source from the company Keithley and a high sensitivity voltmeter enables a high voltage to be applied to the sample at different temperatures, with or without UV light illumination. A resistor element is connected in series as a safety switch in case of an electrical breakthrough. Figure 3.1.10(c) shows a back-gated $AlO_x/SrTiO_3$ sample, in which the top electrode is the 2DEG formed on the $SrTiO_3$ interface and connected via four wires with the ground. The backside of the sample has been pasted with silver paint onto a ceramic plate, which serves as an electrical insulator.

3.2 Raman spectroscopy

Raman spectroscopy is nowadays a common method to investigate phenomena in physics, chemistry, materials science as well as in metrology and atmospheric physics. Especially for solid state and materials science it enables the study of different types of elementary vibrations and excitations in a wide range of materials.
When light is reflected from a medium, it contains not only an elastically scattered contribution but also inelastic scattering, also known as *Raman scattering*. This effect was discovered in 1928 by two Indian physicists[8] called C.V. Raman and K.S. Krishan, when they irradiated monochromatic sunlight onto some liquids and gases, and saw that the elastically scattered light reflected back is *'accompanied by a modified scattered radiation of degraded frequency'* [139]. Since then, from a technical point of view, the quality of this method was improved by enhancing the signal-to-noise ratio and acquisition time of the spectra. This progress was made possible by the introduction of the laser as light source in 1960 [140], the development of triple monochromators, and the replacement of grating spectrometers by prism spectrographs and photographic plates by charge-coupled devices (CCDs), respectively.

In the following section, the Raman process is described from a classical phenomenological point of view, in which some parts need a quantum mechanical treatment. A description of the experimental setup used for this thesis is provided, together with a brief introduction to other types of advanced Raman techniques, which are not the focus of this study, but nevertheless deserve a short discussion.

3.2.1 Classical Raman process

As displayed in the previous section *Infrared spectroscopy*, electromagnetic waves radiated onto matter can be either reflected, transmitted or absorbed. Most of the light is scattered elastically (so-called *Rayleigh scattering*), whereby the scattered photon has the same energy as the incident one ($\omega_{in} = \omega_{out}$). However, a small portion of the reflected light is inelastically scattered, which means that there is some transfer of energy and momentum between the incoming light and the material. This process leads to the creation (*Stokes*) or annihilation (*Anti-Stokes*) of an elementary excitation [113]. The portion of the light being inelastically scattered is fairly small, approximately one photon is inelastically scattered to 10^6 - 10^8 elastically scattered photons. The whole process can be described in a Jablonski diagram, see Figure 3.2.1(a).

In a simple picture, a certain material system contains the energetic ground state E_0, and virtual states which are non-stationary states lying in between vibrational energy levels and the energies electronic states higher in energy. If the incoming probing light with a certain energy ω_{LASER} excites the system, this can fall back to E_0 (Rayleigh) or to an energy level $E_n > E_0$, where the reflected light 'lost' some energy to the material (Stokes), $\omega_{LASER} > \omega_{STOKES}$. Some higher energy levels might be occupied at $T > 0$ K before even shining light on the sample. The probing light then de-excites the system (Anti-Stokes) and the scattered light has more energy $\omega_{LASER} < \omega_{ANTI\text{-}STOKES}$. This makes Raman scattering quite different to the infrared process (orange arrow), where the incoming energy directly fits certain energy differences in the Jablonksi diagram.

[8] Note, that in the same year G. Landsberg and L. Mandelstam discovered independently the same effect, which is nowadays known as *Raman* scattering. They published their findings even one week before Raman and Krishnan in a preliminary report. Later in that year, their results appeared in the journal *Naturwissenschaften* [284].

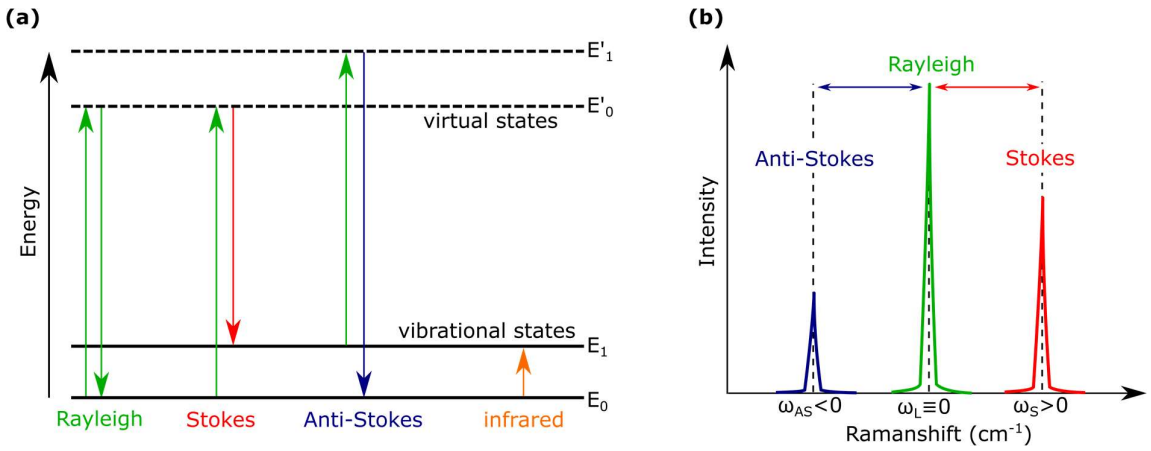

Figure 3.2.1 Schematic of the Raman scattering process. (a) *Light matter interaction displayed as a Jablonski diagram.* ***(b)*** *Schematic of a Raman spectrum. The Rayleigh-line, i.e. the incoming laser beam with energy ω_L is usually defined as zero energy, whereas the Stokes (Anti-Stokes) scattering is displayed at positive (negative) frequencies.*

A schematic of a resulting Raman spectrum is pictured in Figure 3.2.1(b). The energy difference between the incoming and scattered light is the so-called *Raman shift* ω (*x*-axis), which is typically in units of cm^{-1}. The zero position therefore defines the Rayleigh line. The intensity (*y*-axis) of the mode is given by the Raman cross section, discussed later in this chapter. The Stokes part, conventionally assigned to positive ω, is normally chosen in research articles to display the excitations of a certain material. The Anti-Stokes part is assigned to negative ω and can be very useful for analyzing the data, to verify if a certain mode in the Stokes spectrum is not an artefact and, most crucially, to determine the sample temperature via Boltzmann statistics, as discussed in the next section.

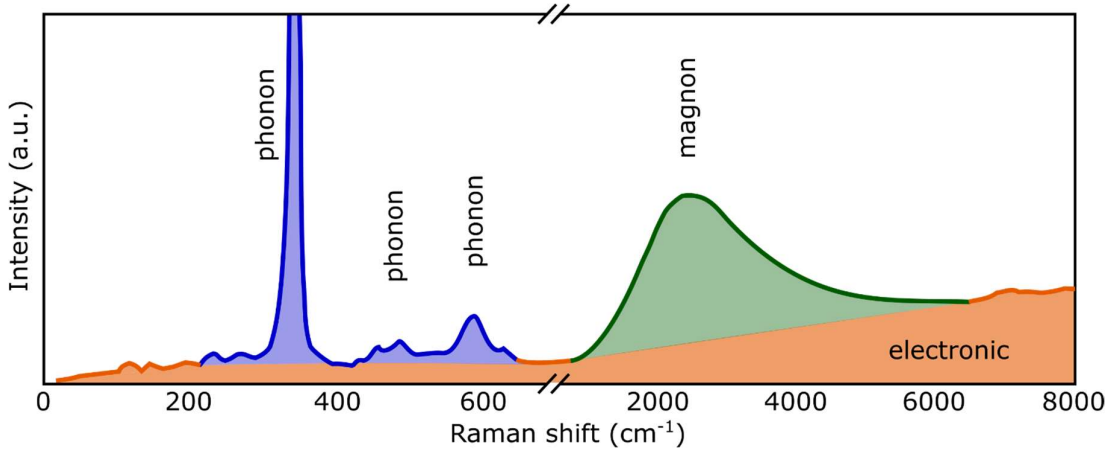

Figure 3.2.2 Typical Raman spectrum of a $(Y_{0.93}Ca_{0.08})Ba_2Cu_3O_{6.3}$ crystal *(adapted from [141]). Several phonons (blue), a magnon (green) causes a broad peak around 2500 cm^{-1}. The background in red color is due electronic contribution.*

Raman experiments are mostly carried out with visible photons (~1 eV) and give access to low-energy excitations such as phonons (~10 meV) and magnons (~300 meV), or electronic scattering. As an example, a Raman spectrum (Stokes line) for the high-T_c superconductor $(Y_{0.93}Ca_{0.08})Ba_2Cu_3O_{6.3}$ is displayed in Figure 3.2.2.

Related forms of Raman scattering and *photoluminescence*, i.e. the phenomena in which a material relaxes by emitting photons in response to electromagnetic radiation, are *fluorescence* and *phosphorescence*.

Fluorescence

After a photoexcitation brings the system from the ground state to a higher energy level (see also Figure 3.2.1(a)), the system relaxes by emitting photons. This process called *fluorescence* is likely to occur and therefore typically fast on the timescale of nanoseconds. In most materials which exhibit fluorescent behavior, so-called *fluorophores*, the emitted photon has less energy than the one used for photoexcitation. The remaining energy $E_{remain} = E_{excite} - E_{emit}$ is for instance transferred into vibrational states, so that the system relaxes in a non-radiative manner. In this case, E_{remain} equals the Stokes shift in Raman spectroscopy, which provides information about the vibration states of the system. Therefore, some materials can emit fluorescent light in the visible range even when the exciting photons are in the ultraviolet region and therefore not visible to the human eye.

Fluorescence microscopy or spectroscopy [142] is widely used in natural science and medicine. Fluorescence can be used for the labeling of molecules in medicine and life science, LED lamps or as fluorescent lamps. Importantly to mention is the term of fluorescent quenching, which refers to any process that decreases the fluorescence light intensity of a sample [142]. An efficient fluorescent quencher is for instance molecular oxygen, due its unique triple state nature. Note that in the context of Raman spectroscopy, a material with strong fluorescence can be problematic when the fluorescent signal overlaps with and might even overwhelms the Raman signal. Therefore, Raman and Fluorescence spectroscopy are usually seen as complementary techniques.

Phosphorescence

If the excited electron does not jump back to a lower energy single state via an allowed transition, it might instead become trapped in a triplet state. From this state it can jump into the lower singlet state via a f*orbidden* transition, which will still occur in quantum mechanics, but, being a less likely process, it has much longer decay time than fluorescence-like relaxation. This type of emission is called *phosphorescence*, where the luminescence continues long after the photoexcitation has ceased where the timescales can range from microseconds up to minutes and even hours. Therefore, in such materials the energy of the absorbed photons from the incident beam is stored for much longer times than for fluorescent materials. Children might experience the effect of phosphorescence, i.e. slowly degrading excited electron states, as 'glow-in the dark-stickers' in their bedrooms.

3.2.2 Theoretical description of Raman scattering

The theory of Raman scattering is well explained in the quantum mechanical picture, and documented in several textbooks (e.g. [113]). This treatment is essential when it comes to describe accurately experiments involving resonant Raman scattering, magnon scattering etc. In the case of high-temperature superconductors, for example, it was found that the electronic background in the spectra can provide information on the symmetry of the superconducting gap and capture the spectral weight redistribution at T_c (e.g. [141]).

In this case, the Hamiltonian is a sum of the un-perturbed contribution (H_0) and the one which includes the phonon-phonon, the electron-phonon, phonon-electron etc. interactions:

$$H = H_0 + H_{interaction} \tag{37}$$

In general, the regular Raman-scattering process is already well described by the classical picture, which will be presented in the following. Exceptions include the use of the Bose-Einstein-statistics to derive the sample temperature.

We recall the basic formalism for the interaction between a plane wave $\boldsymbol{E}(r,t) = \hat{\boldsymbol{e}} E_0 e^{i(Kr-\omega t)}$ with matter, in which the polarization $\boldsymbol{P}$ was described by the electrical susceptibility χ (section 3.1.1). In the Born-Oppenheimer approximation, the electrons move rapidly compared to the slower motion of the atomic nuclei. With this adiabatic assumption, the susceptibility can be expressed as a function of the atomic displacement $\boldsymbol{u}$ around their equilibrium position. For small displacements compared to the unit cell dimensions, we can derive the Taylor expansion:

$$\chi(\boldsymbol{u}) = \underbrace{\chi_0}_{Rayleigh} + \underbrace{\frac{\partial \chi}{\partial \boldsymbol{u}}|_0 \, \boldsymbol{u}}_{\substack{1^{st}-order \\ Raman\ scattering}} + \underbrace{\frac{1}{2}\frac{\partial^2 \chi}{\partial^2 \boldsymbol{u}}|_0 \, \boldsymbol{u}^2 + \ \ldots}_{\substack{higher\ orders \\ Raman\ scattering}} \tag{38}$$

Here we focus on the first-order Raman scattering and neglect the higher order terms. This yields the relation for the induced macroscopic polarization

$$\boldsymbol{P} = \varepsilon_0 \chi \boldsymbol{E}(t) = \varepsilon_0 \chi_0 \boldsymbol{E}(\boldsymbol{t}) + \frac{1}{2}\frac{\partial \chi}{\partial \boldsymbol{u}} \boldsymbol{u_0} \cdot \boldsymbol{E}(\boldsymbol{t}) \tag{39}$$

In analogy to Eq. (38), the first term accounts for the oscillations of $\boldsymbol{P}$ which are in phase with the incident radiation (i.e. elastic scattering) and the second one for first-order Raman process (i.e. inelastic scattering). Expressing the electric field as a plane wave with its components thus yields:

$$\begin{aligned} \boldsymbol{P} = \frac{\partial \chi}{\partial \boldsymbol{u}}|_0 \, \boldsymbol{u} \hat{\boldsymbol{e}} E_0 \big\{ & \cos\big[\big((K+q)\cdot r\big) - (\omega_0 + \omega_R)t\big] \\ & + \cos\big[\big((K-q)\cdot r\big) - (\omega_0 - \omega_R)t\big]\big\} \end{aligned} \tag{40}$$

Notably, the energy of the incident light is shifted by $\pm\omega_R$. The term including $(\omega_0 - \omega_R)$ is denoted for the Stokes part and the one with $(\omega_0 + \omega_R)$ for the Anti-Stokes part. Both terms describe the same excitation inside the material, generated or absorbed by the scattering process, respectively.

Raman tensor

In Raman sepctrosocopy and the analysis of the spectra, one important quantity is the Raman tensor $\widetilde{\boldsymbol{R}}$, which is depending on the suceptibility as

$$\widetilde{\boldsymbol{R}} = \frac{\partial \chi}{\partial \boldsymbol{u}}|_0 \, \boldsymbol{u} \tag{41}$$

The Raman tensor reflects the symmetry of the collective lattice vibration. Performing a polarization-dependent Raman analysis can thus serve as a tool to reveal a materials symmetry. The *Raman cross section* and the *intensity* of a certain Raman excitation are directly related to $\widetilde{\boldsymbol{R}}$.

The power of the incident light being inelastically scattered into an area $d\Omega$ with an energy between ω and dω is typically expressed as the power cross section

$$\left(\frac{\partial \sigma^2}{\partial \Omega \partial \omega}\right)_{Power} \sim (\omega \pm \omega_R)^4 \left|\hat{\boldsymbol{e}}_s \widetilde{\boldsymbol{R}} \hat{\boldsymbol{e}}_i\right|^2 \tag{42}$$

Here, $\hat{\boldsymbol{e}}_s$ ($\hat{\boldsymbol{e}}_i$) is the unit vector along the scattered (incident) wave's polarization. The power cross section measures the ratio of scattering to incident power, which is the case for e.g. photomultipliers and –plates. *Photon counting devices* on the other hand, such as CCD cameras, measure the ratio of scattered to incident photons. This relation is termed as the *quantum cross section*

$$\left(\frac{\partial\sigma^2}{\partial\Omega\partial\omega}\right)_{Quantum} \sim (\omega \pm \omega_R)^3 \left|\hat{\boldsymbol{e}}_s\tilde{\boldsymbol{R}}\hat{\boldsymbol{e}}_i\right|^2 \tag{43}$$

Therefore, one needs to pay close attention what kind of detector is used. This is important for instance when calculating the sample temperatues via the Stokes/Anti-Stokes-relation, as will be discussed below.

The probability of a Raman process to occur is expressed as the Raman intensity

$$I_{Raman} \sim \left(\frac{\partial\sigma^2}{\partial\Omega\partial\omega}\right) \sim \left|\boldsymbol{e}_s\tilde{\boldsymbol{R}}\boldsymbol{e}_i\right|^2 \tag{44}$$

Whether or not a peak is seen in the Raman spectrum, and with which strength, depends on the polarization of the incident and scattered light, as well as on the Raman tensor $\tilde{\boldsymbol{R}}$. Different combinations of incident-to-scattered light polarization thus probe different components of the Raman tensor. Note that the intensity can be become zero even though the single elements of $\tilde{\boldsymbol{R}}$ are finite.

Determination of the sample's temperature via the intensity ratio of the Stokes/Anti-Stokes lines

Since the studied collective lattice vibrations can be described as bosonic quasiparticles, the thermal population $n(v)$ is described by the *Bose-Einstein statistics*, which yields

$$n(v) = \left(e^{\frac{hv}{k_BT}} - 1\right)^{-1} \tag{45}$$

For Anti-Stokes scattering, the incoming photon interacts with an already excited state (see Figure 3.2.1), which makes it a less probable process, leading to a smaller peak intensity I_{AS} of a certain mode than I_S in the Stokes spectrum. According to the *Bose-Einstein distribution* (or in the classical picture the *Boltzmann distribution*), this intensity relation is given by

$$\frac{I_{as}}{I_s} \sim e^{-\frac{hv_R}{k_BT}} \tag{46}$$

with the Boltzmann constant $k_B \sim 1.381 \times 10^{-23}$ Joule/Kelvin, the Planck constant $h \sim 6.626 \times 10^{-34}$ Joule·second and the $v_R = 2\pi \cdot \omega_R$ as the Raman shift of a certain mode. In this formula, both frequencies v_r and v_0 need to be in SI units of THz in order to fulfill the equation. Including the energy of the laser light v_0, this relation can thus serve as a powerful tool to accurately determine the sample temperature [143, 144]:

$$T_{sample} = (h \cdot v_R) \Big/ \left[k_B\left(\log\left(\frac{I_S}{I_{AS}}\right) + 3 \cdot \log\left(\frac{v_0 + v_R}{v_0 - v_R}\right)\right)\right] \tag{47}$$

Note that the factor '3' is instrumentation-dependent. The detector used in our work is a CCD camera, which measures the amount of photons coming in, and therefore the *quantum cross section* needs to be considered. Older types of Raman instrumentation might use photo-multipliers or plates, which measure the power cross section and one needs to use the pre-factor '4' instead [145].

Figure 3.2.3 shows an example how to determine the sample's temperature via the Bose-Einstein relation. Here, the application of an electric field on a $SrTiO_3$ crystal leads to a broken inversion symmetry such that infrared-active modes become Raman-active. The electric-field-induced soft mode (TO_1 mode; in red color) is subtracted from the spectra where no voltage was applied and therefore without the TO_1 mode (black line). The small peak at around 15 cm^{-1} is an R-mode, which is visible in the tetragonal phase of $SrTiO_3$ for $T < T^* \approx 105$ K.

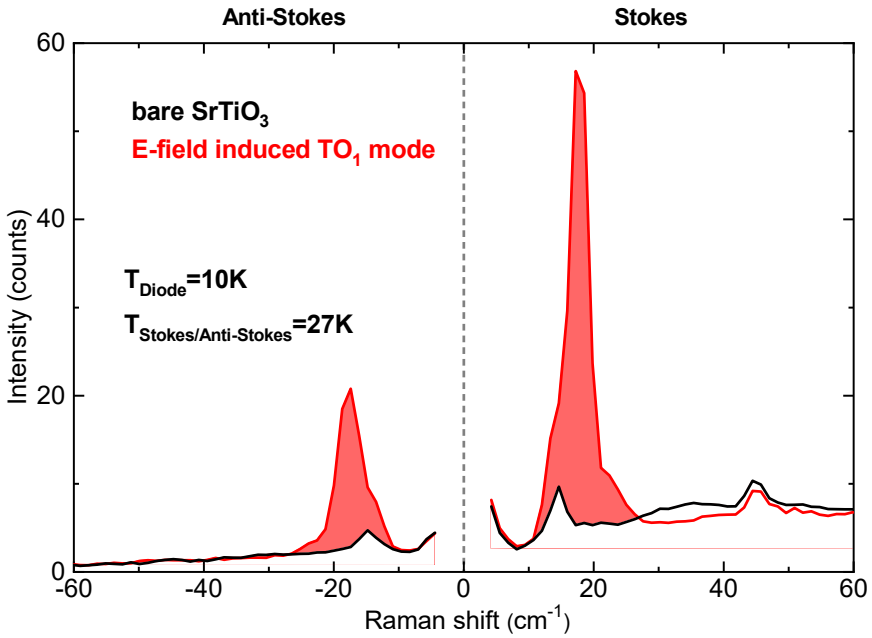

Figure 3.2.3 Temperature determination via Bose-Einstein relation of the intensity ratio of the Stokes and Anti-stokes signals for a cryo-cooled $SrTiO_3$ crystal. *The peak area of the electric-field-induced TO_1-mode (red colored areas) of the Stokes side is compared to the one at the Anti-Stokes side, from which according to Eq. (47) a sample temperature of ca. 27 K is deduced. During the measurement, a sensor diode, which was placed inside the cryostat close to the sample, showed a value of 10 K. This temperature difference is due to the laser heating, and gets smaller toward higher temperatures as the thermal conductivity and the heat capacity of the sample increases.*

Raman spectra are typically presented in terms of the measured Intensity I_{raw} (in counts) as a function of energy, as in Figure 3.2.3. The spectra can also be corrected by the *Bose thermal factor* (following Eq. (45) and (46)), in order to derive the electronic Raman susceptibility $\chi''(\omega)$, or simply the imaginary part of the susceptibility, $Im\ \chi(\omega)$, which is connected to I_{raw} as

$$\chi''(\omega) = \frac{I_{raw}}{Bose\ thermal\ factor} \tag{48}$$

This approach is especially convenient when comparing a sample's excitations at different temperatures. For the Stokes-Scattering this leads to

$$\chi''(\omega) \backsimeq I_{raw}\left[1 - e^{-\frac{h\nu_R}{k_B T}}\right] \tag{49}$$

and for Anti-Stokes scattering to

$$\chi''(\omega) \backsimeq I_{raw}\left[e^{\frac{|h\nu_R|}{k_B T}} - 1\right] \tag{50}$$

Higher-order Raman scattering

When the electric polarization in the material couples non-linearly to the electric field of the incident light, then ***P*** has higher-order terms; these phenomena are treated in the regime of non-linear optics (NLO). The physical principles are somewhat different than in the classical optics picture. For instance, in NLO the superposition principle does not hold anymore. Non-linear effects are typically observed only at very high laser intensities. One example is the second harmonic generation (SHG): Two photons of the same energy are annihilated to create a single photon with double-frequency. Higher-order harmonic generation is also possible, and require even more intense light sources. This is an entire different area of science and is well explained in further literature (e.g. [146]).

3.2.3 Raman instrumentation

Nowadays, there is an immense variety of different kinds of Raman setups used in research and industry, mostly depending on the materials of interest. In general, the instrumentation can be classified into *Macro Raman* and *Micro Raman* instrumentation. Macro Raman is used for rather fast measurements on large samples (crystalline or liquids), with no microscope coupled to the spectrometer. This type is found for instance in industrial process control, at airports and customs. Micro Raman instrumentation on the other hand, as used for the work presented in this thesis, includes a microscope with an amplifying objective lens, which focuses the laser light onto the sample. This type enables precise measurements on smaller samples and even mapping of the sample surface.

The experiments in this study were performed on a commercial HORIBA LabRAM HR800 spectrometer [147], displayed in Figure 3.2.4, which is located in the laboratory of Prof. Bernhard Keimer at the Max-Planck Institute for Solid State Research in Stuttgart, Germany.

Figure 3.2.4(b) displays a schematic of the main components of the setup, including the optical elements inside the spectrometer. For a more detailed picture with all elements included, please see [147, 117]. A *He-Ne laser* radiates coherent light with the wavelength of $\lambda_L = 632.8$ nm. Any additional laser lines that differ from λ_L are suppressed by the *filter* at the entrance of the spectrometer. In the neutral density *filter wheel*, the laser intensity radiated onto the sample can be adjusted by choosing an attenuator with a certain degree of opacity. A *fresnel rhomb* polarizes the light linearly in a way that the plane of polarization can be rotated relative to the crystallographic orientation of the sample. The following mirror has two purposes: firstly, it reflects the incident light through the *microscope* onto the *sample*. It then lets pass the backscattered light (consisting of the Rayleigh line as well as inelastic scattered components), which goes on to the *notch filter*. This consists of two elements, an ultra-low-frequency (ULF) filter module and a Bragg filter. Together they cut out most of the Rayleigh line and only the inelastic scattered light can be transmitted. An optional second linear polarizer (called *analyzer*) can be inserted (the two options of linear polarization are rotated by 90 degrees to each other). The *confocal hole* is a pinhole with a tunable size, in order to cut out photons scattered from regions out-of-focus of the sample (see Fig. 3.2.5(b)).

The light enters then the spectrograph, where the diverging beam is first collimated by a spherical mirror with a 800 mm focal length, and then directed to an optical grating (one of two options: 1800 or 600 lines/mm), which defines the resolution of the Raman spectra. The energy calibration is checked by measuring crystalline silicon, which exhibits a strong and characteristic phonon excitation at 520 cm^{-1} [10]. The diffracted light is finally focused by another spherical mirror, also with an 800 mm focal length, onto the CCD camera. The collected data are transferred via an optical fiber to a computer, and the spectra can be visualized and corrected via the dedicated software program *LabSpec*.

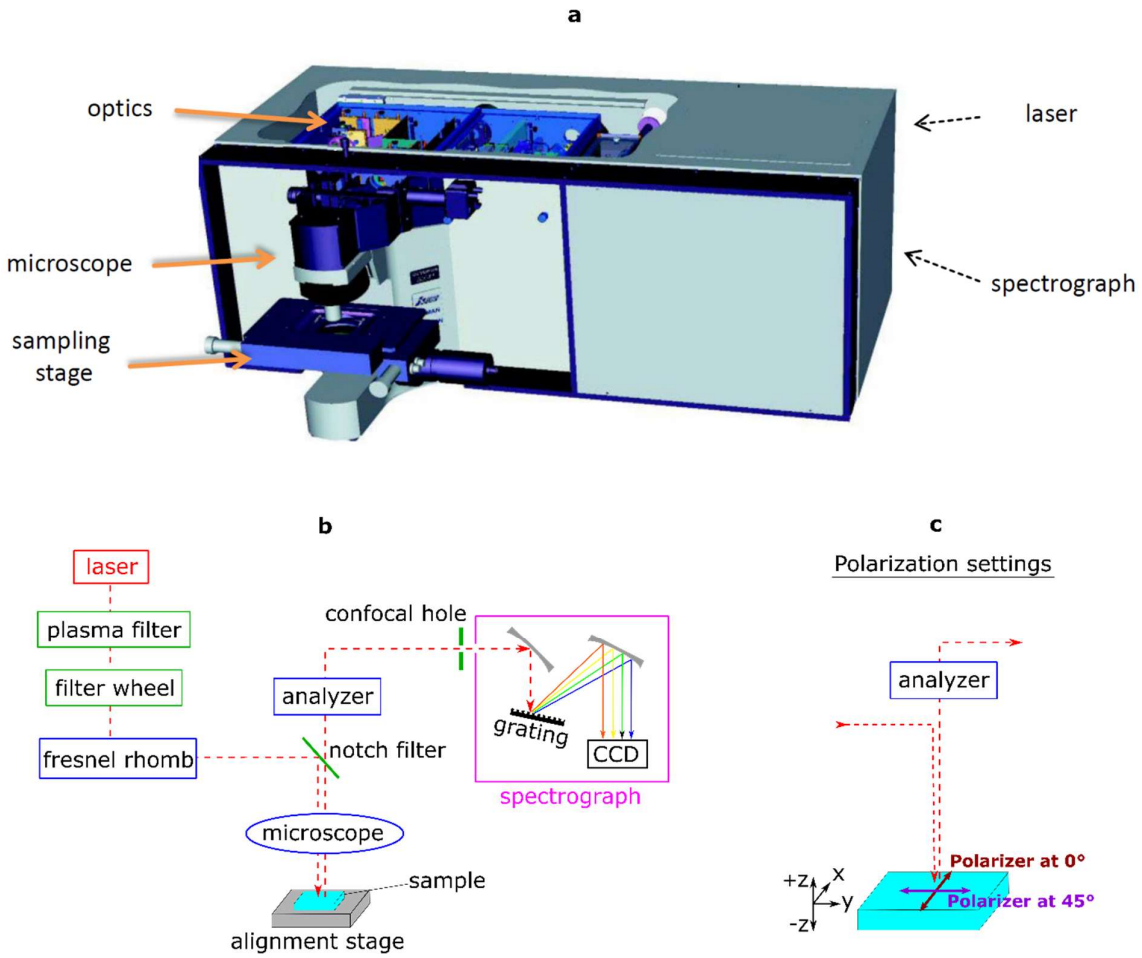

Figure 3.2.4 Schematic of the confocal Raman instrumentation. (a) *Sketch of the Raman instrumentation (from [147]).* ***(b)*** *Main optical elements of the Raman setup, together with the spectrograph, the microscope and the alignment stage.* ***(c)*** *Polarization settings: The fresnel rhomb (polarizer) can be set to several values from 0 to 360 degrees. For instance, if it is set to zero (45) degree, the electric field vector of the incident laser beam is parallel to the x-axis (y-axis) of the alignment stage, shown in dark red color (purple color). The analyzer on the other hand can be set only to two positions, i.e. being parallel to either the x- or the y-axis, or alternatively be taken out completely.*

An advantage of this confocal Raman setup is due to the enhanced resolution that arises from three design elements:

- The *confocal hole* in front of the spectrograph helps the short depth of focus of a ×100 objective lens in rejecting the Raman signal originating out of focus, in particular along the z-direction. Unfortunately, a smaller confocal hole also causes an overall drop in throughput.

- The high precision *alignment stage* can move the sample in all three spatial direction, with a resolution of ~0.5 µm.
- An internal *laser diode* shines light back from the end of the optical path and serves as an accurate alignment tool of the optical elements.

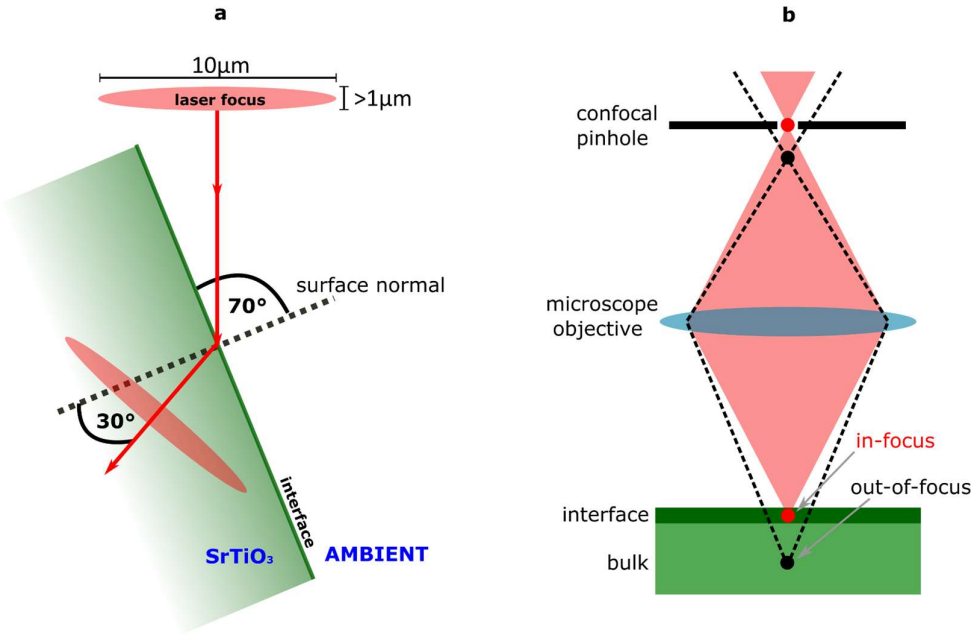

Figure 3.2.5 (a) *Schematic showing an estimate of the depth resolution for a confocal Raman experiment with the sample mounted on a wedged sample holder. The incident laser beam in the ambient (inside the sample) is at 70 degrees (ca. 30 degrees) with respect to the surface normal of a $SrTiO_3$ sample with a refractive index n ≈ 2 for the red laser. Indicated with a red ellipse is the horizontal and vertical resolution that is defined by the focusing components (i.e. lenses etc.).* ***(b)*** *Principle of confocal Raman spectroscopy (adapted from [148]). The confocal pinhole suppresses residual scattered light from out-of-focus points.*

For a normal incidence arrangement and for a ×100 long working distance objective lens and a D0.6 filter, the resolution in the horizontal (vertical) direction is estimated to be around 10 µm (a few micrometers – although in practice, for some samples, we find it to be approximately 100 nm). This makes it a powerful experimental tool, especially for studying thin film where a strong substrate response is normally dominating the signal. It also enables depth-dependent studies, which is an essential part of this thesis.

An additional complication comes when placing the sample on a wedge holder, in which the incoming light comes in at a grazing angle, shown in Fig. 3.2.5(a) and Fig. 3.2.6. With this arrangement, not only the optical response of the in-plane but also of the out-of-plane can be investigated. The setup is furthermore equipped with a cryostat as well as with electrical wires, so that temperature-dependent (ca. 10 - 300 K, using liquid helium) and voltage-dependent (±400 V) experiments are possible. The temperature is obtained by a diode sensor, placed inside the cryostat close to the sample. In contrast to infrared spectroscopy, there is the issue of 'laser heating' in Raman spectroscopy, which can be solved by calculating the sample temperature via comparing the Stokes with the Anti-Stokes line, as described above.

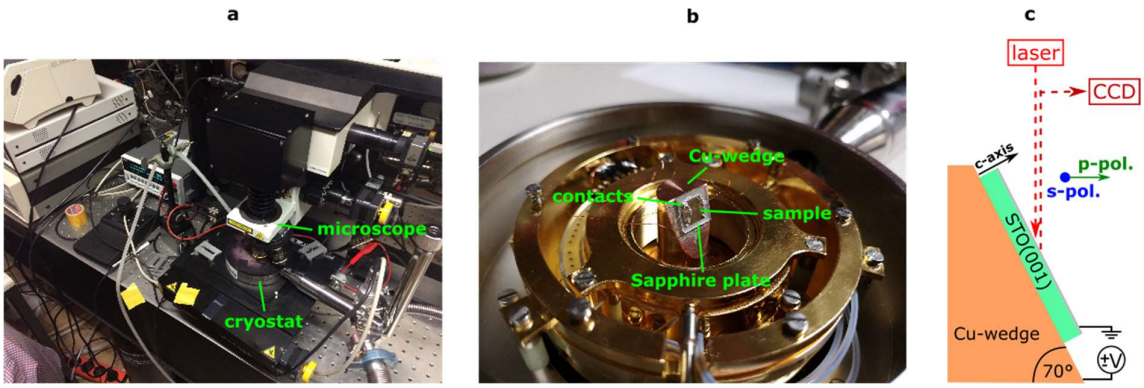

Figure 3.2.6 Temperature and voltage-dependent measurements with a confocal Raman setup. (a) *Setup with inserted cryostat.* ***(b)*** *and* ***(c)****: Electric-field-dependent measurement of a $SrTiO_3$ (001) sample. The sample is placed on a copper wedge, to enable measuring the in-plane and out-of-plane components of the electric field vector of the incident and scattered radiation. The sapphire plate functions as (i) a good thermal conductor between sample and copper wedge and (ii) an electric insulator, which enables electrical back-gate experiments at low temperatures.*

3.2.4 Perspectives of advanced Raman techniques

A conventional Raman spectroscope/microscope has in general a rather small cross section, in which the fluorescence signal is often dominating in materials with little Raman scattering volumes. The Raman signal can be enhanced e.g. by using a confocal setup which was done in this study; by *resonance Raman scattering,* in which the wavelength of the incoming light coincides with a certain electronic energy state of the system, leading to an enhancement of vibrational modes; or by *hyper Raman*, in which the 2nd harmonic of an high intensity laser beam is used to see normally *silent* modes. Especially with the latter approach one risks that the enhanced laser intensity leads to a strong heating of the sample. These *far-field* techniques further have spatial resolutions of ~200 nm due to the diffraction limit of the laser light (which is typically in the visible region), which hinders the study of e.g. nanoparticles [149].

An alternative to increase the Raman cross section is to generate an additional plasmonic *near-field*, which can yield enhancement factors of around 10^2 - 10^7, and spatial resolutions of down to ~20 nm [150, 151]. Going from far-field to near-field methods can cause a change in selection rules, a reduced Rayleigh tail and strong surface enhancement [152] can be therefore rather advantageous to study low-frequency properties. Prominent representatives are *tip-enhanced Raman spectroscopy* (TERS) and *surface-enhanced Raman spectroscopy* (SERS).

For **TERS**, the tip of an AFM or STM apparatus is approached close to the sample surface [149, 151]. The laser must be focused at the tip apex and the region between the tip and the sample in order to generate a plasmonic field. The detected Raman signal is then a combination of near- and far-field response, which originates form the Raman excitation arriving directly to the detector. The spatial resolution and strength of the TERS signal, and thus the resulting enhancement factor, is mostly defined by the tip radius of ~20 nm. The spectrum can be taken at one spot of the sample, but also a mapping is possible. Performing a TERS measurement imply a further technical difficulty, as it requires placing the focus spot in between sample and tip apex to have highest plasmonic response. In some setups, the spectrometer and STM/AFM tip are coupled, where the focus is automatically changed.

In **SERS**, the plasmonic field is not generated by an AFM/STM tip, but instead by a pattern of gold particles with radii of ∼10 nm, deposited onto the sample surface. Here, enhancement factors of around 10^7 can be achieve [153, 154]. Note that both SERS and TERS techniques are very surface-sensitive. The plasmonic near-field decays exponentially for longer distances to the tip (TERS) or gold-particles (SERS). Therefore, the penetration depth is strongly reduced, which enables for instance the study of surface states/effects. For thin films, the contribution from the substrate is also strongly reduced.

3.3 Limitations of the Raman and infrared techniques

Both infrared and Raman spectroscopy can be very powerful tools for understanding the fundamental properties of strongly correlated electron systems, and even more useful as combined techniques. However, both methods are typically limited to excitations at the Brillouin zone center Γ (except e.g. two-phonon-processes). This is due to the small momentum of the incident light (in the infrared to visible range), as compared to the momentum of the excitations within the first Brillouin zone of a solid crystal ($q = \frac{2\pi}{\lambda} \sim 0$). Let us illustrate this with one simple calculation: For an optical photon with an energy of e.g. 2 eV, its momentum is $\hbar q = 10^{-27}$ kgm/s, or in other terms, has a wave vector of $q = 10^{-3}$ Å^{-1}. In a crystal with a lattice constant $a = 3$ Å on the other hand, the elementary excitations up to the end of the first Brillouin zone have wave vectors of $q = \frac{2\pi}{a} \sim 2$ Å^{-1}, which is three orders of magnitude bigger [112].

In order to perform a momentum-dependent measurement, i.e. derive a material's dispersion curve, other techniques with incoming light energies of ≥1 keV are necessary. In the following, the spectroscopy techniques *RIXS* and *ARPES* will be briefly introduced to give an example. Both methods use photons as the incoming probing beam, just like IR and Raman spectroscopy. They have been proven to be powerful tools in the study of emergent phases of strongly correlated materials, such as high-temperature superconductors.

ARPES (Angle-resolved photoemission spectroscopy)

ARPES is probably the most direct way to map the electronic structure of complex materials. It is based on the photoelectric effect, which was one of the first indications that light can be regarded as quantum particles, a 'photon'. This was experimentally found by Heinrich Hertz in 1887 [155] and theoretically described by Albert Einstein in 1905 [156], for which he received the Nobel Prize in 1921. The basic experimental procedure is the following: A material is radiated with high-energy photons (ranging from a few eV to thousands eV). When the system absorbs this energy, is its afterwards liberating electron(s) (so-called *photoelectrons*), if the incoming photon energy (*hv*) is higher than the sum of the working function Φ and the binding energy E_B of the core electron.

The photoelectrons are then detected via e.g. a CCD camera, and analyzed with respect to their kinetic energy E_{kin} and their emission angle θ. Due to conservation of energy and momentum parallel to the sample surface [157], those parameters are directly coupled to the internal electronic states.

$$E_{kin} = hv - \Phi - |E_B|$$
$$p_{II} = \hbar\, k_{II} = \sqrt{2mpE_{kin}} \cdot sin\theta \qquad (51)$$

The light source is typically a laser, discharge lamp or synchrotron. In the latter case it is possible to tune the energy from several eV to thousands of eV, and thus making it possible to probe even several Brillouin zones [157]. Also, the measurements are rather surface-sensitive and one can study even samples with rather small surfaces of several mm^2.

This makes ARPES a sophisticated tool to probe energy and momentum-resolved the electronic structure of quantum materials. It is possible to derive band dispersion curves, the topology of the Fermi surface or electron self-energy. Thanks to this method, great process has been achieved especially for high-T_c superconductors (like cuprates or pnictides), where large parts of the phase diagram could be revealed [158].

However, the acquired information is restricted to the first few nanometers of the surface, and rather little bulk information is obtained. The samples are normally specially treated to have extremely clean surfaces and the measurements must take place in UHV (10^{-11} mbar). Also, the application of a magnetic field or pressure as an external perturbation parameter is complicated.

RIXS (Resonant inelastic x-ray scattering)

RIXS, such as Raman and infrared spectroscopy, is a *photon-in -> photon-out* experiment. It is used to study the low-energy charge, spin, orbital and lattice excitations of solids, and their full dispersion [112]. Here, x-ray photons are in-elastically scattered off matter. One unique thing about RIXS is, that you can tune the incident photon energy to coincide (and therefore resonate) with a specific atomic transition (so-called *absorption edges*) of the studied material. This makes it not only element- and orbital-specific, but one can also distinguish between the same chemical elements at different sites with varying bonding, valances etc. Also, the scattering cross-section is greatly enhanced due to the resonance effect. Unlike ARPES, RIXS is bulk-sensitive, since the x-ray photons have large penetration depths of a few μm in the hard x-ray regime (∼10 keV), or 0.1 μm in the soft-ray range (∼1 keV). The photon-matter interaction is strong (compared to e.g. neutron scattering), therefore only small sample volumes are required for an experiment. Also, similar like in Raman and infrared measurements, the polarization dependence of the incoming to the scattered photon can be utilized, to derive information about the materials' symmetry via selection rules.

RIXS is essentially a two-step process: The incident photon is absorbed by a deep-lying core electron and excited into an empty valence shell. In the 2nd step, analog to fluorescence, the system decays by re-filling empty core states with electrons and emission of a x-ray photons. This emitted photon are detected via e.g. a CCD camera.

RIXS is a fairly modern experimental technique, which scientists started using only in the last decades, and not yet a well-established technique such as ARPES or neutron scattering. This is mostly due to the recent development in instrumentation, because carrying out those experiments requires a very high photon flux, which is only realized at synchrotrons.

Chapter 4

Magnetic field effect on the infrared response of underdoped $YBa_2Cu_3O_{6.6}$

4.1 Introduction

Revealing the role of charge density waves (CDWs) in cuprates for the superconducting pairing mechanism is currently a hot topic. In zero magnetic field, the charge density wave is incipient and short-ranged. Applying magnetic fields along the *c*-axis of the crystal enhances this order, and, in addition, induces another long-ranged CDW for larger fields than 15 to 20 Tesla. Alternatively, uniaxial pressure along the *a*-axis also induces this 3D CDW. With respect to the electronic properties of this high-magnetic field CDW state, apart from magneto-transport experiments, there is hardly any information available from spectroscopy techniques.
The goal of this study was to fill this gap by means of infrared (IR) spectroscopy at high magnetic fields. IR spectroscopy has already proved to be a suitable technique to investigate the low-energy dynamics of superconductors in zero magnetic field. Since IR spectroscopy probes the change of the dipole moment at a relatively short measurement timescale of picoseconds, it is expected to be highly sensitive to the 3D CDW order in cuprates.

In the following paper, we performed magneto-optical measurements up to 30 Tesla on an underdoped $YBa_2Cu_3O_{6.6}$ crystal, and compared these with the temperature-dependent spectra.
We observed a full suppression of the macroscopic response of the superconducting condensate above ~20 Tesla, and a relatively weak reduction of the Drude peak (~3 %) which is accompanied most prominently by an enhancement of an electronic mode at 240 cm^{-1} and of the broad mid-infrared band. Interestingly, these latter features are already present in the spectra with no magnetic field applied, for elevated temperatures and for an extended doping range, at least up to optimal doping. The findings suggest that prominent CDW correlations exist in large parts of the phase diagram, not only at high magnetic fields. Moreover, the relationship between SC and CDW correlations is presumably not of purely competitive nature, but instead is more intricate and depends on the correlation length and the dynamics of the CDW phase.

4.2 Infrared spectroscopy study of the in-plane response of $YBa_2Cu_3O_{6.6}$ in magnetic fields up to 30 Tesla

F. Lyzwa[1], B. Xu[1], P. Marsik[1], E. Sheveleva[1], I. Crassee[2], M. Orlita[2], C. Bernhard[1]

[1]University of Fribourg, Department of Physics and Fribourg Center for Nanomaterials, Chemin du Musée 3, CH-1700 Fribourg, Switzerland

[2]Laboratoire National des Champs Magnétiques Intenses (LNCMI), CNRS-UGA-UPS-INSA, 25, Avenue des Martyrs, 38042 Grenoble, France

Published in Physical Review Research **2**, 023218 (2020)

With terahertz and infrared spectroscopy we studied the in-plane response of an underdoped, twinned $YBa_2Cu_3O_{6.6}$ single crystal with $T_c = 58(1)$ K in high magnetic fields up to $B = 30$ Tesla applied along the *c*-axis. Our goal was to investigate the field-induced suppression of superconductivity and to observe the signatures of the three-dimensional (3D) incommensurate copper charge density wave (Cu-CDW) which was previously shown to develop at such high magnetic fields. Our study confirms that a B field in excess of 20 Tesla gives rise to a full suppression of the macroscopic response of the superconducting condensate. However, it reveals surprisingly weak signatures of the 3D Cu-CDW at high magnetic fields. At 30 Tesla there is only a weak reduction of the spectral weight of the Drude response (by about 3 %), which is accompanied by an enhancement of the so-called mid-infrared (MIR) band as well as a narrow electronic mode around 240 cm^{-1} (and, possibly, another one around 90 cm^{-1}), which is interpreted in terms of a pinned phase mode of the CDW. The pinned phase mode and the MIR band are strong features already without magnetic field, which suggests that prominent but short-ranged and slowly fluctuating (compared to the picosecond infrared timescale) CDW correlations exist all along, i.e., even at zero magnetic field.

I. Introduction

The cuprate high-T_c superconductors (HTSC) that were discovered in 1986 [13] still hold the record T_c value [11] for materials at atmospheric pressure with $T_c = 135$ K in Hg-1223 [15]. These cuprates have a rich phase diagram with various charge or spin ordered states that coexist or compete with superconductivity (SC). Recently, the observation of a two-dimensional charge density wave (2D CDW) in the CuO_2 planes of underdoped $YBa_2Cu_3O_{6+x}$ (YBCO) with NMR [159] and x-ray diffraction techniques [160, 27, 28] has obtained great attention. The 2D CDW has a maximal strength for a hole doping level of $p \approx 0.11$ - 0.12 (equivalent to an oxygen content of $x \approx 0.5$ - 0.6), with an in-plane wave vector of about $q \approx 0.3$ r.l.u. (reciprocal lattice units) and typically a short correlation length of less than $\xi \approx 10$ nm [26]. It develops below about 150 K and its strength increases gradually with decreasing temperature until it sharply decreases below T_c [27, 26], presumably due to the competition with superconductivity.

When applying a large magnetic field along the *c*-axis [24, 30-32] or uniaxial pressure along the *a*-axis [33], this 2D CDW can be enhanced, such that its strength keeps increasing towards low temperature. Notably, even a long-ranged, three-dimensional charge density-wave order (3D CDW) can be induced in underdoped YBCO with a hole doping of p ≈ 0.11 - 0.12 and T_c ≈ 55 - 60 K by applying a magnetic field in excess of 15-20 Tesla (T) [30, 29] or likewise by applying uniaxial pressure along the *a*-axis [33]. A concise review about the two types of charge orders in YBCO can be found in [35]. Meanwhile, it was shown that the short-ranged quasi-2D charge density correlations exist in large parts of the temperature and doping phase diagram of YBCO [11] as well as in other compounds like $La_{2-x}Sr_xCuO_4$ [161], Bi-2212 [162], Bi-2201 [163] and Hg-1201 [164]. These observations raise important questions about the role of CDW fluctuations in the superconducting pairing interaction [165] and in the so-called pseudogap phenomenon which leads to a severe suppression of the low-energy electronic excitations already well above T_c in the underdoped part of the phase diagram [166-168].

Infrared (IR) spectroscopy is a well-suited technique to study the gap formation, collective modes and pair breaking excitations of correlated quantum states [39] as well as IR-active phonon modes that can be renormalized or even activated by the coupling to the electronic excitations [169]. This technique has already provided valuable information about the superconducting state of various superconductors [169, 170]. For conventional BCS superconductors [171] or the unconventional iron-based high-T_c pnictides [172] it was used successfully to determine the energy gap, Δ^{SC}, and the density of the superconducting condensate, n_s. For the case of an isotropic superconducting gap (in the so-called dirty limit for which the superconducting coherence length, ξ_{SC}, is larger than the mean-free path of the carriers) the real part of the optical conductivity at $T << T_c$ is fully suppressed up to a threshold energy of $2\Delta^{SC}$. Above this value, the conductivity rises steeply and gradually approaches the normal state value. The corresponding missing spectral weight (defined as the frequency integral of the conductivity difference spectrum of $\sigma_1(T_c)$ - $\sigma_1(T << T_c)$ is shifted to a δ function at zero frequency that accounts for the inductive and loss-free response of the superconducting condensate. The response of the condensate is also seen at finite frequency in the imaginary part of the optical conductivity, σ_2, or the real part of the dielectric function, $\varepsilon_1 = 1 - Z_0/2\pi \times 1/\omega \times \sigma_2$, where $Z_0 = 377\ \Omega$ is the vacuum impedance (and σ_2 is in units of $(\Omega\ cm)^{-1}$). In the latter it leads to a downturn to negative values at low frequency as described by the equation: $\varepsilon_1^{\delta} \sim 1 - \omega^2_{pl,SC}/\omega^2$, where $\omega_{pl,SC}$ is the plasma frequency of the superconducting condensate.

The IR spectroscopy technique has also been widely used to explore the CDW order in various materials [170], for some of which it can even coexist with superconductivity, like in the organic $(TMTSF)_2$-compounds [173], bismuthates [174], $NbSe_2$ [175, 176], and the cuprates [38, 41, 177-179]. Similar to the SC state, the CDW order gives rise to a gaplike suppression of the optical conductivity below a threshold energy that corresponds to twice the energy gap of the CDW, $2\Delta^{CDW}$. In contrast to the SC case, the missing spectral weight (SW) below $2\Delta^{CDW}$ is shifted to higher energies where it gives rise to a broad band above the gap edge that originates from the excitations across the CDW gap. The collective phase mode of the CDW is typically coupled to the lattice. Accordingly, this mode has a strongly reduced spectral weight and is shifted away from the origin (zero frequency) to finite frequency due to defects on which the CDW is pinned [25].

The IR response of the cuprate HTSC has been intensively investigated [39, 180] but the interpretation of the superconducting gap features remains controversial. The expected characteristics in terms of a sharp gap edge at $2\Delta^{SC}$ and a full suppression of the optical conductivity at $\omega < 2\Delta^{SC}$ are not observed here.

Instead, there is only a partial suppression of the low-frequency optical conductivity without a clear gap feature and typically only a relatively small fraction of the free carrier spectral weight condenses and contributes to the superconducting condensate [181-183]. The nature of the rather large amount of residual low-energy SW is still debated. Conflicting interpretations are ranging from a gapless SC state due to disorder and pair-breaking effects to competing orders due to charge- and/or spin density wave correlations and fluctuations, which are slow on the IR spectroscopy timescale [38, 41, 178]. The latter interpretation has obtained renewed attention due to the observation of a static CDW order in underdoped cuprates and by recent reports of fluctuating CDW correlations that persist in a wide doping range and at elevated temperatures [184].
This calls for a study of the magnetic field effect on the in-plane IR response of underdoped cuprates for which a static and long-range ordered CDW state is established in the range above 15 to 20 T. To our best knowledge, previous magneto-optical studies (with the *B* field applied along the *c*-axis) of the in-plane response of YBCO are limited to 7 T for single crystals [44] and 15.5 T for thin films [42]. Within their signal-to-noise ratio, they show hardly any change of the free carrier response. Corresponding studies of the *c*-axis response (perpendicular to the CuO_2 planes) revealed only a weak suppression of the superconducting condensate density [43].

Here we present a study of the IR response of an underdoped, twinned YBCO crystal in high magnetic fields up to 30 T which has been reported to suppress superconductivity [132, 185, 186] and induce a 3D CDW [30]. We observe indeed a full suppression of the superconducting condensate above 20 T but only weak changes of spectroscopic features that can be associated with a 3D CDW. In particular, the magnetic field leads to a weak reduction of the spectral weight of the Drude response due to the free carriers (by about 3 %) and a corresponding, moderate enhancement of an electronic mode around 240 cm^{-1} (and, possibly, a second one around 90 cm^{-1}) and of the so-called mid-infrared (MIR) band. These features are interpreted in terms of a pinned phase mode and the excitations across the CDW gap, respectively. Notably, these characteristic CDW features are prominent even in zero magnetic field. In return, our data suggest that fairly strong, but likely short-ranged and slowly-fluctuating CDW correlations exist already in zero magnetic field.

II. Experiments

A single crystal of $YBa_2Cu_3O_{6.6}$ was synthesized using a flux-based growth technique with Y-stabilized Zr_2O crucibles [187] and post-annealing in air at 650 °C for 1 day with subsequent rapid quenching into liquid nitrogen. The twinned crystal had a flat and shiny *ab*-plane with a size of about 3.5 × 3.5 mm^2 that was mechanically polished to optical grade using oil-based solutions of diamond powder with diameters of first 3 µm and then 1 µm. Its superconducting transition temperature of $T_c = 58(1)$ K has been determined with dc magnetization in field-cooling mode in 30 Oersted applied parallel to the sample surface, using the vibrating sample magnetometer (VSM) option of a physical property measurement system (PPMS) from Quantum Design.
The *ab*-plane reflectivity spectra R(ω) in zero magnetic field were measured in Fribourg, at a near-normal angle of incidence using an ARS-Helitran flow-cryostat attached to a Bruker VERTEX 70v Fourier transform IR spectrometer. Spectra from 40 to 8000 cm^{-1} were collected at different temperatures ranging from 300 to 12 K. The absolute reflectivity values have been obtained with a self-referencing technique for which the sample is measured with an overfilling technique, first with the bare surface and subsequently with a thin gold coating (that is *in situ* evaporated) [188, 126].

In addition, for each spectrum the intensity has been normalized by performing an additional measurement on a reference mirror made of polished steel. In the near-infrared to ultraviolet range (5000 –50 000 cm^{-1}) the complex dielectric function has been obtained with a commercial ellipsometer (Woollam VASE) for each temperature and at an angle of incidence of φ = 70°. The ellipsometric spectra have been obtained for two different geometries with the plane of incidence either along the *ab*-plane or the *c*-axis. The latter was only measured at room temperature assuming that it has just a weak temperature dependence. The obtained spectra have been corrected for anisotropy effects using the standard Woollam software to obtain the true *ab*- and *c*-axis components of the complex dielectric function. The optical conductivity was obtained by performing a Kramers-Kronig (KK) analysis of R(ω) [170]. Below 40 cm^{-1}, we used a superconducting extrapolation ($R = 1 - A\omega^4$) for $T < T_c$ or a Hagen-Rubens one ($R = 1 - A\sqrt{\omega}$) for $T > T_c$. On the high-frequency side, we assumed a constant reflectivity up to 28.5 eV that is followed by a free-electron (ω^{-4}) response.

The corresponding magnetic-field-dependent reflectivity measurements have been performed at the LNCMI in Grenoble, with a Bruker VERTEX 80v Fourier transform IR spectrometer attached to the experimental setup to create magnetic fields up to 30 T. The sample was placed in a sealed volume with low-pressure helium exchange gas that was inserted into a liquid helium bath with T = 4.2 K (or a nitrogen bath with T = 77 K). The measurements were carried out, starting from 0 Tesla, at different magnetic fields up to 30 T, by taking at each field the intensity ratio between the sample and a gold reference mirror, $I(B)$. Prior to these measurements, the magnetic field was ramped up and down two times to settle any field-induced movement of the optical components. In addition, to ensure reproducibility, the measurement sequence was repeated at least 4 times. From the measured sample/reference intensity ratio at a given field $I(B)$ the corresponding reflectivity spectrum $R(B)$ has been obtained using the relationship

$$R(B) = \frac{I(B)}{I(0T)}\, R(0T).$$

With $R(0T)$, as obtained with the setup in Fribourg (see description above), we thus derived an absolute reflectivity spectrum $R(B)$ in the range from 50 to 6000 cm^{-1} at different magnetic fields up to 30 Tesla. Subsequently, we obtained the optical conductivity via a KK analysis using a Hagen-Rubens ($R = 1 - A\sqrt{\omega}$) extrapolation below 50 cm^{-1}. On the high-frequency side, we tested different extrapolations that are further discussed below and shown in Fig. 4.2.2(d). More details about the experimental procedure can be found in the appendix and in the Supplementary Material of Ref. [189].

III. Results

A. Temperature-dependent optical response in zero magnetic field

The optical response of the $YBa_2Cu_3O_{6.6}$ crystal in zero magnetic field at selected temperatures above and below the superconducting transition temperature T_c is summarized in Fig. 4.2.1. The reflectivity spectra in Fig. 4.2.1(a) and the KK-derived spectra of the real parts of the optical conductivity $\sigma_1(\omega)$ and of the dielectric function $\varepsilon_1(\omega)$ in Figs. 4.2.1(b) and (c), respectively, are typical for such an underdoped and twinned YBCO crystal. The spectra in the normal state are governed by a Drude peak with an anomalously strong tail towards the high frequency side. With decreasing temperature the Drude peak becomes narrower and electronic spectral weight is redistributed from the tail towards the head of the Drude peak.

In addition, there is a band around 240 cm^{-1} that becomes narrower and more pronounced with decreasing temperature that is apparently of electronic origin (since its oscillator strength is way too strong for an IR-active phonon mode) and was previously interpreted in terms of the pinned CDW mode along the *b*-axis [38, 41]. Superimposed on this electronic background are also several IR-active phonon modes that give rise to comparably much weaker and narrower peaks.

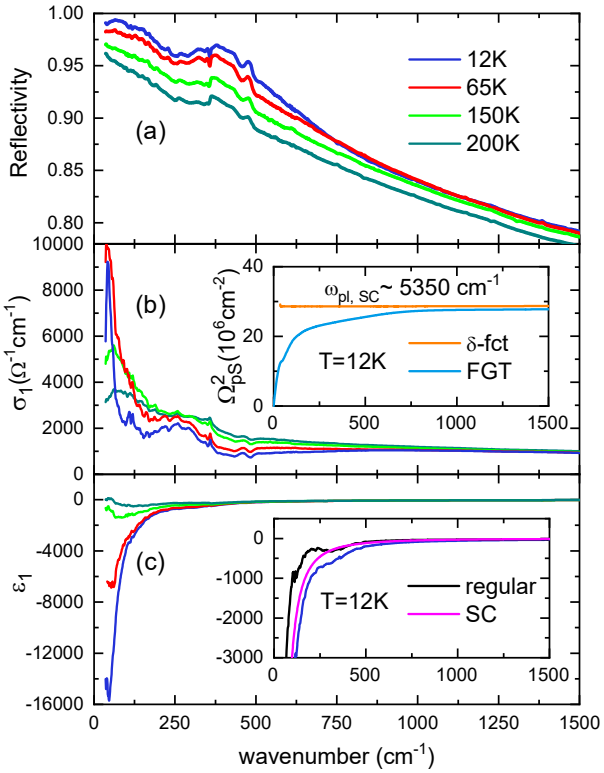

Figure 4.2.1 *The ab-plane response of a twinned, underdoped $YBa_2Cu_3O_{6.6}$ crystal in zero magnetic field and at selected temperatures above and below T_c = 58 K shown in terms of **(a)** the reflectivity, **(b)** the real part of the optical conductivity σ_1 and **(c)** the real part of the dielectric function ε_1. Inset of (b): Superfluid density Ω^2_{pS} at 12 K as deduced from the missing spectral weight in σ_1 according to the FGT sum rule (light blue line) and, alternatively, from the purely inductive term in the real part of the dielectric function (orange line). Inset of (c): Superconducting component in the real part of the dielectric function $\varepsilon_{1,SC}$ (magenta line) that has been obtained by subtracting the contribution of the regular part (black line), as derived via a KK-analysis of $\sigma_1(\omega > 0)$, from the measured spectrum at 12 K (blue line).*

In the superconducting state at 12 K << T_c = 58 K, there is only a partial suppression of the low-frequency optical conductivity due to the formation of a superconducting energy gap below $2\Delta^{SC}$. The so-called missing spectral weight, which is transferred to a δ function at zero frequency and contributes to the loss-free response of the superconducting condensate, amounts to a fairly small portion of the available low-energy electronic spectral weight (SW). The large amount of residual low-frequency spectral weight differs from the predicted behavior of a BCS-type superconductor, even considering that the SC order parameter has a *d*-wave symmetry with line nodes on which the gap vanishes [190, 191]. It is also in strong contrast with the nearly complete superconducting gap that is typically observed in the IR spectra of the iron-arsenide superconductors [172, 188, 37, 192-196].

The inset of Fig. 4.2.1(b) shows that the plasma frequency of the superconducting condensate is $\omega_{pl,SC} \equiv \Omega_{pS} \approx 5350$ cm^{-1}. This value was obtained, following the procedure outlined in Ref. [37], from the missing spectral weight in the optical conductivity, via the so-called Ferrel-Glover-Tinkham (FGT) sum rule, and, alternatively from the inductive term in the imaginary part. The former FGT sum rule is fulfilled in the high frequency limit where the spectra of σ_1 in the normal and superconducting states are indistinguishable, or at least very similar. The inductive term due to the superconducting δ function at zero frequency, $\varepsilon_{1,SC}$, has been obtained, as shown in the inset of Fig. 4.2.1(c) for the real part of the dielectric function, by first deriving the contribution of the regular (nonsuperconducting) response at finite frequency via a KK analysis of the spectrum of $\sigma_1(\omega > 0)$, and then subtracting this term from the measured spectrum, $\varepsilon_{1,SC} = \varepsilon_{1,measured} - \varepsilon_{1,regular}$. Overall, these spectra and the value of the SC plasma frequency compare well with previous reports [38, 197, 198].

B. Magnetic field dependence

Figure 4.2.2 summarizes the IR spectra of the $YBa_2Cu_3O_{6.6}$ crystal that were taken at different magnetic fields up to 30 Tesla at the high magnetic field laboratory (LNCMI) in Grenoble at a constant temperature of 4.2 K (or 77 K). Fig. 4.2.2(a) shows for different magnetic fields up to 30 T at 4.2 K the ratio of the measured reflectivity with respect to the one at zero magnetic field. It reveals that the *B*-field gives rise to weak but clearly noticeable, systematic and reproducible changes in the reflectivity. Note that the overall stability of the experimental setup is significantly better than 1 % in a broad range of fields. The magnetic field leads to an overall decrease of the reflectivity in the entire measured frequency range. This rate of decrease is strongest between 10 and 20 T and it saturates around 25 T. There are also some relatively narrow dip features forming around 500, 200 and 80 cm^{-1} that grow in magnitude with the magnetic field. For comparison, Fig. 4.2.2(b) shows that these magnetic-field-induced changes of the reflectivity do not occur (or are much smaller) when the sample is kept at 77 K where it is in the normal state already at zero magnetic field.

Fig. 4.2.2(c) shows a comparison of the effects on the IR reflectivity spectrum when applying a magnetic field of 30 T to suppress superconductivity (at 4.2 K) or increasing the temperature to $T = 65$ K > T_c at $B = 0$ T. It reveals that similar changes occur below about 700 cm^{-1} where the overall reflectivity decreases and a rather pronounced dip develops around 500 cm^{-1}. In the following, we show that these features arise from the suppression of the δ function of the superconducting condensate and the related closing of the SC gap. There are additional features in the reflectivity spectra that are more pronounced at high magnetic field, such as two rather sharp dips around 80 cm^{-1} and 200 cm^{-1} as well as a decrease of the overall reflectivity above about 700 cm^{-1} that persists beyond the upper limit of the measured spectra of 6000 cm^{-1}. These features are not related to the suppression of superconductivity, since they are absent for the spectrum at 65 K and 0 T, and are thus interpreted as signatures of the 3D CDW.

For a further analysis and discussion of the magnetic-field-induced changes we performed a KK analysis of the reflectivity spectra to derive the complex optical conductivity, σ, and dielectric function, ε. Figure 4.2.2(d) shows for the case of the spectrum at 30 T the different high frequency extrapolations that we have used for this analysis. In the appendix and in the Supplementary Materials of Ref. [189] we show that these different extrapolations yield virtually identical results below about 1000 cm^{-1} and only comparably small differences up to about 6000 cm^{-1}.

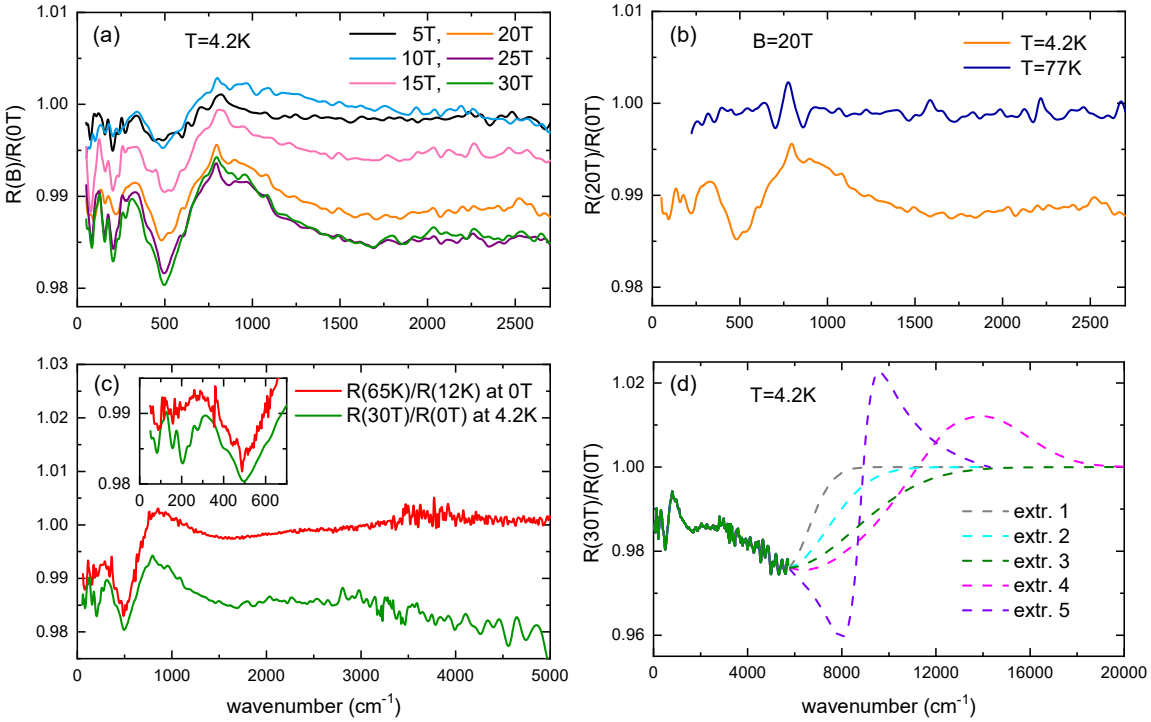

Figure 4.2.2 *Reflectivity ratio between high and zero magnetic field of underdoped $YBa_2Cu_3O_{6.6}$.* ***(a)*** *Evolution of the reflectivity ratio for different applied magnetic fields at 4.2 K.* ***(b)*** *Comparison of the magnetic field effect in the superconducting state (orange line; at 4.2 K) and the normal state (blue line; at 77 K).* ***(c)*** *Comparison of the effect of suppressing superconductivity with a magnetic field of 30 T at 4.2 K (green line) and heating the sample to 65 K > T_c at 0 T (red line). The inset points out the enhanced dips around 200 cm^{-1} and 80 cm^{-1}, caused by the magnetic field.* ***(d)*** *Spectrum of the measured reflectivity ratio at 30 T and 4.2 K (green line) together with different extrapolations to higher energy that were used for a KK analysis of the data to obtain the spectra of the complex optical conductivity, σ, and the dielectric function, ε, shown in Fig. 4.2.3.*

Figure 4.2.3 shows the spectra for σ_1 and ε_1 at 30 T (green lines) as obtained using the extrapolation type 3 (if not explicitly mentioned otherwise) together with the zero field spectra in the SC state at 12 K (blue lines) and in the normal state at 65 K (red lines). Fig. 4.2.3(a) reveals that a magnetic field of 30 T (applied at 4.2 K) gives rise to a similar increase of the optical conductivity below about 800 cm^{-1} (green versus blue line) as the one that occurs when superconductivity is suppressed upon raising the temperature above T_c in zero magnetic field (red versus blue line). Fig. 4.2.3(b) displays the corresponding spectra of the real part of the dielectric function. It confirms that the 30 T field (at 4.2 K) causes a similar decrease of the inductive response (in terms of the downturn of ε_1 towards large negative values at low frequency) as in the normal state at 65 K and zero magnetic field.

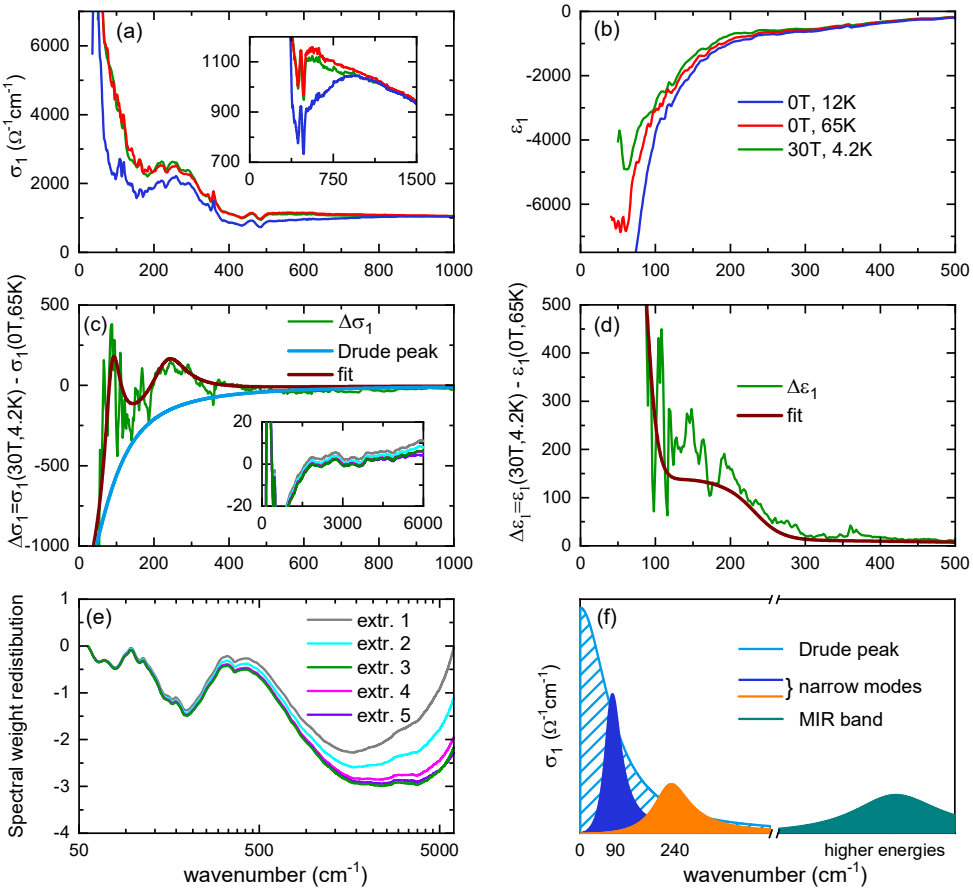

Figure 4.2.3 *Comparison of the effects of suppressing superconductivity in underdoped $YBa_2Cu_3O_{6.6}$ with $T_c = 58$ K with a magnetic field of 30 T at 4.2 K and by increasing the temperature to 65 K at 0 T.* ***(a), (b)*** *Real parts of the optical conductivity σ_1 and the dielectric function ε_1, respectively, in the superconducting state at 0 T, 12 K (blue lines) and in the normal state at 0 T, 65 K (red lines) and at 30 T, 4.2 K (green lines). The inset in* ***(a)*** *shows a magnified view of the suppression of σ_1 in the SC state.* ***(c), (d)*** *Difference plots between the spectra of σ_1 and ε_1, respectively, when SC is suppressed at 30 T, 4.2 K and at 0 T, 65 K. The light blue line in* ***(c)*** *shows the contribution due to the reduction of the SW of the Drude peak at 30 T. The dark red lines in* ***(c)*** *and* ***(d)*** *show a fit that accounts for the transfer of SW at 30 T from the Drude peak towards the narrow peaks at 90 and 240 cm^{-1} and a broad MIR band. Inset of* ***(c):*** *Magnified view of the effect of the different extrapolation procedures outlined in Fig. 4.2.2(d) on the $\Delta\sigma_1$ spectrum.* ***(e)*** *Redistribution of the spectral weight (SW) lost by the Drude peak shown in terms of the frequency dependence of the integral of $\Delta\sigma_1$ in panel (c), $SW(\omega)=\int_{55cm^{-1}}^{\omega'} \Delta\sigma_1(\omega)d\omega$ [in units of ($10^4\ \Omega^{-1}cm^{-2}$)] for the different extrapolation procedures outlined in Fig. 4.2.2(d).* ***(f)*** *Schematic summary of the magnetic-field-induced spectral weight redistribution from the Drude peak to the narrow modes at 90 cm^{-1} and 240 cm^{-1} and the broad MIR band.*

The difference plots in Figs. 4.2.3(c) and (d) still reveal some small, yet significant differences between the normal state spectrum at 30 T and 4.2 K and the one at 0 T and 65 K (green line). They show that the magnetic field enhances the electronic modes around 90 and 240 cm^{-1}.

Specifically, for the 240 cm^{-1} mode which can be identified and analysed already in zero magnetic field, the spectral weight increases by about 50 000 $\Omega^{-1}cm^{-2}$. The corresponding estimate for the 90 cm^{-1} mode is less reliable since it is close to the lower limit of the measured spectrum and superimposed on the narrow head of the Drude response for which the conductivity is steeply rising up towards low frequency. Nevertheless, its enhancement at 30 T is evident from Figs. 4.2.3(b) and (c) where it gives rise to a resonance feature in ε_1 and a maximum in the spectrum of $\Delta\sigma_1$, respectively.
Furthermore, the difference plots in Figs. 4.2.3(c) and (d) establish that in the normal state at 30 Tesla the Drude peak has a reduced SW as compared to the one at 65 K and 0 T. The light blue line in Fig. 4.2.3(c) shows a fit with a Drude function which yields a SW loss of about 3 % as compared to the total SW of the free carrier response with a plasma frequency of $\omega_{pl} \approx 15\,000$ cm^{-1}. The evolution of the integrated spectral weight of the difference plot, $SW(\omega)=\int_{55cm^{-1}}^{6000cm^{-1}} \Delta\sigma_1(\omega)d\omega$ in Fig. 4.2.3(e), shows that the SW loss of the Drude peak is compensated by the growth of the peaks at 90 and 240 cm^{-1} and, at higher energy, by an increase of the MIR band. The magnitude and the energy scale of the latter effect are somewhat uncertain since towards the upper limit of our measurement of 6000 cm^{-1}, the spectra are increasingly affected by the choice of the high energy extrapolation for the KK analysis. Nevertheless, it is evident that some of the SW loss of the Drude peak is compensated by a SW gain of the MIR band. A schematic summary of the above described magnetic-field-induced spectral weight redistribution is displayed in Fig. 4.2.3(f).

IV. Discussion

Our IR data reveal that a magnetic field in excess of 20 Tesla causes a complete suppression of the δ function at zero frequency that represents the loss-free response of the coherent SC condensate, since the magnetic-field-induced optical response is similar to the one for $B = 0$ and $T > T_c$. This finding is consistent with previous reports on YBCO, based on thermal conductivity measurements which concluded that the upper critical field, H_{c2}, has a minimum around $p \approx 0.1$ - 0.12 where it falls to about 20 Tesla [132], as well as spin susceptibility [185] and specific heat [186] measurements. Nevertheless, we remark that our IR data do not prove that a magnetic field above 20 T restores a true normal state. They are likewise consistent with a superconducting state that lacks macroscopic phase coherence but exhibits local superconducting correlations, see e.g. Ref. [199], that can fluctuate and give rise to dissipation and thus are difficult to distinguish from a Drude response of normal state carriers.
Apart from the suppression of the coherent superconducting response, we find that the IR spectra exhibit surprisingly weak changes that can be associated with the 3D CDW that develops above 15-20 T [200], which was also observed in NMR measurements [185]. The only noticeable effect is a weak reduction of the SW of the Drude response by about 3 % that is compensated by the enhancement of two narrow peaks at 90 and 240 cm^{-1} and of the broad MIR band. In terms of the response of a CDW, the enhanced MIR band can be understood as additional excitations across the CDW gap, whereas the enhanced peak at 240 cm^{-1} and, possibly, also the one at 90 cm^{-1} can be assigned to a pinned phase mode of the CDW. The electronic mode at 240 cm^{-1} was previously observed in IR studies of detwinned YBCO crystals in zero magnetic field where it occurs along the *b*-axis direction parallel to the one-dimensional (1D) CuO chains [38]. Earlier, it was discussed in terms of a CDW within the 1D CuO chains that is mainly activated in the infrared response by defects [40]. Nevertheless, in the light of the more recent observation of a CDW order of the CuO_2 planes and our present finding that the 240 cm^{-1} mode is enhanced by a large magnetic field, we reconsider it in terms of an intrinsic feature of the CuO_2 planes, that may of course also be influenced by the CuO chains and the structural

disorder therein. In this context, and since the present data were obtained from a twinned single crystal, we can only speculate that the additional mode around 90 cm^{-1} is a corresponding feature (a pinned phase mode of the CDW) in the *a*-axis response. Irrespective of the uncertainty of this assignment, the finding that the magnetic-field-induced spectral weight changes are rather small implies that the 3D CDW order is weak and involves only a relatively small fraction of the low-energy electronic states. Moreover, since the pinned phase mode and the MIR band are pronounced features already at zero magnetic field, our data suggest that strong CDW correlations exist irrespective of the magnetic field, even deep in the superconducting state at $T << T_c$. Note that the IR spectroscopy technique is even sensitive to rather short-ranged and fluctuating (on the picosecond timescale) CDW correlations. The above described scenario is therefore not necessarily in disagreement with the very weak, quasi 2D CDW order that is observed with x-ray diffraction at zero magnetic field and its suppression at $T << T_c$ [160, 27]. Evidence for such an incipient CDW order has also been obtained in a recent RIXS study in which it was found that very broad (quasi-elastic) Bragg peaks exist over a wide temperature and doping regime, without magnetic field [184]. The scenario of a slowly fluctuating CDW order that involves a substantial part of the low-energy states already at zero magnetic field can also account for the large residual low-energy spectral weight in the IR spectra that does not condense at $T << T_c$ (blue line in Fig. 4.2.3(a)).

The interpretation of this residual spectral weight in terms of collective excitations, rather than normal (unpaired) carriers, furthermore resolves a seeming contradiction with specific heat [201, 202] and NMR Knight shift [203] measurements which detect only a very low density of unpaired carriers at $T << T_c$.

Finally, we address the question which role the CDW correlations are playing in the formation of the MIR band. Whereas our IR data show that the MIR band is slightly enhanced when a 3D CDW order develops at high magnetic fields, it was previously shown that antiferromagnetic (AF) spin-fluctuations are also strongly involved in the formation of the MIR band [204, 205]. The latter one is indeed most pronounced close to the Mott-insulator state and its doping dependence has been successfully explained in terms of AF correlations that are enhanced by the electron-phonon interaction [206]. A consistent explanation of the MIR band thus may require taking into account the interplay between the spin and charge correlations as well as their coupling to the lattice.

V. Summary and Conclusion

In summary, we have studied the IR in-plane response of an underdoped, twinned $YBa_2Cu_3O_{6.6}$ single crystal with $T_c = 58(1)$ K in high magnetic fields up to $B = 30$ Tesla. We found that a *B* field in excess of 20 T fully suppresses the coherent response of the superconducting condensate and leads to a response that is similar to the one in zero magnetic field at a temperature slightly above T_c. Moreover, we found that the 3D CDW, which develops above about 15 - 20 T in such underdoped YBCO crystals, gives rise to surprisingly weak changes of the IR response. The only noticeable features are due to a weak suppression of the SW of the Drude response by about 3 % and a corresponding spectral weight increase of two narrow electronic modes around 90 and 240 cm^{-1} and of the MIR band above 1000 cm^{-1}. The weak enhancement of the MIR band can be understood in terms of the electronic excitations across the CDW gap. The electronic mode at 240 cm^{-1} has been assigned to the pinned phase mode of the CDW along the *b*-axis direction and, by analogy, the one at 90 cm^{-1} a corresponding feature in the *a*-axis response.

Notably, the MIR band and the pinned phase mode of the CDW at 240 cm^{-1} are prominent features already in zero magnetic field. This suggests that the pronounced CDW correlations exist not only at high magnetic fields, where they are readily seen with x-ray diffraction in terms of sharp Bragg peaks, but also at zero magnetic field, where only relatively weak and broad CDW Bragg peaks are typically observed with x-rays. We pointed out that this difference can be explained in terms of the high sensitivity of the IR spectroscopy technique to short-ranged and slowly fluctuating CDW correlations. The conjecture that strong but short-ranged and slowly fluctuating CDW correlations exist even in absence of the magnetic field and for a wide temperature range is confirmed by recent RIXS measurements [184]. This study revealed that strong but broad and quasi-static Bragg peaks exist already in zero magnetic field and persist up to elevated temperatures and over an extended doping range. In the IR response, the pinned phase mode at 240 cm^{-1} is indeed observed up to rather high temperatures and for a wide doping range up to (at least) optimum doping.

Moreover, the strength of the pinned phase mode at 240 cm^{-1} shows no sign of a suppression in the superconducting state below T_c. This suggests that the relationship between SC and the CDW correlations is not purely competitive, as has been proposed based on the observed decrease of the CDW Bragg peak seen with XRD in zero magnetic field [160, 27] but, in fact, may be more intricate and dependent on the correlation length as well as the dynamics of the CDW order. These questions are beyond the scope of our present work and will hopefully stimulate further detailed studies, for example of the evolution of the CDW phase mode(s) as a function of temperature, doping, magnetic field or uniaxial pressure.

Acknowledgments

We appreciate the support of the Technical Workshop at Fribourg University and of Gérard Martinez, Leonid Bovkun and Robert Pankow at the LNCMI in Grenoble. We acknowledge Dominik Munzar and Marc-Henri Julien for a critical reading of the manuscript and helpful comments and discussion. This project was funded by the Schweizer Nationalfond (SNF) through project 200020-172611 and by the LNCMI-CNRS, member of the European Magnetic Field Laboratory (EMFL).

4.3 Comments and Outlook

We presented the low-energy optical response of an underdoped $YBa_2Cu_3O_{6.6}$ crystal when being exposed to magnetic fields up to 30 Tesla. In particular, we have found that the macroscopic superconducting condensate is fully suppressed above ~20 T. The surprisingly weak signatures of charge density wave ordering are manifested in the enhancement of the pinned electronic phase mode at 240 cm^{-1}, the mid-infrared band and possibly another pinned phase mode at ~90 cm^{-1}.
These measurements were solely possible due to recent technological progress, in which the experimental setup in Grenoble shows an overall stability better than 0.2 % of the detected signal. Equally crucial is the combination of magnetic-field-dependent studies in Grenoble and temperature-dependent measurements in Fribourg with the gold-coating procedure, which enables the determination of the total reflectivity and the derivation of the optical functions ε(ω) and σ(ω). Previous comparable magneto-optical studies on YBCO were limited to 7 T for single crystals [44] and 15.5 T for thin films [42], and within their low signal-to-noise ratio there was hardly any change observed in the IR spectra.

In order to derive more information on the ground state orders and their interactions in YBCO, it will be interesting to further investigate the electronic 'CDW mode' at 240 cm^{-1}, since it is observed even without a magnetic field, up to rather high temperatures and for a wide doping range (compared to the expected doping level for charge ordering in cuprates, displayed in Fig. 2.1.2). For instance, we observed an enhancement of the 240 cm^{-1} mode when repeating the zero field reflectivity measurements after one year (see Figure 4.3.1). A detailed study of this 'aging-effect' could provide additional information on the extent of the CDWs' role in the cuprates.

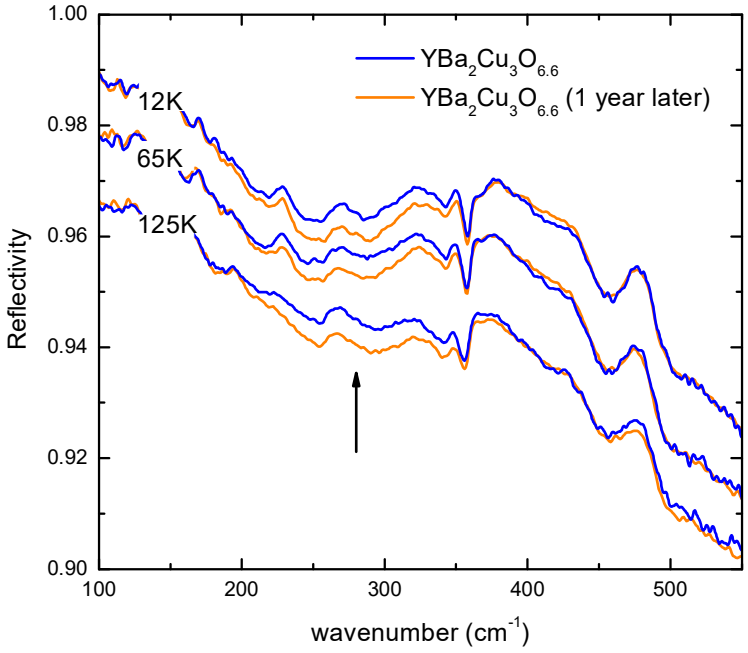

Figure 4.3.1 Change of the reflectivity spectra of an $YBa_2Cu_3O_{6.6}$ single crystal over a period of about one year. *The curves are overlapping at each temperature, except for the spectral region around the 240 cm^{-1} mode, which shows significantly more absorption one year later (orange line).*

Another aspect for further magnetic-field-dependent experiments is the sample cooling procedure. The here presented results were obtained by cooling the crystal down to 4.2 K (or 77 K) and then applying different magnetic fields. Future studies could include, besides these *zero field cooling*, *in field cooling* experiments, i.e. first applying a magnetic field and lowering the temperature below T_c. During our measurements in Grenoble we have tried these kinds of experiments by placing a heating element and a temperature sensor diode onto the sample holder. Due to the rather good thermal connection between the sample rod and the helium (or nitrogen) bath, both, sensor and heating element were poorly working. In order to perform temperature-dependent studies in combination with a magnet, we are planning to install a double-wall jacket of the probe which would enable to thermally shield the sample from the environment. In addition, Milan Orlita from Grenoble installed an infrared spectrometer that is coupled to a new superconducting magnet with magnetic fields up to 16 Tesla, which leads to less noise in the spectra. Also, it has a bore of 50 mm (instead of 40 mm in the previous setup), which allows more space for technical components inside the sample rod.
Moreover, the charge density wave in thin films of YBCO and e.g. manganite could be studied at high magnetic fields, in order to investigate the interaction of the CDW in the cuprate layer with the properties of the manganite layer.

Chapter 5

Observation of backfolded acoustic phonons in metal-oxide heterostructures

5.1 Introduction

Among thin films, superlattices are of particular scientific and technological importance. Their periodicity presents an additional control parameter, which allows modifications of their electronic and phononic behavior. Especially interesting are superlattices with constituent metal-oxide layers, which exhibit a variety of interesting properties, such as superconductivity, ferro- and flexoelectricity, that could serve for future technological applications.

In order to investigate such exotic phenomena, it is crucial to control the design and quality of superlattices. Besides the great progress which has been achieved in thin film deposition techniques, like pulsed laser deposition, molecular beam epitaxy and chemical vapor deposition, it is likewise important to improve existing characterization and monitoring techniques to ensure high-quality samples with sharp interfaces down to the atomic scale.
One prominent approach is the use of ultrasonics as an incisive probe for internal interfaces. However, in thin film structures the detected signal is dominated by the substrate response. Desirable is a substrate-insensitive diagnostic tool for superlattices in order to obtain information on the sample quality, film thickness and the speed of sound in the material.

In the following, we present such an accurate thin-film characterization tool in form of backfolded acoustic phonon modes, which are observed for the first time in metal-oxide superlattices by means of Raman spectroscopy. We theoretically describe these modes with the Rytov model and show that they arise from multiple reflections of acoustic waves at the internal interfaces of the superlattice, and are insensitive to the substrate response. Usually neither Raman nor infrared spectroscopy are sensitive to acoustic phonons, but the superlattice periodicity leads to a backfolding of the Brillouin zone, which brings new low-energy Raman-active excitations onto the Γ–point. Thanks to the high spatial and spectral resolution of the Raman microscope, these superlattice modes can be used to determine the bilayer thickness and sound velocity within the superstructures, as well as to perform a spatial mapping across the sample surface and even for temperature-dependent studies. The relatively short acquisition time (∼15-30 min), and no requirement to derive a complex theoretical model (which is the case e.g. for XRR and optical ellipsometry), makes them an appealing diagnostic for future studies of superstructures - not limited to metal-oxide samples.

5.2 Backfolded acoustic phonons as ultrasonic probes in metal-oxide superlattices

F. Lyzwa[1], A. Chan[2,3], J. Khmaladze[1], K. Fürsich[4], B. Keimer[4], C. Bernhard[1], M. Minola[4] and B.P.P. Mallett[2,5]

[1]*Department of Physics and Fribourg Center for Nanomaterials, University of Fribourg, Chemin du Musée 3, CH-1700 Fribourg, Switzerland*
[2]*The MacDiarmid Institute for Advanced Materials and Nanotechnology and The Dodd Walls Centre for Quantum and Photonic Technologies, 1010 Auckland, New Zealand*
[3]*School of Chemical Sciences, The University of Auckland, 1010 Auckland, New Zealand*
[4]*Max-Planck-Institut für Festkörperforschung, Heisenbergstrasse 1, 70569 Stuttgart, Germany*
[5]*Department of Physics, The University of Auckland, 1010 Auckland, New Zealand*

Published in Physical Review Materials **4**, 043606 (2020)

Ultrasonics have been an incisive probe of internal interfaces in a wide variety of systems ranging from stars to solids. For thin-film structures however, ultrasound is largely ineffective because the signal is dominated by the substrate. Using confocal Raman spectromicroscopy, we show that multiple reflection of sound waves at internal interfaces of a metal-oxide superlattice generates standing waves that are insensitive to the substrate. Such modes had previously been observed only in high-quality superlattices of elemental semiconductors, and their observation in complex metal-oxide heterostructures is testimony to recent progress in this field. We use the high spatial resolution of the Raman microscope to demonstrate the high sensitivity of the mode frequency to atomic-scale thickness variations of the superlattice. Spectroscopy of acoustic standing waves can hence serve as a powerful characterization tool of thin-film structures. In analogy to ultrasound spectroscopy of bulk solids, lineshape analysis of these modes has the potential to yield detailed information about the internal structure of the interfaces as well as the coupling of sound waves to the low-frequency spin, charge, and orbital dynamics in metal-oxide superlattices.

I. Introduction

Thin-film multilayers of metal oxides host a wide range of emergent, tunable and potentially useful properties [207-113, 8, 22, 49] beyond those observed in multilayers of more conventional semiconductors such as Si or GaAs [214, 215]. This is due to the various types of magnetic, charge, ferroelectric and superconducting orders that the constituent metal-oxide layers can host [216, 11]. The novel properties of thin-film multilayers and superlattices result from interactions across the interface, such as spin and orbital reconstruction, charge transfer and phonon coupling [8, 209, 210, 212] as well as some hitherto unidentified mechanisms [22, 6]. The additional periodicity introduced in superlattice structures with smooth interfaces can also be used to tune the thermal conductivity via the opening of phononic band gaps [217]. As such, multilayers of metal oxides constitute a fertile playground both to discover interesting physics and to tailor functionalities that could shape future electronics and phononics [217, 218].

Besides the scientific challenge of understanding the properties of metal-oxide superlattices, there is the persistent technical challenge of maintaining the quality of the crystal structure, interfaces and layer thickness in such samples [219]. Growth techniques for such samples include pulsed laser deposition (PLD) [220], molecular beam epitaxy [221], and sputtering [222].

Here we report on the observation of low-frequency Raman modes in metal-oxide superlattices, with a focus on superlattices of the high-temperature superconductor $YBa_2Cu_3O_7$ (YBCO) and $RMnO_3$ manganites, which are exemplary multilayers for displaying the effects described above [212, 22, 6]. The low-energy modes are optical phonons which arise in superlattices due to the backfolding of the *c*-axis acoustic phonon branch and, to the best of our knowledge, are detected for the first time in metal-oxide heterostructures. Until now the observation of backfolded acoustic phonon modes has only been reported in superlattices of high-quality molecular-beam-epitaxy-grown semiconductor superlattices, such as GaAs/AlAs [223-227]. The occurrence and the properties of these modes were fully explained and described within a comprehensive theoretical framework [225, 228-230]. The modes can thus be used to characterize the quality and properties of the superlattice, such as the speed of sound and the bilayer thickness, and signify the opening of a small phononic band gap [218]. Given the fast acquisition time of the measurement and the potential for micrometer spatial resolution, such modes can be a useful diagnostic for characterizing superlattices of given materials.

II. Methods

In the present work we study epitaxial superlattices of $YBa_2Cu_3O_7$ and manganite compositions $RMnO_3$, with R = $Pr_{0.5}La_{0.2}Ca_{0.3}$ (PLCMO), $Nd_{1-x}(Ca_{1-y}Sr_y)_x$ (NCSMO) or $La_{1-x}Ca_x$ (LCMO). Details of the sample compositions can be found in the Supplementary Material of Ref. [50]. The samples are grown by PLD on $La_{0.3}Sr_{0.7}Al_{0.65}Ta_{0.35}O_3$ (LSAT) substrates that are (0 0 1) oriented following the process described in Refs. [6] and [231]. The superlattices involve 10 repetitions of cuprate-manganite layers, whose thickness we denote using the following scheme: PLCMO(10 nm)/YBCO(7 nm) translates to a 7-nm-thick YBCO layer grown on top of a 10-nm-thick PLCMO layer. The topmost layer is the manganite, followed by a 2-nm-thick $LaAlO_3$ capping layer to protect the film from degradation.

We performed *ex situ* studies with x-ray diffraction, x-ray reflectivity, and polarized neutron reflectivity to measure the layer thickness, uniformity, and interface roughness. Representative results can be found in the Supplementary Materials of Refs. [22] and [6]. These show that our samples are of a high quality, with a small interface roughness (∼0.5 nm) that tends to increase with additional cuprate/manganite layers and minimal chemical diffusion across the interface.

The Raman spectra were recorded with a Jobin-Yvon LabRam HR800 spectrometer using the 632.8 nm excitation line of a HeNe laser [148]. The measurements were carried out in full backscattering with geometry indicated by Porto's notation. For example, $z(Y'X')\underline{z}$ indicates backscattering with incident polarization 45° to the Mn-O nearest-neighbor bond with the cross-polarized scattered light measured. We find spurious reflections in our spectrometer that lead to artefacts around 7 cm^{-1} and 15.8 cm^{-1}; these spectral regions are removed from the reported spectra for clarity. Unless noted otherwise, the spectra shown were recorded at room temperature. The 1800 lines/mm gratings give a spectral resolution of 0.3 cm^{-1}. The laser was focused with a ×100 long-working distance objective lens with a short depth of focus, NA = 0.6, which was positioned with an accuracy of 0.5 µm such that the focus is centered on the film [148]. In order to further minimize the signal from the LSAT substrate we use a 50-µm confocal hole along the scattered light path.

The penetration depth of the laser light in our samples is about 70 nm. As such, the residual substrate contribution is small, but nevertheless it is subtracted from the spectra using reference measurements for which the beam focus was moved into the substrate (see Fig. S1 of the Supplementary Material of Ref. [50]).
All reported spectra have been divided by the Bose thermal factors to obtain the imaginary part of the Raman scattering susceptibility, $\mathrm{Im}\chi(\omega)$. Further details and exemplary raw spectra of the superlattices and substrates can be found in the Supplementary Material of Ref. [50].

III. Results

A. Exemplary case

To set the scene, Fig. 5.2.1(a) shows the Raman Stokes signal from a PLCMO(10 nm)/YBCO(7 nm) superlattice (sketched) collected at room temperature in $z(X'X')\underline{z}$ geometry over a wide spectral range. The spectrum reveals multiple broad overlapping phonon modes above 50 cm^{-1} arising from both YBCO, manganite, and the interaction between them. A rich spectral fingerprint is expected, as a simplified space group of the manganite, *Pmma*, allows 21 Raman-active modes [232] (the more realistic *P21/m* symmetry, which includes the MnO_6 octahedral tilts, having 54 Raman-active phonon modes). The manganite spectra are also consistent with a disordered rhombohedral phase with space group $R\bar{c}3$ [233]. YBCO has five main Raman-active phonon modes, with additional modes in special cases of charge and oxygen ordering [234]. An analysis of this spectral region will be presented elsewhere, as here we focus on the Raman scattering below 30 cm^{-1}.

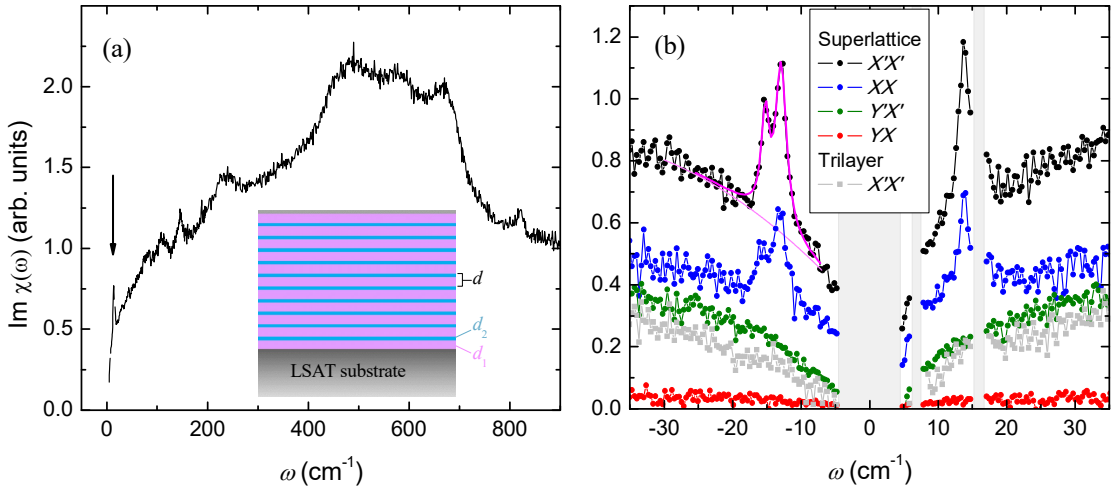

Figure 5.2.1 (a) *Spectrum of a PLCMO(10 nm)/YBCO(7 nm) superlattice, illustrated bottom center, in z(X'X')z scattering geometry showing the comparatively intense and narrow line width of the low-frequency modes compared with the phonon modes above 70 cm^{-1}.* ***(b)*** *Polarization analysis of the low-frequency modes. The thick magenta line for the z(X'X')z superlattice spectrum shows a fit to the data with the modeled background as the thin magenta line. The gray data (offset by -0.5 for clarity) are for a trilayer sample of the same composition which indicates that the low-energy modes are inherent to the superlattice samples only.*

In particular, we focus on two prominent features in the low-energy spectra, which are marked by the arrow in panel Fig. 5.2.1(a) and highlighted in Fig. 5.2.1(b). In Fig. 5.2.1(b), both the Stokes and the anti-Stokes signals at *T*=300 K in a narrow spectral region around the elastic line are shown. The modes are clearly pronounced for both the *z*(*XX*)$\underline{z}$ and *z*(*X'X'*)$\underline{z}$ geometries, but they are not observed for the cross-polarized geometries. Importantly, these sharp modes are only observed in superlattice samples. For example, we include in Fig. 5.2.1(b) a spectrum from a trilayer of the same material, PLCMO(20 nm)/YBCO(7 nm)/PLCMO(20 nm), in which the sharp low-energy features are absent.

To quantitatively characterize these peaks, we fit them using a quadratic background and a pseudo-Voigt line shape, as detailed in the Supplementary Material of Ref. [50]. An exemplary fit is represented by the magenta line superimposed on the *z*(*X'X'*)$\underline{z}$ superlattice data in Fig. 5.2.1(b), whereas the modeled background is a lighter-colored thin magenta line. The fitted peaks shown in Fig. 5.2.1(b) are centered at $\omega_0 =$ -12.9 and -15.2 cm^{-1}, with the absolute uncertainty in the peak positions estimated to be 0.3 cm^{-1}, primarily due to systematic uncertainties. The half-widths at half-maximum (HWHM) are $\gamma =$ 1.0 and 0.5 cm^{-1} respectively. The area of each mode, *SW*, is proportional to its Raman susceptibility. While we cannot quantify the Raman susceptibility from our data in absolute terms, we can compare the Bose-corrected areas of these new modes with that of a regular phonon mode. In particular, we find an area of *SW* ≈ 0.2 (a.u.) for the phonon excitation at $\omega_0 \approx$ 145 cm^{-1} and areas of *SW* = 0.5 and 0.3 for the two low-energy modes, respectively. This illustrates that the new modes have Raman cross sections comparable to the weaker phonon modes above 70 cm^{-1}.

In transition-metal oxides like those studied here, modes in this frequency range might be ascribed to magnetic excitations [235]. However, for several reasons this is unlikely in our case, despite the significant Mn magnetic moments. First, long-range magnetic order is established only below $T \approx$ 140 K in our PLCMO and NCSMO samples [6, 22, 23], whereas these peaks are intense and sharp already at room temperature. Second, the new modes are only observed for superlattice samples, and not in films of the pure manganite material with a thickness comparable to that of the superlattices. Third, whereas magnons are usually observed in crossed polarization, the *z*(*XY*)$\underline{z}$ and *z*(*X'Y'*)$\underline{z}$ polarization channels of our superlattices do not exhibit low-energy modes (Fig. 5.2.1(b)). In addition, the low-energy modes are not observed in trilayer samples, which rules out that they originate solely due to an interaction between the cuprate and manganite.

B. Sample dependence

Furthermore, Fig. 5.2.2 illustrates that the position of these peaks depends on the bilayer thickness in the superlattice samples (i.e. the sum of the YBCO and manganite film thicknesses). Figure 5.2.2(a) shows *z*(*X'X'*)$\underline{z}$ spectra for superlattice samples with a range of bilayer thicknesses, d. Spectra have been offset for clarity. The shift of the modes to lower energies with larger bilayer thicknesses is clearly seen from the raw data. Figure 5.2.2(b) shows the fitted energies of the two observable low-energy modes, ω_0, as data points plotted versus d^{-1}. The solid line in the figure has the form $\omega_0 = v_s d^{-1}$, where the meaning and choice of the value v_s are discussed below. The peak areas, *SW*, and widths, γ, do not appear to show any systematic variation across the samples studied. Finally, we note the possible presence of additional low-energy peaks barely resolved by our measurements, except in particular cases such as the $d =$ 16.5 nm sample (brown curve).

These observations show that the low-energy modes most probably arise from a backfolding of the Brillouin zone, due to the superlattice periodicity, which brings new Raman-active excitations at low energies onto the Γ point.

Such a situation has been well documented and analyzed in superlattices comprised of GaAs-AlAs semiconductors for acoustic phonon branches [223, 225-227, 229]. There are well-established models for this situation, starting from either a continuum approximation or linear-chain type models [225, 228, 229], of which detailed versions have been developed in order to capture finite-size effects of the sample [230]. All such models agree, however, with the general behavior captured by the simpler Rytov model [236]. Within this model, the phonon dispersion is described by

$$\cos(qd) = \cos\left(\frac{\omega d_1}{v_{s,1}}\right)\cos\left(\frac{\omega d_2}{v_{s,2}}\right) - \left(\frac{1+\kappa^2}{2\kappa}\right)\sin\left(\frac{\omega d_1}{v_{s,1}}\right)\sin\left(\frac{\omega d_2}{v_{s,2}}\right) \tag{52}$$

where the subscripts 1 and 2 denote the two materials in the superlattice and $v_{s,1} = \sqrt{c_{33}/\rho}$ is the sound velocity (with ρ the density of the material and c_{33} the elastic modulus along the *c*-axis direction). d_1 and d_2 are the thicknesses of the layers comprising the superlattice and $\kappa \equiv v_{s,2}\rho_2/v_{s,1}\rho_1$. This expression describes a folding of the phonon dispersions about d^{-1}, where $d = d_1 + d_2$, and the opening of gaps at the zone center and boundaries.

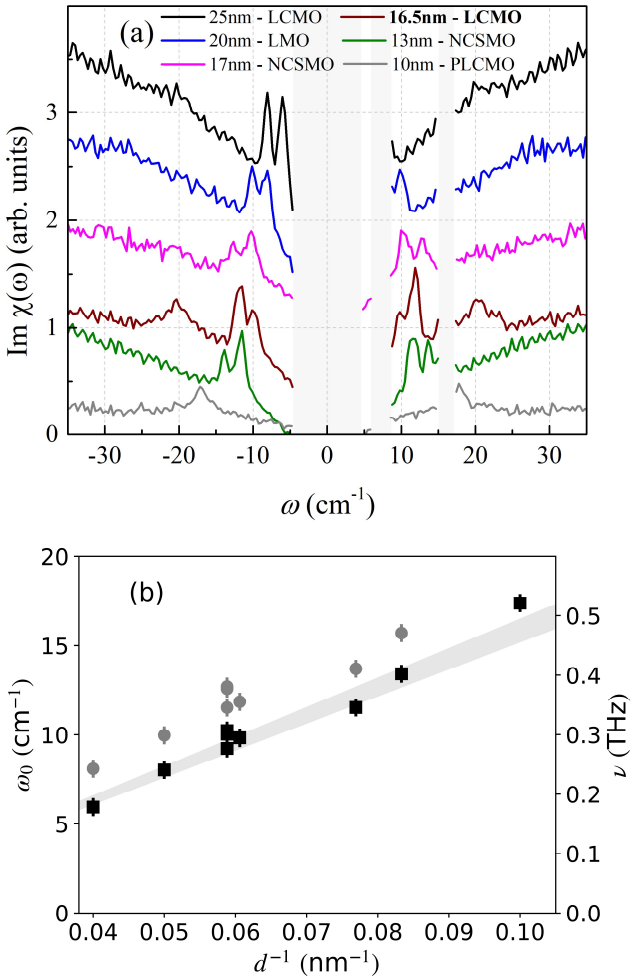

Figure 5.2.2 (a) *Spectra from multiple superlattice samples with bilayer thickness, d, and the manganite compositions indicated in the legend.* ***(b)*** *Center positions of the two observable low-energy modes versus d^{-1}. The shaded line represents the expected average position of the two low-frequency modes based on the speed of sound in the superlattice.*

Fig. 5.2.3(a) sketches the backfolding effect with approximate values for our experiments. With the Raman measurements, we (de)excite the phonon modes at $q = n\lambda^{-1}$, where n is the refractive index of the superlattice and λ the laser wavelength.

This model describes our observations accurately. In particular, the straight line in Fig. 5.2.2(b) is given by $v_s d^{-1}$, where d is obtained from the nominal layer thicknesses (estimated from x-ray reflectivity measurements) and $v_s = \frac{7}{17}v_{s,\mathrm{YBCO}} + \frac{10}{17}v_{s,\mathrm{manganite}}$ is the weighted average of the *c*-axis speed of sound in the two materials (here we are using the most common 7-nm YBCO layer and 10-nm manganite layer thicknesses) [225]. The value of v_s is 4750±200 ms^{-1} as determined from the bulk-moduli and densities [237, 238], but similar values are obtained from other measurements of the speed of sound [239-242]. The width of the line in Fig. 5.2.2(b) comes from the uncertainty in v_s for the individual YBCO and manganite layers. $v_s d^{-1}$ represents an average of the two peak positions, which are split due to the mixing and the finite q of the laser line [228]. Therefore, our experimental results are consistent with the slightly higher value of $v_s \approx 5150$ ms^{-1}.

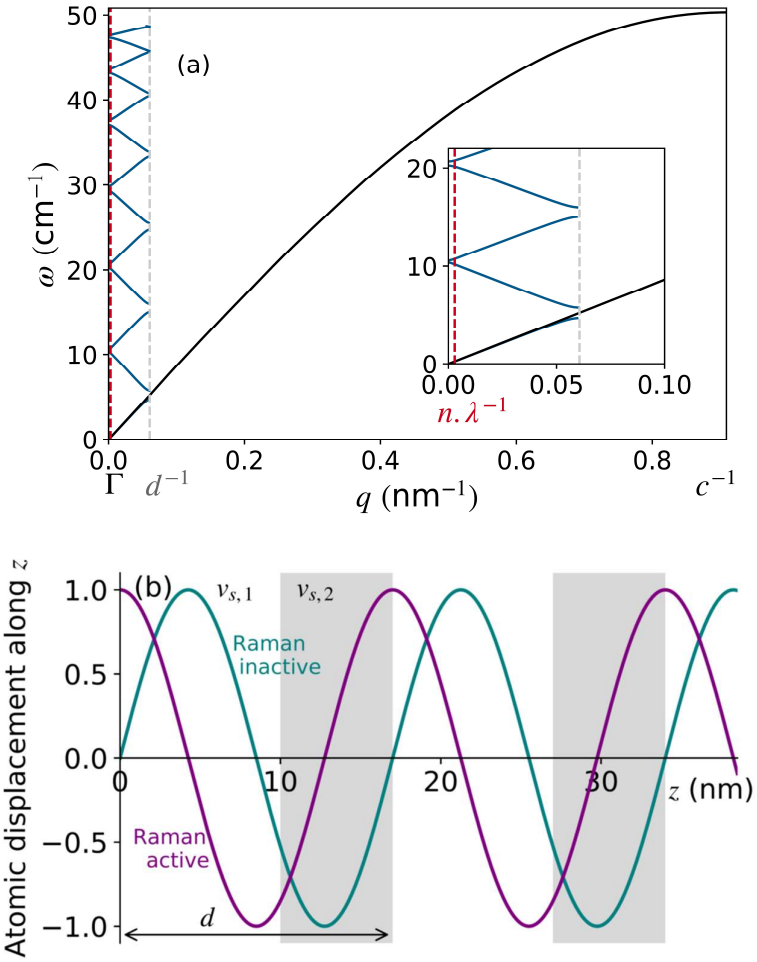

Figure 5.2.3 (a) *Sketch of phonon backfolding with approximate values for our samples. The black line shows a typical dispersion of an acoustic phonon branch. The additional periodicity of the superlattice, d, backfolds the phonon branch around d^{-1}. There is a splitting of the phonon branches near $q = 0$ and d^{-1} creating phonon bandgaps there. The Raman experiment probes the phonon modes with $q = n\lambda^{-1}$, shown by the dashed red line.* ***(b)*** *Sketch of the amplitude of atomic displacement for the two first-order backfolded modes at Γ. Shaded regions represent the material with the higher speed of sound, $v_{s,2} > v_{s,1}$.*

A generalized relaxation time of the mode can be expressed as $\tau = \gamma^{-1}$, which is between 30 to 60 ps, depending on the mode. If we take $\tau = 40$ ps and $v_s = 5150$ ms^{-1}, then the scattering length of the mode is $l = v_s\tau \approx 200$ nm. This is close to the total film thickness and suggestive of dissipative scattering of the phonon at the top surface of the superlattice and bottom interface with the substrate rather than the YBCO/manganite interfaces. Similar conclusions were made by Li *et al.* from pump-probe reflection measurements of superlattices with two different bilayer thicknesses [240]. This conclusion is also supported by the observation that the ratio of the mode width to the resonant frequency, γ/ω_0, is approximately 0.07 and much higher than the ratio of $\sim 10^{-3}$ that is measured for acoustic modes at room temperature by resonant ultrasound spectroscopy on single crystals of YBCO [243] or manganites [244]; i.e. the phonon scattering is enhanced in the superlattices with respect to the bulk crystals. On the other hand, we cannot rule out alternate explanations for the shortened phonon lifetime that we infer from the phonon linewidth, such as from inhomogeneity across the beam spot.

We now discuss the intensity of the peaks. Close to the Brillouin-zone center, the phonon mode upper and lower branches of the backfolded dispersion have Raman-active and Raman-inactive symmetries. The atomic displacement amplitude for the modes, that is, the two first-order backfolded phonon modes at the Brillouin-zone center, are sketched in Fig. 5.2.3(b) following Ref. [223]. One mode is a symmetric stretch of the bilayer unit that causes a change in polarizability and is hence expected to be Raman active. This mode has maximal amplitude at $z = 0$ and is represented by the purple curve in Fig. 5.2.3(b). The other mode is an antisymmetric stretch and is not expected to be Raman active (off-resonance). We note that the finite q of phonon branches that we measure in backscattering geometry leads to a mixing of the two symmetries [223, 245, 246], but we still expect the relative Raman cross section of the two branches to be different in our experiments.

The relative thickness and speed of sound of the manganite and YBCO layers determine whether the upper or lower branch has dominant Raman-active symmetry. We denote these d_1 and d_2, respectively, whereby layer 1 (the manganite) has a slower speed of sound than layer 2 (YBCO): $v_{s,1} < v_{s,2}$. For $d_1 < d_2$, the Raman-inactive mode has a lower energy than the Raman-active mode, and this results in the lower energy mode having a lower intensity in the spectra. The sample representing this case is shown in boldface in the legend of Fig. 5.2.2(a). For most of our samples the $d_1 > d_2$ condition instead holds so that the situation is reversed, with the higher-energy mode having the lower intensity. For $d_1 = d_2$, the second-order backfolded phonon branch will not be Raman active, and this is the case for the 20-nm LMO sample in Fig. 5.2.2(a).

However, for all samples we barely see the second-order modes. We are not certain of the reason for this, but it could be an indication of interface roughness, as we note that in GaAs/AlAs superlattices the intensity of the backfolded modes was observed to decrease upon annealing of the sample at 850°C, a process that introduces interface roughness by diffusion of the ions across the interface [228]. The $d = 16.5$ nm sample (brown curve) is a possible exception, where there is a clear peak at the expected position for the second-order backfolded modes. Here we also note that backfolding of the acoustic phonon branch was seen by terahertz/infrared spectroscopy of bulk manganites due to the additional periodicity of the charge-ordered state [247], as well as a disorder-activated "boson peak" at approximately 20 cm^{-1} and temperatures below 120 K. We do not believe this to be a plausible origin of the 20 cm^{-1} peak in our data that were obtained at room temperature. More quantitative predictions of the phonon intensities require first-principles calculations of the photoelastic coefficients [228, 245].

Finally we note that we observe similar low-frequency modes in superlattices grown in our laboratory where the YBCO is replaced with another metal oxide. These include $SrFeO_3/La_{2/3}Ca_{1/3}MnO_3$ [248] and $SrRuO_3/La_{2/3}Ca_{1/3}MnO_3$ superlattices.

C. Spatial dependence

The results above show that these low-energy modes can be used to determine the spatial variation in a superlattice's bilayer thickness (or more generally its repeat-unit thickness), d, because (i) their position, ω_0, is a function of d and (ii) the micro-Raman technique we use here has a 10 μm^2 spatial resolution in the plane. Spatial uniformity is of particular interest for growth techniques wherein the deposition rate of the films may not be constant across the sample. One particularly important example in terms of oxide materials is the growth by PLD on substrates with a surface area comparable to the size of the plasma plume. The spatial dependence of the intensity and HWHM may also be used to characterize the film quality.

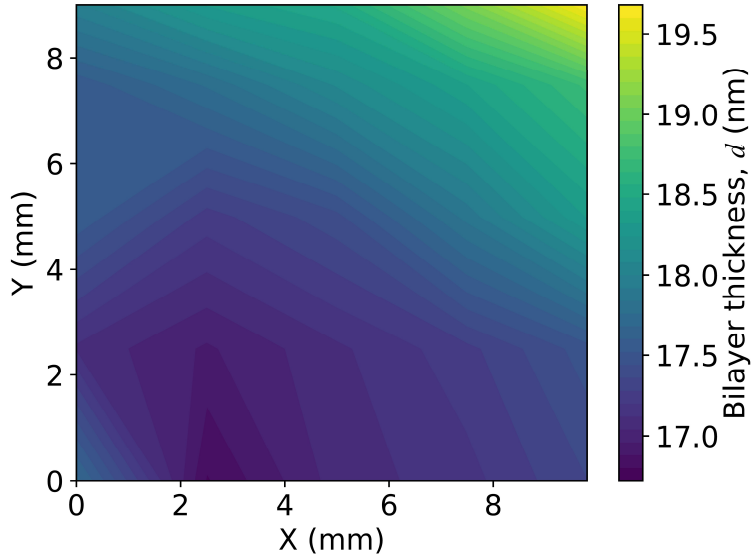

Figure 5.2.4 *A contour plot of the combined thickness of the LCMO and YBCO layers, d, determined from ω_0 of the low-frequency modes. There is a smooth gradient in d from one corner to the opposite.*

To exemplify the potential of our method, we performed measurements on a 7 × 7-point grid across the surface of a nominally LCMO(10 nm)/YBCO(10 nm) superlattice grown by PLD on an LSAT substrate with surface area 10 × 10 mm^2. The results are summarized in Fig. 5.2.4. The color scale represents d as determined from the fitted ω_0 of the two low-energy modes at each point and $v_s = 5000$ ms^{-1} as determined in Fig. 5.2.2(b). The data are linearly interpolated between the measurement points and we estimate the uncertainty in d to be ~1 nm. Figure 5.2.4 shows that the LCMO-YBCO layer thicknesses are not uniform across the approximate 9 × 9 mm^2 area that was measured. Instead, we identify a smooth gradient in the value of d from one corner to the opposite corner.

D. Temperature dependence

The multilayers studied here exhibit a range of electronic and magnetic phase transitions at temperatures below 300 K [6, 22, 23, 249, 250] and the materials are known for significant electron-phonon and spin-lattice coupling [8, 210, 212, 216]. As such, we investigated the temperature dependence of the backfolded phonon modes.

Figure 5.2.5(a) shows the Stokes signal for a NCSMO(10 nm)/YBCO(7 nm) superlattice with nominal x = 0.5 and y = 0.33 for NCSMO between room temperature and a nominal temperature of 10 K. We find only a subtle temperature dependence, except for a possible increase in intensity below 50 K (the Bose thermal correction at low energies is particularly large and, hence, sensitive to imperfect background signal subtraction and laser-heating effects). Qualitatively similar temperature dependencies were observed for other superlattices, where measured.

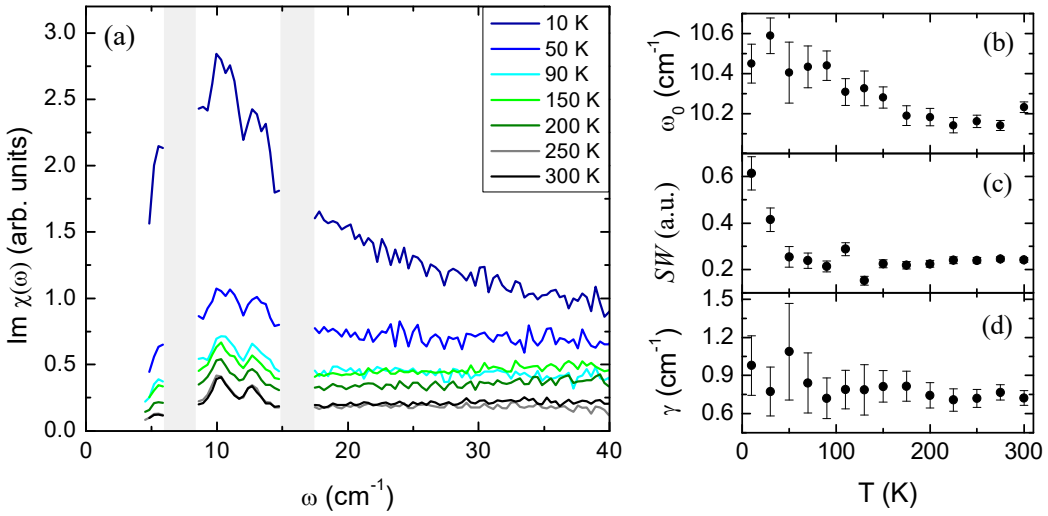

Figure 5.2.5 (a) *Representative temperature dependence of the low-frequency spectra in z(XX)z̲ geometry, from a NCSMO(10 nm)/YBCO(7 nm) superlattice.* ***(b)*** *Fitted center position,* ***(c)*** *intensity, and* ***(d)*** *HWHM of the lower-energy peak.*

Figures 5.2.5(b)-(d) show the results of fitting the Stokes signal from the lower-energy mode. We note here that first the background was subtracted, then the Bose thermal factor correction applied, before fitting the peaks. This procedure was adopted to reduce the uncertainty of the background contribution to the peak intensity. The ω_0 of the mode shows only slight variation across the whole temperature range. In absolute terms, the variation is comparable to the absolute uncertainty in ω of 0.3 cm^{-1} that we estimate, as shown in Fig. 5.2.5(b). Figure 5.2.5(c) shows the temperature dependence of the fitted peak area, *SW*. *SW* is proportional to the Raman cross section and shows an increase at low temperatures. From the Stokes/anti-Stokes ratio of the low-frequency modes we have obtained laser-heating estimates of up to 40 K at base temperature (which is nominally 10 K) following the method of Herman [143], although the uncertainty/scatter in such estimates is of the order of 50 K. A 40 K laser-heating effect would be enough to compensate the low-temperature increase in *SW* and recover the customary temperature-*in*dependent *SW*, and we cannot yet rule this out as an explanation for the increased peak area below the nominal temperature of 50 K.

Figure 5.2.5(d) shows that there is no observable temperature dependence of the HWHM, suggesting no significant additional relaxation/scattering channels for the phonons open in the various magnetic, charge, and superconducting ordered phases at lower temperatures.

IV. Discussion and Conclusions

These results demonstrate the remarkable quality of transition-metal oxide films that can now be grown with pulsed laser deposition. The experimental methodology we used to characterize the superlattices is nondestructive, relatively accessible, and rapid. There are several ways in which future measurements could be improved to gain a richer characterization of the superlattice film quality. First, higher-resolution spectra would better resolve the peak positions, intensity, widths, and asymmetry. Such higher-resolution spectra would be desirable for low-temperature studies of these materials in order to study the coupling between this phonon branch and the spin or low-energy electronic systems. Furthermore, it may be possible to observe the fine structure of these peaks, which would allow an analysis beyond the continuum Rytov model, for example, using finite-size, linear-chain-type models that can model thickness variations in the superlattice [230]. Second, it would be possible to independently determine both d and v_s from the Raman data alone, with measurements using multiple laser wavelengths. Such measurements, or the more challenging forward-scattering geometry measurements [245, 246], would also reveal in more detail the splitting of the two phonon branches that is caused by interatomic coupling between the two metal-oxide layers [228].

In summary, we report systematic measurements of low-frequency modes in metal-oxide superlattices grown by pulsed laser deposition. We show that these modes arise from a backfolded *c*-axis acoustic phonon branch. As such, their observation demonstrates the high quality of the thin-film superlattices. The modes can be used to characterize the bilayer thickness of the superlattice and/or the *c*-axis speed of sound. We utilized the spatial resolution of the Raman microscopy to map the film thickness inhomogeneity across a larger, 10 × 10 mm sample. This information is important for monitoring and improving the quality of future metal-oxide superlattices which might comprise the building blocks of next-generation electronic devices.

Acknowledgments

We thank Dr. F. Weber and Dr. R. Heid for valuable discussions on this work. The work was supported by the Schweizerische Nationalfonds (SNF) through Grant No. 200020-172611. B.P.P.M. acknowledges support from the Rutherford Foundation of New Zealand. A.C. acknowledges support from the MacDiarmid Institute.

5.3 Comments and Outlook

We have experimentally observed and theoretically explained backfolded acoustic phonons, for the first time, in metal-oxide superlattices. Theses modes, detected via confocal Raman spectromicroscopy, have been demonstrated to be an accurate characterization tool for superstructures because of the relatively short acquisition time, the high sensitivity on atomic-scale thickness variations, and the enhanced signal-to-noise ratio.

The results are not only appealing for fundamental solid state research, but can readily be applied in industry for investigating the quality of superstructures. Superlattices and other thin film structures are for instance crucial for the fabrication of certain laser cavities, which is done e.g. in the group of Prof. Ursula Keller at ETH Zürich. Moreover, phononic bandgaps can be studied in order to control the thermal conductivity of the material. In addition, superlattice-type structures might play a role in making next-generation electronic and phononic devices more efficient, rather than using 'conventional' single thin films or bilayers.

These backfolded modes are in principle applicable to any superstructure and not limited to superlattices of transition metal oxides, and can also be observed e.g. in semiconductors, as displayed in Fig. 5.3.1. Here, the backfolded modes are clearly seen at least up to the 3rd order, which is probably because of the high quality of the sample. The number of observable orders might present an additional indicator of the quality of the superstructures.

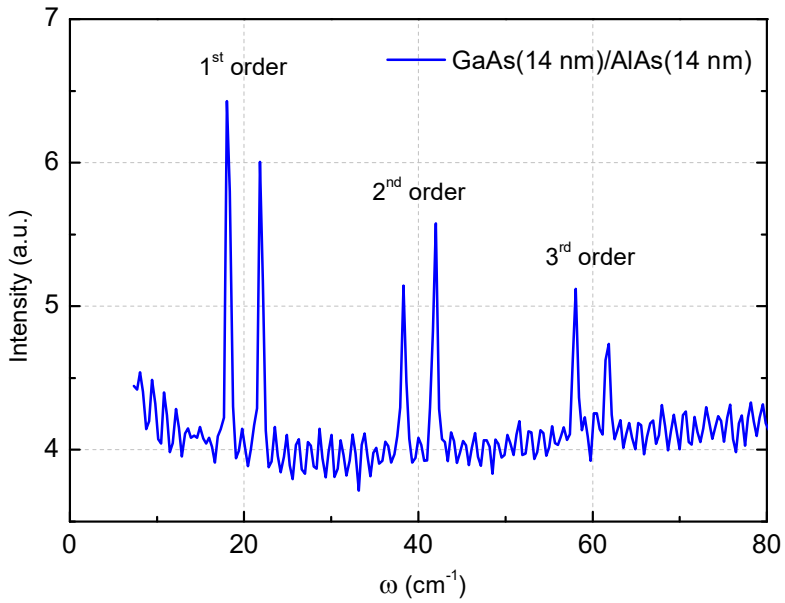

Figure 5.3.1 Low-frequency modes in GaAs/AlAs superlattices.

Future work includes a more detailed investigation of the backfolded phonon modes' lineshape, their temperature dependence as well as their magnetic field dependence. Such experiments could yield important information on the coupling of acoustic modes to spin, charge and orbital dynamics of the system. Certain phase transitions of the material (as a function of e.g. temperature or doping) could potentially be detected.

In the presented data, we could not see a clear trend in neither the line shape nor the temperature-dependence. One limitation might be the spectral resolution of $\backsim 0.3$ cm^{-1}. Further technological improvements, such as the use of spectrometers with thinner optical gratings and thus higher spectral resolution, will provide answers on these questions.

Chapter 6

Electric field effect on $SrTiO_3$- and $KTaO_3$-based heterostructures

6.1 Introduction

$SrTiO_3$ has been studied for many decades because it is highly susceptible to an external perturbation and can be tuned into exotic states. At low temperatures, it is termed a *quantum paraelectric*, since a ferroelectric order is inhibited by quantum fluctuations of the lattice, but can be stabilized, e.g. by doping of the *A*-site with calcium [251, 252]. The low-temperature properties of $SrTiO_3$ are mostly governed by the unusual behavior of its TO_1-mode (vibration of the titanium center atom with respect to the oxygen octahedral): Towards low temperatures, the dielectric permittivity diverges to values up to $\varepsilon_0 \approx 20.000$ [53, 54], which also scales with the magnitude of induced flexoelectric fields [75].

Moreover, $SrTiO_3$ has been widely used as a substrate and as a source of two-dimensional electron gases (2DEG) at the interface with e.g. $LaAlO_3$ or AlO_x. Of particular interest is the electric field effect of such heterostructures, as it opens up a wide platform of novel physics. It can for instance enable a superconductor-insulator [4] or metal-insulator transition [109, 3], or the increase of the magnitude of the Rashba spin-orbit interaction [5] and thus of spin-charge-conversion effects [2, 111]. These exotic effects raise questions regarding the underlying polarization mechanism, and the relationship of the substrate with the 2DEG.

We tackle these questions by a unique combination of infrared ellipsometry and confocal Raman spectroscopy, which are both highly sensitive to polarization effects and operate as complementary techniques. This approach enables us to obtain separate information on the in-plane and the out-of-plane components of the induced polarization. It is possible to distinguish between effects arising from the surface and the bulk, and to perform a depth-dependent study.
Here, we investigate this electric field effect (up to ±8 kV/cm) on $SrTiO_3$-based heterostructures, and compare it with $AlO_x/KTaO_3$ heterostructures, which also exhibit a confined 2DEG at the interface. For the $SrTiO_3$ samples, we observe a highly asymmetric electric field modulation, which is remnant and non-collinear with the applied electric field. This effect initiates and is strongest at the interface, but it also determines the bulk properties to a large amount. We provide evidence that this unusual behavior originates from the interplay of the oxygen vacancies and the tetragonal domain boundaries, which occur in $SrTiO_3$ below around $T^* = 105$ K, and are absent at all temperatures in $KTaO_3$. In addition, we found an optical switching mechanism in form of UV light illumination, which fully restores the original state, and can potentially be readily used for technological applications.

6.2 Non-collinear and strongly asymmetric polar moments at back-gated $SrTiO_3$ interfaces

F. Lyzwa[1], Yu. G. Pashkevich[2], P. Marsik[1], A. Sirenko[3], A. Chan[4], B.P.P. Mallett[4,5], M. Yazdi-Rizi[1], B. Xu[1], L.M. Vicente-Arche[6], D.C. Vaz[6], G. Herranz[7], M. Cazayous[8], P. Hemme[8], K. Fürsich[9], M. Minola[9], B. Keimer[9], M. Bibes[6], and C. Bernhard[1]

[1]*Department of Physics and Fribourg Center for Nanomaterials, University of Fribourg, Chemin du Musée 3, CH-1700 Fribourg, Switzerland*

[2]*O. O. Galkin Donetsk Institute for Physics and Engineering NAS of Ukraine, UA-03028 Kyiv, Ukraine*

[3]*Department of Physics, New Jersey Institute of Technology, Newark, New Jersey 07102, USA*

[4]*School of Chemical Sciences and the MacDiarmid Institute for Advanced Materials and Nanotechnology, The University of Auckland, Auckland, New Zealand*

[5]*Robinson Research Institute, Victoria University of Wellington, 69 Gracefield Rd., Lower Hutt 5010, New Zealand*

[6]*Unité Mixte de Physique, CNRS, Thales, Université Paris-Saclay, 91767 Palaiseau, France*

[7]*Institut de Ciència de Materials de Barcelona (ICMAB-CSIC), Campus UAB, 08193 Bellaterra, Catalonia, Spain*

[8]*Laboratoire Matériaux et Phénomènes Quantiques (UMR 7162 CNRS), Université de Paris, 75205 Paris Cedex 13, France*

[9]*Max-Planck-Institut für Festkörperforschung, Heisenbergstrasse 1, 70569 Stuttgart, Germany*

submitted, arXiv:2109.06673v1

The highly mobile electrons at the interface of $SrTiO_3$ with other oxide insulators, such as $LaAlO_3$ or AlO_x, are of great current interest. A vertical gate voltage allows controlling a metal/superconductor-to-insulator transition, as well as electrical modulation of the spin-orbit Rashba coupling for spin-charge conversion. These findings raise important questions about the origin of the confined electrons as well as the mechanisms that govern the interfacial electric field. Here we use infrared ellipsometry and confocal Raman spectroscopy to show that an anomalous polar moment is induced at the interface that is non-collinear, highly asymmetric and hysteretic with respect to the vertical gate electric field. Our data indicate that an important role is played by the electromigration of oxygen vacancies and their clustering at the antiferrodistortive domain boundaries of $SrTiO_3$, which generates local electric and possibly also flexoelectric fields and subsequent polar moments with a large lateral component. Our results open new perspectives for the defect engineering of lateral devices with strongly enhanced and hysteretic local electric fields that can be manipulated with various other parameters, like strain, temperature, or photons.

I. Introduction

At room temperature, $SrTiO_3$ (STO) exhibits a cubic perovskite structure and a band-insulating electronic ground state with an energy gap of 3.25 eV [253, 51]. Its macroscopic properties are typical for this class of materials, except for mobile oxygen vacancies which make it an interesting ion conductor [254]. At $T^* = 105$ K, STO undergoes an antiferrodistortive (AFD) transition into a state with tetragonal symmetry that arises from an antiphase rotation of the TiO_6 octahedra around the tetragonal axis [255, 256]. If no preferred direction of the tetragonal axis is imposed, e.g. by applying external pressure or electric fields, a multi-domain state develops for which the tetragonal axis is either along the x-, y-, or z-direction of the perovskite structure. The resulting AFD domain boundaries are strained and tend to be attractive for oxygen vacancies, ferroelastic and even polar [58, 57, 257, 258].

Below about 50 K, the dielectric properties of STO become highly anomalous as it approaches a ferroelectric instability that is avoided only by the quantum fluctuations of the lattice [259]. This quantum paraelectric regime is characterized by a divergence of the dielectric constant toward giant low-temperature values of up to $\varepsilon_0 \approx 20.000$ that is caused by an anomalously strong softening of the lowest infrared-active transverse phonon (TO_1 mode) (see e.g. [53, 54] and the Appendix B). This so-called 'soft mode' involves the off-center displacement of the titanium ions with respect to the surrounding octahedron of oxygen ions, which, in the static limit, represents the ferroelectric (FE) order parameter. The FE order can be readily induced, e.g. by isoelectronic cation substitution in $Sr_{1-x}Ca_xTiO_3$ [251, 252], via strain from a lattice mismatch with the substrate in thin films [66], by external pressure [260], by electric fields in excess of 2 kV/cm [80], and even by replacing the oxygen isotope ^{16}O with ^{18}O [77]. The large ε_0 values furthermore enhance flexoelectric effects for which strain gradients give rise to a polar moment [75].

More recently, heterostructures and devices based on STO have obtained considerable attention thanks to a great general interest in the electronic conduction along oxide-based interfaces and domain boundaries [261] as well as on the effect of oxygen intercalation on the electronic properties of metal-oxide thin films and devices, especially in the context of liquid gating [262]. In particular, the interface of STO with $LaAlO_3$ (LAO) or AlO_x has been intensively studied because it hosts highly mobile and even superconducting electrons (below ~0.3 K [4]) that are very susceptible to electric field gating [4, 94, 95, 109, 208, 263]. The field-gating also allows tuning of the spin-orbit Rashba coupling and thus of spin-charge interconversion effects [2, 111, 264]. The origin of the confined electrons and the mechanism(s) underlying the efficient field-gating are still debated.
For LAO/STO heterostructures, the polarity of the stacking of the $SrO^0/TiO_2^0/LaO^+/AlO_2^-$ layers causes a diverging electric potential with increasing LAO layer thickness, which can lead to an electronic reconstruction in terms of an electron transfer from the LAO to the STO layer ('*polar catastrophe*' scenario) [95, 109]. An alternative (or additional) mechanism involves oxygen vacancies in the vicinity of the interface that have a very low ionization energy, since ε_0 is very large [265, 98]. The latter mechanism is expected to dominate in AlO_x/STO, which has no obvious polar discontinuity [263, 266, 111, 2].

Here, we show with infrared ellipsometry and confocal Raman spectroscopy that for both LAO/STO (001) and AlO_x/STO (001) heterostructures a vertical gate voltage (V) induces highly anomalous polar moments in the vicinity of the interface, which are non-collinear and strongly asymmetric with respect to the nominal gate field. Our data indicate that the structural domain boundaries act as conduits of

oxygen interstitials and thus generate large local electric fields that can greatly affect the performance of oxide devices and give rise to new functionalities.

II. Infrared ellipsometry

In infrared ellipsometry on electric-field-gated STO-based devices, an induced polar moment is manifested in characteristic changes of some of the phonon modes. This is shown in Fig. 6.2.1(a) and Fig. 6.2.1(b) for the so-called R-mode at 438 cm^{-1} in AlO_x/STO, which exhibits a characteristic splitting at negative voltages. The R-mode becomes weakly infrared-active in the tetragonal state below T^* = 105 K (already at 0V), where the anti-phase rotation of the neighboring TiO_6 octahedra leads to a backfolding from the R-point of the cubic Brillouin-zone and a mixing with the antiferroelectric displacement of the Ti ions [267, 57].

In the presence of an electric-field-induced polar moment, ***P***, caused by a static off-center displacement of the Ti ions, this R-mode develops a second peak (colored arrows) that is redshifted and gains spectral weight at the expense of the unshifted peak. The right panels of Fig. 6.2.1(a),(b) show the gate-voltage loops of the magnitude of the peak splitting, which is strongly asymmetric and vanishes at large +V. A corresponding R-mode splitting was previously observed in field-gated LAO/STO as well as in bulk $SrTi^{18}O_3$ where the polar moment develops in the FE state below $T_{Curie} \approx 25$ K [56]. For LAO/STO, the asymmetric gate-voltage dependence of the R-mode splitting was interpreted in terms of a built-in, vertical electric field due to the discontinuity of the polar layer stacking to which the gate field adds (is opposed) at -V (+V), such that the threshold for inducing a static polar moment is overcome (not reached). This interpretation is however challenged by our finding that this kind of R-mode splitting occurs also in AlO_x/STO for which no polar discontinuity is expected [263]. Moreover, based on a symmetry analysis of the infrared response of the R-mode in the presence of a polar distortion (see appendix B) we find that the R-mode splitting can only be seen with ellipsometry if the polar moment has a sizeable horizontal component and thus is non-collinear with respect to the vertical gate field. Our new findings therefore indicate that additional effects are at play that govern the local electric fields and the related induced polar moments in the vicinity of the AlO_x/STO and LAO/STO interfaces.

An anomalous origin of the induced polar moments is also suggested by the unusual training and hysteresis effects of the gate-field loops of the R-mode splitting in the right panels of Fig. 6.2.1(a),(b). Its onset field during the first cycle (starting from the pristine state after cooling in zero field) is strongly dependent on the sign of the variation of V. This is shown in the top-right panel of Fig. 6.2.1(a) where no R-mode splitting occurs as the voltage is first increased to +8 kV/cm, whereas it starts to develop around +2 kV/cm as the gate voltage is subsequently reduced. For the opposite cycle in the top-right panel of Fig. 6.2.1(b), the R-mode splitting develops right away as the voltage is ramped to -V. Note that these highly asymmetric polarization and hysteresis loops are markedly different from the ones of bulk STO, for which a ferroelectric order with a symmetric hysteresis loop is induced above a threshold of about $\pm$2 kV/cm [54].

Complementary information about the interfacial polar moments has been obtained from a related phonon anomaly at the longitudinal optical (LO_4) edge of STO around 800 cm^{-1} that is shown in Fig. 6.2.1(c). It arises from a transverse optical (TO) mode that is induced by the polar distortion and is infrared active only in the direction parallel to ***P*** (details are given in the appendix B).

Near such an LO edge, the ellipsometric response is sensitive to both the horizontal and the vertical components of the dielectric function [268, 135, 137]. Accordingly, the analysis of this LO_4 anomaly yields further information about the vertical component of ***P*** (in addition to the one from the R-mode splitting on the horizontal component). Figure 6.2.1c reveals that the LO_4 edge anomaly cannot be reproduced if ***P*** is predominantly laterally orientated with $\boldsymbol{P}_{ab} >> \boldsymbol{P}_c$ (dashed dark blue line), whereas it is well described assuming that ***P*** is oriented along a diagonal with respect to the surface normal with $\boldsymbol{P}_{ab} = \boldsymbol{P}_c$ (dashed purple line).

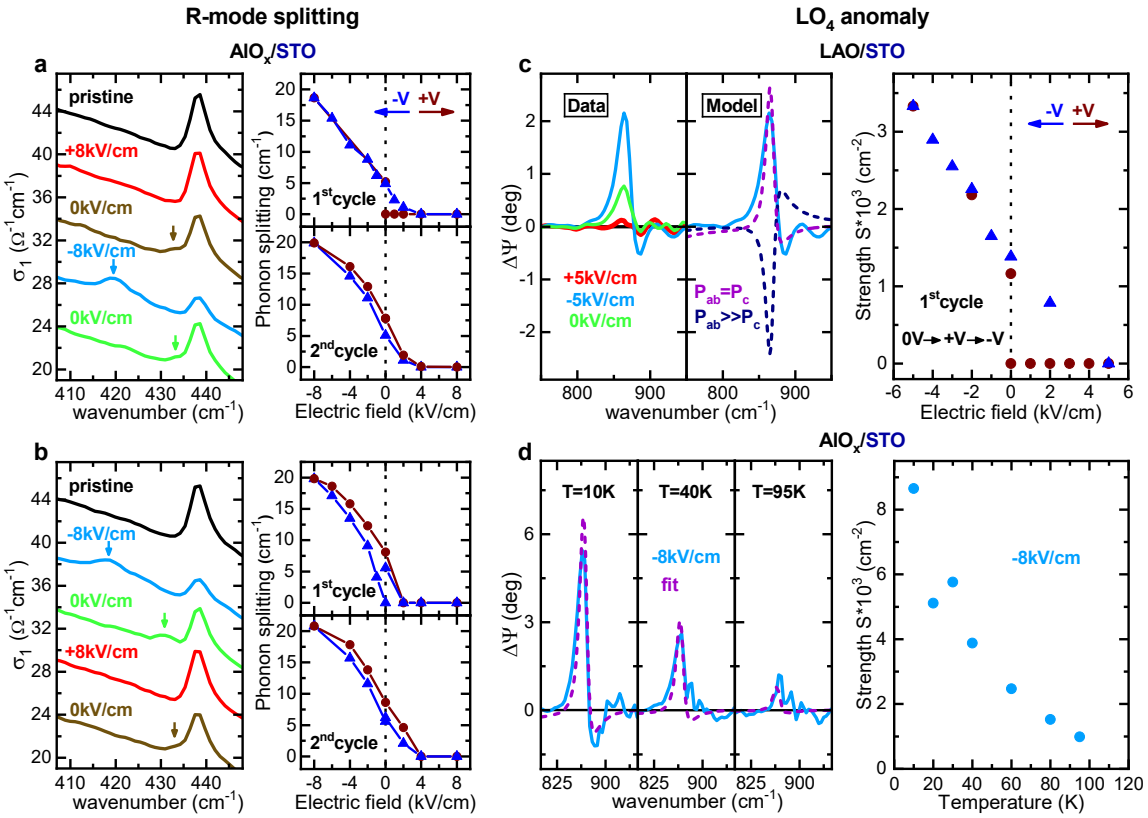

Figure 6.2.1 Infrared ellipsometry study of phonon anomalies due to the electric-field-induced polar moment. ***(a)*** *Spectra of the optical conductivity, σ_1, showing the asymmetric R-mode splitting due to $\boldsymbol{P}_{ab}$ for gate-voltage cycles from 0V to +V to -V (left panel) and the corresponding hysteresis loops (right panel) for the magnitude of the R-mode splitting (and thus of $\boldsymbol{P}_{ab}$) at 10 K.* ***(b)*** *Spectra and hysteresis loops of the R-mode splitting for the reverse voltage cycling direction, i.e. from 0V to -V to +V.* ***(c)*** *LO_4 anomaly. Left panel: The difference spectra of the ellipsometric angle $\Delta\Psi=\Psi_{exp} - \Psi_{0V,\ pristine}$ at the longitudinal optical LO_4 edge show the signatures of an infrared-active TO mode that is induced at -V. This new TO mode can only be modeled by assuming a polarization with a sizeable vertical component (dashed purple), instead of a polarization of pure horizontal character (dashed dark blue). Right panel: Corresponding voltage loops of the oscillator strength, S, of the field-induced TO mode.* ***(d)*** *Temperature dependence of the LO_4 anomaly. Left panel: Spectra of the field-induced TO mode (cyan) together with the fit (dashed purple) at selected temperatures. Right panel: Temperature dependence of S for the field-induced TO mode (at -8kV/cm).*

The right panel of Fig. 6.2.1(c) displays the gate-field loop of the amplitude of the transverse mode at the LO_4 edge, as obtained with the diagonal polarization model ($\boldsymbol{P}_{ab} = \boldsymbol{P}_c$), which shows a similarly asymmetric behavior as the R-mode splitting in the top-right panel of Fig. 6.2.1(a). This confirms the common origin of these phonon anomalies and suggests that the underlying polar moments are

strongly (but not fully) inclined toward the interface. A likely scenario is that ***P*** is directed along a diagonal with respect to the Ti-O bonds (or the surface normal), similar as in orthorhombic or rhombohedral bulk $BaTiO_3$ [269].
Finally, Fig. 6.2.1(d) displays the temperature dependence of the LO_4 edge anomaly which shows that the interfacial polar moments persist to much higher temperature than the field-induced ferroelectric order in bulk STO [54] and vanishes along with the AFD domain boundaries near $T^* = 105$ K.

III. Oxygen vacancy clustering scenario

A scenario which can account for the above described asymmetric and non-collinear interfacial polar moment, ***P***, and its close link with the AFD domain boundaries of STO is sketched in Fig. 6.2.2. Here, the positively charged oxygen vacancies are assumed to migrate in response to the gate voltage, whereby they get trapped and cluster at the AFD domain boundaries. The latter act as extended pinning centers that are strengthened (weakened) at -V (+V).
In the pristine state (before the gate voltage is applied), the oxygen vacancies are more or less randomly distributed in the vicinity of the interface and probably weakly pinned at some local defects (see Fig. 6.2.2(b)). A positive gate voltage (+V) pushes the positive oxygen vacancies toward the interface (see Fig. 6.2.2(c)). It also increases the concentration and thickness of the 2DEG layer, which thus screens most of the oxygen vacancies and prevents the formation of extended clusters and subsequent polar moments close to the interface. Accordingly, as shown in Fig. 6.2.2(c), the induced polarization at large +V has a predominant vertical orientation and develops only at a rather large distance from the interface that exceeds the probing depth of the infrared ellipsometry experiment (of about one micrometer, as shown in Fig. 3.1.1). Note that whereas the majority of the confined electrons reside within a few nanometers from the interface [270], their depth profile has a long tail that can extend over hundreds of nanometers (especially at +V) [271, 272] due to the large dielectric constant of STO.
As the gate voltage is subsequently reduced toward -V, the 2DEG becomes depleted and its thickness decreases. Hence, the positive oxygen vacancies, as they start moving away from the interface, get trapped at the AFD domain boundaries which thus become charged and give rise to local electric fields and induced polar moments with sizeable lateral components (see Fig. 6.2.2(d)) that are close to the interface and thus readily seen in the infrared ellipsometry spectra. Note that an additional contribution to these local fields may arise from the flexoelectric behavior of STO that is strongly enhanced by the large low-temperature dielectric constant [75]. As shown in Fig. 6.2.2(e)-(g), the clustering of the oxygen vacancies causes an increase of the lattice parameter [63] and a subsequent strain gradient across the AFD domain boundaries. The latter creates a flexoelectric field, $\boldsymbol{E}^{flexo}$, which is parallel to the Coulomb-field, $\boldsymbol{E}^{Coul}$, and therefore helps to induce interfacial polar moments that are strongly asymmetric and non-collinear with respect to the applied gate field. Note that at large -V the 2DEG may also become laterally inhomogeneous [273] and thus may further enhance the above described local electric fields (see the appendix B).
As shown in Fig. 6.2.2(d), the direction of the induced polar moments depends on the type of domain boundaries, i.e. ***P*** is mainly laterally oriented for the boundaries between the x- and y-domains (denoted as x/y-boundaries) whereas it is at 45 degrees with respect to the surface normal ($\boldsymbol{P}_{ab} \approx \boldsymbol{P}_c$) for the x/z- and y/z-boundaries [59]. The above described results therefore suggest a preferred clustering of the oxygen vacancies at the x/z- and y/z-boundaries.

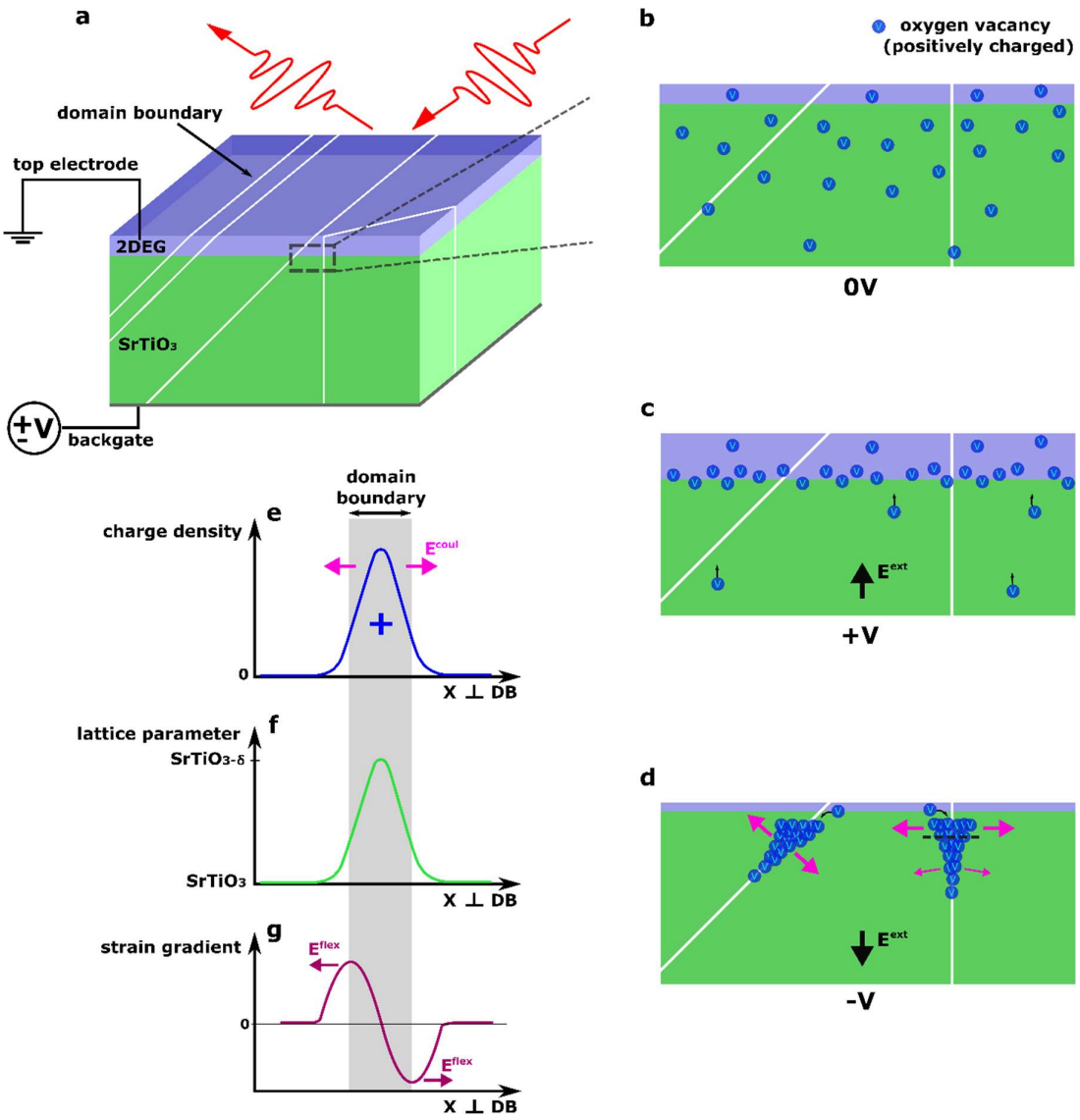

Figure 6.2.2 Sketch of a field-gated STO-based heterostructure, showing the electromigration of oxygen vacancies and their clustering at the AFD domain boundaries, which gives rise to the anomalous horizontal polarization, P_{ab}, at -V. (a) *Sketch of the heterostructure and its gating between the 2DEG and a silver contact on the backside of STO. The white lines show the AFD domain boundaries that appear at $T < T^*$.* ***(b)*** *Magnified view of the 2DEG (purple) and the distribution of the positively charged oxygen vacancies (blue) in the vicinity of the interface in the pristine state at 0V.* ***(c)*** *A positive gate voltage +V pushes the positive oxygen vacancies towards the interface and thereby induces a polarization and an electric field (magenta arrows) that is perpendicular to the interface, i.e. $P_c > 0$. Note that the additional contribution due to the electric-field-induced ferroelectric polarization of bulk STO is not shown (this is also valid for (d)).* ***(d)*** *At -V the oxygen vacancies are pulled away from the interface and get preferably trapped at the AFD domain boundaries. The resulting electric charging and the flexoelectric effect induced by the strain gradients due the oxygen clustering create a polarization with a large horizontal component, P_{ab}, which is strongest close to the interface.* ***(e,f,g)*** *Cross-section of a domain boundary at -V (black dashed line in d). The accumulated, positively charged, oxygen vacancies create an electric field E^{coul}* ***(e)*** *as well as and an expansion of the lattice parameter of $SrTiO_3$* ***(f)****. This induces a strain gradient* ***(g)*** *and thus strong flexoelectric fields E^{flex}, which are perpendicular to the domain boundaries.*

IV. Raman spectroscopy

Complementary information on the gate-voltage-induced polar moments has been obtained with confocal Raman spectroscopy, which has a larger probe depth than infrared ellipsometry and enables scans of the polarization depth profile [148, 50].

Figure 6.2.3(a) shows a sketch of the Raman experiment performed in grazing incidence geometry with the sample mounted on a wedged holder. The red laser beam (λ = 633 nm) is incident at 70° to the surface normal and the refracted beam inside STO with n ≈ 2 is near 30° [274, 48]. The electric field vector $\boldsymbol{\epsilon}$ of the light has therefore a sizeable (zero) vertical component in p-polarization (s-polarization).
Figure 6.2.3(b) shows the Raman spectra of AlO_x/STO at 10 K with incoming p-polarization at 0 V and ±4 kV/cm. The background with several broad maxima, arising from multi-phonon excitations, is characteristic for STO (e.g. [256, 275, 65]) and hardly affected by the gate voltage. At 0 V (black line) the direct phonon excitations are due to R-modes at 15, 45, 144, 229 and 447 cm^{-1} (black stars) that become Raman-active below T^* = 105 K (the cubic phase has no Raman-active phonons) [256, 275, 255]. At ±4 kV/cm, several additional peaks develop around 25, 175, 540 and 795 cm^{-1} (green arrows) which correspond to the infrared-active TO_1, TO_2, TO_4 and LO_4 modes (the TO_3 peak at ⌣263 cm^{-1} is barely resolved) which are activated by a polar distortion which breaks the inversion symmetry [65]. Figure 6.2.3(c) magnifies the low-energy range with the TO_1 soft mode that exhibits the largest field-effect. The inset of Fig. 6.2.3(c) shows corresponding s-polarized spectra (normalized to the multi-phonon background) for which the soft mode intensity is significantly weaker.
Considering that the Raman intensity of the soft mode is expected to be maximal for $\boldsymbol{\epsilon} \parallel \boldsymbol{P}$ and minimal (but finite) for $\boldsymbol{\epsilon} \perp \boldsymbol{P}$, the polarization dependence in Fig. 6.2.3(c) is therefore consistent with the above described scenario of induced polar moments that are oriented along the diagonal (vertical) direction at -4 kV/cm (+4 kV/cm). Note that a quantitative analysis with respect to the orientation of $\boldsymbol{P}$ would require a much more extensive polarization study and a lateral scanning, as to resolve individual domains with different orientation of $\boldsymbol{P}$, which is beyond the scope of this study.

Next, we discuss the depth dependence of the soft mode intensity at ±4 kV/cm in Figure 6.2.3(d). At +4 kV/cm, the soft mode intensity shows only a weak variation that agrees with the scenario of a vertical and laterally homogeneous polarization that extends deep into the STO substrate (see Fig. 6.2.2(c)). Close to the interface, where the ellipsometry spectra indicate the absence of polar moments since they are screened by the enhanced 2DEG layer, the soft mode intensity exhibits indeed a clear decrease. The circumstance that this decrease is only partial can be understood in terms of the probe depth of the confocal Raman experiment, which is of the order of several micrometers and therefore larger than for infrared spectroscopy.
The corresponding depth scan at -4 kV/cm highlights a remarkably different trend. Here, the soft mode intensity is strongly enhanced at the interface but decreases rapidly toward the bulk of STO, where it becomes comparable to the one at +V. Similar soft mode intensities at ±V in the bulk of STO are also seen in a conventional macro-Raman experiment that probes deep into the STO substrate. These characteristic differences in the depth profile of the gate-voltage-induced polarization agree with the scenario sketched in Fig. 6.2.2(d). At -V, the polar moments close to the interface are strongly enhanced by the local fields due to the charged and flexoelectric AFD domain boundaries and, in addition, are barely screened by the depleted 2DEG.

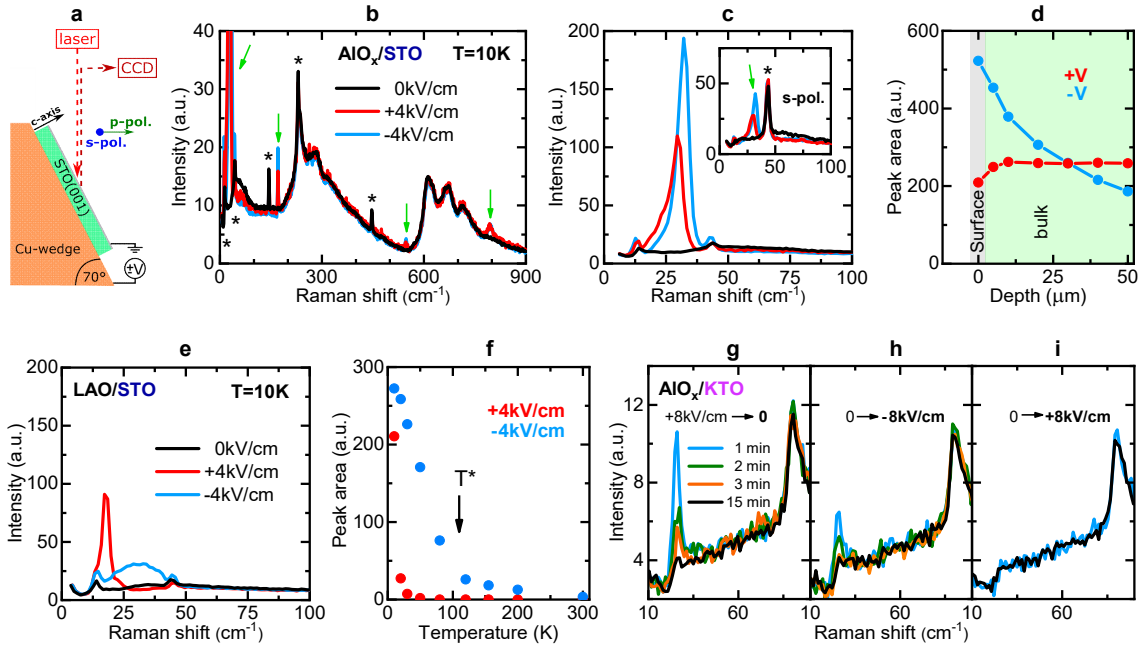

Figure 6.2.3 Confocal Raman study of the induced polar moment, as a function of gate voltage, distance from the interface, and temperature. ***(a)*** *Sketch of the measurement geometry.* ***(b)*** *Gate-voltage dependent spectra of an $AlO_x/SrTiO_3$ heterostructure at 10 K. A Stokes/Anti-Stokes comparison yields a temperature offset of max. ~20 K, caused by laser heating. Black stars mark the R-modes at 15, 45, 144, 229 and 447 cm^{-1} that become Raman-active below T* = 105 K. Green arrows show the field-induced infrared-active phonon modes at 25, 175, 540 and 795 cm^{-1}.* ***(c)*** *Magnified view of the field-induced soft mode (TO_1) and its asymmetry with respect to ±V. Inset: Corresponding spectra taking in s-polarization (normalized to the multi-phonon background).* ***(d)*** *Depth profile of the normalized peak area of the soft mode for +V and -V.* ***(e)*** *Field-dependence of the soft mode of an LAO/STO structure.* ***(f)*** *Temperature dependence of the peak area of the soft mode for +V and -V.* ***(g-i)*** *Low-frequency Raman spectra of an $AlO_x/KTaO_3$ heterostructure, showing a weak and rapidly decaying (within minutes) soft mode signal that occurs only after the voltage has been decreased, i.e. either from +V to 0V* ***(g)*** *or from 0V to -V* ***(h)****, but is absent after a corresponding voltage increase from 0V to +V* ***(i)*** *or from -V to 0V (not shown).*

Figures 6.2.3(c) and 6.2.3(e) show a comparison of the gate-voltage-induced Raman soft modes of the AlO_x/STO and LAO/STO heterostructures. Whereas the field-induced soft mode peaks are similar for both samples at +4 kV/cm (red curves), they are dramatically different at -4 kV/cm (cyan curves) where the peak is much stronger and sharper in AlO_x/STO than in LAO/STO. This trend can be understood in terms of the higher oxygen vacancy concentration in AlO_x/STO, which gives rise to larger clusters at the AFD domain boundaries and, correspondingly, to larger local electric fields. The mobility of the oxygen vacancies might also depend on the strain that is imposed by the top layer. For the amorphous AlO_x layer, the strain is weakly tensile and thus more favorable for creating large oxygen vacancy clusters than the strongly compressive strain of the epitaxial LAO layer.

Another difference between the induced polarizations at ±4 kV/cm is evident in Fig. 6.2.3(f) from the temperature dependence of the Raman soft mode intensity (here shown for LAO/STO). At +4 kV/cm, the soft mode intensity decreases rapidly and vanishes above 40 K, in accordance to the the electric-field-induced ferroelectric order in bulk STO [54]. The soft mode at -4 kV/cm, however, persists to about T^* = 105 K where it vanishes together with the AFD domain boundaries. The weak signal above T^* arises most likely from remnant AFD surface domains that persist well above T^* [70].

Figures 6.2.3(g)-(i) show a corresponding Raman study of an $AlO_x/KTaO_3$ (001) heterostructure which corroborates the central role of the AFD domain boundaries in the above described interfacial polarization phenomena of the STO-based structures. KTO is also a quantum paraelectric with a diverging ε_0 at low temperature, albeit not as close to the ferroelectric critical point as STO [93, 276]. Unlike STO, the structure of KTO remains cubic down to the lowest temperature such that in the quantum paraelectric regime it has no AFD domains. The KTO-based devices also host a 2DEG [103-106, 277] that can be readily modified with a back-gate voltage, although with less pronounced carrier localization effects at -V than in the STO devices [110]. Figures 6.2.3(g)-(i) show that in the Raman spectra of AlO_x/KTO the back-gate voltage induces only a weak and short-lived soft mode peak. The metastable soft mode vanishes within minutes and has a similar intensity in s- and p-polarization (see appendix B). Importantly, the induced peak appears only after the gate voltage has been decreased, i.e. after reducing the field from +8 kV/cm to 0 V or from 0 V to -8 kV/cm, but not after an increase from -8 kV/cm to 0 V or from 0 V to +8 kV/cm.
This behavior is consistent with the oxygen vacancies becoming weakly pinned by some local defects, which, unlike the AFD domain boundaries of STO, are not extended and oriented along a particular direction. In return, this highlights the central role of the AFD domain boundaries for the strongly asymmetric and non-collinear polarization behavior of the STO-based devices.

V. UV illumination

Figure 6.2.4 demonstrates that the anomalous interfacial polarization of an AlO_x/STO device can be readily modified with other external stimuli, such as UV light. Figure 6.2.4(a) reveals that the splitting of the R-mode in the ellipsometry spectra at -8 kV/cm (cyan line) can be fully suppressed upon UV illumination (violet line) and remains almost completely absent even after the UV light has been switched off (orange line). The original R-mode splitting can be restored by cycling the gate voltage to +8 kV/cm (red line) and then back to -8 kV/cm (dark blue line). Figure 6.2.4(c) confirms that the same kind of optical 'switch-off' effect occurs for the gate-field-induced anomaly at the LO_4 edge. The underlying mechanism indicate that photo-generated charge carriers (across the band gap of STO) enhance the population of the 2DEG and thus make the screening of the oxygen vacancy clusters more efficient. Figures 6.2.4(b) and 6.2.4(d) demonstrate that the UV light can also erase the remnant polarization (and thus the memory) at 0 V after a complete electric field cycle.

We expect that this demonstration of an electric 'switch on' and optical 'switch off' mechanism of the interfacial polarization is only one of potentially many examples of how the local and extended defects of STO and their interplay with the 2DEG can be used for engineering STO-based devices with improved or new functionalities (see e.g. Ref. [278]). Further promising candidates are external pressure, internal strain, chemical substitution, doping and different surface cuts of STO.

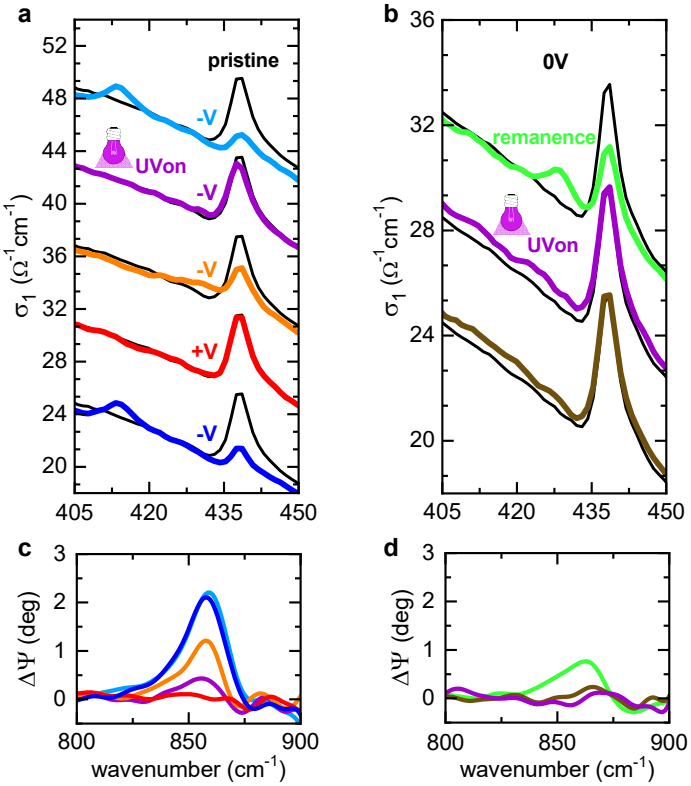

Figure 6.2.4 Optical switching of the anomalous polarization in $AlO_x/SrTiO_3$ at 10 K. (a) *Infrared spectra showing that the pronounced R-mode spitting at -8 kV/cm (cyan) can be erased by UV illumination (violet) and is only partially restored after the illumination (orange). The original R-mode splitting is restored after a field cycle to +8 kV/cm (red) and back to -8 kV/cm (blue).* ***(b)*** *Infrared spectra at 0V showing that the remnant R-mode splitting (green) is erased by the UV light (violet) even after it has been turned off again (brown).* ***(c,d)*** *Corresponding infrared spectra of the polarization induced TO mode at the LO_4 edge. Shown are the difference spectra with respect to the pristine state at 0V, i.e. $\Delta\Psi=\Psi_{exp}-\Psi_{0V,\,pristine}$. The data are smoothened with a FFT filter.*

VI. Conclusions

In summary, with infrared ellipsometry and confocal Raman spectroscopy we have shown that electric back-gating of LAO/STO and AlO_x/STO heterostructures gives rise to interfacial polar moments that are non-collinear and strongly asymmetric with respect to the vertical gate field. Our results provide evidence for an important role of oxygen vacancies which tend to form extended clusters at the AFD domain boundaries that give rise to electric charging and flexoelectric effects. The subsequent interfacial polar moments with large horizontal components are induced at lower gate voltages and persists to much higher temperatures than in bulk STO.

The training and hysteresis effects due to these anomalous interfacial polar moments are reflected in the magneto-transport properties of related devices [111, 2]. However, since the laterally inhomogeneous polarization effects tend to be cancelled out in vertical structures, their real potential can only be exploited with lateral device structures. The control of the AFD domain boundaries and their interaction with the oxygen vacancies likely enables new device concepts and functionalities. Recently, there have indeed been great advances in patterning ferroelectric domains [279], which may also be effective in STO due to its polar nature.

Acknowledgments

F.L. and C.B. acknowledge enlightening discussions with S. Das, J. Maier, R. Merkle, A. Dubroka, and B. I. Shklovskii. Work at the University of Fribourg was supported by the Schweizerische Nationalfonds (SNF) by Grant No. 200020-172611. M.B. acknowledges support from the ERC Advanced grant n° 833973 "FRESCO" and the QUANTERA project "QUANTOX". GH acknowledges financial support from Spanish Ministry of Science, Innovation and Universities, through the "Severo Ochoa" Programme (CEX2019-000917-S) and the MAT2017-85232-R (AEI/FEDER, EU) projects, and Generalitat de Catalunya (2017 SGR 1377).

6.3 Comments and Outlook

We have presented a study on the electric field effect on $SrTiO_3$- and $KTaO_3$-based heterostructures by means of infrared ellipsometry and confocal Raman spectroscopy. For all $SrTiO_3$ samples, we observed an anomalous electric field modulation that is non-collinear and asymmetric with respect to the applied back-gate voltage, as well as strongly remnant and hysteretic. Since the effect only occurs in the tetragonal state of $SrTiO_3$ ($T < T^*$) and is absent for the $KTaO_3$ samples (which remain cubic at all temperatures), we attribute this ferroelectric- and possibly flexoelectric behavior to an interplay of oxygen vacancies and the tetragonal domain boundaries which serve as extended pinning centers. We also demonstrated an optical switching mechanism of this anomalous interfacial polarization that is based on the illumination with UV light.

Several key aspects need to be addressed in future work to shine more light onto the mechanism of this anomalous electric-field-induced polarization, which include revealing the interplay of ferroelectric and flexoelectric orders. For instance, it will be important to determine the role of the induced strain gradient in the domain boundaries at negative back-gate voltages and the resulting flexoelectric fields. In order to verify this flexoelectricity scenario, other technical approaches might be more suitable than the optical techniques used in this thesis, such as high harmonic generation or x-ray diffraction. In the following, two research topics are chosen to be outlined for further confocal Raman and infrared spectroscopy studies.

Domain-behavior under electric fields

The mechanism underlying this anomalous polarization might be even more complex than has been believed up to now. Further confocal Raman spectroscopy measurements are providing evidence that the orientation of the tetragonal domain (i.e. the C_4-axis) could play a crucial role (see Fig. 6.3.1). The R-modes, located at 15, 45 and 144 cm^{-1}, appear only in the tetragonal state of $SrTiO_3$ and are reliable indicators for labelling the type of domain which is studied. Figure 6.3.1 shows the electric-field-induced modes (magenta and green arrows) for positive voltages, which are depending on the structural domain orientation and reveal a field-induced in-plane anisotropy. The second mode (green) is not emerging when rotating the polarization of the laser light by 90 degrees in the 1st and 2nd domain, and is completely absent in the 3rd domain.
In future work, this domain-dependent polarization needs to be investigated in detail for different voltage magnitudes (and especially negative voltages). The confocal Raman spectroscopy setup can be used to perform a mapping of the different polarization states, which can also yield information on the domain-(wall) size and behavior under electric field back-gating.

Up to now, solely $SrTiO_3$(001) samples were studied. In order to obtain more information on the electric field effect on the structural domains, comparable heterostructures of STO(110) substrates need to be investigated, for which the domain state can be more easily controlled by applying external pressure [55]. Depending on the pressure direction, one can switch from a polydomain state to a monodomain state and in this way erase all domain boundaries, which as a consequence, should suppress the polarization state. The application of mechanical pressure would therefore present an additional control parameter for these types of polarization effects.

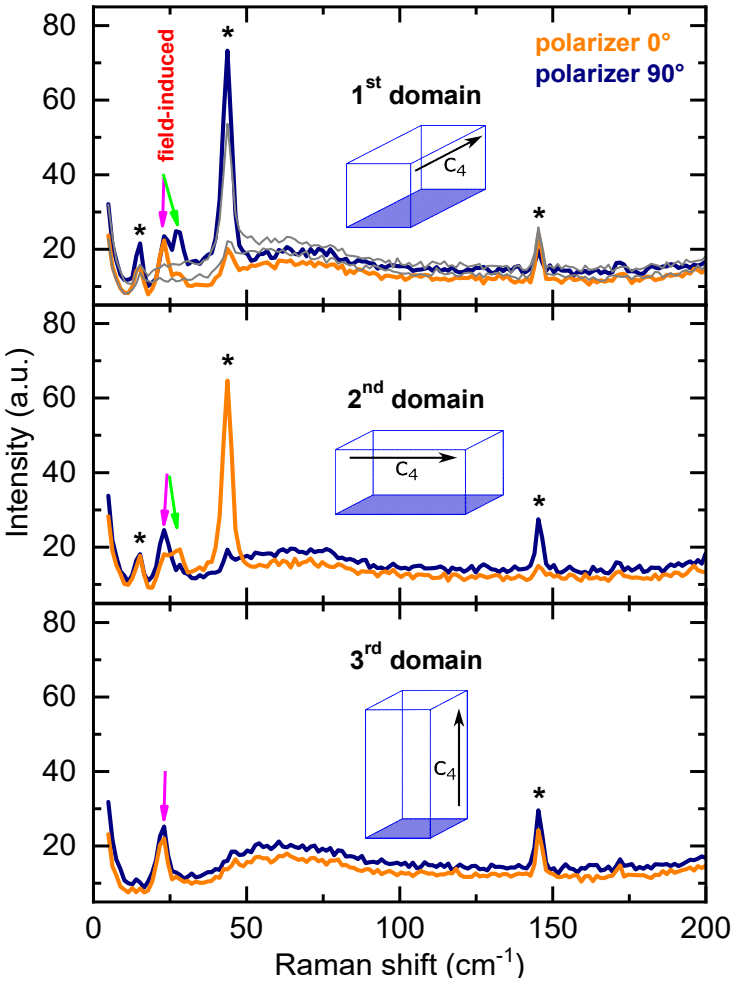

***Figure 6.3.1 Domain-dependent polarization effects in LAO/STO heterostructures**. The spectra are obtained by normal-incidence confocal Raman spectroscopy at +6 kV/cm. The thin gray lines in the upper panel represent the spectra taken at zero Volt, for both polarizer settings. The R-modes are indicated by black stars.*

Towards device fabrication from untreated $SrTiO_3$ crystals

Especially appealing for technological purposes are AlO_x/STO samples, since they are much easier to fabricate than the LAO/STO structures. They could be used e.g. for designing nanowires, in which the in-plane polarization might play a crucial role.

In addition to these heterostructures, we observed comparable polarization effects in pristine, non-conducting $SrTiO_3$ (001) crystals, which have been illuminated with UV light prior to electric field-gating (see Fig. 6.3.2). The UV light, which has a higher energy than the bandgap of STO, generates electron-hole pairs and was previously shown to create a conducting surface layer (e.g. [101]). In analogy to the $SrTiO_3$-based heterostructures, a subsequent illumination with UV light fully restores the original state (brown). Further research in this direction, such as a study of using light with energies below and above the bandgap of STO, will provide further information on to what extent this illumination can be utilized for manipulating the properties of these materials.

This paves a new way of fabricating and *in-situ* tuning of high-mobility devices, with simple material ingredients such as bare substrates and by means of using 'only' light.

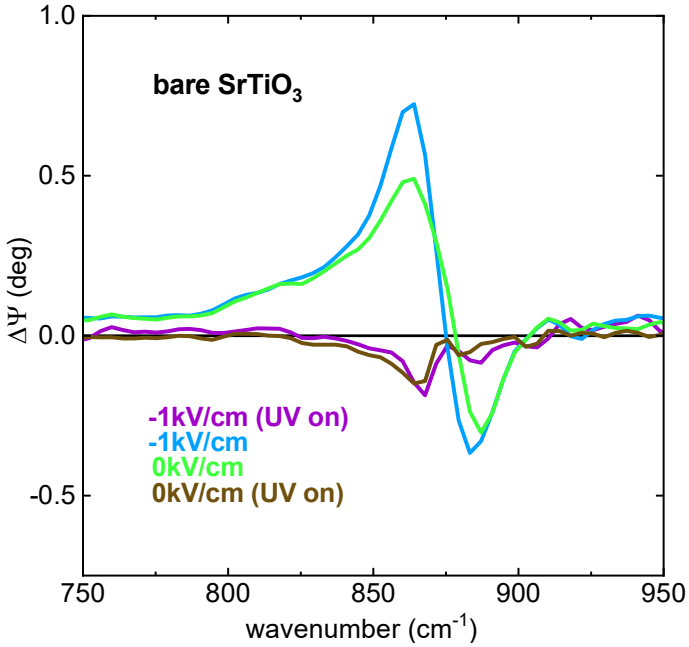

Figure 6.3.2 Electric-field-induced polarization in UV-light-treated pristine $SrTiO_3$ crystals. *Shown are the difference spectra of the ellipsometric angle $\Delta\Psi=\Psi_{exp} - \Psi_{0V,\,UVon}$ at the longitudinal optical LO_4 edge, measured by infrared ellipsometry. The field-induced TO mode can also be seen in a pristine $SrTiO_3$ substrate, which is prior illiminated with UV light. The remnant state (green) can be erased by illumination with UV light (brown), in analogy to the $SrTiO_3$-based heterostructures.*

Chapter 7

Summary and Conclusion

In this thesis, a collection of various complex oxide systems, including both bulk and thin film structures, has been investigated with advanced infrared and Raman spectroscopy techniques. The obtained results have an impact on several topics in this research field.

We studied the infrared response of underdoped bulk $YBa_2Cu_3O_{6.6}$ when exposed to high magnetic fields up to 30 Tesla and compared these results with the temperature-dependent spectra. We have found a complete suppression of the macroscopic superconducting response above 20 Tesla, with surprisingly small changes in the optical spectra up to 30 Tesla. In particular, the magnetic field suppresses a small amount of the Drude term (i.e. the free carriers in the normal state) by about 3 % at 30 Tesla, which is compensated by an enhancement of the electronic modes at 240 cm^{-1} and 90 cm^{-1} and of the mid-infrared band. The electronic modes were interpreted as pinned phase modes of the CDW and the enhancement of the MIR-band as electronic excitations across the CDW gap. These features are readily seen at higher temperatures, for a wide doping range and even at zero magnetic field, which leads to the conclusion that the relationship between superconductivity and the charge ordering is not purely competitive.

In another project, we have observed backfolded acoustic phonons for the first time in metal-oxide superlattices by means of confocal Raman spectromicroscopy, and have demonstrated the modes' immense potential as a reliable characterization tool for, in principle, any type of superstructures. These modes are not affected by the substrate and are highly sensitive to atomic-scale variations of the bilayer thickness. Hence, they yield important information on the sample quality, the speed of sound within the material, and potentially on the coupling of sound waves to spin, charge and orbital dynamics.

Finally, the electric field effect on $SrTiO_3$- and $KaTiO_3$-based heterostructures was explored using a unique combination of infrared ellipsometry and confocal Raman spectroscopy. We have observed a large electric field modulation in the $SrTiO_3$ samples. In particular, the electric-field-induced polarization is non-collinear with respect to the applied electric field, highly asymmetric and exhibits a remanence and a hysteresis. These observations were explained by an interplay of the oxygen vacancies and the tetragonal domain boundaries in $SrTiO_3$, yielding ferroelectric and flexoelectric fields. Indeed, these anomalous polarization effects are not observed in the corresponding $KaTiO_3$-heterostructures, for which the tetragonal domain boundaries are absent. In addition, we have demonstrated that illumination with UV light restores the original state, and thus can serve as an 'optical switch' that could be readily used for technological applications.

These results will be relevant for the growing research fields of oxide electronics and domain wall nanoelectronics, where the control of the interaction of extended defects and oxygen vacancies can enhance the performance of oxide devices and give rise to new functionalities.

The presented work has also demonstrated the state of the art capabilities of infrared and Raman spectroscopy as suitable diagnostics for investigating the low-energy dynamics in complex oxides.

Even though these complementary techniques are well-established characterization tools for exploring the bulk and interface properties of solid state samples, they have rarely been used in this combination

of external and internal conditions, e.g. high magnetic/electric fields or heterostructures, as was done in this thesis.
These complex measurements with a high signal-to-noise ratio and a sufficiently high spectral resolution enabled the study of specific phononic and electronic excitations in the material. The investigation of the phases that compete in the ground state by using optical spectroscopy lead to a better understanding of the macroscopic effects observed in these oxide materials.

For future pathways to explore quantum materials, a next step could involve the combination of the experimental methods used in this thesis.
The confocal Raman microscope was used to perform a mapping of the backfolded acoustic phonons in metal-oxide superlattices but it could equally serve to image the domain-dependent polarization states in $SrTiO_3$-based heterostructures. A similar type of mapping via conventional infrared spectroscopy is not possible because of the lateral spatial resolution, which is limited by the wavelength of the infrared light and is on the order of hundreds of micrometers to millimeters. These limitations, however, could be overcome by means of s-SNOM (***s**cattering-type **s**canning **n**ear-field **o**ptical **m**icroscopy*), which allows to probe the optical response with a spatial resolution of 10-20 nm [280]. This method operates in a similar manner as TERS (which was described in subsection 3.2.4): In s-SNOM, an atomic force microscope tip is illuminated with infrared light, instead of the visible laser light of a Raman spectrometer. A downside in using this not yet established modern technique is that the interpretation of the obtained data is complex.
Another interesting project would be to explore the magnetic field effect on the $SrTiO_3$ and $KTaO_3$ samples. As presented in this work, our electric field study indicates that the induced polarization at negative back-gate voltages arises from the electromigration of oxygen vacancies and their pinning at the tetragonal domain boundaries. Therefore, an external magnetic field is expected to also induce a movement of the carriers and thus to yield similar observations. This type of measurement could be carried out at the LNCMI in Grenoble, France, in order to study the infrared and Raman response at magnetic fields up to 30 Tesla.

The author of this thesis hopes that these scientific findings and experimental approaches will encourage other groups and future PhD students to pursue further research in the field of oxide science, and on other material families, by means of optical spectroscopy.

Appendix A

High-frequency extrapolation of the $YBa_2Cu_3O_{6.6}$ crystal

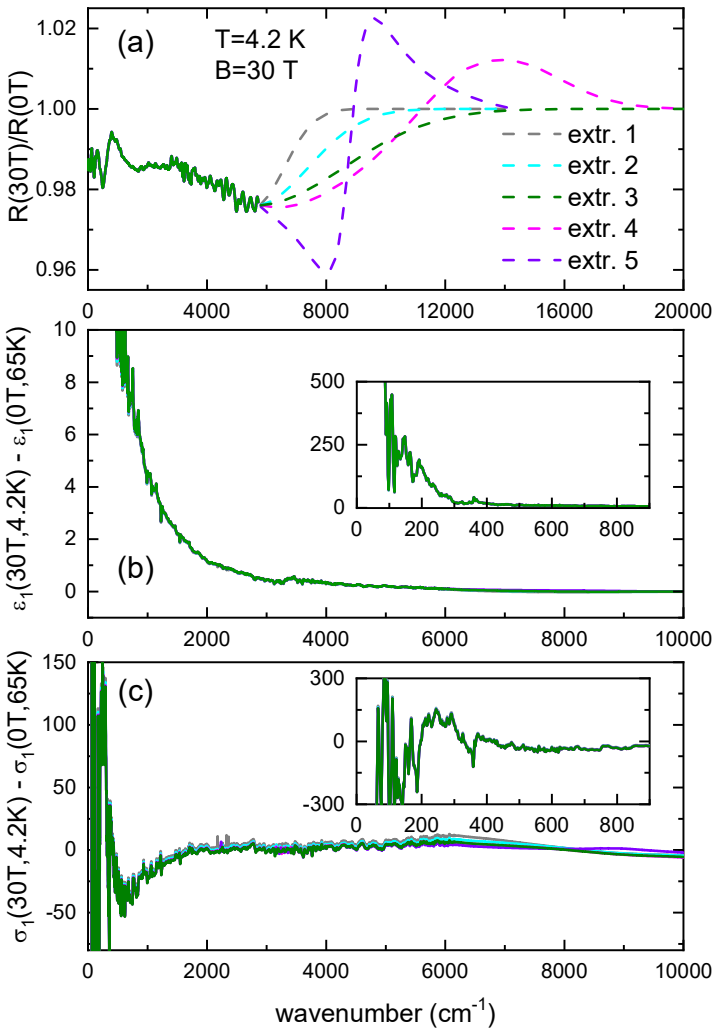

Figure A.1 Impact of the high energy extrapolation on the low-frequency properties of the $YBa_2Cu_3O_{6.6}$ crystal. ***(a)*** *Possible extrapolations for the high-energy side of the magnetic-field-dependent data. In order to perform a Kramers-Kronig transformation, we assumed that the off-diagonal terms of the dielectric function tensor are relatively small and can therefore be neglected.* ***(b), (c)*** *The choice of the extrapolation does not lead to significant differences for the low-energy region of the spectra, as can be seen in the difference plots $\Delta\varepsilon_1$ and $\Delta\sigma_1$.*

Appendix B

Supplementary information on $SrTiO_3$- and $KTaO_3$-based heterostructures

Zero field infrared response of bulk $SrTiO_3$

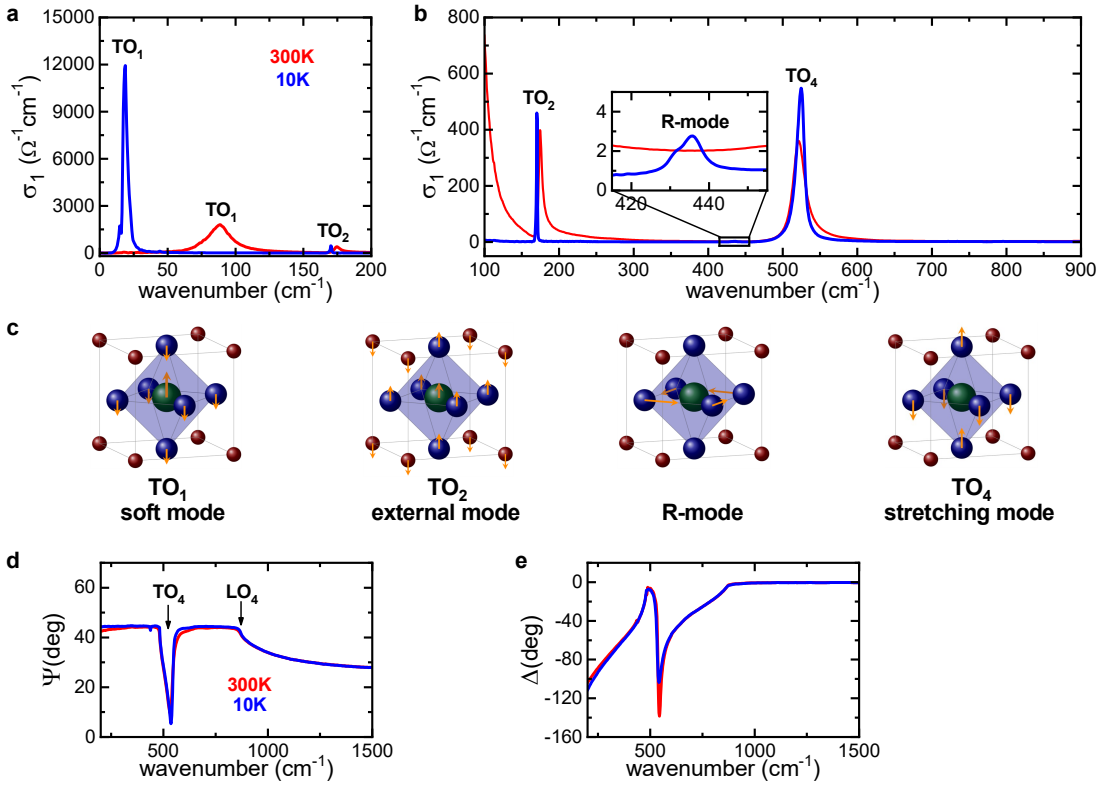

Figure B.1 Temperature-dependent infrared spectra of bulk $SrTiO_3$ at zero electric field. *The data have been obtained via a combination of normal incidence reflectivity and spectroscopic ellipsometry (at an incidence angle of 80 degrees).* ***(a), (b)*** *Spectra of the real part of the optical conductivity σ_1 of $SrTiO_3$ at 300 K (red curve) and 10 K (blue curve), which are governed by four infrared-active phonon modes. The soft mode (TO_1, shown in (a)), softens and increases drastically in strength when cooling from 300 K to 10 K. The R-mode in (b) originates from the antiphase rotation of the neighboring oxygen octahedra. It develops only in the tetragonal state and thus below the antiferrodistortive (AFD) transition at $T^* \approx 105$ K.* ***(c)*** *Schematics of the atomic vibrations for the corresponding phonon mode (adapted from [52]). Note that the TO_3 mode is silent and therefore does not appear in the infrared spectra [256].* ***(d), (e)*** *Spectra of the ellipsometric angles Ψ and Δ showing the TO_4 mode and the corresponding LO_4 edge at which the real part of the dielectric function crosses zero.*

Polar distortion and the R-mode splitting in infrared ellipsometry

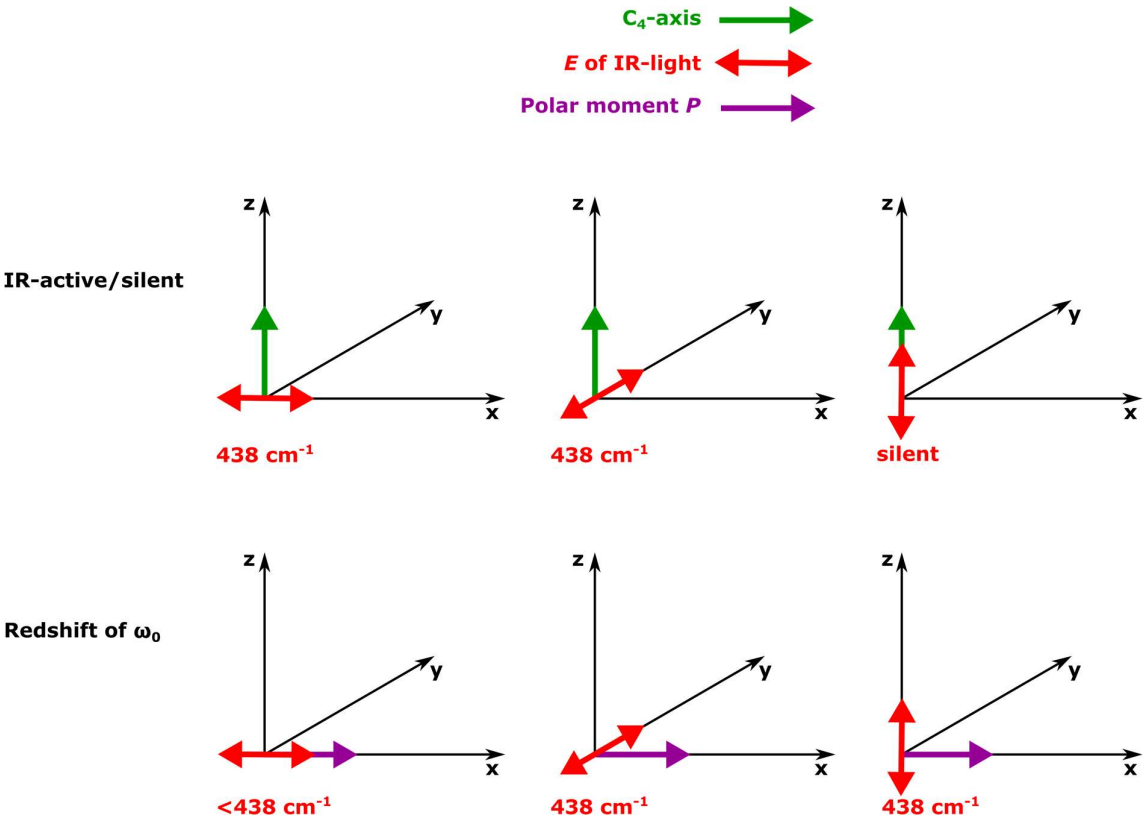

Figure B.2 Sketch of the dependence of the frequency and IR-activity of the R-mode on the orientation of the electric field vector E (red) with respect to the C_4-axis (green) and the polar moment P (purple).

The frequency and the IR-activity of the R-mode depends on the orientation of the polarization, ***P***, and the C_4-axis as follows (and sketched in Fig. B.2):

1. The R-mode at 438 cm^{-1} is IR-active only in the tetragonal state below $T^* = 105$ K and only if the light polarization vector, ***E***, is perpendicular to the tetragonal C_4-axis (upper panel of Fig. B.2).

2. The redshift of the eigenfrequency ω_0 of the R-mode occurs only for the component of the vibration that is parallel to the polar distortion, ***P***. The eigenfrequency ω_0 of the perpendicular components of the R-mode is not (or hardly) affected and remains at 438 cm^{-1} (bottom panel of Fig. B.2).

3. Despite the grazing angle of incidence of φ=75 degrees, the infrared ellipsometry response in the vicinity of the R-mode (i.e. well away from the LO_4 edge) is governed by the in-plane component of the dielectric function.

Consequently, there are three different possible scenarios:

<u>Scenario I</u>: *P* is parallel to the C_4-axis

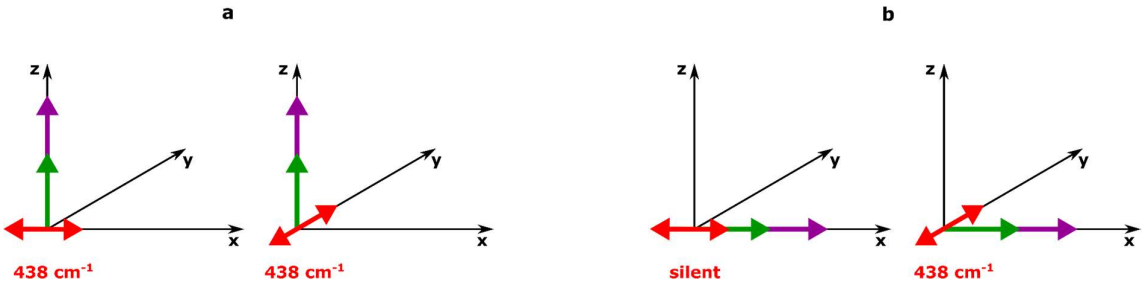

Figure B.3 Scenario I. *The polar moment* ***P*** *is parallel to the C_4-axis. Then,* ***P*** *and the C_4-axis can be either parallel (a) or perpendicular (b) to the z-axis of the crystal (or the surface normal). In both cases, no R-mode splitting can be seen.*

The above shown Scenario I thus demonstrates that the R-mode splitting can only be seen, if ***P*** has a sizeable component perpendicular to the C_4-axis. This is the case in the following Scenario II and III.

<u>Scenario II</u>: *P* is perpendicular to the C_4-axis

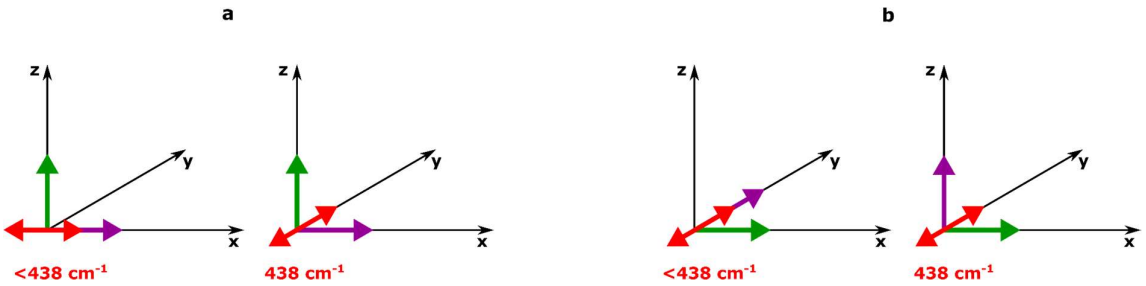

Figure B.4 Scenario II. *The polar moment* ***P*** *is perpendicular to the C_4-axis, which can be oriented out-of-plane (a) or in-plane (b). A softening of the R-mode can be observed only for the in-plane component of the polar moment $\boldsymbol{P}_{\parallel}$, whereas for the perpendicular component $\boldsymbol{P}_{\perp}$ it remains constant. The R-mode splitting occurs when both kinds of domains are present in the sample.*

<u>Scenario III</u>: *P* is along the diagonal direction

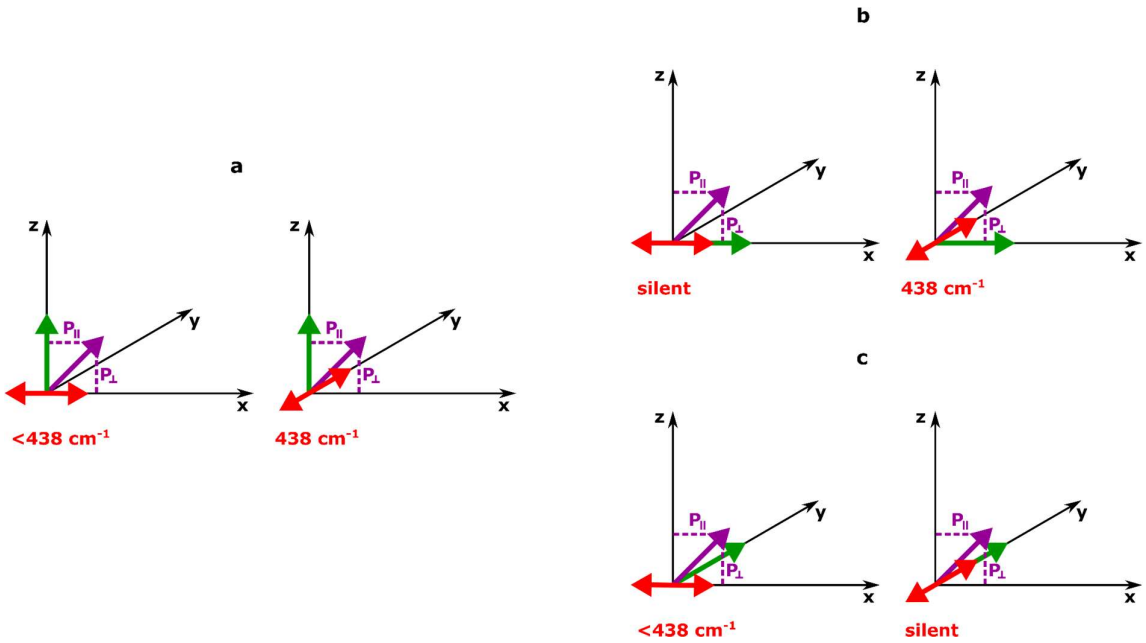

Figure B.5 Scenario III. *The polar moment **P** is along a diagonal crystallographic direction, where the C_4-axis is parallel (a) or perpendicular (b,c) to the z-axis. In all cases, a splitting of the R-mode occurs. Note that in (b,c), the R-mode splitting occurs via a mixture of domains.*

As a result, in both the Scenario II and the Scenario III, the R-mode splitting occurs due to the in-plane component of ***P***.

Theoretical Model of the LO_4 anomaly

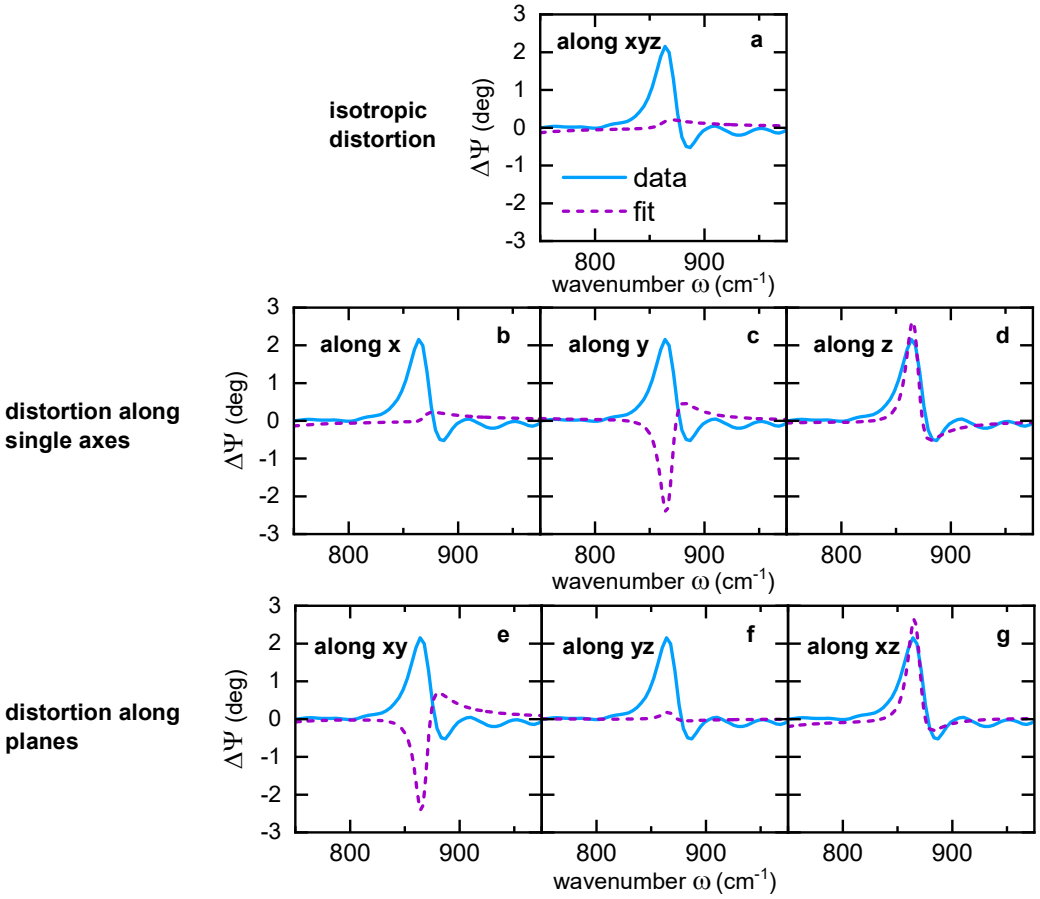

Figure B.6 Theoretical model to describe the gate-voltage induced LO_4 edge anomaly. *Shown are the difference plots of $\Delta\Psi=\Psi_{-5kV/cm} - \Psi_{0V,\ pristine}$ in the vicinity of the LO_4 edge of LAO/STO at 40 K, for several model scenarios. In all graphs, the parameters of the electric-field-induced TO mode were set to ω_{pl}^2 = 3329.3 cm^{-2}, ω_0 = 710 cm^{-1} and γ = 75 cm^{-1}. The data are shown by the solid cyan lines, the fits by the dashed purple lines.*

The dielectric function of $SrTiO_3$ is governed by infrared-active phonons and is well described as a sum of Lorentz oscillators, according to Eq. (16). The contribution from the 2DEG is small and therefore neglected in the model. In order to properly fit the new TO mode which arises close to the LO_4 edge when applying a negative back-gate voltage on the sample (-V), it is necessary to use an anisotropic model (since the only component becoming IR active is the one parallel to the induced polar moment, ***P***).

Figure B.6 shows a comparison of the fits for which ***P*** and thus the IR-active component of the TO-mode is assumed to have (a) equal x-, y- and z- components, (b) only a x-component , (c) only a y-component, (d) only a z-component, (e) equal x- and y- components, (f) equal y- and z- components, and (g) equal x- and z- components. Note that the *x*-axis is defined by the cross-section of the sample surface with the plane of incidence of the photons, and y- and z- are the corresponding orthogonal axes that are parallel and perpendicular to the sample surface, respectively. It is evident from Fig. B.6 that a reasonable fit of the LO_4 edge anomaly at -V can requires that the TO mode and thus ***P*** has a finite z-component.

Simulation of electric field lines

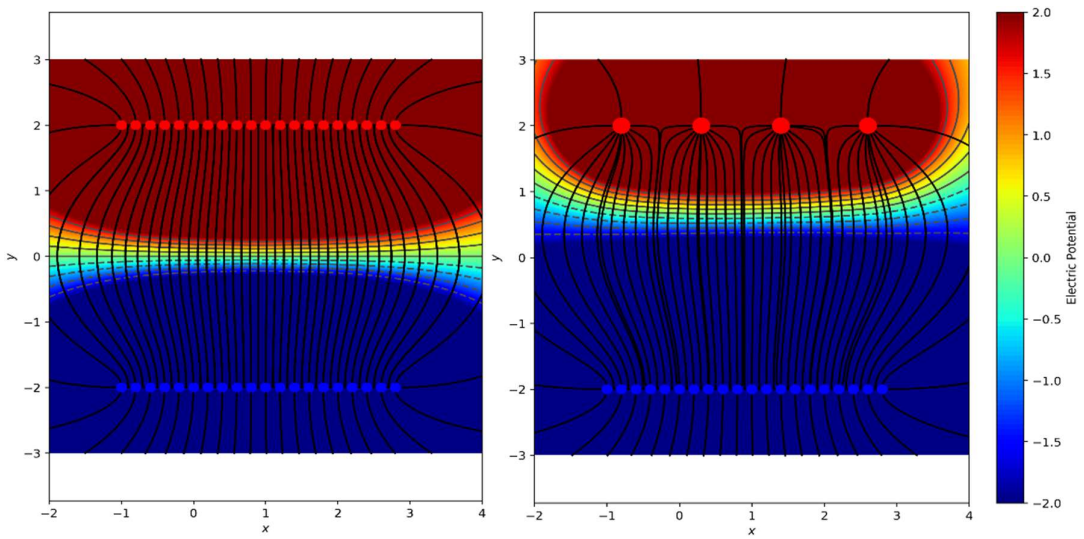

Figure B.7 Simulation of electric field lines. *Simulated electric field for a homogeneous top-electrode (left), in which the positive back-gate voltage induces a usual capacitor, and an inhomogeneous top-electrode (right) for the case of a negative back-gate, where the surface electrode is depleted and leads to in-plane electric field lines (black color).*

Infrared and Raman response of $AlO_x/KTaO_3$

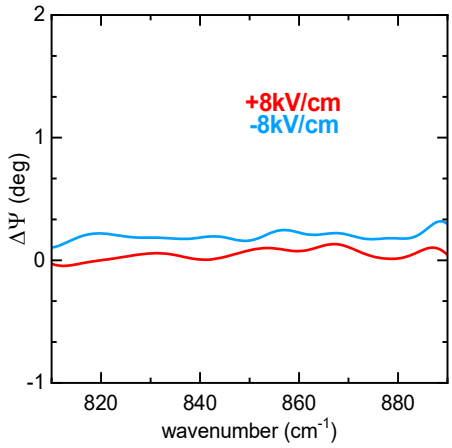

Figure B.8. Gate-voltage dependence of the infrared response of $AlO_x/KTaO_3$ at 10 K. *Since $KTaO_3$ remains cubic down to low temperatures, there is no infrared-active R-mode (around 438 cm^{-1}) that can be used to study to study the polarization behavior. Nevertheless, the corresponding anomaly at the LO_4 edge should still occur in response an induced anomalous polarization at -8 kV/cm. Figure B.8 shows that this is not the case, i.e. that a corresponding polarization does not develop in the vicinity of the AlO_x/KTO interface.*

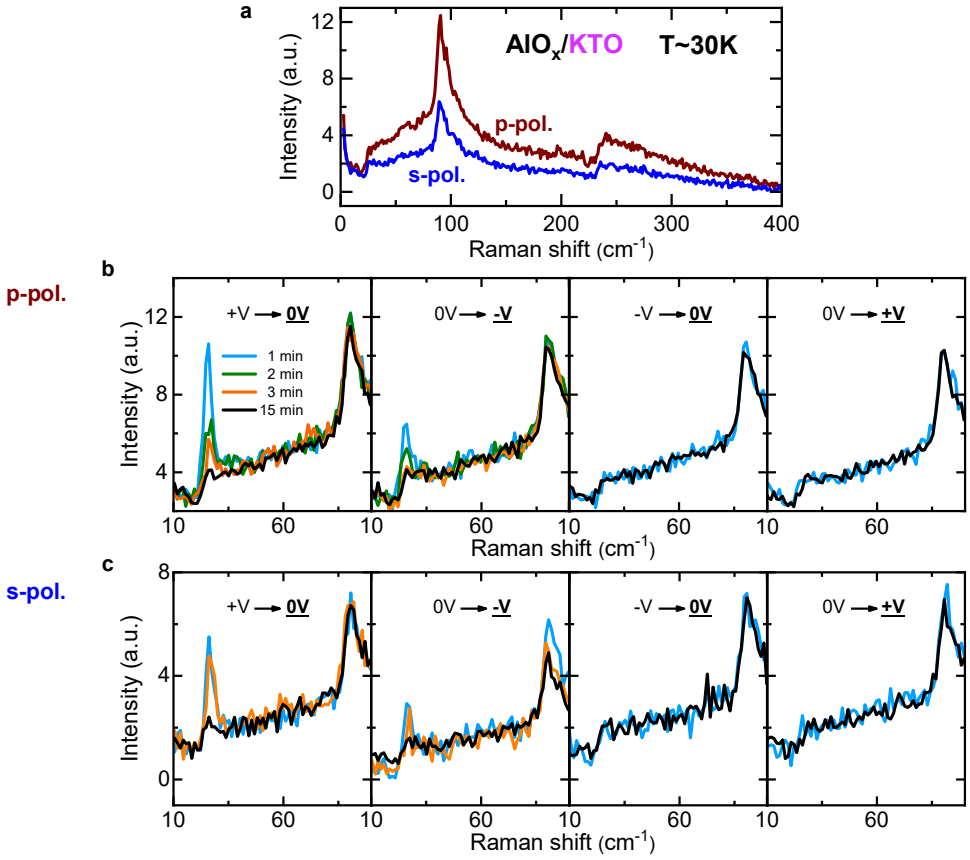

Figure B.9 Confocal Raman spectra of back-gated $AlO_x/KTaO_3$ measured in grazing-incidence, with +-8 kV/cm. *(a) Zero voltage spectra for different polarization geometries. Note that the detector is more efficient for the dark red curve (p-polarization) than for the blue one (s-polarization). The induced soft mode occurs only after the voltage has been decreased (from +V → 0V or from 0V → -V) but not after a corresponding increase of V. The amplitudes of the induced soft modes for p-pol. (b) and for s-pol. (c) are comparable. The induced soft mode occurs only below ca. 30 K and has only a weak depth dependence.*

Bibliography

[1] M. Born "Physics and Politics" *Oliver and Boyd LTD.*, Edinburgh (1962)

[2] P. Noël, F. Trier, L. M. Vicente Arche, J. Bréhin, D. C. Vaz, V. Garcia, S. Fusil, A. Barthélémy, L. Vila, M. Bibes and J.-P. Attané "Non-volatile electric control of spin-charge conversion in a $SrTiO_3$ Rashba system" *Nature,* vol. 580, pp. 483-486, 4 (2020)

[3] Y. C. Liao, T. Kopp, C. Richter, A. Rosch and J. Mannhart "Metal-insulator transition of the $LaAlO_3$-$SrTiO_3$ interface electron system" *Phys. Rev. B,* vol. 83, no. 7, p. 075402, 2 (2011)

[4] A. D. Caviglia, S. Gariglio, N. Reyren, D. Jaccard, T. Schneider, M. Gabay, S. Thiel, G. Hammerl, J. Mannhart and J.-M. Triscone "Electric field control of the $LaAlO_3/SrTiO_3$ interface ground state" *Nature,* vol. 456, pp. 624-627, 12 (2008)

[5] A. D. Caviglia, M. Gabay, S. Gariglio, N. Reyren, C. Cancellieri and J.-M. Triscone "Tunable Rashba Spin-Orbit Interaction at Oxide Interfaces" *Phys. Rev. Lett.,* vol. 104, no. 12, p. 126803, 3 (2010)

[6] E. Perret, C. Monney, S. Johnston, J. Khmaladze, F. Lyzwa, R. Gaina, M. Dantz, J. Pelliciari, C. Piamonteze, B. P. P. Mallett, M. Minola, B. Keimer, T. Schmitt and C. Bernhard "Coupled Cu and Mn charge and orbital orders in $YBa_2Cu_3O_7/Nd_{0.65}(Ca_{1-y}Sry)_{0.35}MnO_3$ multilayers" *Communications Physics,* vol. 1, p. 45, 8 (2018)

[7] R. Andrés Prada "Pulsed laser deposition and nanofabrication of mesoscopic devices based on cuprates and manganites" PhD thesis, Fribourg University (2019)

[8] H. Y. Hwang, Y. Iwasa, M. Kawasaki, B. Keimer, N. Nagaosa and Y. Tokura "Emergent phenomena at oxide interfaces" *Nature Materials,* vol. 11, pp. 103-113, 2 (2012)

[9] C. Enss and S. Hunklinger "Tieftemperaturphysik" Springer (2000)

[10] S. Hunklinger "Festkörperphysik" Oldenbourg (2011)

[11] B. Keimer, S. A. Kivelson, M. R. Norman, S. Uchida and J. Zaanen "From quantum matter to high-temperature superconductivity in copper oxides" *Nature,* vol. 518, pp. 179-186, 2 (2015)

[12] J. Bardeen, L. N. Cooper and J. R. Schrieffer "Theory of Superconductivity" *Phys. Rev.,* vol. 108, no. 5, pp. 1175-1204, 12 (1957)

[13] J. G. Bednorz and K. A. Müller "Possible high T_c superconductivity in the Ba−La−Cu−O system" *Zeitschrift für Physik B Condensed Matter,* vol. 64, pp. 189-193, 6 (1986)

[14] M. K. Wu, J. R. Ashburn, C. J. Torng, P. H. Hor, R. L. Meng, L. Gao, Z. J. Huang, Y. Q. Wang and C. W. Chu "Superconductivity at 93 K in a new mixed-phase Y-Ba-Cu-O compound system at ambient pressure" *Phys. Rev. Lett.,* vol. 58, no. 9, pp. 908-910, 3 (1987)

[15] A. Schilling, M. Cantoni, J. D. Guo and H. R. Ott "Superconductivity above 130 K in the Hg-Ba-Ca-Cu-O system" *Nature,* vol. 363, pp. 56-58, 5 (1993)

[16] D. N. Basov and A. V. Chubukov "Manifesto for a higher T_c" *Nature Physics,* vol. 7, pp. 272-276, 4 (2011)

[17] F. Steglich, J. Aarts, C. D. Bredl, W. Lieke, D. Meschede, W. Franz and H. Schäfer "Superconductivity in the Presence of Strong Pauli Paramagnetism: $CeCu_2Si_2$" *Phys. Rev. Lett.,* vol. 43, no. 25, pp. 1892-1896, 12 (1979)

[18] A. P. Drozdov, M. I. Eremets, I. A. Troyan, V. Ksenofontov and S. I. Shylin "Conventional superconductivity at 203 Kelvin at high pressures in the sulfur hydride system" *Nature,* vol. 525, pp. 73-76, 9 (2015)

[19] Y. Cao, V. Fatemi, A. Demir, S. Fang, S. L. Tomarken, J. Y. Luo, J. D. Sanchez-Yamagishi, K. Watanabe, T. Taniguchi, E. Kaxiras, R. C. Ashoori and P. Jarillo-Herrero "Correlated insulator behaviour at half-filling in magic-angle graphene superlattices" *Nature,* vol. 556, pp. 80-84, 4 (2018)

[20] J. E. Hirsch and F. Marsiglio "Understanding electron-doped cuprate superconductors as hole superconductors" *Physica C: Superconductivity and its Applications,* vol. 564, pp. 29-37 (2019)

[21] R. J. Cava, B. Batlogg, R. B. Dover, D. W. Murphy, S. Sunshine, T. Siegrist, J. P. Remeika, E. A. Rietman, S. Zahurak and G. P. Espinosa "Bulk superconductivity at 91 K in single-phase oxygen-deficient perovskite $Ba_2YCu_3O_{9-\delta}$" *Phys. Rev. Lett.,* vol. 58, no. 16, pp. 1676-1679, 4 (1987)

[22] B. P. P. Mallett, J. Khmaladze, P. Marsik, E. Perret, A. Cerreta, M. Orlita, N. Biškup, M. Varela and C. Bernhard "Granular superconductivity and magnetic-field-driven recovery of macroscopic coherence in a cuprate/manganite multilayer" *Phys. Rev. B,* vol. 94, no. 18, p. 180503, 11 (2016)

[23] J. Khmaladze, S. Sarkar, M. Soulier, F. Lyzwa, R. Andres Prada, E. Perret, B. P. P. Mallett, M. Minola, B. Keimer and C. Bernhard "Granular superconductivity and charge/orbital order in $YBa_2Cu_3O_7$/manganite trilayers" *Phys. Rev. Materials,* vol. 3, no. 8, p. 084801, 8 (2019)

[24] T. Wu, H. Mayaffre, S. Krämer, M. Horvatić, C. Berthier, W. N. Hardy, R. Liang, D. A. Bonn and M.-H. Julien "Magnetic-field-induced charge-stripe order in the high-temperature superconductor $YBa_2Cu_3O_y$" *Nature,* vol. 477, p. 191, 9 (2011)

[25] G. Grüner "The dynamics of charge-density waves" *Rev. Mod. Phys.,* vol. 60, no. 4, pp. 1129-1181, 10 (1988)

[26] S. Blanco-Canosa, A. Frano, E. Schierle, J. Porras, T. Loew, M. Minola, M. Bluschke, E. Weschke, B. Keimer and M. Le Tacon "Resonant x-ray scattering study of charge-density wave correlations in $YBa_2Cu_3O_{6+x}$" *Phys. Rev. B,* vol. 90, no. 5, p. 054513, 8 (2014)

[27] J. Chang, E. Blackburn, A. T. Holmes, N. B. Christensen, J. Larsen, J. Mesot, R. Liang, D. A. Bonn, W. N. Hardy, A. Watenphul, M. v. Zimmermann, E. M. Forgan and S. M. Hayden "Direct observation of competition between superconductivity and charge density wave order in $YBa_2Cu_3O_{6.67}$" *Nature Physics,* vol. 8, p. 871, 10 (2012)

[28] M. Le Tacon, A. Bosak, S. M. Souliou, G. Dellea, T. Loew, R. Heid, K.-P. Bohnen, G. Ghiringhelli, M. Krisch and B. Keimer "Inelastic X-ray scattering in $YBa_2Cu_3O_{6.6}$ reveals giant phonon anomalies and elastic central peak due to charge-density-wave formation" *Nature Physics,* vol. 10, p. 52, 11 (2014)

[29] J. Chang, E. Blackburn, O. Ivashko, A. T. Holmes, N. B. Christensen, M. Hücker, R. Liang, D. A. Bonn, W. N. Hardy, U. Rütt, M. v. Zimmermann, E. M. Forgan and S. M. Hayden "Magnetic field controlled charge density wave coupling in underdoped $YBa_2Cu_3O_{6+x}$" *Nature Communications,* vol. 7, p. 11494, 5 (2016)

[30] S. Gerber, H. Jang, H. Nojiri, S. Matsuzawa, H. Yasumura, D. A. Bonn, R. Liang, W. N. Hardy, Z. Islam, A. Mehta, S. Song, M. Sikorski, D. Stefanescu, Y. Feng, S. A. Kivelson, T. P. Devereaux, Z.-X. Shen, C.-C. Kao, W.-S. Lee, D. Zhu and J.-S. Lee "Three-dimensional charge density wave order in $YBa_2Cu_3O_{6.67}$ at high magnetic fields" *Science,* vol. 350, pp. 949-952 (2015)

[31] F. Laliberté, M. Frachet, S. Benhabib, B. Borgnic, T. Loew, J. Porras, M. Le Tacon, B. Keimer, S. Wiedmann, C. Proust and D. LeBoeuf "High field charge order across the phase diagram of $YBa_2Cu_3O_y$" *npj Quantum Materials,* vol. 3, p. 11, 3 (2018)

[32] T. Wu, H. Mayaffre, S. Krämer, M. Horvatić, C. Berthier, P. L. Kuhns, A. P. Reyes, R. Liang, W. N. Hardy, D. A. Bonn and M.-H. Julien "Emergence of charge order from the vortex state of a high-temperature superconductor" *Nature Communications,* vol. 4, p. 2113, 7 (2013)

[33] H.-H. Kim, S. M. Souliou, M. E. Barber, E. Lefrançois, M. Minola, M. Tortora, R. Heid, N. Nandi, R. A. Borzi, G. Garbarino, A. Bosak, J. Porras, T. Loew, M. König, P. J. W. Moll, A. P. Mackenzie, B. Keimer, C. W. Hicks and M. Le Tacon "Uniaxial pressure control of competing orders in a high-temperature superconductor" *Science,* vol. 362, pp. 1040-1044 (2018)

[34] E. Fradkin, S. A. Kivelson and J. M. Tranquada "Colloquium: Theory of intertwined orders in high temperature superconductors" *Rev. Mod. Phys.,* vol. 87, no. 2, pp. 457-482, 5 (2015)

[35] M.-H. Julien "Magnetic fields make waves in cuprates" *Science,* vol. 350, pp. 914-915 (2015)

[36] C. Proust and L. Taillefer "The Remarkable Underlying Ground States of Cuprate Superconductors" *Annual Review of Condensed Matter Physics,* vol. 10, pp. 409-429 (2019)

[37] B. Xu, Z. C. Wang, E. Sheveleva, F. Lyzwa, P. Marsik, G. H. Cao and C. Bernhard "Band-selective clean-limit and dirty-limit superconductivity with nodeless gaps in the bilayer iron-based superconductor $CsCa_2Fe_4As_4F_2$" *Phys. Rev. B,* vol. 99, no. 12, p. 125119, 3 (2019)

[38] C. Bernhard, T. Holden, J. Humlicek, D. Munzar, A. Golnik, M. Kläser, T. Wolf, L. Carr, C. Homes, B. Keimer and M. Cardona "In-plane polarized collective modes in detwinned YBa2Cu3O6.95 observed by spectral ellipsometry" *Solid State Communications,* vol. 121, pp. 93-97 (2002)

[39] D. N. Basov and T. Timusk "Electrodynamics of high-T_c superconductors" *Rev. Mod. Phys.,* vol. 77, no. 2, pp. 721-779, 8 (2005)

[40] C. C. Homes, D. A. Bonn, R. Liang, W. N. Hardy, D. N. Basov, T. Timusk and B. P. Clayman "Effect of Ni impurities on the optical properties of $YBa_2Cu_3O_{6+y}$" *Phys. Rev. B,* vol. 60, no. 13, pp. 9782-9792, 10 (1999)

[41] C. Bernhard, T. Holden, A. V. Boris, N. N. Kovaleva, A. V. Pimenov, J. Humlicek, C. Ulrich, C. T. Lin and J. L. Tallon "Anomalous oxygen-isotope effect on the in-plane far-infrared conductivity of detwinned $YBa_2Cu_3{}^{16,18}O_{6.9}$" *Phys. Rev. B,* vol. 69, no. 5, p. 052502, 2 (2004)

[42] A. M. Gerrits, T. J. B. M. Janssen, A. Wittlin, N. Y. Chen and P. J. M. Bentum "Far infrared reflectance of $YBa_2Cu_3O_{7-\delta}$ at high magnetic fields" *Physica C: Superconductivity,* Vols. 235-240, pp. 1115-1116 (1994)

[43] A. D. LaForge, W. J. Padilla, K. S. Burch, Z. Q. Li, A. A. Schafgans, K. Segawa, Y. Ando and D. N. Basov "Sum Rules and Interlayer Infrared Response of the High Temperature $YBa_2Cu_3O_y$ Superconductor in an External Magnetic Field" *Phys. Rev. Lett.,* vol. 101, no. 9, p. 097008, 8 (2008)

[44] Y. S. Lee, Z. Q. Li, W. J. Padilla, S. V. Dordevic, C. C. Homes, K. Segawa, Y. Ando and D. N. Basov "Strong-coupling effects in cuprate high-T_c superconductors by magneto-optical studies" *Phys. Rev. B,* vol. 72, no. 17, p. 172511, 11 (2005)

[45] V. Moshnyaga and K. Samwer "Polaronic Emergent Phases in Manganite-based Heterostructures" *Crystals,* vol. 9 (2019)

[46] A. Ichimiya and P. I. Cohen "Reflection High Energy Electron Diffraction" Cambridge University Press (2004)

[47] M. Jungbauer, S. Hühn, R. Egoavil, H. Tan, J. Verbeeck, G. Van Tendeloo and V. Moshnyaga "Atomic layer epitaxy of Ruddlesden-Popper $SrO(SrTiO_3)_n$ films by means of metalorganic aerosol deposition" *Applied Physics Letters,* vol. 105, p. 251603 (2014)

[48] F. Lyzwa, P. Marsik, V. Roddatis, C. Bernhard, M. Jungbauer and V. Moshnyaga "*In situ* monitoring of atomic layer epitaxy via optical ellipsometry" *Journal of Physics D: Applied Physics,* vol. 51, p. 125306, 3 (2018)

[49] M. Keunecke, F. Lyzwa, D. Schwarzbach, V. Roddatis, N. Gauquelin, K. Müller-Caspary, J. Verbeeck, S. J. Callori, F. Klose, M. Jungbauer and V. Moshnyaga "High-T_C Interfacial Ferromagnetism in $SrMnO_3$/$LaMnO_3$ Superlattices" *Advanced Functional Materials,* vol. 30, p. 1808270 (2020)

[50] F. Lyzwa, A. Chan, J. Khmaladze, K. Fürsich, B. Keimer, C. Bernhard, M. Minola and B. P. P. Mallett "Backfolded acoustic phonons as ultrasonic probes in metal-oxide superlattices" *Phys. Rev. Materials,* vol. 4, no. 4, p. 043606, 4 (2020)

[51] K. Benthem, C. Elsässer and R. H. French "Bulk electronic structure of $SrTiO_3$: Experiment and theory" *Journal of Applied Physics,* vol. 90, pp. 6156-6164 (2001)

[52] M. Rössle, "Infrared ellipsometry study of the lattice and charge dynamics in bulk SrTiO3, thin $SrTiO_3$ films, and $LaAlO_3$/$SrTiO_3$ heterostructures" PhD thesis, University Fribourg (2012)

[53] H. Vogt "Refined treatment of the model of linearly coupled anharmonic oscillators and its application to the temperature dependence of the zone-center soft-mode frequencies of $KTaO_3$ and $SrTiO_3$" *Phys. Rev. B,* vol. 51, no. 13, pp. 8046-8059, 4 (1995)

[54] J. Hemberger, M. Nicklas, R. Viana, P. Lunkenheimer, A. Loidl and R. Böhmer "Quantum paraelectric and induced ferroelectric states in $SrTiO_3$" *Journal of Physics: Condensed Matter,* vol. 8, pp. 4673-4690, 6 (1996)

[55] M. Yazdi-Rizi, P. Marsik, B. P. P. Mallett and C. Bernhard "Anisotropy of infrared-active phonon modes in the monodomain state of tetragonal $SrTiO_3$ (110)" *Phys. Rev. B,* vol. 95, no. 2, p. 024105, 1 (2017)

[56] M. Rössle, K. W. Kim, A. Dubroka, P. Marsik, C. N. Wang, R. Jany, C. Richter, J. Mannhart, C. W. Schneider, A. Frano, P. Wochner, Y. Lu, B. Keimer, D. K. Shukla, J. Strempfer and C. Bernhard "Electric-Field-Induced Polar Order and Localization of the Confined Electrons in $LaAlO_3/SrTiO_3$ Heterostructures" *Phys. Rev. Lett.,* vol. 110, no. 13, p. 136805, 3 (2013)

[57] L. He and D. Vanderbilt "First-principles study of oxygen-vacancy pinning of domain walls in $PbTiO_3$" *Phys. Rev. B,* vol. 68, no. 13, p. 134103, 10 (2003)

[58] E. K. H. Salje, O. Aktas, M. A. Carpenter, V. V. Laguta and J. F. Scott "Domains within Domains and Walls within Walls: Evidence for Polar Domains in Cryogenic $SrTiO_3$" *Phys. Rev. Lett.,* vol. 111, no. 24, p. 247603, 12 (2013)

[59] M. Honig, J. A. Sulpizio, J. Drori, A. Joshua, E. Zeldov and S. Ilani "Local electrostatic imaging of striped domain order in $LaAlO_3/SrTiO_3$" *Nature Materials,* vol. 12, pp. 1112-1118, 12 (2013)

[60] D. Kan, T. Terashima, R. Kanda, A. Masuno, K. Tanaka, S. Chu, H. Kan, A. Ishizumi, Y. Kanemitsu, Y. Shimakawa and M. Takano "Blue-light emission at room temperature from Ar^+-irradiated $SrTiO_3$" *Nature Materials,* vol. 4, pp. 816-819, 11 (2005)

[61] D. Bäuerle and W. Rehwald "Structural phase transitions in semiconducting $SrTiO_3$" *Solid State Communications,* vol. 27, pp. 1343-1346 (1978)

[62] J. F. Schooley, W. R. Hosler and M. L. Cohen "Superconductivity in Semiconducting $SrTiO_3$" *Phys. Rev. Lett.,* vol. 12, no. 17, pp. 474-475, 4 (1964)

[63] W. Gong, H. Yun, Y. B. Ning, J. E. Greedan, W. R. Datars and C. V. Stager "Oxygen-deficient $SrTiO_{3-x}$, x = 0.28, 0.17, and 0.08. Crystal growth, crystal structure, magnetic, and transport properties" *Journal of Solid State Chemistry,* vol. 90, pp. 320-330 (1991)

[64] F. W. Lytle "X-Ray Diffractometry of Low-Temperature Phase Transformations in Strontium Titanate" *Journal of Applied Physics,* vol. 35, pp. 2212-2215 (1964)

[65] I. A. Akimov, A. A. Sirenko, A. M. Clark, J.-H. Hao and X. X. Xi "Electric-Field-Induced Soft-Mode Hardening in $SrTiO_3$ Films" *Phys. Rev. Lett.,* vol. 84, no. 20, pp. 4625-4628, 5 (2000)

[66] J. H. Haeni, P. Irvin, W. Chang, R. Uecker, P. Reiche, Y. L. Li, S. Choudhury, W. Tian, M. E. Hawley, B. Craigo, A. K. Tagantsev, X. Q. Pan, S. K. Streiffer, L. Q. Chen, S. W. Kirchoefer, J. Levy and D. G. Schlom "Room-temperature ferroelectricity in strained $SrTiO_3$" *Nature,* vol. 430, pp. 758-761, 8 (2004)

[67] P. Marsik, K. Sen, J. Khmaladze, M. Yazdi-Rizi, B. P. P. Mallett and C. Bernhard "Terahertz ellipsometry study of the soft mode behavior in ultrathin $SrTiO_3$ films" *Applied Physics Letters,* vol. 108, p. 052901 (2016)

[68] A. A. Sirenko, C. Bernhard, A. Golnik, A. M. Clark, J. Hao, W. Si and X. X. Xi "Soft-mode hardening in $SrTiO_3$ thin films" *Nature,* vol. 404, pp. 373-376, 3 (2000)

[69] T. Ostapchuk, J. Petzelt, V. Železný, A. Pashkin, J. Pokorný, I. Drbohlav, R. Kužel, D. Rafaja, B. P. Gorshunov, M. Dressel, C. Ohly, S. Hoffmann-Eifert and R. Waser "Origin of soft-mode stiffening and reduced dielectric response in $SrTiO_3$ thin films" *Phys. Rev. B,* vol. 66, no. 23, p. 235406, 12 (2002)

[70] E. D. Mishina, T. V. Misuryaev, N. E. Sherstyuk, V. V. Lemanov, A. I. Morozov, A. S. Sigov and T. Rasing "Observation of a Near-Surface Structural Phase Transition in $SrTiO_3$ by Optical Second Harmonic Generation" *Phys. Rev. Lett.,* vol. 85, no. 17, pp. 3664-3667, 10 (2000)

[71] D. P. Osterman, K. Mohanty and J. D. Axe "Observation of the antiferroelectric order parameter in surface layers of $SrTiO_3$" *Journal of Physics C: Solid State Physics,* vol. 21, pp. 2635-2640, 5 (1988)

[72] S. Doi and I. Takahashi "Critical behaviour of the $SrTiO_3$(001) surface at the structural phase transition" *Philosophical Magazine A,* vol. 80, pp. 1889-1899 (2000)

[73] J. Chrosch and E. K. H. Salje "Near-surface domain structures in uniaxially stressed" *Journal of Physics: Condensed Matter,* vol. 10, pp. 2817-2827, 4 (1998)

[74] R. Loetzsch, A. Lübcke, I. Uschmann, E. Förster, V. Große, M. Thuerk, T. Koettig, F. Schmidl and P. Seidel "The cubic to tetragonal phase transition in $SrTiO_3$ single crystals near its surface under internal and external strains" *Applied Physics Letters,* vol. 96, p. 071901 (2010)

[75] P. Zubko, G. Catalan and A. K. Tagantsev "Flexoelectric Effect in Solids" *Annual Review of Materials Research,* vol. 43, pp. 387-421 (2013)

[76] J. Hemberger, P. Lunkenheimer, R. Viana, R. Böhmer and A. Loidl, "Electric-field-dependent dielectric constant and nonlinear susceptibility in $SrTiO_3$" *Phys. Rev. B,* vol. 52, no. 18, pp. 13159-13162, 11 (1995)

[77] M. Itoh, R. Wang, Y. Inaguma, T. Yamaguchi, Y.-J. Shan and T. Nakamura "Ferroelectricity Induced by Oxygen Isotope Exchange in Strontium Titanate Perovskite" *Phys. Rev. Lett.,* vol. 82, no. 17, pp. 3540-3543, 4 (1999)

[78] T. Mitsui and W. B. Westphal "Dielectric and X-Ray Studies of $Ca_xBa_{1-x}TiO_3$ and $Ca_xSr_{1-x}TiO_3$" *Phys. Rev.,* vol. 124, no. 5, pp. 1354-1359, 12 (1961)

[79] W. J. Burke and R. J. Pressley "Stress induced ferroelectricity in $SrTiO_3$" *Solid State Communications,* vol. 9, pp. 191-195 (1971)

[80] P. A. Fleury and J. M. Worlock "Electric-Field-Induced Raman Scattering in $SrTiO_3$ and $KTaO_3$" *Phys. Rev.,* vol. 174, no. 2, pp. 613-623, 10 (1968)

[81] C. Hubert, J. Levy, A. C. Carter, W. Chang, S. W. Kiechoefer, J. S. Horwitz and D. B. Chrisey "Confocal scanning optical microscopy of $Ba_xSr_{1-x}TiO_3$ thin films" *Applied Physics Letters,* vol. 71, pp. 3353-3355 (1997)

[82] M. Takesada, M. Itoh and T. Yagi "Perfect Softening of the Ferroelectric Mode in the Isotope-Exchanged Strontium Titanate of $SrTi^{18}O_3$ Studied by Light Scattering" *Phys. Rev. Lett.,* vol. 96, no. 22, p. 227602, 6 (2006)

[83] J. Narvaez, F. Vasquez-Sancho and G. Catalan "Enhanced flexoelectric-like response in oxide semiconductors" *Nature,* vol. 538, pp. 219-221, 10 (2016)

[84] F. Vasquez-Sancho, A. Abdollahi, D. Damjanovic and G. Catalan "Flexoelectricity in Bones" *Advanced Materials,* vol. 30, p. 1705316 (2018)

[85] S. M. Park, B. Wang, S. Das, S. C. Chae, J.-S. Chung, J.-G. Yoon, L.-Q. Chen, S. M. Yang and T. W. Noh "Selective control of multiple ferroelectric switching pathways using a trailing flexoelectric field" *Nature Nanotechnology,* vol. 13, pp. 366-370, 5 (2018)

[86] S. M. Park, B. Wang, T. Paudel, S. Y. Park, S. Das, J. R. Kim, E. K. Ko, H. G. Lee, N. Park, L. Tao, D. Suh, E. Y. Tsymbal, L.-Q. Chen, T. W. Noh and D. Lee "Colossal flexoresistance in dielectrics" *Nature Communications,* vol. 11, p. 2586, 5 (2020)

[87] A. Hippel "Ferroelectricity, Domain Structure, and Phase Transitions of Barium Titanate" *Rev. Mod. Phys.,* vol. 22, no. 3, pp. 221-237, 7 (1950)

[88] B. Ravel, E. A. Stern, R. I. Vedrinskii and V. Kraizman "Local structure and the phase transitions of $BaTiO_3$" *Ferroelectrics,* vol. 206, pp. 407-430 (1998)

[89] S. H. Wemple "Some Transport Properties of Oxygen-Deficient Single-Crystal Potassium Tantalate ($KTaO_3$)" *Phys. Rev.,* vol. 137, no. 5A, pp. A1575--A1582, 3 (1965)

[90] H. Uwe, K. B. Lyons, H. L. Carter and P. A. Fleury "Ferroelectric microregions and Raman scattering in $KTaO_3$" *Phys. Rev. B,* vol. 33, no. 9, pp. 6436-6440, 5 (1986)

[91] H. Uwe and T. Sakudo "Electrostriction and Stress-Induced Ferroelectricity in $KTaO_3$" *Journal of the Physical Society of Japan,* vol. 38, pp. 183-189 (1975)

[92] M. Tyunina, J. Narkilahti, M. Plekh, R. Oja, R. M. Nieminen, A. Dejneka and V. Trepakov, "Evidence for Strain-Induced Ferroelectric Order in Epitaxial Thin-Film $KTaO_3$" *Phys. Rev. Lett.,* vol. 104, no. 22, p. 227601, 6 (2010)

[93] S. E. Rowley, L. J. Spalek, R. P. Smith, M. P. M. Dean, M. Itoh, J. F. Scott, G. G. Lonzarich and S. S. Saxena "Ferroelectric quantum criticality" *Nature Physics,* vol. 10, pp. 367-372, 5 (2014)

[94] A. Ohtomo and H. Y. Hwang, "A high-mobility electron gas at the $LaAlO_3/SrTiO_3$ heterointerface," *Nature,* vol. 427, pp. 423-426, 1 (2004)

[95] N. Nakagawa, H. Y. Hwang and D. A. Muller "Why some interfaces cannot be sharp" *Nature Materials,* vol. 5, pp. 204-209, 3 (2006)

[96] Y. Hotta, T. Susaki and H. Y. Hwang "Polar Discontinuity Doping of the $LaVO_3/SrTiO_3$ Interface" *Phys. Rev. Lett.,* vol. 99, no. 23, p. 236805, 12 (2007)

[97] P. Moetakef, T. A. Cain, D. G. Ouellette, J. Y. Zhang, D. O. Klenov, A. Janotti, C. G. Van de Walle, S. Rajan, S. J. Allen and S. Stemmer "Electrostatic carrier doping of $GdTiO_3/SrTiO_3$ interfaces" *Applied Physics Letters,* vol. 99, p. 232116 (2011)

[98] A. Kalabukhov, R. Gunnarsson, J. Börjesson, E. Olsson, T. Claeson and D. Winkler "Effect of oxygen vacancies in the $SrTiO_3$ substrate on the electrical properties of the $LaAlO_3/SrTiO_3$ interface" *Phys. Rev. B,* vol. 75, no. 12, p. 121404, 3 (2007)

[99] A. F. Santander-Syro, O. Copie, T. Kondo, F. Fortuna, S. Pailhès, R. Weht, X. G. Qiu, F. Bertran, A. Nicolaou, A. Taleb-Ibrahimi, P. Le Fèvre, G. Herranz, M. Bibes, N. Reyren, Y. Apertet, P. Lecoeur, A. Barthélémy and M. J. Rozenberg "Two-dimensional electron gas with universal subbands at the surface of $SrTiO_3$" *Nature,* vol. 469, pp. 189-193, 1 (2011)

[100] S. Hühn and V. Moshnyaga, private correspondence, (2019)

[101] M. Yazdi-Rizi, P. Marsik, B. P. P. Mallett, K. Sen, A. Cerreta, A. Dubroka, M. Scigaj, F. Sánchez, G. Herranz and C. Bernhard, "Infrared ellipsometry study of photogenerated charge carriers at the (001) and (110) surfaces of $SrTiO_3$ crystals and at the interface of the corresponding $LaAlO_3/SrTiO_3$ heterostructures," *Phys. Rev. B,* vol. 95, no. 19, p. 195107, 5 (2017)

[102] D. Kan, R. Kanda, Y. Kanemitsu, Y. Shimakawa, M. Takano, T. Terashima and A. Ishizumi "Blue luminescence from electron-doped $SrTiO_3$" *Applied Physics Letters,* vol. 88, p. 191916 (2006)

[103] K. Zou, S. Ismail-Beigi, K. Kisslinger, X. Shen, D. Su, F. J. Walker and C. H. Ahn "$LaTiO_3/KTaO_3$ interfaces: A new two-dimensional electron gas system" *APL Materials,* vol. 3, p. 036104 (2015)

[104] K. Ueno, S. Nakamura, H. Shimotani, H. T. Yuan, N. Kimura, T. Nojima, H. Aoki, Y. Iwasa and M. Kawasaki "Discovery of superconductivity in $KTaO_3$ by electrostatic carrier doping" *Nature Nanotechnology,* vol. 6, pp. 408-412, 7 (2011)

[105] H. Zhang, H. Zhang, X. Yan, X. Zhang, Q. Zhang, J. Zhang, F. Han, L. Gu, B. Liu, Y. Chen, B. Shen and J. Sun "Highly Mobile Two-Dimensional Electron Gases with a Strong Gating Effect at the Amorphous $LaAlO_3/KTaO_3$ Interface" *ACS Appl. Mater. Interfaces,* vol. 9, pp. 36456-36461, 10 (2017)

[106] H. Zhang, X. Yan, X. Zhang, S. Wang, C. Xiong, H. Zhang, S. Qi, J. Zhang, F. Han, N. Wu, B. Liu, Y. Chen, B. Shen and J. Sun "Unusual Electric and Optical Tuning of $KTaO_3$-Based Two-Dimensional Electron Gases with 5d Orbitals" *ACS Nano,* vol. 13, pp. 609-615, 1 (2019)

[107] A. Brinkman, M. Huijben, M. Zalk, J. Huijben, U. Zeitler, J. C. Maan, W. G. Wiel, G. Rijnders, D. H. A. Blank and H. Hilgenkamp "Magnetic effects at the interface between non-magnetic oxides" *Nature Materials,* vol. 6, pp. 493-496, 7 (2007)

[108] L. Li, C. Richter, J. Mannhart and R. C. Ashoori "Coexistence of magnetic order and two-dimensional superconductivity at $LaAlO_3/SrTiO_3$ interfaces," *Nature Physics,* vol. 7, pp. 762-766, 10 (2011)

[109] S. Thiel, G. Hammerl, A. Schmehl, C. W. Schneider and J. Mannhart "Tunable Quasi-Two-Dimensional Electron Gases in Oxide Heterostructures" *Science,* vol. 313, pp. 1942-1945 (2006)

[110] Z. Chen, Z. Liu, Y. Sun, X. Chen, Y. Liu, H. Zhang, H. Li, M. Zhang, S. Hong, T. Ren, C. Zhang, H. Tian, Y. Zhou, J. Sun and Y. Xie "Two-Dimensional Superconductivity at the $LaAlO_3/KTaO_3(110)$ Heterointerface" *Phys. Rev. Lett.,* vol. 126, no. 2, p. 026802, 1 (2021)

[111] D. C. Vaz, P. Noël, A. Johansson, B. Göbel, F. Y. Bruno, G. Singh, S. McKeown-Walker, F. Trier, L. M. Vicente-Arche, A. Sander, S. Valencia, P. Bruneel, M. Vivek, M. Gabay, N. Bergeal, F. Baumberger, H. Okuno, A. Barthélémy, A. Fert, L. Vila, I. Mertig, J.-P. Attané and M. Bibes "Mapping spin-charge conversion to the band structure in a topological oxide two-dimensional electron gas" *Nature Materials,* vol. 18, pp. 1187-1193, 11 (2019)

[112] L. J. P. Ament, M. Veenendaal, T. P. Devereaux, J. P. Hill and J. Brink "Resonant inelastic x-ray scattering studies of elementary excitations" *Rev. Mod. Phys.,* vol. 83, no. 2, pp. 705-767, 6 (2011)

[113] M. Cardona "Light Scattering in Solids" Springer, Berlin, Heidelberg (1975)

[114] W. Demtröder "Electrodynamics and Optics" Springer (2019)

[115] P. Marsik "Advanced ellipsometry techniques and studies of low-k dielectric films" PhD thesis, Masaryk University (2009)

[116] R. H. Lyddane, R. G. Sachs and E. Teller "On the Polar Vibrations of Alkali Halides" *Phys. Rev.,* vol. 59, no. 8, pp. 673-676, 4 (1941)

[117] M. Hepting "Ordering Phenomena in Rare-Earth Nickelate Heterostructures" PhD thesis, University of Stuttgart (2017)

[118] B. Xu, Y. M. Dai, L. X. Zhao, K. Wang, R. Yang, W. Zhang, J. Y. Liu, H. Xiao, G. F. Chen, S. A. Trugman, J.-X. Zhu, A. J. Taylor, D. A. Yarotski, R. P. Prasankumar and X. G. Qiu "Temperature-tunable Fano resonance induced by strong coupling between Weyl fermions and phonons in TaAs" *Nature Communications,* vol. 8, p. 14933, 3 (2017)

[119] B. Xu, E. Cappelluti, L. Benfatto, B. P. P. Mallett, P. Marsik, E. Sheveleva, F. Lyzwa, T. Wolf, R. Yang, X. G. Qiu, Y. M. Dai, H. H. Wen, R. P. S. M. Lobo and C. Bernhard "Scaling of the Fano Effect of the In-Plane Fe-As Phonon and the Superconducting Critical Temperature in $Ba_{1-x}K_xFe_2As_2$" *Phys. Rev. Lett.,* vol. 122, no. 21, p. 217002, 5 (2019)

[120] R. A. Ferrell and R. E. Glover "Conductivity of Superconducting Films: A Sum Rule" *Phys. Rev.,* vol. 109, no. 4, pp. 1398-1399, 2 (1958)

[121] M. Tinkham and R. A. Ferrell "Determination of the Superconducting Skin Depth from the Energy Gap and Sum Rule" *Phys. Rev. Lett.,* vol. 2, no. 8, pp. 331-333, 4 (1959)

[122] F. Wooten "Optical Properties of Solids" Elsevier (1972)

[123] bruker.com/en/products-and-solutions/infrared-and-raman/ft-ir-research-spectrometers/vertex-research-ft-ir-spectrometer/vertex-70v-ft-ir-spectrometer.html

[124] A. Subramanian and L. Rodriguez-Saona, "Chapter 7 - Fourier Transform Infrared (FTIR) Spectroscopy in *Infrared Spectroscopy for Food Quality Analysis and Contro"l*, D. Sun, Ed., San Diego, Academic Press (2009)

[125] www.jawoollam.com/products/vase-ellipsometer

[126] C. C. Homes, M. Reedyk, D. A. Cradles and T. Timusk "Technique for measuring the reflectance of irregular, submillimeter-sized samples" *Appl. Opt.,* vol. 32, pp. 2976-2983, 6 (1993)

[127] C. Wang "Infrared Spectroscopy and Muon Spin Rotation Study of Superconductivity and Magnetism in Iron-based superconductors" PhD thesis, University of Fribourg (2014)

[128] J. Levallois, I. O. Nedoliuk, I. Crassee and A. B. Kuzmenko "Magneto-optical Kramers-Kronig analysis" *Review of Scientific Instruments,* vol. 86, p. 033906 (2015)

[129] W. J. Padilla, Y. S. Lee, M. Dumm, G. Blumberg, S. Ono, K. Segawa, S. Komiya, Y. Ando and D. N. Basov "Constant effective mass across the phase diagram of high-T_c cuprates" *Phys. Rev. B,* vol. 72, no. 6, p. 060511, 8 (2005)

[130] R. Liang, P. Dosanjh, D. A. Bonn, W. N. Hardy and A. J. Berlinsky "Lower critical fields in an ellipsoid-shaped $YBa_2Cu_3O_{6.95}$ single crystal" *Phys. Rev. B,* vol. 50, no. 6, pp. 4212-4215, 8 (1994)

[131] R. Liang, D. A. Bonn, W. N. Hardy and D. Broun "Lower Critical Field and Superfluid Density of Highly Underdoped $YBa_2Cu_3O_{6+x}$ Single Crystals" *Phys. Rev. Lett.,* vol. 94, no. 11, p. 117001, 3 (2005)

[132] G. Grissonnanche, O. Cyr-Choinière, F. Laliberté, S. René de Cotret, A. Juneau-Fecteau, S. Dufour-Beauséjour, M. È. Delage, D. LeBoeuf, J. Chang, B. J. Ramshaw, D. A. Bonn, W. N. Hardy, R. Liang, S. Adachi, N. E. Hussey, B. Vignolle, C. Proust, M. Sutherland, S. Krämer, J. H. Park, D. Graf, N. Doiron-Leyraud and L. Taillefer "Direct measurement of the upper critical field in cuprate superconductors" *Nature Communications,* vol. 5, p. 3280, 2 (2014)

[133] A. B. Kuzmenko "Kramers-Kronig constrained variational analysis of optical data" *Review of Scientific Instruments,* vol. 76, p. 083108 (2005)

[134] H. Fujiwara "Spectroscopic Ellipsometry: Principles and Applications" John Wiley & Sons (2003)

[135] M. Schubert "Infrared Ellipsometry on Semiconductor Layer Structures" G. Höhler, Ed., Springer (2004)

[136] J. Humlícek and C. Bernhard "Diffraction effects in infrared ellipsometry of conducting samples" *Thin Solid Films,* vol. 455, pp. 177-182 (2004)

[137] C. Bernhard, J. Humlícek and B. Keimer "Far-infrared ellipsometry using a synchrotron light source—the dielectric response of the cuprate high T_c superconductors" *Thin Solid Films,* Vols. 455-456, pp. 143-149 (2004)

[138] M. Yazdi-Rizi "Infrared ellipsometry study of the photo-generated and intrinsic charge carriers at the surface of $SrTiO_3$ crystals and the interfaces of $LaAlO_3/SrTiO_3$ and γ-$Al_2O_3/SrTiO_3$ heterostructures" PhD thesis, University of Fribourg (2017)

[139] C. V. Raman and K. S. Krishnan "A New Type of Secondary Radiation" *Nature,* vol. 121, pp. 501-502, 3 (1928)

[140] T. H. Maiman "Stimulated Optical Radiation in Ruby" *Nature,* vol. 187, pp. 493-494, 8 (1960)

[141] T. P. Devereaux and R. Hackl "Inelastic light scattering from correlated electrons" *Rev. Mod. Phys.,* vol. 79, no. 1, pp. 175-233, 1 (2007)

[142] J. R. Lakowicz "Principles of Fluorescence Spectroscopy" Springer (2006)

[143] I. P. Herman "Peak temperatures from Raman Stokes/anti-Stokes ratios during laser heating by a Gaussian beam" *Journal of Applied Physics,* vol. 109, p. 016103 (2011)

[144] K. Fürsich, J. Bertinshaw, P. Butler, M. Krautloher, M. Minola and B. Keimer "Raman scattering from current-stabilized nonequilibrium phases in Ca_2RuO_4" *Phys. Rev. B,* vol. 100, no. 8, p. 081101, 8 (2019)

[145] K. Fürsich "X-ray and Raman scattering studies of novel phases in 3d and 4d transition metal oxides" PhD thesis, University of Stuttgart (2020)

[146] G. New "Introduction to Nonlinear Optics" Cambridge University Press (2011)

[147] Horiba Jobin Yvon Labram HR800 user manuel

[148] M. Hepting, M. Minola, A. Frano, G. Cristiani, G. Logvenov, E. Schierle, M. Wu, M. Bluschke, E. Weschke, H.-U. Habermeier, E. Benckiser, M. Le Tacon and B. Keimer "Tunable Charge and Spin Order in $PrNiO_3$ Thin Films and Superlattices" *Phys. Rev. Lett.,* vol. 113, no. 22, p. 227206, 11 (2014)

[149] B.-S. Yeo, J. Stadler, T. Schmid, R. Zenobi and W. Zhang "Tip-enhanced Raman Spectroscopy – Its status, challenges and future directions" *Chemical Physics Letters,* vol. 472, pp. 1-13 (2009)

[150] S. Merten "Polaronic behaviour at manganite interfaces studied by advanced Raman scattering techniques" PhD thesis, University of Goettingen (2019)

[151] C. Meyer "Ordnungs-/Unordnungsphänomene in korrelierten Perowskitschichten anhand von fortgeschrittener Raman-Spektroskopie" PhD thesis, University of Goettingen (2018)

[152] H. D. Hallen, M. A. Paesler and C. L. Jahncke "Raman spectroscopy: probing the border between near-field and far-field spectroscopy" *Far- and Near-Field Optics: Physics and Information Processing* (1998)

[153] S. Merten, V. Roddatis and V. Moshnyaga "Metalorganic-aerosol-deposited Au nanoparticles for the characterization of ultrathin films by surface-enhanced Raman spectroscopy" *Applied Physics Letters,* vol. 115, p. 151902 (2019)

[154] S. Merten, V. Bruchmann-Bamberg, B. Damaschke, K. Samwer and V. Moshnyaga "Jahn-Teller reconstructed surface of the doped manganites shown by means of surface-enhanced Raman spectroscopy" *Phys. Rev. Materials,* vol. 3, no. 6, p. 060401, 6 (2019)

[155] H. Hertz "Ueber einen Einfluss des ultravioletten Lichtes auf die electrische Entladung" *Annalen der Physik,* vol. 267, pp. 983-1000 (1887)

[156] A. Einstein "Über einen die Erzeugung und Verwandlung des Lichtes betreffenden heuristischen Gesichtspunkt" *Annalen der Physik,* vol. 322, pp. 132-148 (1905)

[157] B. Lv, T. Qian and H. Ding "Angle-resolved photoemission spectroscopy and its application to topological materials" *Nature Reviews Physics,* vol. 1, pp. 609-626, 10 (2019)

[158] D. Lu, I. M. Vishik, M. Yi, Y. Chen, R. G. Moore and Z.-X. Shen "Angle-Resolved Photoemission Studies of Quantum Materials" *Annual Review of Condensed Matter Physics,* vol. 3, pp. 129-167 (2012)

[159] T. Wu, H. Mayaffre, S. Krämer, M. Horvatić, C. Berthier, W. N. Hardy, R. Liang, D. A. Bonn and M.-H. Julien "Incipient charge order observed by NMR in the normal state of $YBa_2Cu_3O_y$" *Nature Communications,* vol. 6, p. 6438, 3 (2015)

[160] G. Ghiringhelli, M. Le Tacon, M. Minola, S. Blanco-Canosa, C. Mazzoli, N. B. Brookes, G. M. De Luca, A. Frano, D. G. Hawthorn, F. He, T. Loew, M. M. Sala, D. C. Peets, M. Salluzzo, E. Schierle, R. Sutarto, G. A. Sawatzky, E. Weschke, B. Keimer and L. Braicovich "Long-Range Incommensurate Charge Fluctuations in $(Y,Nd)Ba_2Cu_3O_{6+x}$" *Science,* vol. 337, pp. 821-825 (2012)

[161] T. P. Croft, C. Lester, M. S. Senn, A. Bombardi and S. M. Hayden "Charge density wave fluctuations in $La_{2-x}Sr_xCuO_4$ and their competition with superconductivity" *Phys. Rev. B,* vol. 89, no. 22, p. 224513, 6 (2014)

[162] L. Chaix, G. Ghiringhelli, Y. Y. Peng, M. Hashimoto, B. Moritz, K. Kummer, N. B. Brookes, Y. He, S. Chen, S. Ishida, Y. Yoshida, H. Eisaki, M. Salluzzo, L. Braicovich, Z.-X. Shen, T. P. Devereaux and W.-S. Lee "Dispersive charge density wave excitations in $Bi_2Sr_2CaCu_2O_{8+\delta}$" *Nature Physics,* vol. 13, p. 952, 6 (2017)

[163] J. A. Rosen, R. Comin, G. Levy, D. Fournier, Z.-H. Zhu, B. Ludbrook, C. N. Veenstra, A. Nicolaou, D. Wong, P. Dosanjh, Y. Yoshida, H. Eisaki, G. R. Blake, F. White, T. T. M. Palstra, R. Sutarto, F. He, A. Fraño Pereira, Y. Lu, B. Keimer, G. Sawatzky, L. Petaccia and A. Damascelli "Surface-enhanced charge-density-wave instability in underdoped $Bi_2Sr_{2-x}La_xCuO_{6+\delta}$" *Nature Communications,* vol. 4, p. 1977, 7 (2013)

[164] W. Tabis, B. Yu, I. Bialo, M. Bluschke, T. Kolodziej, A. Kozlowski, E. Blackburn, K. Sen, E. M. Forgan, M. v. Zimmermann, Y. Tang, E. Weschke, B. Vignolle, M. Hepting, H. Gretarsson, R. Sutarto, F. He, M. Le Tacon, N. Barisic, G. Yu and M. Greven "Synchrotron x-ray scattering study of charge-density-wave order in $HgBa_2CuO_{4+\delta}$" *Phys. Rev. B,* vol. 96, no. 13, p. 134510, 10 (2017)

[165] S. Caprara, C. Di Castro, G. Seibold and M. Grilli "Dynamical charge density waves rule the phase diagram of cuprates" *Phys. Rev. B,* vol. 95, no. 22, p. 224511, 6 (2017)

[166] H. Alloul, T. Ohno and P. Mendels, "^{89}Y NMR evidence for a fermi-liquid behavior in $YBa_2Cu_3O_{6+x}$" *Phys. Rev. Lett.,* vol. 63, no. 16, pp. 1700-1703, 10 (1989)

[167] C. C. Homes, T. Timusk, R. Liang, D. A. Bonn and W. N. Hardy "Optical conductivity of c axis oriented $YBa_2Cu_3O_{6.70}$: Evidence for a pseudogap" *Phys. Rev. Lett.,* vol. 71, no. 10, pp. 1645-1648, 9 (1993)

[168] J. W. Loram, K. A. Mirza, J. R. Cooper and W. Y. Liang "Electronic specific heat of $YBa_2Cu_3O_{6+x}$ from 1.8 to 300 K" *Phys. Rev. Lett.,* vol. 71, no. 11, pp. 1740-1743, 9 (1993)

[169] D. N. Basov, R. D. Averitt, D. Marel, M. Dressel and K. Haule "Electrodynamics of correlated electron materials" *Rev. Mod. Phys.,* vol. 83, no. 2, pp. 471-541, 6 (2011)

[170] M. Dressel and G. Grüner "Electrodynamics of Solids" Cambridge University Press (2002)

[171] D. M. Ginsberg and M. Tinkham "Far Infrared Transmission through Superconducting Films" *Phys. Rev.,* vol. 118, no. 4, pp. 990-1000, 5 (1960)

[172] G. Li, W. Z. Hu, J. Dong, Z. Li, P. Zheng, G. F. Chen, J. L. Luo and N. L. Wang "Probing the Superconducting Energy Gap from Infrared Spectroscopy on a $Ba_{0.6}K_{0.4}Fe_2As_2$ Single Crystal with T_c=37 K" *Phys. Rev. Lett.,* vol. 101, no. 10, p. 107004, 9 (2008)

[173] R. Bozio, C. Pecile, K. Bechgaard, F. Wudl and D. Nalewajek "Infrared study on the formation of charge density waves in $(TMTSF)_2X$ (X = Reo_4− and PF_6− at atmospheric pressure" *Solid State Communications,* vol. 41, pp. 905-910 (1982)

[174] S. H. Blanton, R. T. Collins, K. H. Kelleher, L. D. Rotter, Z. Schlesinger, D. G. Hinks and Y. Zheng "Infrared study of $Ba_{1-x}K_xBiO_3$ from charge-density-wave insulator to superconductor" *Phys. Rev. B,* vol. 47, no. 2, pp. 996-1001, 1 (1993)

[175] U. Chatterjee, J. Zhao, M. Iavarone, R. Di Capua, J. P. Castellan, G. Karapetrov, C. D. Malliakas, M. G. Kanatzidis, H. Claus, J. P. C. Ruff, F. Weber, J. Wezel, J. C. Campuzano, R. Osborn, M. Randeria, N. Trivedi, M. R. Norman and S. Rosenkranz "Emergence of coherence in the charge-density wave state of 2H-$NbSe_2$" *Nature Communications,* vol. 6, p. 6313, 2 (2015)

[176] X. Xi, L. Zhao, Z. Wang, H. Berger, L. Forró, J. Shan and K. F. Mak "Strongly enhanced charge-density-wave order in monolayer $NbSe_2$" *Nature Nanotechnology,* vol. 10, p. 765, 7 (2015)

[177] M. Ortolani, S. Lupi, A. Lucarelli, P. Calvani, A. Perla, P. Maselli, M. Capizzi, N. Kikugawa and T. Fujita "Imprints of charge stripe excitations in the infrared conductivity of $La_{2-x}Sr_xCuO_4$," *Physica C: Superconductivity,* Vols. 408-410, pp. 439-440 (2004)

[178] A. Lucarelli, S. Lupi, M. Ortolani, P. Calvani, P. Maselli, M. Capizzi, P. Giura, H. Eisaki, N. Kikugawa, T. Fujita, M. Fujita and K. Yamada "Phase Diagram of $La_{2-x}Sr_xCuO_4$ Probed in the Infared: Imprints of Charge Stripe Excitations" *Phys. Rev. Lett.,* vol. 90, no. 3, p. 037002, 1 (2003)

[179] M. Dumm, D. N. Basov, S. Komiya, Y. Abe and Y. Ando "Electromagnetic Response of Static and Fluctuating Stripes in Cuprate Superconductors" *Phys. Rev. Lett.,* vol. 88, no. 14, p. 147003, 3 (2002)

[180] S. Tajima "Optical studies of high-temperature superconducting cuprates" *Reports on Progress in Physics,* vol. 79, p. 094001, 7 (2016)

[181] D. B. Tanner, H. L. Liu, M. A. Quijada, A. M. Zibold, H. Berger, R. J. Kelley, M. Onellion, F. C. Chou, D. C. Johnston, J. P. Rice, D. M. Ginsberg and J. T. Markert "Superfluid and normal fluid density in high-T_c superconductors" *Physica B: Condensed Matter,* vol. 244, pp. 1-8 (1998)

[182] S. Tajima, Y. Fudamoto, T. Kakeshita, B. Gorshunov, V. Železný, K. M. Kojima, M. Dressel and S. Uchida "In-plane optical conductivity of $La_{2-x}Sr_xCuO_4$: Reduced superconducting condensate and residual Drude-like response" *Phys. Rev. B,* vol. 71, no. 9, p. 094508, 3 (2005)

[183] S. Tajima, T. Kakeshita, Y. Fudamoto, N. L. Wang, V. Železný, K. M. Kojima, S. Uchida, B. Gorshunov and M. Dressel "Strongly reduced superfluid density in the inhomogeneous high-T_c cuprates: far-infrared study" *Journal of Physics and Chemistry of Solids,* vol. 67, pp. 321-324 (2006)

[184] R. Arpaia, S. Caprara, R. Fumagalli, G. De Vecchi, Y. Y. Peng, E. Andersson, D. Betto, G. M. De Luca, N. B. Brookes, F. Lombardi, M. Salluzzo, L. Braicovich, C. Di Castro, M. Grilli and G. Ghiringhelli "Dynamical charge density fluctuations pervading the phase diagram of a Cu-based high-T_c superconductor" *Science,* vol. 365, pp. 906-910 (2019)

[185] R. Zhou, M. Hirata, T. Wu, I. Vinograd, H. Mayaffre, S. Krämer, A. P. Reyes, P. L. Kuhns, R. Liang, W. N. Hardy, D. A. Bonn and M.-H. Julien, "Spin susceptibility of charge-ordered $YBa_2Cu_3O_y$ across the upper critical field" *Proceedings of the National Academy of Sciences,* vol. 114, pp. 13148-13153 (2017)

[186] C. Marcenat, A. Demuer, K. Beauvois, B. Michon, A. Grockowiak, R. Liang, W. Hardy, D. A. Bonn and T. Klein "Calorimetric determination of the magnetic phase diagram of underdoped ortho II $YBa_2Cu_3O_{6.54}$ single crystals" *Nature Communications,* vol. 6, p. 7927, 8 (2015)

[187] C. T. Lin, W. Zhou, W. Y. Liang, E. Schönherr and H. Bender "Growth of large and untwinned single crystals of YBCO" *Physica C: Superconductivity,* vol. 195, pp. 291-300 (1992)

[188] K. W. Kim, M. Rössle, A. Dubroka, V. K. Malik, T. Wolf and C. Bernhard "Evidence for multiple superconducting gaps in optimally doped $BaFe_{1.87}Co_{0.13}As_2$ from infrared spectroscopy" *Phys. Rev. B,* vol. 81, no. 21, p. 214508, 6 (2010)

[189] F. Lyzwa, B. Xu, P. Marsik, E. Sheveleva, I. Crassee, M. Orlita and C. Bernhard "Infrared spectroscopy study of the in-plane response of $YBa_2Cu_3O_{6.6}$ in magnetic fields up to 30 Tesla" *Phys. Rev. Research,* vol. 2, no. 2, p. 023218, 5 (2020)

[190] P. A. Lee "Localized states in a d-wave superconductor" *Phys. Rev. Lett.,* vol. 71, no. 12, pp. 1887-1890, 9 (1993)

[191] J. Corson, J. Orenstein, S. Oh, J. O'Donnell and J. N. Eckstein "Nodal Quasiparticle Lifetime in the Superconducting State of $Bi_2Sr_2CaCu_2O_{8+x}$" *Phys. Rev. Lett.,* vol. 85, no. 12, pp. 2569-2572, 9 (2000)

[192] P. Marsik, K. W. Kim, A. Dubroka, M. Rössle, V. K. Malik, L. Schulz, C. N. Wang, C. Niedermayer, A. J. Drew, M. Willis, T. Wolf and C. Bernhard "Coexistence and Competition of Magnetism and Superconductivity on the Nanometer Scale in Underdoped $BaFe_{1.89}Co_{0.11}As_2$" *Phys. Rev. Lett.,* vol. 105, no. 5, p. 057001, 7 (2010)

[193] Y. M. Dai, B. Xu, B. Shen, H. H. Wen, X. G. Qiu and R. P. S. M. Lobo "Optical conductivity of $Ba_{0.6}K_{0.4}Fe_2As_2$: The effect of in-plane and out-of-plane doping in the superconducting gap" *EPL (Europhysics Letters),* vol. 104, p. 47006, 11 (2013)

[194] B. P. P. Mallett, P. Marsik, M. Yazdi-Rizi, T. Wolf, A. E. Böhmer, F. Hardy, C. Meingast, D. Munzar and C. Bernhard "Infrared Study of the Spin Reorientation Transition and Its Reversal in the Superconducting State in Underdoped $Ba_{1-x}K_xFe_2As_2$" *Phys. Rev. Lett.,* vol. 115, no. 2, p. 027003, 7 (2015)

[195] A. Charnukha, K. W. Post, S. Thirupathaiah, D. Pröpper, S. Wurmehl, M. Roslova, I. Morozov, B. Büchner, A. N. Yaresko, A. V. Boris, S. V. Borisenko and D. N. Basov "Weak-coupling superconductivity in a strongly correlated iron pnictide" *Scientific Reports,* vol. 6, p. 18620, 1 (2016)

[196] E. van Heumen, Y. Huang, S. Jong, A. B. Kuzmenko, M. S. Golden and D. Marel "Optical properties of $BaFe_{2-x}Co_xAs_2$" *EPL (Europhysics Letters),* vol. 90, p. 37005, 5 (2010)

[197] J. Hwang, J. Yang, T. Timusk, S. G. Sharapov, J. P. Carbotte, D. A. Bonn, R. Liang and W. N. Hardy, "a-axis optical conductivity of detwinned ortho-II $YBa_2Cu_3O_{6.50}$" *Phys. Rev. B,* vol. 73, no. 1, p. 014508, 1 (2006)

[198] T. Kakeshita, T. Masui and S. Tajima "In-plane charge dynamics in underdoped YBCO" *Physica C: Superconductivity,* Vols. 426-431, pp. 184-188 (2005)

[199] D. Sonora, J. Mosquiera, F. Vladl "Comment on 'Temperature range of superconducting fluctuations above T_c in $YBa_2Cu_3O_{7-d}$ single crystals' " arXiv:1911.00733v1 (2019)

[200] J. Kacmarcik, I. Vinograd, B. Michon, A. Rydh, A. Demuer, R. Zhou, H. Mayaffre, R. Liang, W. N. Hardy, D. A. Bonn, N. Doiron-Leyraud, L. Taillefer, M.-H. Julien, C. Marcenat and T. Klein "Unusual Interplay between Superconductivity and Field-Induced Charge Order in $YBa_2Cu_3O_y$" *Phys. Rev. Lett.,* vol. 121, no. 16, p. 167002, 10 (2018)

[201] J. W. Loram, K. A. Mirza, J. R. Cooper and J. L. Tallon " Specific heat evidence on the normal state pseudogap" *Journal of Physics and Chemistry of Solids,* vol. 59, pp. 2091-2094 (1998)

[202] J. W. Loram, J. Luo, J. R. Cooper, W. Y. Liang and J. L. Tallon "Evidence on the pseudogap and condensate from the electronic specific heat" *Journal of Physics and Chemistry of Solids,* vol. 62, pp. 59-64 (2001)

[203] G. V. M. Williams, J. L. Tallon, J. W. Quilty, H. J. Trodahl and N. E. Flower "Absence of an Isotope Effect in the Pseudogap in $YBa_2Cu_4O_8$ as Determined by High-Resolution ^{89}Y NMR" *Phys. Rev. Lett.,* vol. 80, no. 2, pp. 377-380, 1 (1998)

[204] D. Munzar, C. Bernhard and M. Cardona "Does the peak in the magnetic susceptibility determine the in-plane infrared conductivity of YBCO? A theoretical study" *Physica C: Superconductivity,* vol. 312, pp. 121-135 (1999)

[205] J. P. Carbotte, E. Schachinger and D. N. Basov "Coupling strength of charge carriers to spin fluctuations in high-temperature superconductors" *Nature,* vol. 401, pp. 354-356 (1999)

[206] A. S. Mishchenko, N. Nagaosa, Z.-X. Shen, G. De Filippis, V. Cataudella, T. P. Devereaux, C. Bernhard, K. W. Kim and J. Zaanen "Charge Dynamics of Doped Holes in High T_c Cuprate Superconductors: A Clue from Optical Conductivity" *Phys. Rev. Lett.,* vol. 100, no. 16, p. 166401, 4 (2008)

[207] J. Chakhalian, J. W. Freeland, H.-U. Habermeier, G. Cristiani, G. Khaliullin, M. Veenendaal and B. Keimer "Orbital Reconstruction and Covalent Bonding at an Oxide Interface" *Science,* vol. 318, pp. 1114-1117 (2007)

[208] N. Reyren, S. Thiel, A. D. Caviglia, L. F. Kourkoutis, G. Hammerl, C. Richter, C. W. Schneider, T. Kopp, A.-S. Rüetschi, D. Jaccard, M. Gabay, D. A. Muller, J.-M. Triscone and J. Mannhart "Superconducting Interfaces Between Insulating Oxides" *Science,* vol. 317, pp. 1196-1199 (2007)

[209] M. Bibes, J. E. Villegas and A. Barthélémy "Ultrathin oxide films and interfaces for electronics and spintronics" *Advances in Physics,* vol. 60, pp. 5-84, 9 (2011)

[210] N. Driza, S. Blanco-Canosa, M. Bakr, S. Soltan, M. Khalid, L. Mustafa, K. Kawashima, G. Christiani, H.-U. Habermeier, G. Khaliullin, C. Ulrich, M. Le Tacon and B. Keimer "Long-range transfer of electron-phonon coupling in oxide superlattices" *Nature Materials,* vol. 11, pp. 675-681, 8 (2012)

[211] K. Rogdakis, J. W. Seo, Z. Viskadourakis, Y. Wang, L. F. N. Ah Qune, E. Choi, J. D. Burton, E. Y. Tsymbal, J. Lee and C. Panagopoulos "Tunable ferroelectricity in artificial tri-layer superlattices comprised of non-ferroic components" *Nature Communications,* vol. 3, p. 1064, 9 (2012)

[212] J. Chakhalian, J. W. Freeland, A. J. Millis, C. Panagopoulos and J. M. Rondinelli "Colloquium: Emergent properties in plane view: Strong correlations at oxide interfaces" *Rev. Mod. Phys.,* vol. 86, no. 4, pp. 1189-1202, 10 (2014)

[213] M. Lorenz "The 2016 oxide electronic materials and oxide interfaces roadmap" *Journal of Physics D: Applied Physics,* vol. 49, p. 433001, 9 (2016)

[214] D. L. Smith and C. Mailhiot "Theory of semiconductor superlattice electronic structure" *Reviews of Modern Physics,* vol. 62, pp. 173-234, 9 (1990)

[215] J. Mannhart and D. G. Schlom "Oxide Interfaces - An Opportunity for Electronics" *Science,* vol. 327, pp. 1607-1611, 9 (2010)

[216] Y. Tokura "Critical features of colossal magnetoresistive manganites" *Reports on Progress in Physics,* vol. 69, pp. 797-851, 2 (2006)

[217] J. Ravichandran, A. K. Yadav, R. Cheaito, P. B. Rossen, A. Soukiassian, S. J. Suresha, J. C. Duda, B. M. Foley, C.-H. Lee, Y. Zhu, A. W. Lichtenberger, J. E. Moore, D. A. Muller, D. G. Schlom, P. E. Hopkins, A. Majumdar, R. Ramesh and M. A. Zurbuchen "Crossover from incoherent to coherent phonon scattering in epitaxial oxide superlattices" *Nature Materials,* vol. 13, p. 168, 12 (2014)

[218] M. Maldovan "Phonon wave interference and thermal bandgap materials" *Nature Materials,* vol. 14, pp. 667-674, 7 (2015)

[219] D. P. Norton "Synthesis and properties of epitaxial electronic oxide thin-film materials" *Materials Science and Engineering: R: Reports,* vol. 43, pp. 139-247, 9 (2004)

[220] D. Dijkkamp, T. Venkatesan, X. D. Wu, S. A. Shaheen, N. Jisrawi, Y. H. Min-Lee, W. L. McLean and M. Croft "Preparation of Y-Ba-Cu oxide superconductor thin films using pulsed laser evaporation from high T_c bulk material" *Applied Physics Letters,* vol. 51, pp. 619-621 (1987)

[221] D. G. Schlom, J. N. Eckstein, E. S. Hellman, S. K. Streiffer, J. S. Harris, M. R. Beasley, J. C. Bravman, T. H. Geballe, C. Webb, K. E. Dessonneck and F. Turner "Molecular beam epitaxy of layered Dy-Ba-Cu-O compounds" *Appl. Phys. Lett.,* vol. 53, pp. 1660-1662, 10 (1988)

[222] R. A. Rao, Q. Gan, C. B. Eom, Y. Suzuki, A. A. McDaniel and J. W. P. Hsu, "Uniform deposition of $YBa_2Cu_3O_7$ thin films over an 8 inch diameter area by a 90° off-axis sputtering technique" *Appl. Phys. Lett.,* vol. 69, pp. 3911-3913, 10 (1996)

[223] C. Colvard, R. Merlin, M. V. Klein and A. C. Gossard "Observation of Folded Acoustic Phonons in a Semiconductor Superlattice" *Phys. Rev. Lett.,* vol. 45, no. 4, pp. 298-301, 7 (1980)

[224] B. Jusserand, D. Paquet and F. Mollot "Dispersive character of optical phonons in GaAlAs alloys from Raman scattering in superlattices" *Phys. Rev. Lett.,* vol.63, no. 21, pp. 2397-2400, 11 (1989)

[225] M. Cardona "Folded, confined, interface, surface, and slab vibrational modes in semiconductor superlattices" *Superlattices and Microstructures,* vol. 5, pp. 27-42 (1989)

[226] B. D. Rouhani and E. Khoudifi "Localised and extended acoustic waves in superlattices light scattering by longitudinal phonons" *Light scattering in Semiconductor Structures and Superlattices (Springer US) pp. 139-158,* vol. 89, 8 (1991)

[227] J. Sapriel and J. He "Interaction of light with acoustic waves in superlattices and related devices" *Light scattering in Semiconductors Structures and Superlattices (Springer) pp. 123-138,* vol. 107, 9 (1991)

[228] C. Colvard, T. A. Gant, M. V. Klein, R. Merlin, R. Fischer, H. Morkoc and A. C. Gossard "Folded acoustic and quantized optic phonons in (GaAl)As superlattices" *Phys. Rev. B,* vol. 31, no. 4, pp. 2080-2091, 2 (1985)

[229] B. Jusserand and M. Cardona "Light Scattering in Solids V" M. Cardona and G. Güntherodt, Eds., Springer (1989)

[230] M. W. C. Dharma-wardana, P. X. Zhang and D. J. Lockwood "Finite-size effects on superlattice acoustic phonons" *Physical Review B,* vol. 48, pp. 11960-11964, 5 (1993)

[231] V. K. Malik, I. Marozau, S. Das, B. Doggett, D. K. Satapathy, M. A. Uribe-Laverde, N. Biskup, M. Varela, C. W. Schneider, C. Marcelot, J. Stahn and C. Bernhard "Pulsed laser deposition growth of heteroepitaxial $YBa_2Cu_3O_7/La_{0.67}Ca_{0.33}MnO_3$ superlattices on $NdGaO_3$ and $Sr_{0.7}La_{0.3}Al_{0.65}Ta_{0.35}O_3$ substrates" *Phys. Rev. B,* vol. 85, no. 5, p. 054514, 2 (2012)

[232] M. V. Abrashev, J. Bäckström, L. Börjesson, M. Pissas, N. Kolev and M. N. Iliev "Raman spectroscopy of the charge- and orbital-ordered state in $La_{0.5}Ca_{0.5}MnO_3$" *Phys. Rev. B,* vol. 64, no. 14, p. 144429, 9 (2001)

[233] M. N. Iliev, M. V. Abrashev, V. N. Popov and V. G. Hadjiev "Role of Jahn-Teller disorder in Raman scattering of mixed-valence manganites" *Phys. Rev. B,* vol. 67, no. 21, p. 212301, 6 (2003)

[234] M. Bakr, S. M. Souliou, S. Blanco-Canosa, I. Zegkinoglou, H. Gretarsson, J. Strempfer, T. Loew, C. T. Lin, R. Liang, D. A. Bonn, W. N. Hardy, B. Keimer and M. Le Tacon "Lattice dynamical signature of charge density wave formation in underdoped $YBa_2Cu_3O_{6+x}$" *Phys. Rev. B,* vol. 88, no. 21, p. 214517, 12 (2013)

[235] P. Murugavel, C. Narayana, A. K. Sood, S. Parashar, A. R. Raju and C. N. R. Rao "Magnetic excitations in charge-ordered: A Brillouin scattering study" *Europhysics Letters,* vol. 52, pp. 461-467, 9 (2000)

[236] S. Rytov, Akusticheskii Zhurnal 2, 71 (1956) [*Sov. Phys. Acoust. 2, 68* (1956)]

[237] H. Hazama, Y. Nemoto, T. Goto, A. Asamitsu and Y. Tokura "Ultrasonic study of perovskite manganites $La_{1-x}Sr_xMnO_3$" *Physica B: Condensed Matter,* Vols. 281-282, pp. 487-488, 2000.

[238] J. D. Jorgensen, S. Pei, P. Lightfoot, D. G. Hinks, B. W. Veal, B. Dabrowski, A. P. Paulikas, R. Kleb and I. D. Brown "Pressure-induced charge transfer and dT_c/dP in $YBa_2Cu_3O_{7-x}$" *Physica C: Superconductivity,* vol. 171, pp. 93-102 (1990)

[239] M. M. Seikh, C. Narayana, S. Parashar and A. K. Sood "Temperature-dependent Brillouin scattering studies of surface acoustic modes in $Nd_{0.5}Sr_{0.5}MnO_3$" *Solid State Communications,* vol. 127, pp. 209-214 (2003)

[240] W. Li, B. He, C. Zhang, S. Liu, X. Liu, S. Middey, J. Chakhalian, X. Wang and M. Xiao "Coherent acoustic phonons in $YBa_2Cu_3O_7/La_{1/3}Ca_{2/3}MnO_3$ superlattices" *Applied Physics Letters,* vol. 108, p. 132601 (2016)

[241] L. Pintschovius and W. Reichardt "Phonon Dispersions and Phonon Density-of-States in Copper-Oxide Superconductors" *edited by A. Furrer, Neutron Scattering in Layered Copper-Oxide Superconductors (Springer, Dordrecht),* vol. 29, p. 495601, 11 (1998)

[242] F. Weber, S. Rosenkranz, J.-P. Castellan, R. Osborn, H. Zheng, J. F. Mitchell, Y. Chen, S. Chi, J. W. Lynn and D. Reznik "Response of Acoustic Phonons to Charge and Orbital Order in the 50% Doped Bilayer Manganite $LaSr_2Mn_2O_7$" *Physical Review Letters,* vol. 107, p. 207202, 9 (2011)

[243] A. Shekhter, B. J. Ramshaw, R. Liang, W. N. Hardy, D. A. Bonn, F. F. Balakirev, R. D. McDonald, J. B. Betts, S. C. Riggs and A. Migliori "Bounding the pseudogap with a line of phase transitions in $YBa_2Cu_3O_{6+\delta}$" *Nature,* vol. 498, pp. 75-77, 6 (2013)

[244] M. A. Carpenter, C. J. Howard, R. E. A. McKnight, A. Migliori, J. B. Betts and V. R. Fanelli "Elastic and anelastic relaxations associated with the incommensurate structure of $Pr_{0.48}Ca_{0.52}MnO_3$" *Phys. Rev. B,* vol. 82, no. 13, p. 134123, 10 (2010)

[245] B. Jusserand, F. Alexandre, J. Dubard and D. Paquet, "Raman scattering study of acoustical zone-center gaps in GaAs/AlAs superlattices" *Phys. Rev. B,* vol. 33, no. 4, pp. 2897-2899, 2 (1986)

[246] B. Jusserand, D. Paquet, F. Mollot, F. Alexandre and G. Le Roux "Influence of the supercell structure on the folded acoustical Raman line intensities in superlattices" *Phys. Rev. B,* vol. 35, no. 6, pp. 2808-2817, 2 (1987)

[247] B. Gorshunov, E. Zhukova, V. I. Torgashev, L. S. Kadyrov, E. A. Motovilova, F. Fischgrabe, V. Moshnyaga, T. Zhang, R. Kremer, U. Pracht, S. Zapf and M. Dressel "Boson peak in overdoped manganites $La_{1-x}Ca_xMnO_3$" *Phys. Rev. B,* vol. 87, no. 24, p. 245124, 6 (2013)

[248] E. Perret, K. Sen, J. Khmaladze, B. P. P. Mallett, M. Yazdi-Rizi, P. Marsik, S. Das, I. Marozau, M. A. Uribe-Laverde, R. Andrés Prada, J. Strempfer, M. Döbeli, N. Biškup, M. Varela, Y.-L. Mathis and C. Bernhard "Structural, magnetic and electronic properties of pulsed-laser-deposition grown $SrFeO_{3-\delta}$ thin films and $SrFeO_{3-\delta}/La_{2/3}Ca_{1/3}MnO_3$ multilayers" *Journal of Physics: Condensed Matter,* vol. 29, p. 495601, 11 (2017)

[249] T. Golod, A. Rydh, V. M. Krasnov, I. Marozau, M. A. Uribe-Laverde, D. K. Satapathy, T. Wagner and C. Bernhard "High bias anomaly in $YBa_2Cu_3O_{7-x}/LaMnO_{3+\delta}/YBa_2Cu_3O_{7-x}$ superconductor/ferromagnetic insulator/superconductor junctions: Evidence for a long-range superconducting proximity effect through the conduction band of a ferromagnetic insulator" *Phys. Rev. B,* vol. 87, no. 13, p. 134520, 4 (2013)

[250] K. Sen, E. Perret, A. Alberca, M. A. Uribe-Laverde, I. Marozau, M. Yazdi-Rizi, B. P. P. Mallett, P. Marsik, C. Piamonteze, Y. Khaydukov, M. Döbeli, T. Keller, N. Biškup, M. Varela, J. Vašátko, D. Munzar and C. Bernhard "X-ray absorption study of the ferromagnetic Cu moment at the $YBa_2Cu_3O_7/La_{2/3}Ca_{1/3}MnO_3$ interface and variation of its exchange interaction with the Mn moment" *Phys. Rev. B,* vol. 93, no. 20, p. 205131, 5 (2016)

[251] J. G. Bednorz and K. A. Müller "$Sr_{1-x}Ca_xTiO_3$: An XY Quantum Ferroelectric with Transition to Randomness" *Phys. Rev. Lett.,* vol. 52, no. 25, pp. 2289-2292, 6 (1984)

[252] C. W. Rischau, X. Lin, C. P. Grams, D. Finck, S. Harms, J. Engelmayer, T. Lorenz, Y. Gallais, B. Fauqué, J. Hemberger and K. Behnia "A ferroelectric quantum phase transition inside the superconducting dome of $Sr_{1-x}Ca_xTiO_{3-\delta}$" *Nature Physics,* vol. 13, pp. 643-648, 7 (2017)

[253] M. Cardona "Optical Properties and Band Structure of $SrTiO_3$ and $BaTiO_3$" *Phys. Rev.,* vol. 140, no. 2A, pp. A651-A655, 10 (1965)

[254] R. A. De Souza, J. Fleig, R. Merkle and J. Maier "$SrTiO_3$: A Model Electroceramic" *Zeitschrift für Metallkunde,* vol. 94, pp. 218-225 (2003)

[255] P. A. Fleury, J. F. Scott and J. M. Worlock "Soft Phonon Modes and the 110 °K Phase Transition in $SrTiO_3$" *Phys. Rev. Lett.,* vol. 21, no. 1, pp. 16-19, 7 (1968)

[256] J. Petzelt, T. Ostapchuk, I. Gregora, I. Rychetský, S. Hoffmann-Eifert, A. V. Pronin, Y. Yuzyuk, B. P. Gorshunov, S. Kamba, V. Bovtun, J. Pokorný, M. Savinov, V. Porokhonskyy, D. Rafaja, P. Vaněk, A. Almeida, M. R. Chaves, A. A. Volkov, M. Dressel and R. Waser "Dielectric, infrared, and Raman response of undoped $SrTiO_3$ ceramics: Evidence of polar grain boundaries" *Phys. Rev. B,* vol. 64, no. 18, p. 184111, 10 (2001)

[257] S. Van Aert, S. Turner, R. Delville, D. Schryvers, G. Van Tendeloo and E. K. H. Salje "Direct Observation of Ferrielectricity at Ferroelastic Domain Boundaries in $CaTiO_3$ by Electron Microscopy" *Advanced Materials,* vol. 24, pp. 523-527 (2012)

[258] P. Zubko, G. Catalan, A. Buckley, P. R. L. Welche and J. F. Scott "Strain-Gradient-Induced Polarization in $SrTiO_3$ Single Crystals" *Phys. Rev. Lett.,* vol. 99, no. 16, p. 167601, 10 (2007)

[259] K. A. Müller and H. Burkard "$SrTiO_3$: An intrinsic quantum paraelectric below 4 K" *Phys. Rev. B,* vol. 19, no. 7, pp. 3593-3602, 4 (1979)

[260] H. Uwe and T. Sakudo "Stress-induced ferroelectricity and soft phonon modes in $SrTiO_3$" *Phys. Rev. B,* vol. 13, no. 1, pp. 271-286, 1 (1976)

[261] J. Seidel, L. W. Martin, Q. He, Q. Zhan, Y.-H. Chu, A. Rother, M. E. Hawkridge, P. Maksymovych, P. Yu, M. Gajek, N. Balke, S. V. Kalinin, S. Gemming, F. Wang, G. Catalan, J. F. Scott, N. A. Spaldin, J. Orenstein and R. Ramesh "Conduction at domain walls in oxide multiferroics" *Nature Materials,* vol. 8, pp. 229-234, 3 (2009)

[262] C. Leighton "Electrolyte-based ionic control of functional oxides" *Nature Materials,* vol. 18, pp. 13-18, 1 (2019)

[263] Y. Z. Chen, N. Bovet, F. Trier, D. V. Christensen, F. M. Qu, N. H. Andersen, T. Kasama, W. Zhang, R. Giraud, J. Dufouleur, T. S. Jespersen, J. R. Sun, A. Smith, J. Nygård, L. Lu, B. Büchner, B. G. Shen, S. Linderoth and N. Pryds "A high-mobility two-dimensional electron gas at the spinel/perovskite interface of γ-Al_2O_3/$SrTiO_3$" *Nature Communications,* vol. 4, p. 1371, 1 (2013)

[264] F. Trier, D. C. Vaz, P. Bruneel, P. Noël, A. Fert, L. Vila, J.-P. Attané, A. Barthélémy, M. Gabay, H. Jaffrès and M. Bibes "Electric-Field Control of Spin Current Generation and Detection in Ferromagnet-Free $SrTiO_3$-Based Nanodevices" *Nano Lett.,* vol. 20, pp. 395-401, 1 (2020)

[265] G. Herranz, M. Basletić, M. Bibes, C. Carrétéro, E. Tafra, E. Jacquet, K. Bouzehouane, C. Deranlot, A. Hamzić, J.-M. Broto, A. Barthélémy and A. Fert "High Mobility in $LaAlO_3$/$SrTiO_3$ Heterostructures: Origin, Dimensionality, and Perspectives" *Phys. Rev. Lett.,* vol. 98, no. 21, p. 216803, 5 (2007)

[266] T. C. Rödel, F. Fortuna, S. Sengupta, E. Frantzeskakis, P. L. Fèvre, F. Bertran, B. Mercey, S. Matzen, G. Agnus, T. Maroutian, P. Lecoeur and A. F. Santander-Syro "Universal Fabrication of 2D Electron Systems in Functional Oxides" *Advanced Materials,* vol. 28, pp. 1976-1980 (2016)

[267] B. Casals, A. Schiaffino, A. Casiraghi, S. J. Hämäläinen, D. López González, S. Dijken, M. Stengel and G. Herranz "Low-Temperature Dielectric Anisotropy Driven by an Antiferroelectric Mode in $SrTiO_3$" *Phys. Rev. Lett.,* vol. 120, no. 21, p. 217601, 5 (2018)

[268] R. Azzam, N. Bashara and D. Burns "Ellipsometry and polarized light" North Holland, Amsterdam, *Analytica Chimica Acta,* vol. 199, pp. 283-284 (1987)

[269] P. R. Potnis, N.-T. Tsou and J. E. Huber "A Review of Domain Modelling and Domain Imaging Techniques in Ferroelectric Crystals" *Materials,* vol. 4, pp. 417-447 (2011)

[270] A. Dubroka, M. Rössle, K. W. Kim, V. K. Malik, L. Schultz, S. Thiel, C. W. Schneider, J. Mannhart, G. Herranz, O. Copie, M. Bibes, A. Barthélémy and C. Bernhard "Dynamical Response and Confinement of the Electrons at the $LaAlO_3/SrTiO_3$ Interface" *Phys. Rev. Lett.,* vol. 104, no. 15, p. 156807, 4 (2010)

[271] K. V. Reich, M. Schecter and B. I. Shklovskii "Accumulation, inversion, and depletion layers in $SrTiO_3$" *Phys. Rev. B,* vol. 91, no. 11, p. 115303, 3 (2015)

[272] H. Fu, K. V. Reich and B. I. Shklovskii "Anomalous conductivity, Hall factor, magnetoresistance, and thermopower of accumulation layer in $SrTiO_3$" *Phys. Rev. B,* vol. 94, no. 4, p. 045310, 7 (2016)

[273] B. Kalisky, E. M. Spanton, H. Noad, J. R. Kirtley, K. C. Nowack, C. Bell, H. K. Sato, M. Hosoda, Y. Xie, Y. Hikita, C. Woltmann, G. Pfanzelt, R. Jany, C. Richter, H. Y. Hwang, J. Mannhart and K. A. Moler "Locally enhanced conductivity due to the tetragonal domain structure in $LaAlO_3/SrTiO_3$ heterointerfaces" *Nature Materials,* vol. 12, pp. 1091-1095, 12 (2013)

[274] M. Rössle, C. N. Wang, P. Marsik, M. Yazdi-Rizi, K. W. Kim, A. Dubroka, I. Marozau, C. W. Schneider, J. Humlíček, D. Baeriswyl and C. Bernhard "Optical probe of ferroelectric order in bulk and thin-film perovskite titanates" *Phys. Rev. B,* vol. 88, no. 10, p. 104110, 9 (2013)

[275] D. J. Gray, T. A. Merz, Y. Hikita, H. Y. Hwang and H. Mabuchi "Orientation-resolved domain mapping in tetragonal $SrTiO_3$ using polarized Raman spectroscopy" *Phys. Rev. B,* vol. 94, no. 21, p. 214107, 12 (2016)

[276] H. Fujishita, S. Kitazawa, M. Saito, R. Ishisaka, H. Okamoto and T. Yamaguchi "Quantum Paraelectric States in $SrTiO_3$ and $KTaO_3$: Barrett Model, Vendik Model, and Quantum Criticality" *Journal of the Physical Society of Japan,* vol. 85, p. 074703 (2016)

[277] L. M. Vicente-Arche, J. Bréhin, S. Varotto, M. Cosset-Cheneau, S. Mallik, R. Salazar, P. Noël, D. C. Vaz, F. Trier, S. Bhattacharya, A. Sander, P. Le Fèvre, F. Bertran, G. Saiz, G. Ménard, N. Bergeal, A. Barthélémy, H. Li, C.-C. Lin, D. E. Nikonov, I. A. Young, J. E. Rault, L. Vila, J.-P. Attané and M. Bibes "Spin-Charge Interconversion in $KTaO_3$ 2D Electron Gases" *Advanced Materials*, vol. 33, p. 2102102 (2021)

[278] Y. Chen, Y. Lechaux, B. Casals, B. Guillet, A. Minj, J. Gázquez, L. Méchin and G. Herranz "Photoinduced Persistent Electron Accumulation and Depletion in $LaAlO_3/SrTiO_3$ Quantum Wells" *Phys. Rev. Lett.,* vol. 124, no. 24, p. 246804, 6 (2020)

[279] D. Li and D. A. Bonnell "Controlled Patterning of Ferroelectric Domains: Fundamental Concepts and Applications" *Annual Review of Materials Research,* vol. 38, pp. 351-368 (2008)

[280] W. Luo, M. Boselli, J.-M. Poumirol, I. Ardizzone, J. Teyssier, D. Marel, S. Gariglio, J.-M. Triscone and A. B. Kuzmenko "High sensitivity variable-temperature infrared nanoscopy of conducting oxide interfaces" *Nature Communications,* vol. 10, p. 2774, 6 (2019)

[281] J. Nagamatsu, N. Nakagawa, T. Muranaka, Y. Zenitani and J. Akimitsu "Superconductivity at 39 K in magnesium diboride" *Nature,* vol. 410, pp. 63-64, 3 (2001)

[282] E. Snider, N. Dasenbrock-Gammon, R. McBride, M. Debessai, H. Vindana, K. Vencatasamy, K. V. Lawler, A. Salamat and R. P. Dias "Room-temperature superconductivity in a carbonaceous sulfur hydride" *Nature,* vol. 586, pp. 373-377, 10 (2020)

[283] J. E. Hirsch and F. Marsiglio "Absence of high temperature superconductivity in hybrides under pressure" arxiv.org/abs/2010.10307 (2020)

[284] G. Landsberg and L. Mandelstam "Eine neue Erscheinung bei der Lichtzerstreuung in Krystallen" *Naturwissenschaften,* vol. 16, pp. 557-558, 7 (1928)